Blast and Post-Fire Behaviour of Glued-Laminated Timber Panels

by

Abla Krouma

Thesis submitted to the University of Ottawa

in partial fulfillment of the requirements for the degree of

Doctor of Philosophy

in Civil Engineering

Under the auspices of the Ottawa-Carleton Institute for Civil Engineering

uOttawa

Department of Civil Engineering

Faculty of Engineering

University of Ottawa

Abstract

The increasing trend toward taller timber structures, built with mass timber panels, has made it essential to understand the multi-hazard response of these structural elements and how subsequent or simultaneous hazards affect their performance. Current design standards provide guidelines for individual hazards, such as fire, blast, seismic, and wind in isolation, and only conceptual holistic design frameworks have been proposed, focusing mainly on redundancy and stability under multiple hazards. Limitations in conducting research on structural elements subjected to multi-hazard scenarios are largely driven by the high cost and practical challenges associated with such experiments.

An experimental program was developed that included twenty-three full-scale uncharred and charred glued-laminated timber panels tested under static and dynamic loading, with a focus on establishing their performance before and after exposure to a short-duration real fire. Simulated blast tests were conducted at the University of Ottawa Shock Tube facility, and the charred panels were extracted from the Mass Timber Demonstration Fire Test Program, a full-scale field fire test conducted in Ottawa, Canada, in 2022. In addition to the full-scale structural tests, twenty-five charred samples were examined using image analysis software.

The experimental results showed that the theoretical dynamic zero-strength layer value exceeds the static value, suggesting rate-dependent effects. The findings also demonstrated that a single-degree-of-freedom model with the Reduced Cross-Section Method can be a reliable predictive tool with proper inputs to simulate the dynamic response of structural elements for fire followed by blast loading scenario; a methodology that can be extended to other timber structural elements. Based on the experimental results, recommendations for Canadian design provisions were highlighted and discussed, and a detailed design example was presented.

Acknowledgements

After years of hard work and dedication, I am writing this note to thank everyone who supported me throughout this journey. It has been a great experience, not only on the academic side, but also on a personal level. The road was far from easy or straight, but I managed to overcome challenges with the support of those I mention here. Completing my PhD was one of the greatest goals of my life, and I am forever grateful to all the people who helped me reach it.

First and foremost, I thank my beloved mother, Nehal, for her unconditional love, support, and unwavering belief in me. Her guidance and encouragement were the greatest gifts anyone could ever receive. Without her, this PhD would never have been possible. This one is for you, Mom. To my angel, my sister Laila, thank you for your endless motivation and support throughout the years. To my brothers, Assem and Bashar and my sister-in-law, Sviatlana, thank you for your support and always being there since the very beginning.

I extend my deepest gratitude to my thesis supervisor, Prof. Ghasan Doudak. Thanks for being an amazing supervisor and a friend during this journey and for celebrating with me the good times and for being there during the difficult times. I could not have done this without your encouragement and trust. You gave me the freedom to learn, explore, and grow both academically and professionally. Thanks a million for the knowledge, opportunities, laughter, coffees and countless moments that made this journey memorable.

Special thanks go to the lab technical officers for their unwavering support and expertise. Dr. Gamal Elnabelsya, I could not have survived the lab without your support and the KitKats, and Dr. Muslim Majeed, I will always remember our chats. I also thank Luc Cloutier for his support. Special thanks to Dr. Joseph Su for his support and for sharing data. I am also sincerely grateful to Prof. Christian Viau for generously sharing his knowledge and support, Prof. Sam Salem for his constructive feedback, and Prof. Murat Saatcioglu and Prof. Hassan Aoude for their insightful comments.

To my friends: Rasha Alayash and Malak Hurqes, thank you for being by my side through this journey. Glenn Macdonald, thanks for your friendship and support. I am also thankful to all the friends who helped me during this journey: Osamah Mahmood, Esmaeil Morshedi, Lucas Civel, Issa Fowai, Antoine Bérubé, Dalu Xing, Saba Seyedrazavi, Cassandra Trottier, Fernanda Scussiato Lago, Bita Hosseinian Ahangarnazhad, and many others whose names I may not recall, but whose support I deeply appreciate. Special thanks go to Algonquin College Co-op team for their support and encouragement.

Finally, I would like to thank myself for not giving up, even when giving up felt so close. Great things take time, effort, and sacrifice. This achievement is not mine alone; it was made possible by my own persistence and by the support of those who care about me and believe in me.

Table of Contents

List of Tables

List of Figures

Symbols and Notations

Acronym	Definition
ABS	Absolute
ASTM	American Society for Testing and Materials
Avg.	Average
CEN	European Committee for Standardization
CLT	Cross-Laminated Timber
CSA	Canadian Standard Association
CV	Coefficient of variation
DAS	Data acquisition system
DIF	Dynamic increase factor
EAC	Energy-absorbing connection
EWP	Engineered wood products
FEA	Finite element analysis
FJ	Finger-joints
FRP	Fibre-reinforced polymer
GLT	Glued-Laminated Timber
ISO	International Organization for Standardization
LTD	Load transfer device
LVDT	Linear variable displacement transducer
LVL	Laminated veneer lumber
MC	Moisture content
MOE	Modulus of elasticity
MOR	Modulus of rupture
MSR	Machine stress rated
MTDFTP	Mass Timber Demonstration Fire Test Program
OSB	Oriented strand board
PUR	Polyurethane adhesive
RCSM	Reduced cross-section method
RPM	Reduced properties method
SD	Standard deviation
SDOF	Single-degree-of-freedom
SIF	Strength increase factor
SPF	Spruce Pine Fir
TDOF	Two-degree-of-freedom
TNT	Trinitrotoluene
TWS	Trainable Weka Segmentation
USACE	U.S. Army Corps of Engineers
ZSL	Zero-strength layer

Symbol	Definition
A	Loaded area
b	Panel width
b_{ef}	Effective width
b_i	Measured width of the panel
d	Panel depth
d_{ef}	Effective depth
d_i	Panel depth before char removal
d_r	Residual depth after char removal
d_{rc}	Thickness of the residual char layer
$\bar{e}_{Rmax}$	Mean error in maximum dynamic resistance
$\bar{e}_{\Delta Rmax}$	Mean error in displacement at maximum resistance
$\bar{e}_{tRmax}$	Mean error in time to maximum resistance
F(t)	Total external force as a function of time
f_b	Bending strength
I	Moment of inertia
I_R	Experimental reflected impulse
i_s	Positive impulse
i_s^-	Negative impulse
K	Stiffness
k_D	Load duration factor
k_H	System factor
k_L	Lateral stability factor
k_{LM}	Load-mass transformation factor
k_{sb}	Service condition factor
k_T	Treatment factor
k_{Zb}	Size factor
K_{fi}	Adjustment factor for fire resistance
L	Clear span length
m	Mass
m_c	Half of the LTD mass
P(t)	Pressure-time history
P_R	Experimental reflected pressure
P_o	Ambient pressure
$P_r(t)$	Reflected pressure-time history
P_{so}	Incident pressure
P_{so}^-	Negative pressure
R(t)	Dynamic resistance as a function of time
S	Section modulus
S_{ef}	Section modulus of the effective cross-section
t	Time
T(t)	Temperature as a function of time

T_0	Initial temperature
t_o	Positive phase duration
t_o^-	Negative phase duration
V(t)	Average dynamic reactions as function of time
$x_{p,i}$	Pyrolysis layer thickness using image analysis
$x_{p,v}$	Pyrolysis layer thickness using calliper
$x_{rc,i}$	Residual char layer thickness using image analysis
$x_{rc,v}$	Residual char layer thickness using calliper
x_c	Char depth
x_e	Deflection at elastic limit
x_t	thickness of ZSL
Z	Scaled distance
β	Charring rate
ɛ́	Strain-rate
ε_T	Tensile strain
ε_c	Compression strain
φ	Resistance factor

Chapter 1 Introduction

1.1 General

Glued-Laminated Timber (GLT) panels are engineered wood products (EWP) used mainly as roof or floor systems in mass timber structures. GLT is manufactured in different profiles by gluing lumber laminates oriented in the same direction using adhesive. Profiles include standard (the focus of the current study) and fluted, which provides enhanced acoustics, aesthetics, and insulation (Figure 1-1). The panels are commonly manufactured in a range of depths (80 mm to 350 mm) and widths up to 1,200 mm, depending on the manufacturer and project requirements. While these dimensions may vary, they represent standard production ranges frequently used in the construction industry unless customization is required.

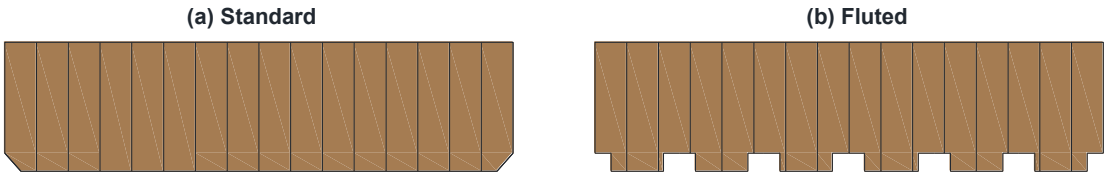

Figure 1-1 GLT panels profile types

An example of GLT use in buildings is the Mosaic Centre in Edmonton, Alberta, Canada (Figure 1-2 (a)), where GLT floor and roof panels are supported by a glulam post-and-beam frame system, and the Evergreen Line Transit stations in Vancouver, British Colombia, Canada (Figure 1-2 (b)).

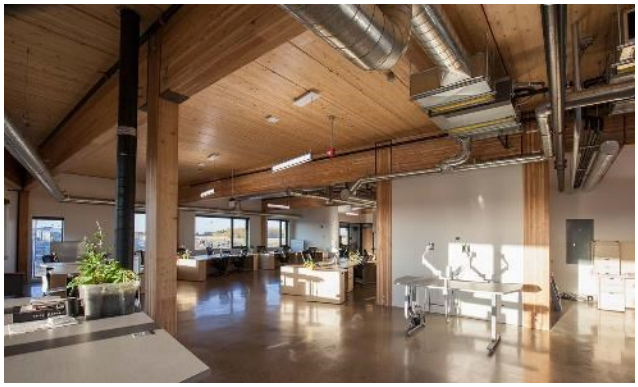

(a)

(b)

Figure 1-2 (a) The Mosaic Centre, and (b) Evergreen Line Transit station (*Western Archrib*, 2025)

Although glulam beams and GLT panels both consist of lumber boards with similar fibre orientation connected using finger joints and assembled using adhesive, they differ in terms of loading direction (Figure 1-3 (a)), lamination layup, and design approach. As shown in Figure 1-3 (b), while glulam beam members are typically manufactured using layup with higher grade materials in the outer laminates and lower grade materials in the core, i.e. $E1 > E2 > E3$, GLT panels typically have random laminations. As these laminations are randomly positioned in the panel, they do not develop the unique optimization obtained in glulam beams, and as such, they are treated in design as sawn lumber members of "No.2 or better" grade. In the Canadian wood design standard (CSA, 2024), GLT panels are referred to as vertically glued laminated timber beams. It is noteworthy to mention that the size factor used in the design of these elements is usually conservatively assumed to be based on the depth of the panel and the width of the individual laminations rather than the width of the full panel.

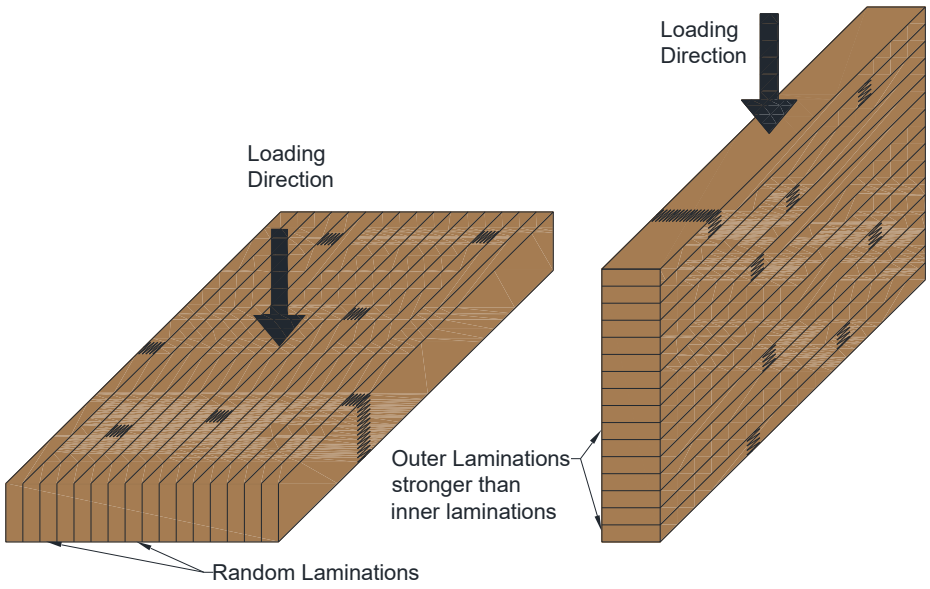

(a)

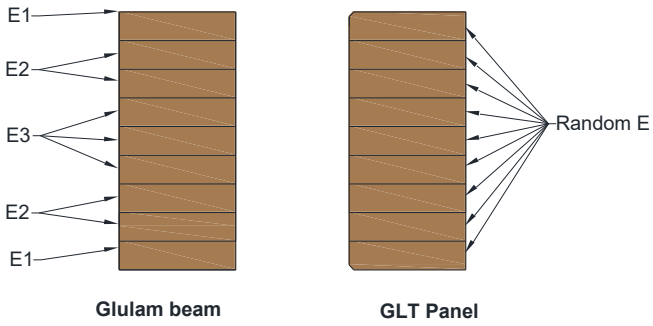

(b)

Figure 1-3 Glulam beam vs GLT panel: (a) Loading direction, and (b) Lamination layup

1.2 Research Needs

Mass timber construction is on the rise, primarily due to its structural and sustainability attributes, as well as heightened levels of prefabrication and rapid construction speed. The number of tall timber buildings, defined by the Council on Tall Buildings and Urban Habitat as having at least eight stories, was 89 buildings as of February 2022 (Safarikrch et al., 2022). Moreover, the Ontario Building Code (2024) in Canada was amended to allow encapsulated mass timber construction up to 18 storeys, which is an increase from the previous limit of 12

storeys (Ashworth et al., 2025). Although these trends present clear indication that several major challenges related to structural, fire as well as serviceability performances have been overcome, they also lead to heightened potential for exposure and risk of timber buildings to accidental or intentional blast explosions and fire. Furthermore, consideration for multi-hazard scenarios, such as an explosion due to fire, has not been adequately investigated for these types of buildings (Fink et al., 2023).

The widespread use of GLT panels for roof application is primarily due to the optimized use of fibre especially for one-way bending applications. Their use in floor applications is less frequent, mainly due to limited research on vibration performance (e.g., Ebadi et al., 2017, 2018, 2019). Wall applications are also infrequent due to scarce research on GLT walls under in-plane lateral loads (e.g., D'Arenzo & Seim, 2023, 2024; Wrzesniak & Fragiacomo, 2016). The outcome of the current study will provide the necessary design parameters and facilitate the design of GLT walls and floors to load scenarios such as out-of-plan blast loading as well as blast induced after a short exposure to fire.

Over the past two decades, numerous experimental studies have investigated the behaviour of various timber structural elements under blast loading. A limited number of studies have been conducted using live explosive testing (e.g., Weaver et al., 2018), while other studies have generated high strain-rates using split-Hopkinson pressure bar (e.g., Bragov & Lomunov, 1997) or conducted impact tests using drop-weight impact apparatus (e.g., Sukontasukkul et al., 2000; Wight et al., 2024). A number of studies have used Shock Tube testing to provide significant data on blast load effects on timber elements and connections. Several studies have focused on solid-sawn lumber (e.g., Bragov & Lomunov, 1997; Gerhards, 1977; Jacques et al., 2014), stud walls (e.g., D. Lacroix & Doudak, 2015; Viau et al., 2017; Viau & Doudak, 2016a), as well as Cross-Laminated Timber (CLT) (e.g., Côté & Doudak, 2019; Poulin et al., 2018; Viau & Doudak, 2019a), glulam beams and columns (e.g., D. Lacroix & Doudak, 2018b; D. N. Lacroix

& Doudak, 2019; Viau & Doudak, 2021a) and boundary connections (e.g., Viau & Doudak, 2016b, 2019b, 2021c). Furthermore, few studies have investigated the behaviour of timber elements subjected to blast loading using numerical analysis (e.g., V. T. Le et al., 2021; Oliveira et al., 2023; Šliseris et al., 2017). While the aforementioned studies focused on the dynamic behaviour of solid-sawn lumber, CLT and Glulam elements, to the author's knowledge, no studies have been undertaken on the dynamic behaviour of the GLT panels subjected to blast loading alone or blast following fire exposure.

The behaviour of timber elements under fire has been extensively studied, particularly for glulam elements, CLT panels, and connections. These tests have been conducted in furnace facilities (e.g., Chen et al., 2017; Frangi & Fontana, 2005; Radzi et al., 2021; Vairo et al., 2023) or through field testing with simulated real fire on a large-scale structure (e.g., Brandon et al., 2021; Su et al., 2023). Parameters associated with fire performance, such as char- and zero-strength layer (ZSL) thicknesses, have also been investigated thoroughly for solid-sawn timber, glulam and CLT due to their crucial role in assessing the residual section capacity (e.g., Schaffer et al., 1999; Schmid et al., 2015; Xing et al., 2021). Furthermore, several studies have focused on the behavior of connections under fire (e.g., Hegazi & Salem, 2024; Okunrounmu et al., 2024). However, to the author's knowledge, limited studies have dealt with the behaviour of GLT panels post real fire (e.g., Ranger et al., 2019; Su et al., 2023).

Currently, design standards provide guidelines and design provisions for hazards, such as fire, blast, seismic and wind, in isolation, and only holistic design frameworks have been proposed in the literature, focusing on the redundancy and stability of the structures under multiple hazards (e.g., Roy & Matsagar, 2022). An example of a blast followed by fire is the UNBC's Wood Innovation Research Laboratory explosion (2023), where a gas explosion created a shock wave that damaged the exterior façade and allowed fire to enter the building. An example of fire followed by an explosion is Beirut Port Explosion (2020) in Lebanon. Limited research

investigated fire and blast hazards occurrences using Finite Element Analysis (FEA) on steel and reinforced concrete materials, either simultaneously (e.g., Li et al., 2024; Ruan et al., 2015) or sequentially (e.g., Choudhary et al., 2024; Roy & Matsagar, 2021; S. Zhang et al., 2025). However, to the author's knowledge, no numerical or experimental studies have examined the sequential fire followed by blast scenario for timbers elements.

1.3 Objectives

The overarching goal of this research study is to evaluate the static and dynamic behaviour of GLT panels under blast loads and post real fire. The specific objectives of the research are:

1- Investigate the zero-strength layer (ZSL) thickness in GLT panels post real fire; in order to evaluate the post fire structural performance;
2- Establish dynamic- and strength increase factors for GLT panels and investigate the failure behaviour of uncharred panels under static and dynamic blast loads;
3- Evaluate the structural performance of GLT panels post real fire under static and dynamic blast loads, and assess whether the dynamic and strength increase factors are valid for charred panels;
4- Develop resistance curves to use in a single-degree-of-freedom (SDOF) model capable of capturing the dynamic behaviour of charred and uncharred GLT panels;
5- Examine current blast design values and provide recommendations where applicable.

1.4 Scope and Limitations

To accomplish aforementioned objectives, the following steps were undertaken:

- Conduct a comprehensive literature review on the structural behaviour of timber structural elements subjected to blast loads and fire in addition to review blast wave

characteristics, dynamic analysis methods, and current design codes approaches for blast and fire design;

- Prepare full-scale charred GLT specimens for static and dynamic tests by cleaning them and measuring their char depth;
- Prepare small-scale charred samples and conduct image analysis to determine the discolored heated zone (i.e. pyrolysis layer thickness) and evaluate the applicability of such image analysis tools;
- Test uncharred and charred GLT panels statically to establish strength increase factor (SIF) and static failure modes;
- Test uncharred and charred GLT panels dynamically to establish dynamic increase factor (DIF) and dynamic failure modes; zero-strength layer thickness;
- Quantify ZSL thickness post-real fire under low and high-strain loading
- Discuss the results for charred and uncharred GLT panels and propose design recommendations, where applicable.

The research is limited to Spruce Pine GLT panels, tested under simply-supported boundary conditions. The charred specimens were obtained from a real fire test, which was part of the Mass Timber Demonstration Fire Test Program (MTDFTP) conducted in Ottawa, Canada, in 2022 (Su et al., 2023). The fire test itself is not part of the current study, which focuses primarily on the structural performance. The research outcomes are limited to a post-fire assessment, and the ZSL thickness was found after the fire had self-extinguished naturally and the panels were left to cool down to ambient temperature. The research is focused on Canadian design standards; however, the findings may be generalizable and adapted to other international standards.

1.5 Thesis Structure

Chapter 1 introduces the topic and presents the research needs, scope, and objectives.

Chapter 2 presents a detailed review of the literature on timber structural elements subjected to blast loads and fire.

Chapter 3 introduces the experimental program, including the specimens' description, test matrix, charred specimens' preparations steps and test setups.

Chapter 4 presents the experimental results of the char depth measurements, charring rate, residual char, pyrolysis layer and zero-strength layer thickness, as well as static and dynamic test results for both uncharred and charred GLT panels.

Chapter 5 describes the analytical modelling approach used and provide comparison between analytical and experimental results.

Chapter 6 discusses the experimental and analytical results for charred and uncharred panels and the result's impacts on current design codes.

Chapter 7 presents a summary of the key findings of the research in addition to recommendations for future work.

Appendix A presents the drawing plans and sections of the MTDFTP full-scale structure.

Appendix B describes the full-scale charred GLT specimens before and after char removal and provides char depth measurement results.

Appendix C presents the results of the digital image analysis of the small-scale charred GLT samples.

Appendix D presents detailed results of GLT panels static tests.

Appendix E presents detailed results of GLT panels dynamic tests.

Appendix F presents the SDOF modelling results.

Chapter 2 Literature Review

2.1 General

The behaviour and design of timber elements under fire or blast loading have been widely investigated, while limited research has been conducted on multi-hazard scenarios, where an event such as fire triggers a load like blast several minutes after the initial fire incident and when the structural element likely experienced some reduction in their structural integrity. This chapter presents a comprehensive literature review on blast load characteristics, dynamic analysis method, as well as fire effect on wood elements and current design standards approaches.

2.2 Blast Loads

2.2.1 Blast Wave

Blast is a shock wave that occurs rapidly and decreases with increasing distance from the explosion center. The decrease affects the wave strength, duration, arrival time, and impulse. The explosive materials could be solid, liquid or gas. Trinitrotoluene (*TNT*) is an example of a solid explosion, the effects of which are well established (Department of Defense, 2014).

The energy released from the explosion transforms the blast charge into gas with very high temperature and pressure. This pressure is referred to as incident pressure (P_{so}) and is higher than the ambient pressure (P_o), as shown in Figure 2-1. The peak incident pressure decreases while the duration (t_o) increases when the shock wave propagates until the pressure reaches ambient pressure value. This stage is called the positive phase and is followed by a negative phase with a duration (t_o^-), which is typically longer than the positive one, but with a magnitude (P_{so}^-) that is less than the positive incident pressure, leading to designers neglecting it for main structural elements exposed to blast from all sides. The positive and negative impulses (i_s) and (i_s^-) represent the area under the pressure curve and is vital for design. A simple equation

governing the blast wave is referred to as the modified Friedlander equation, as described in Equation 2-1, where (b) is the decay coefficient, (t) is the time after the arrival of the shock wave (Department of Defense, 2014).

$$P(t) = P_{so}\left(1 - \frac{t}{t_0}\right)e^{-b\frac{t}{t_o}} \qquad 2\text{-}1$$

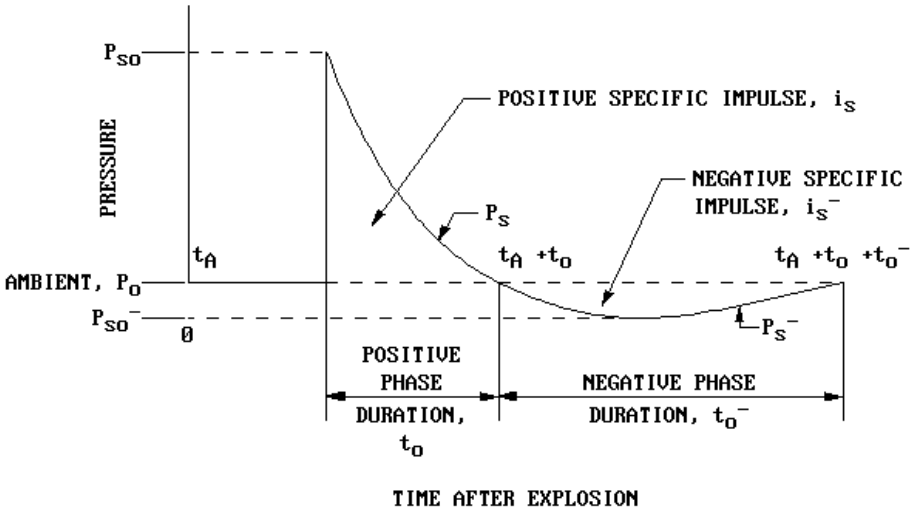

Figure 2-1 Blast wave pressure-time curve (Department of Defense, 2014)

2.2.1 Dynamic Analysis

Due to the short duration of blast loading, dynamic analysis is typically the default analysis, mainly due to the need to include the inertia forces and consider the released energy. Using an SDOF system as a modelling technique to predict various structural elements' behaviour is acceptable for blast loads, due to the uncertainty associated with blast events and the simplicity of using this type of analysis technique (USACE, 2008). The idealized SDOF system is governed by the equation of motion shown in Equation 2-2, represented by a lumped concentrated mass *(m)* in the middle and stiffness *k*, which are equated to the blast force expressed as a function of time *F(t)*. Damping is typically neglected due to the very short duration of the blast and the focus being typically on the maximum behaviour (e.g., displacement) of the structural elements (Biggs, 1964).

$$m\ddot{y}(t) + ky(t) = F(t) \quad 2\text{-}2$$

To use this approach for real systems, transformation factors are required to modify the distributed mass into an equivalent mass through the use of load-mass factor (K_{LM}). The load-mass factor for a simply-support beam with distributed mass and elastic behaviour is equal to 0.87, and the dynamic equation of equilibrium can be written as shown in Equation 2-3, where $R(y)$ is the dynamic resistance, $P_r(t)$ is the reflected pressure-time history, and A is the loaded area (Biggs, 1964).

$$K_{LM}m\ddot{y}(t) + Ry(t) = P_r(t)A \quad 2\text{-}3$$

The SDOF modelling approach have been proven to be effective in modelling various structural elements from different materials subjected to blast loads (e.g., Aoude et al., 2015; Côté & Doudak, 2019; Jacques et al., 2013; Poulin et al., 2018).

2.3 Wood Material Behaviour under High Strain Rate Loading

Liska (1950) conducted one of the earliest studies on the effect of rapid loading rate, which corresponds to higher short-term strain rates, on clear wood samples of softwood and hardwood species. It was found that bending strength was increased with higher loading rate whereas the stiffness was unaffected. Gerhards (1977) reported that the strength in specimens with different moisture contents varied under loading rates and emphasized wood's strain-rate sensitivity.

Mindess & Madsen (1986) investigated the behaviour of spruce beams in an impact apparatus in three different cases: clear wood, clear wood with a long notch sawn on the bottom face of the beam under the impact point, and lastly, beam with a large knot near the bottom face and away from the impact point. The failure behaviour of all specimens was reported to be similar. Failure initiation occurred in crushing under the impact application point followed by

propagation of a single crack on the tension side to the impact application point and tensile failure of the longitudinal fibres.

Bragov & Lomunov (1997) conducted dynamic tests on pine and birch specimens at strain rates of 500 s^{-1} and 1500 s^{-1} and reported that compressive strength increases with rate. Vural & Ravichandran (2003) investigated the dynamic behaviour of balsa and showed that the initial failure stress increased substantially, depending on density, at high strain rates compared to quasi-static loading. Neumann et al. (2011) reported that spruce in axial compression exhibits higher strength and energy absorption with increasing strain rate and that lateral confinement mainly enhances the energy at large deformations rather than the peak strength, emphasising the role of boundary conditions in impact behaviour. Gilbertson & Bulleit (2013) tested maple and pine wood and reported dynamic strengths about 2 to 2.5 times the quasi-static values. Wouts et al. (2016) further demonstrated that compressive crushing and plateau stresses in spruce and beech approximately doubled in the longitudinal direction while perpendicular to grain increases are smaller, confirming strong direction-dependent strain-rate sensitivity of wood.

It should be noted that the majority of these aforementioned studies pertained to small-scale specimens, often free from the natural defects usually occurring in wood structural elements. While some evidence of strain rate effects had been reported, limited conclusions pertaining to full-scale structural elements could be made. Full-scale representative testing is required to obtain applicable data that can be codified and used in design (Barrett & Lau, 1994).

2.4 Full-Scale Timber Elements Behaviour under Simulated Blast Loads

Experimental testing involving blast loading is often achieved via either live testing, where actual explosives are detonated, or Shock Tube testing, which provides a test environment with the capability to obtain high-quality data. Over the last decade, the University of Ottawa Shock

Tube Testing Facility has allowed for the simulation of the effect of blast loads to be imparted onto large and full-scale timber elements. The facility comprises a Shock Tube, which is a test apparatus capable of producing high strain rates similar to those observed during far-field blast explosions. The following sections review existing literature on experimental and numerical studies on blast-loaded wood elements.

2.4.1 Light-Frame Wood Stud Walls

Some of the earliest experimental research on blast load effects on timber structures was conducted on full-scale light-frame homes subjected to nuclear blasts (Kimbell & Fies, 1953; Randall, 1961). Post-test observations revealed that the failure of these structures was heavily dependent on the structural continuity in the systems through properly designed connections.

Marchand (2002) conducted live-explosive testing on full-scale light-frame wood stud wall structures. The study focused on the structure's overall behaviour and was limited to qualitative experimental results. Since no in-situ properties of the structural members were measured during testing, Oswald (2005) used published data to obtain the strength and stiffness of the specimens and conduct damage assessment to develop design provisions and response limits for wood structures.

Jacques et al. (2014) studied the behaviour of spruce-pine-fir studs under static and simulated blast loads at strain rates between $6x10^{-6}$ s^{-1} and 0.4 s^{-1}. The wooden studs showed linear elastic behaviour until failure, and the DIF on the modulus of rupture was reported to be equal to 1.4. Lacroix & Doudak (2015) investigated the behaviour of machine stress-rated (MSR) studs within wall assemblies through static and dynamic testing. The dynamic failure mode was a brash tension failure in the mid-span region, as shown in Figure 2-2. The DIF was 1.18 and 1.4 for stiffness and resistance, respectively. The experimental results showed that increasing sheathing thickness shifted the failure to flexural failure in the stud. Similar observations were

observed by Viau & Doudak (2016a) who investigated similar stud wall configurations against more severe blast loads. The study also included retrofit options for stud walls, including wood-steel composite sheathing and catcher system.

(a) (b)

Figure 2-2 Dynamic Failure mode in Stud Walls with: (a) OSB Sheathing (b) Plywood Sheathing (Lacroix & Doudak, 2015)

The effect of different typical and designed wall-to-floor connections in light-frame wood stud walls subjected to blast loads was investigated by Viau & Doudak (2016b). Experimental results paved the way for establishing damage levels that are suitable for light-frame wood stud wall systems (Viau et al., 2017).

2.4.2 Engineered Wood Products

Sukontasukkul et al. (2000) investigated the failure mechanism of Parallel Strand Lumber (PSL) under impact loads and the failure was characterized as flexure with splinters occurring on the tension side, in addition to shear failure as shown in Figure 2-3.

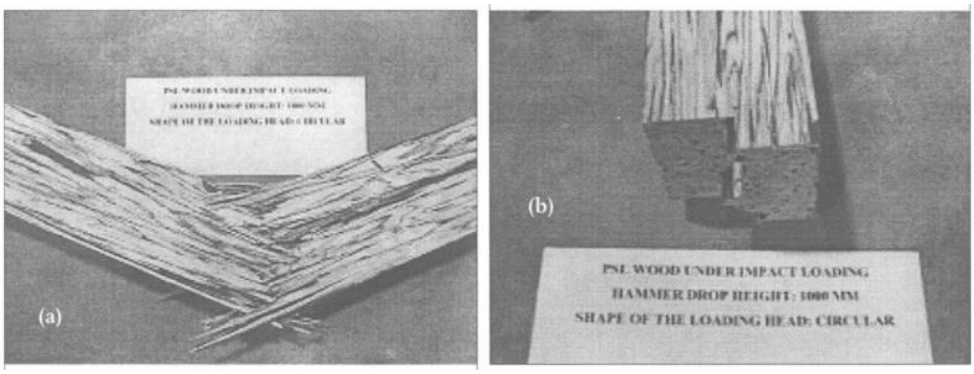

(a) (b)

Figure 2-3 PSL Failure mode: (a) Flexural and (b) Shear failure (Sukontasukkul et al., 2000)

Šliseris et al. (2017) conducted a non-linear numerical study on a CLT wall element under simulated blast loads, however the results of the study were not validated using experimental results. It was found that the blast impulse duration had a significant effect on the strength of the CLT panels, and the shear deformation of CLT layers significantly impacted vibration amplitude. Increasing the number of layers while keeping the depth constant decreased the amplitude and increased the vibration frequency.

Weaver et al. (2018) conducted a full-scale air-blast test on three two-story cross-laminated timber structures at the Air Force Civil Engineer Center, as shown in Figure 2-4. In addition, single CLT panels were tested for comparison purposes. The axial loads reduced blast load damage, and the difference in axially loaded and unloaded panel displacement under the same blast load conditions was around 10%.

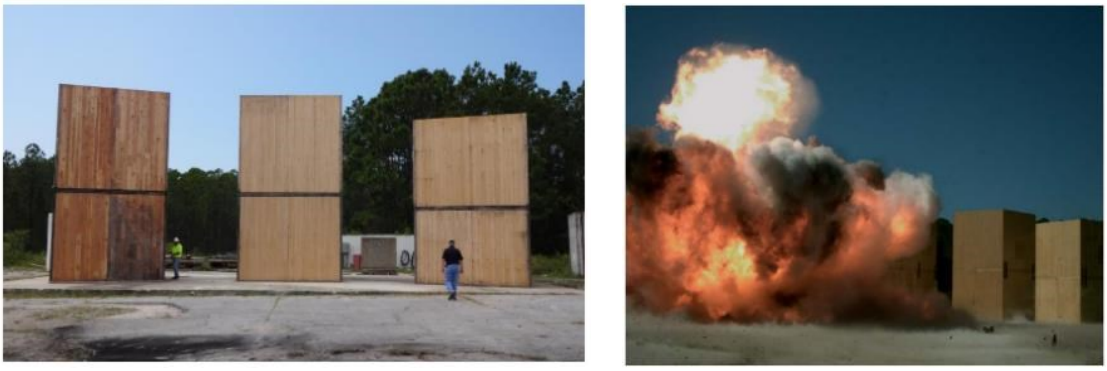

Figure 2-4 Full scale blast test for CLT structures before and after air blast (USACE Protective Design Center Omaha District, 2018).

D. Lacroix & Doudak (2018b) tested Spruce-Pine glulam beams under simply-supported boundary conditions subjected to simulated blast loads. The failure mode observed was flexural brash tension failure. The strength of the glulam elements (beams and columns) increased under simulated blast loads compared to static results. The columns exhibited localized damage in the mid-span region and buckling of laminations on the compression side. Failure modes were reported, as shown in Figure 2-5. D. Lacroix & Doudak (2018a) found that the DIF was equal to 1.14 for strain rates ranging from 0.14 s^{-1} and 0.51s^{-1}.

(a) (b) (c)

Figure 2-5 Failure modes in glulam elements: (a) Beam (b) Column (c) Column midspan damage (D. Lacroix & Doudak, 2018)

Poulin et al. (2018) reported that the observed dynamic failure mode of simply supported CLT panels with different thicknesses under simulated blast loads was flexure and rolling shear, as shown in Figure 2-6. The rolling shear resulted in the longitudinal laminates deflecting as individual laminates. The DIF was reported to be 1.28 for resistance and unity for stiffness. Côté & Doudak (2019) investigated realistic boundary conditions of CLT panels and reported a significant impact on the failure mode when connections were used.

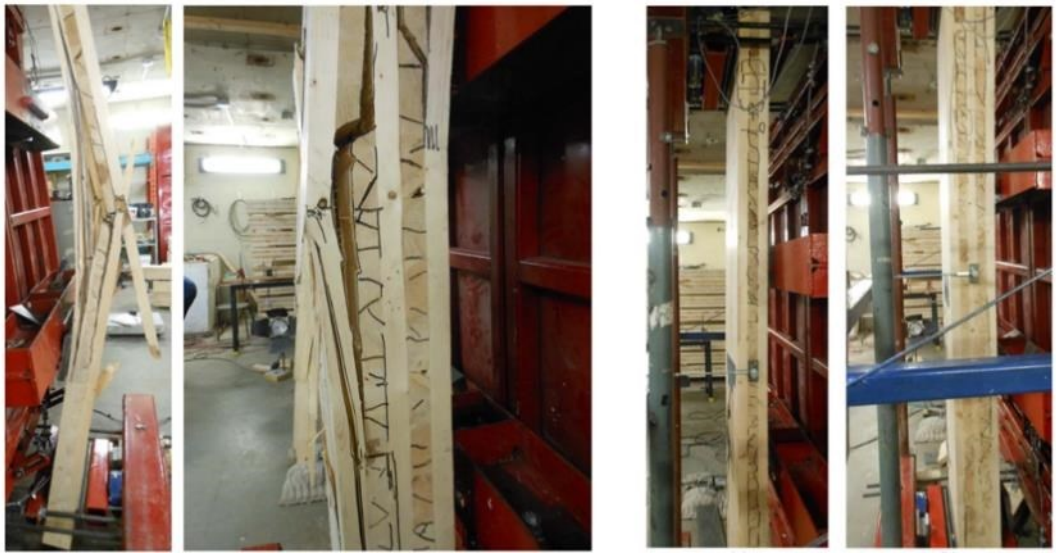

(a) (b)

Figure 2-6 CLT Failure modes under blast loads: (a) Flexural failure (b) Rolling shear (Poulin et al., 2018)

Van Le et al. (2020) investigated simply-supported Radiata pine CLT panels under static and dynamic loads. The blast loads were simulated using Shock Tube apparatus and compared to numerical models. The DIF for the modulus of elasticity was found between 1.05 and 1.43, however, the study did not provide a corresponding DIF for strength, as panels were not tested to failure.

Phillips et al. (2021) investigated the behaviour of simply supported structural insulated panels, which consist of a foam core between two oriented strand boards (OSB) under simulated blast pressures generated using a Shock Tube Facility. Shear in the nail connections was the dominant failure, followed by OSB fracture due to horizontal splitting in the foam and separation between the OSB and foam compression face.

Viau & Doudak (2021a) studied the effect of realistic boundary connections on the behaviour of glulam beam elements using bolted connections or by adding self-tapping screws to reinforce the connections. The latter was found to significantly affect the overall beam

behaviour and failure modes, as shown in Figure 2-7. It was reported that the reinforcement reduced the perpendicular to grain splitting significantly.

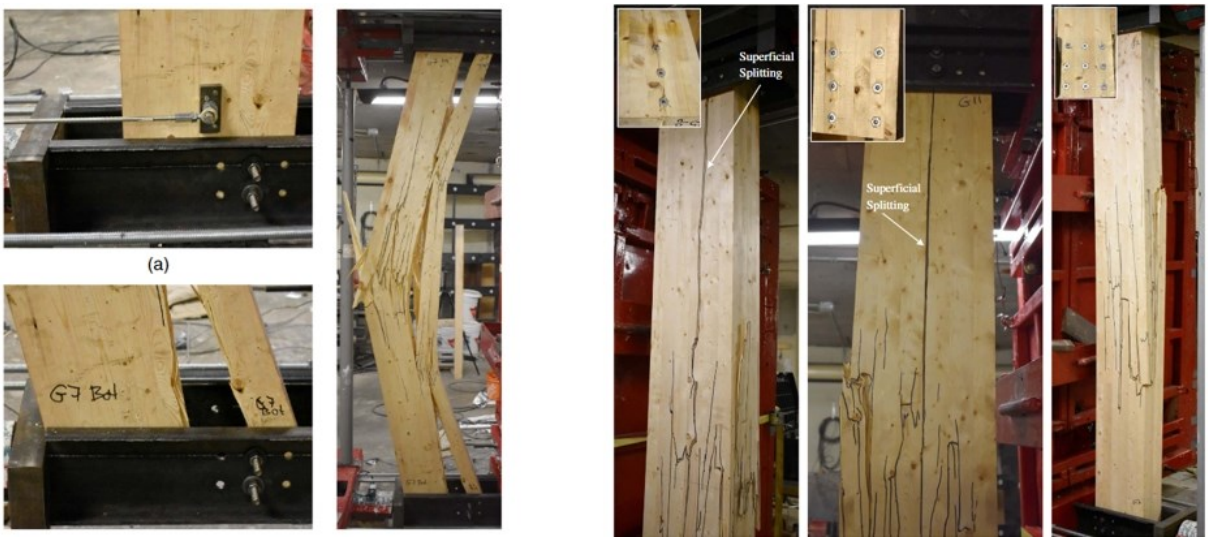

(a) (b)

Figure 2-7 Glulam beams failure modes with realistic boundary conditions: (a) bolted connection, (b) Added self-tapping screws reinforcement (Viau & Doudak, 2021a)

Van Le et al. (2021) conducted an FE numerical simulation of bioinspired conch-like CLT panels, shown in Figure 2-8, with different middle plank angles and widths. It was found that these elements performed better than regular CLT panels under blast loads in terms of energy dissipation, velocity, and reaction force. The angle of the middle plank influenced the blast performance, and angles equal to 30º to 45º performed best. It was also found that plank widths had almost no effect on the energy dissipation.

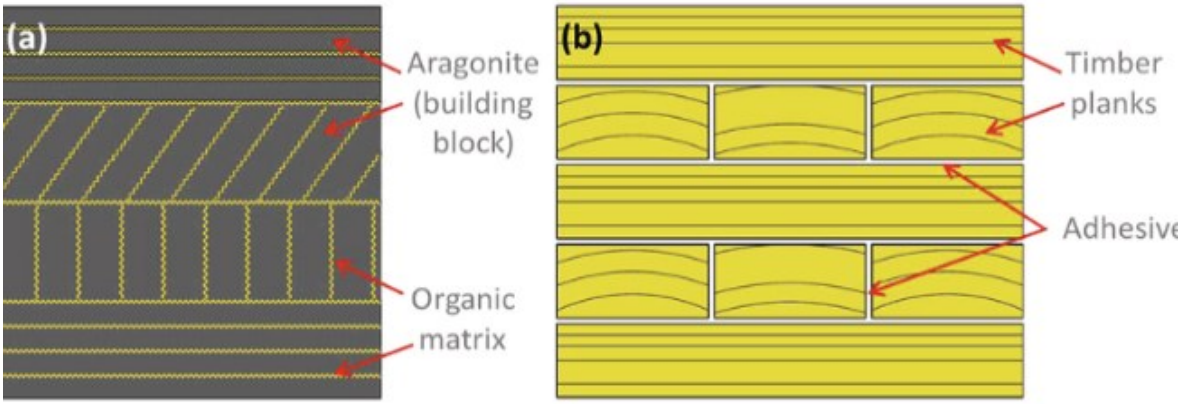

(a) (b)

Figure 2-8 Comparison between the microstructure of conch-like panels: (a) and CLT panels (b) (Van Le et al., 2021)

Extensive research has been carried out to predict the behaviour of CLT panels and glulam beams with realistic boundary conditions under blast loads. The results confirmed that two-degree-of-freedom models (TDOF) provided reasonable results and was capable of predicting the behaviour of the assemblies containing different types of boundary connections (Viau & Doudak, 2021c). Viau & Doudak (2021b) investigated the use of energy-absorbing connections (EAC) in glulam and CLT elements under simulated blast loads and reported that these types of connections performed better than typical bolted and screw-type connections. Additional research on the criteria for selection of EAC was performed, and results were compared to SDOF and finite element model for verifications (Bérubé & Doudak, 2023, 2024).

Retrofit options specific to blast have been explored, such as glulam beams and columns using Fiber Reinforced Polymers (FRP) (D. N. Lacroix & Doudak, 2018), light-frame stud walls retrofitting (Lacroix et al., 2014) and CLT panels (Lopez-Molina & Doudak, 2019).

In summary, full-scale blast testing of timber elements consistently demonstrates that high strain rates enhance dynamic resistance and affect failure modes. Realistic boundary conditions, connections detailing, and panel configuration play a critical role in governing both deformation and failure mechanisms, and numerical models, including SDOF and TDOF, have

shown good agreement with experimental results when calibrated with proper inputs. The following section will provide insights on fire exposure effects on wood as material and structural element.

2.5 Fire in Buildings

2.5.1 Compartment Fires

Fires in buildings that typically occur within enclosed spaces are referred to as 'compartment fires', where the fire development is influenced by the space geometry, ventilation conditions, fuel load, and thermal properties of surrounding surfaces. The fire development stages within a compartment start with ignition, followed by growth, as the fire starts to develop and heat is transferred to structural elements through a combination of convection and radiation, resulting in rapid temperature rise at exposed surfaces. The next stage is the fully developed stage, during which compartment fires can reach gas temperatures exceeding 1000 °C, which leads to significant thermal degradation of structural materials. In the final stage, following fuel consumption or firefighting intervention, the fire starts the decay phase where the temperatures gradually decrease; however, this cooling phase can still result substantial thermal degradation on structural members (Drysdale, 2011).

Compartment fires are highly variable and depend on several parameters, therefore, direct representation of their thermal exposure in structural design is challenging. As a result, idealized fire representations, such as standard fire curves, have been developed to approximate the thermal effects of compartment fires for design and testing purposes.

2.5.2 Fire Curves

The main aim of fire design is to ensure that structural elements can withstand fire exposure for a sufficient duration to allow safe evacuation and to provide firefighters the necessary time to control or extinguish the fire. The fire resistance of structural elements is determined by

exposing the element to a fire in a furnace, where fire based on standard time-temperature curves are applied. Standard curves include ISO 834 (2025), used internationally, and CAN/ULC-S101 (2014) and ASTM E119 (2024), which are primarily used in North America. While these standard curves are based on similar assumptions and represent comparable fire severity, they are defined by different standards and formulations. ISO 834 (2025) standard fire curve is provided in Equation 2-4, where time (t) given in minutes, while (T_0) is the initial temperature in °C.

$$T(t) = T_0 + 345 \log_{10}(8t + 1) \quad \text{2-4}$$

The temperature profile in a real fire differs from standard furnace curves, and terms 'natural fire' and 'parametric fire' are often used to distinguish realistic fire exposures from standard curves. The term 'natural fire' can refer either to the actual fire scenario (i.e., realistic growth, fully developed, and cooling phase) or to the modelled time-temperature curves that approximate such realistic exposure. Whereas a 'parametric fire' refers to simplified time-temperature curves derived from design equations to approximate such natural conditions (Drysdale, 2011). The term 'real fire' refers to measured fire exposures obtained from full-scale compartment tests.

2.5.3 Fire Resistance

Fire resistance requirements depend on the use of the building, size of fire compartments and the building height. One way to achieve a required fire resistance rating is through structural design of the elements by increasing the cross-sections based on the anticipated char depth and ZSL. There are several methods to calculate the fire resistance of structural wood elements. Lie (1977) developed one of the first simplified approaches to estimate the fire resistance as a function time for large wood columns and beams of glulam and solid sawn members. This

method depends on the number of sides exposed to fire and requires the elements' dimensions and load factor based on the element effective length and depth.

There are two approaches to evaluating the resistance of the residual cross-section, namely by treating the cross-section as a single homogeneous material or as a composite material. Within the homogeneous material approach, two methods have been used. The first is the reduced cross-section method (RCSM), which is currently used in design standards. In this method, the cross-section is reduced by removing char depth and ZSL, while material properties at ambient temperature are used for the remaining cross-section. The second method is the reduced properties method (RPM), where resistance is determined by modifying the specified strength at room temperature using a reduction factor. This method has later been removed from Eurocode (CEN, 2025) due to being unconservative compared to RCSM (Schmid et al., 2019). The composite model approach, called the advanced method in Eurocode (CEN, 2025), determines resistance by integrating temperature-dependent mechanical properties across the cross-section, which requires more rigorous calculation complicated compared to the aforementioned models (White, 2024).

Fire safety and design guidelines have long been available in Canadian standards, either for timber elements or other materials such as concrete and steel. National Building Code of Canada (Canadian Board for Harmonized Construction Codes (CBHCC), 2025) provide provisions regarding occupants' safety and building protection from fire. While Part 9 of National Building Code contains generic fire-resistance rating and fire performance ratings information for wood members and assemblies, CSA O86 (2024) provides a method in Annex B to calculate fire-resistance ratings and estimate the residual section capacity for large cross-section wood element. This method applies to solid-sawn timber, CLT, and glued-laminated timber and includes equations to calculate char depth and ZSL.

In order to utilize the RCSM method in this study, the following sections review existing literature on wood material behaviour under fire and charring in wood in addition to experimental and numerical studies on wood elements exposed to standard, parametric and real fire.

2.6 Wood Material Behaviour under Fire

Wood undergoes thermal degradation under fire, which depends on several factors: exposure time, temperature level, moisture content, stress grade, species type, density, and heating medium. The thermal degradation reduces strength, mainly due to depolymerization reactions. Wood pyrolyzation undergoes four main temperature regimes. The first one is between 100 and 200 ºC, where the water evaporates, non-combustible gases, such as CO_2, formic acid and acetic acid, are released and the wood starts to char. The second regime is between 200 to 300 ºC, where additional gases are released, CO in particular, and hemicelluloses and lignin components start to pyrolyze in addition to increasing char occurring in the wood. The third regime is between 300 to 450 ºC, where advanced depolymerization occurs in the cellulose, and further degradation occurs in the lignin in addition to increasing the char amount. At the last stage, above 450 ºC, the remaining wood chars until only ashes remain (Forest Products Laboratory, 2021).

The thermal degradation in wood exposed to fire is illustrated in Figure 2-9, and can be divided into: (1) char layer on the surface with no strength, (2) heat-affected zone with reduced strength, including: a pyrolysis zone, which is a dark brownish transitional layer, and a heated zone that is not fully pyrolyzed but cannot be distinguished by discoloration (i.e., is not visibly charred), and (3) sound wood layer, which is not affected by heat, maintains its strength at ambient temperature, and represents the effective cross-section post-fire (Forest Products Laboratory, 2021).

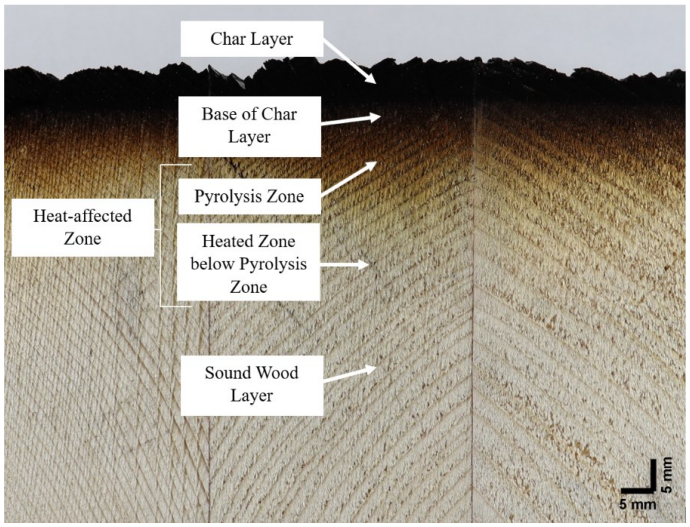

Figure 2-9 Thermal degradation in glued-laminated timber panels post fire

Schmid et al. (2014) reported that the residual cross-section and ZSL are significant for calculating the load-bearing capacity of timber. Due to wood's low thermal conductivity, the temperature at the innermost zone of the char layer is assumed to be 300°C, while the temperature beneath the char layer (around 6 mm inward) can be as low as 180°C, which will result in a reduction in material strength.

Early work on charring rate and ZSL was conducted by Schaffer (1966), who reported that the charring rate is approximately linear and depends on the species, density, moisture content, chemical composition, and permeability of the wood species. Furthermore, Schaffer (1966) investigated various species under ASTM E119 (2023) standard fire and data were used to develop calculation models for char depth while considering the moisture content and density. The study found an average charring rate of 0.8 mm/min for many softwoods, 1.0 mm/min for low-density species, and 0.6 - 0.7 mm/min for denser woods. The study proposed a simplified linear charring rate model for design while adding an extra 20% char depth to account for unseen burn and section corner rounding, which was a first step to introduce the concept of ZSL. White (1988) expanded the work and conducted a comprehensive experimental study on a total of 20 wood species exposed to ASTM E119 (2023) standard fire, and reported consistent

softwood charring rates of 0.6-0.8 mm/min during the first 30 min, decreasing thereafter to 0.6 mm/min. Low-density hardwoods charred at comparable rates, whereas high-density hardwoods charred more slowly (0.5 mm/min).

Subsequent studies investigated the charring rate under both standard and non-standard fire exposures. Mikkola (1991) found that charring under non-standard exposure is proportional to the ratio of external heat flux over density. Collier (1992) and White & Nordheim (1992) reported that density and moisture content affect charring rate. More recent studies have confirmed that charring rates in the range of 0.6 - 0.8 mm/min under standard fire curves are reasonable (e.g., Fahrni et al., 2019)

The aforementioned studies consistently demonstrate that fire exposure reduces wood material strength and that the effective cross-section can be determined when the char layer and ZSL thickness are known, which is essential for determining post-fire resistance. While the fundamental mechanisms of wood degradation under fire are now reasonably well understood, their structural implications depend on the structural element type and fire exposure conditions. Therefore, the following section reviews experimental and numerical studies on the behaviour of full-scale timber elements under standard and non-standard fire exposures.

2.7 Timber Elements Behaviour Under Fire

Fire exposure type has a critical influence on charring, development of the ZSL, and ultimately the residual capacity of timber elements. White & Nordheim (1992) investigated softwood beams exposed to fire for at least 20 min and defined the thermal penetration depth as the distance between the char front and the plane where the temperature returns to ambient in the cross-section. From these tests, an average thermal penetration depth of 33 mm was obtained, but a more conservative value of 40 mm was recommended in other tests conducted by Janssens & White (1994). Schaffer et al. (1999) estimated the ZSL to be 8 mm for beams. Schmid et al.

(2015), however, reported that the ZSL for glulam members in bending, tension and compression exceeded the value used in Eurocode (European Committee for Standardization, 2004). Fahrni et al. (2019) investigated six spruce glulam beams and reported a mean notional charring rate to be equal to 0.73 mm/min, while the mean value of ZSL was 6.4 mm, and reported that local defects and density have an influence on residual capacity. Tang et al. (2022) examined residual capacity under three sides standard fire exposure for mixed-species glulam and found that the residual capacity of mixed-species were significantly higher than the capacity of single-species glulam beam after 20 min of fire exposure.

A significant limitation of standard fire testing is that it typically focuses on elements integrity during fire but overlook the cooling phase when delayed failures may occur. Horio et al. (2016) investigated glulam beams under standard fire exposure for 1 h followed by natural cooling in furnace for up to 3 h, while load is applied in bending. The study reported that internal temperatures kept rising in the cooling period, resulting in continued thermal degradation of the uncharred core. The beam tested immediately at the end of heating retained around 30% of its original bending capacity, whereas the beam tested after 3 h of cooling phased retained only around 14%. Although additional charring during cooling was minimal, the ZSL deepened as heat penetrated (20 mm), and recommendation was made to consider the cooling phase in standard fire tests. Gernay et al. (2023) reached similar conclusions when testing spruce glulam columns exposed to short heating (15 min) followed by controlled cooling, where columns collapsed during the cooling phase, despite furnace gas temperatures having already fallen below 50 °C. Thermocouple results indicated continuous heat penetration, which resulted in a reduction in core strength during the cooling phase.

Quiquero et al. (2018) and Chorlton & Gales (2020) examined non-standard, short-duration, and localized fire exposures, which differ substantially from standard fire-curves. Quiquero et al. (2018) examined the post-fire performance of Spruce-Pine-Fir glulam elements and reported

estimated ZSL value of 23 mm. Further, the study indicated that the assumption in CSA O86 (2024) of ZSL equal to 7 mm was found insufficient, as many factors, such as fire type, duration, and size of the charred area, might affect this value. Chorlton & Gales (2020) examined Spruce glulam and Pine Laminated veneer lumber (LVL) beams. The research showed that the ZSL extended to a minimum of 11.7 mm for LVL and 12.3 mm for glulam, with failure modes varying depending on whether the fire affected the moment or shear zone.

Other studies compared the behaviour of timber elements under parametric and standard fire exposures. Lange et al., (2015) tested Spruce glulam beams exposed to two standard fire scenarios and two parametric fires (a long-cool fire and a short-hot fire). Charring rates varied from 0.36 mm/min (long-cool) to 1.0 mm/min (short-hot), and ZSL values ranged from 8 to 16 mm. The study reported that the ZSL specified in Eurocode (European Committee for Standardization, 2004) was found unconservative, and RCSM overestimated residual capacity unless ZSL was adjusted. Huč et al. (2021) investigated beams exposed 44 ventilation controlled parametric fire scenarios using a numerical approach that combined parametric fire curves, a hygro-thermal model, and a mechanical resistance model. The study reported ZSL values ranging between 8.4 and 30.5 mm, increasing with longer duration and slower cooling rate. Maximum char depth reported was 83.8 mm, and the residual bending resistance dropped to 30% of the initial capacity. Huč et al. (2023) expanded the research by investigating the ZSL thickness in timber beams exposed to 46 fuel controlled parametric fire scenarios and reported an average value of ZSL equal to 12.4 mm, which was strongly influenced by maximum gas temperature, cooling rate, and fire duration, with the best predictive accuracy linked to cooling rate. The study reported that fixed ZSL values in current standards underestimate section loss. Zhang et al. (2022) compared parametric and equivalent standard fires using energy-based time equivalence method and found that differences in charring depth typically remained below

10%. The study validated the time-equivalence method and indicated that parametric fires may be represented by equivalent standard exposures for some applications.

Xing et al. (2021) investigated the behaviour of CLT floors under standard and natural fire test conditions, where the latter was obtained from previous measured temperature fire data. The study reported that Eurocode (European Committee for Standardization, 2004) charring rate assumptions were non-conservative under natural fires due to lamination fall-off, and ZSL values changed substantially after the loss of the first lamination. Huč et al. (2025) investigated beams exposed to 44 natural fire curves that includes heating and cooling phases. The results showed that average charring rate was 0.69 mm/min and average ZSL was 21.4 mm, with charring thickness strongly influenced by maximum gas temperature, while ZSL was mainly dependent on the cooling rate. The study proposed new predictive equations with a simple linear relation between effective thickness and maximum gas temperature and reported that residual capacity loss under natural fire is more severe, and time-dependent compared to standard assumptions.

In 2022, five large-scale fire tests were conducted in Ottawa as part of MTDFTP. The full-scale mass timber structure consisted of a two-story, four-bay building with an area of 3600 ft^2. The building was constructed of glulam columns and beams, CLT, DLT and GLT floor and roof panels, as shown in Figure 2-10. The elements were designed according to Annex B of CSA O86 with at least 2-hour fire resistance rating. The scenarios in all tests assumed that the fire extinguisher system would not work, there would be a delay in fire services, and sprinklers would not go off. The mass timber ceiling, beams, and columns elements, in addition to the CLT walls, were not treated nor protected. However, few elements were protected by gypsum boards. The structure was instrumented with 400 thermocouples and radiation sensors to collect data and information on the fire development. From a structural design point of view, it was found that the average char depth of specimens agreed well with the design requirements of

CSA O86 and remained within the allowable range. Further, the structure remained stable after the fire (Su et al., 2023).

Figure 2-10 Full-scale mass timber structure used in Ottawa Fire Test: Before, during and after the fire test (Su et al., 2023).

Seyedrazavi & Viau (2025) investigated the post real fire performance of five full-scale glulam columns, which were extracted from the MTDFTP. The findings showed average charring rate of 2.3 mm/min, which is 3 times higher than the value in CSA O86 (2024), and the visual degradation layer thickness ranged between 9.7-17.2 mm, exceeding the 7 mm ZSL code value. Predicted axial capacities based on measured section loss were roughly 33% lower than CSA O86 (2024) calculations, even though residual stiffness was near manufacturer values.

2.8 Summary

This chapter provided a comprehensive review of the literature concerning the behaviour of timber members subjected to blast loads and fire exposure independently. Existing research indicates that high strain rates during blast loading enhance the dynamic resistance of timber.

In contrast, fire exposure results in thermal degradation and a loss of cross-sectional area due to charring. Despite these findings, there is a notable gap in the literature regarding the sequential multi-hazard scenario of fire followed by blast. As such, investigating the behaviour of timber elements under fire followed by blast loading is essential to fully understand structural performance during multi-hazard events. These observations prompted the author to explore the idea of blast loading induced by fire experimentally and analytically, as will be described in the following chapters.

Chapter 3 Experimental Program

3.1 General

This section presents the specimen descriptions, test matrix, test types, and the setups used in the experimental program. The aim of the experimental program is to obtain material characteristics such as DIF and SIF, and failure mechanisms in addition to quantify ZSL. The investigation also includes conducting image analysis of twenty-five small-scale charred samples in order to estimate the residual char and pyrolysis layer thickness in GLT panels post real fire.

3.2 Specimens Description

The research project includes testing a total of twenty-three full-scale Spruce-Pine charred and uncharred GLT panels under static and simulated blast loads with simply supported boundary conditions. Sixteen out of the twenty-three GLT panels were uncharred. Eleven panels (seven uncharred and four charred) were tested statically, and twelve panels (nine uncharred and three charred) were tested dynamically until failure. Two different GLT panel depths were considered, namely 130 mm and 215 mm, while maintaining nominal width of 610 mm. The original width and depth of the charred panels prior to fire exposure were 610 mm and 215 mm, respectively. The actual measured width of the panels ranged between 603 and 608 mm. All specimens had a consistent span during testing of 2,235 mm, which was selected to accommodate the end-frame opening of the Shock Tube apparatus. Finger-joints (FJ) in the panels were distributed randomly along the length of the laminations. The specified bending strength and modulus of elasticity of the panels according to the manufacture specifications were 11.8 MPa and 9,500 MPa. These properties are consistent with those published in the CSA (2024) standard for SPF grade No. 1/2.

The charred specimens were obtained from Test (5), as part of the MTDFTP project. Test (5) represented a fire test of a fully furnished open-plan office with 18 working cubicles and a fuel load density of 362 MJ/m^2. This test represented the worst-case scenario, including high fuel load, high ventilation, and absence of fire services and sprinklers (Su et al., 2023). The GLT specimens were roof panels located in Bay 4, between lines 3 and 4 and lines A and B, as shown in Figure 3-1 and Figure 3-2. Additional information about the building layout is presented in the structural drawings provided in Appendix A.

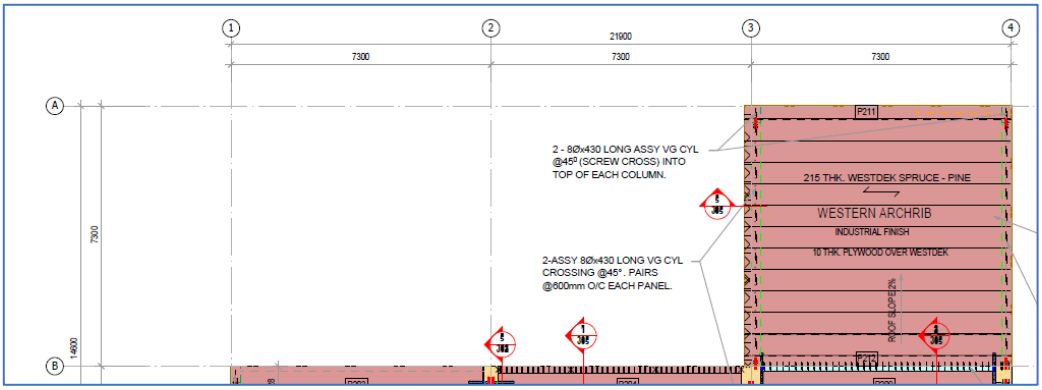

Figure 3-1 Partial second-floor plan – GLT Panels (See Appendix A)

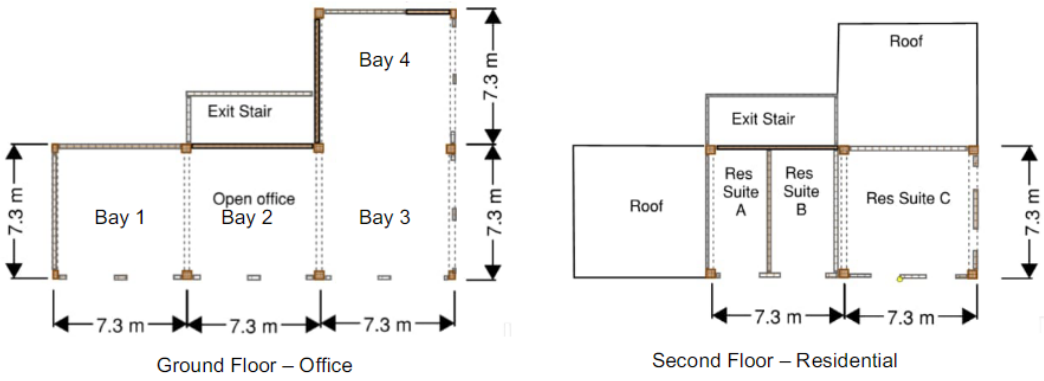

Figure 3-2 Location of bays in the mass timber structure - plan view (Su et al., 2023)

The following sections provide some details on the fire test. Although the fire test is not directly part of the current study, the description provided herein is essential to offer context and

information on the condition of the test samples prior to their arrival to the University of Ottawa's structural lab.

The initial fire growth in Test (5) took 3 min and 40 sec and spread across the exposed timber ceiling within 2 min at an average speed of 140 m/s. The fire spread across the open office plan within 7 to 18 min. The fire started to decay after 18 min and ceased after 21 min on the ceiling, beams and columns, 30 min in the area containing cubicles and within 60 min after all debris was consumed. Flames were observed and reported entering and exiting Bay 4 during approximately 12 min based on video recordings and visual observations (Su et al., 2023). The charred GLT panels in Figure 3-3 are shown immediately after the fire test and prior to dismantling them from the structure.

(a) (b)

Figure 3-3 Charred GLT panels in Bay 4 after the fire: (a) GLT panels on B204 (b) GLT Panels on B206 (Su et al., 2023)

The average char depth was reported to be 24 mm for the floor panels in general and ranged between 15 and 40 mm, as shown in Figure 3-4. A Resistograph (an electronically controlled drilling device), where a long and thin drill is driven through the charred elements, was used to determine the residual depth. (Su et al., 2023).

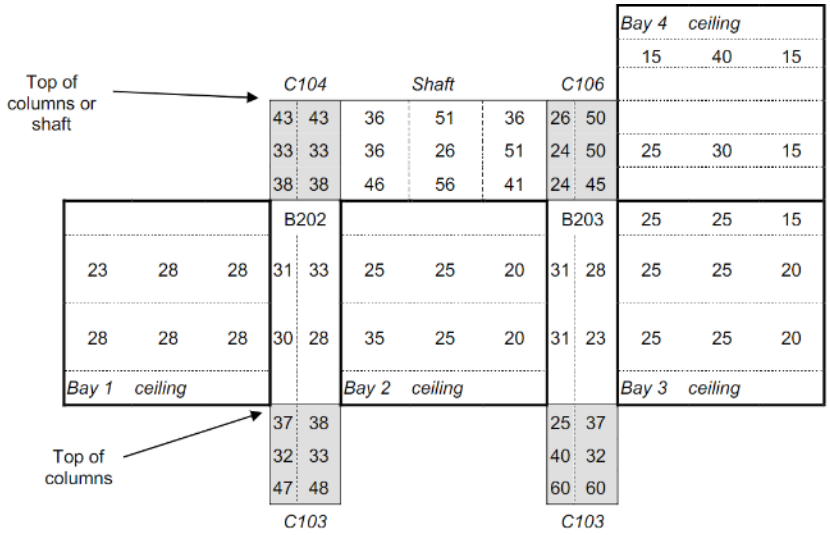

Figure 3-4 Char depth (mm) for Test (5) (Su et al., 2023)

The gas temperature was measured at 150 mm below the ceiling in Bay 4 using nine thermocouples as shown in Figure 3-5. The peak temperature was around 1200 °C, and it occurred approximately 10 min after the initial ignition (Su et al., 2023). The ceiling gas temperatures were non-uniform and varied across the thermocouples due to the large open-plan compartment. As the specific location of the extracted GLT panels in Bay 4 was not clearly defined, the fire exposure duration was evaluated individually for each thermocouple. A threshold temperature of 400 °C was adopted to define fire exposure duration, given that gas temperatures do not directly represent timber surface temperatures because of heat transfer losses and the insulating effect of the char layer. The fire exposure durations in Bay 4 ranged from 25.7 to 43.5 min.

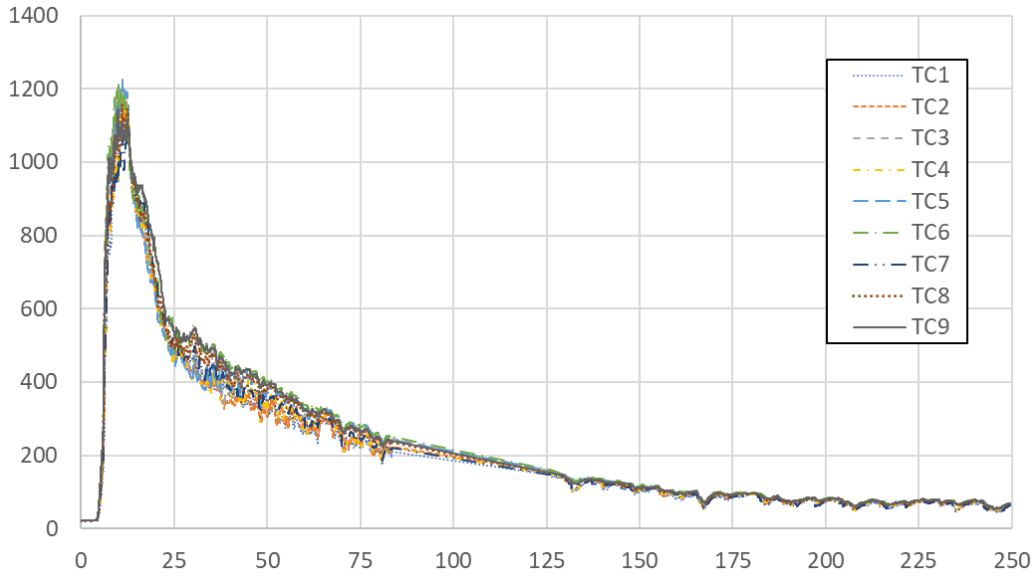

Figure 3-5 Gas temperature at 150 mm below the ceiling in Bay 4 for Test (5) (Su et al., 2023)

A total of twenty-five small-scale samples were obtained from an additional charred specimen, which had an average depth of 198.5 mm, a width of 598 mm and a length 2650 mm. The charred GLT specimen was first sliced across the panel length (Figure 3-6) and five slices were obtained. The specimens' depth was reduced to maintain a manageable size of the charred area, as shown in Figure 3-7 (a). The faces of the slices were smoothed to improve image clarity. Further, each slice was cut into five samples with approximately 120 mm width, as shown in Figure 3-7 (b).

Figure 3-6 Location of the cuts made in the charred GLT specimen along the panel length

(a) (b)

Figure 3-7 An example of image analysis small-scale specimens: (a) Slice (b) Sample

3.3 Test Matrix

The full-scale charred and uncharred specimens tested as part of the current study, along with the destructive loading types (i.e., static or dynamic), are summarized in Table 3-1. The prefix "C" in front of GLT refers to the charred samples. The first number following that notation refers to the specimen number, while the number inside the brackets refers to the panel depth. It should be noted that the panel depth for the charred samples refers to the original dimension prior to charring. In addition to the full-scale structural tests, twenty-five charred samples with dimensions 120x85 mm were examined using an imaging analysis software. The nomenclature for the specimens investigated for imaging analysis starts with the letter S (distinguishing these as small-scale specimens), followed by a number, which refers to the specimen slice number, and a second number referring to the sample number within the slice. For example, S1-2 refers to sample 2 within slice 1.

Table 3-1 Test Matrix for full-Scale specimens

Loading Type	Specimen Type	Specimens Name
Static Destructive	Uncharred	GLT1 [130] – GLT3 [130] GLT4 [215] – GLT7 [215]
	Charred	CGLT1 [215] – CGLT4 [215]
Dynamic Destructive	Uncharred	GLT8 [130] – GLT14 [130] GLT15 [215] – GLT16 [215]
	Charred	CGLT5 [215] – CGLT7 [215]

For the charred panels, in both static and dynamic tests, loading was applied to the uncharred face such that the charred face was subjected to tensile stresses. This configuration represents a conservative failure scenario, which accounts for reduced tensile resistance of fire-damaged timber, including the effects of charring and the zero-strength layer. While some blast scenarios (e.g., internal explosions) may place the uncharred face in tension, the scope of the present study is limited to scenario of interior fire exposure followed by exterior blast loading, where the fire-affected region governs tensile response.

3.4 Full-Scale Charred Specimens Preparation

There is no standardized or agreed-upon procedure for preparing specimens from structural elements which have been exposed to fire, and as such the preparation method and extent was dictated by the purpose of the investigation. Since the aim was to investigate the residual capacity of the specimens, which requires identifying the char depth, in addition to failure behaviour, it was essential to remove the char layer before the destructive tests to measure the char depth and ensure that failure cracks are visible.

Prior to preparing the specimens for the destructive structural testing, measurements of the panel dimensions were taken before and after char removal and any existing visible cracks were documented. The specimen preparation only focused on the face of the panel that was exposed to the fire. The recorded measurements of the panel depth were done using a hand-held digital calliper, which was deemed sufficient to ensure accuracy given the variability in the remaining charred portion. The measurements took place at key selected locations, including supports, load applications, and corners, as outlined in Figure 3-8. The four faces of the specimens were identified as Up (U), Down (D), Right (R), and Left (L) for tracking purposes. The specimens had various total lengths which was reduced before testing, and the clear span was consistent across all specimens.

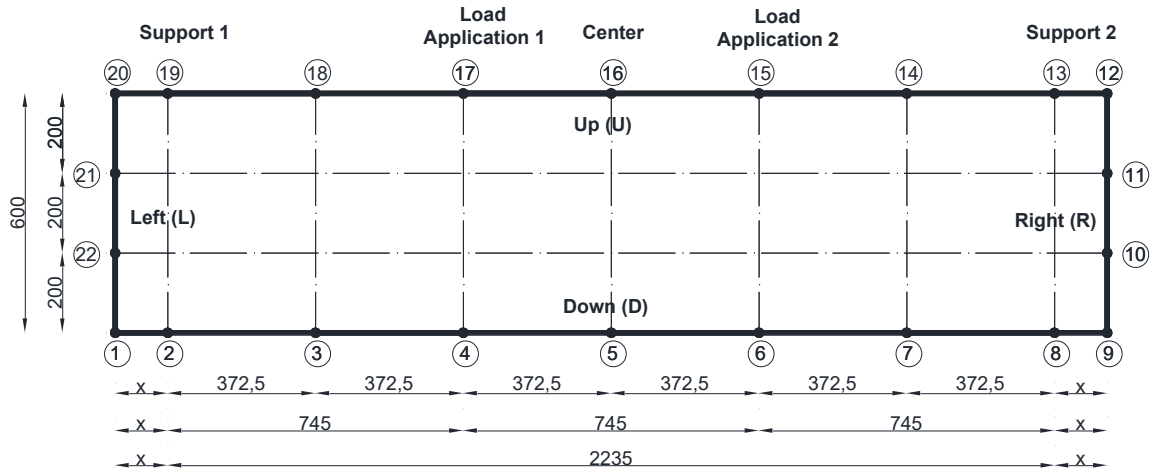

Figure 3-8 Full-scale specimens dimension plan

The specimen condition before char removal is shown in Figure 3-9 (a). The char removal process consisted of three main stages, namely: 1) Removal of char dust using a vacuum (Figure 3-9 (b)); 2) Removal of first layer of char using a drill with a 4-inch brass wire wheel brush (see Figure 3-10); 3) Cleaning residual char spots using a steel brush. 4) Repeating steps while cleaning with an air gun and vacuum to avoid excessive sound wood removal after step 3. The specimen condition after char removal is shown in Figure 3-9 (c).

Since a strain gauge was intended to be added to the mid-span of the specimen, particular attention was made to sanding the area to which the strain gauge would be adhered, such that sound wood was visible. This was judged based solely on the colour of the wood and the absence of visible cracks. Gluing the tension strain gauge required special attention as alternations between adding glue and sanding the location were performed until glue was observed to allow the attachment of the strain gauge. Additionally, the support locations were sanded and levelled prior to fixing steel plates to ensure the specimens' stability and to avoid crushing perpendicular to the grain.

(a) (b) (c)

Figure 3-9 Specimen condition: (a) prior to char removal (b) dust removal (c) after char removal using wire wheel brush

Figure 3-10 Char removal process

3.5 Digital Image Acquisition Setup

A digital single-lens reflex camera, with an image resolution of 24.1 Megapixels and a focal length equal to 18 mm, was used to acquire the images. The lens aberration correction feature

was enabled during image acquisition, and the "Digital Lens Optimizer" function that applies chromatic aberration and diffraction correction was used.

The camera was mounted on a tabletop stand with a horizontal arm to ensure stability. The camera was positioned such that its optical axis was kept perpendicular to the surface and centered relative to the specimen. A white paper with a drawn reference inner frame of 150 x 150 mm was used as background to ensure clarity of the image acquired and to set a baseline for measurement calibration during the image analysis stage. The horizontal arm was placed at a consistent height from the table surface, and the front of the camera was at a fixed height from the specimen surface. An artificial light with a 5500K color temperature was mounted on the overhead light stand on top of the camera stand. Additionally, two artificial lights with a 6000K color temperature were placed at the sides to enhance lightning conditions. Image acquisition was conducted on the same day to ensure consistency in the camera setup, specimen location, and light conditions. All images were obtained under laboratory conditions, and thus, environmental conditions were consistent. The setup is shown in Figure 3-11.

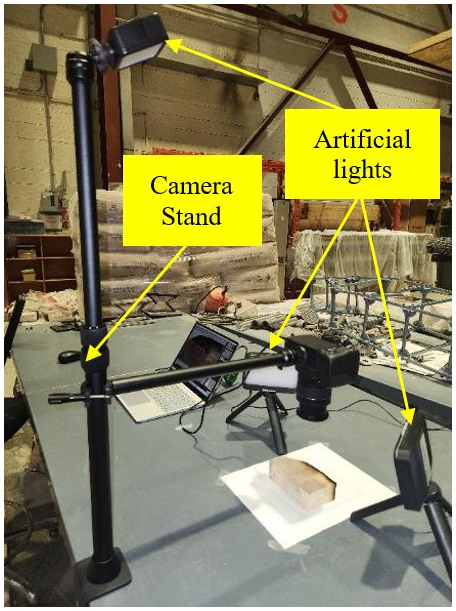

Figure 3-11 Digital Image acquisition setup

3.6 Static Test Setup

Destructive static testing of GLT panels under four-point bending and simply-supported boundary conditions was performed to establish a baseline for their mechanical properties, as shown in Figure 3-12. Idealized pin supports were provided by positioning the metal plates that were attached to the specimen on steel angles connected to the support, as shown in Figure 3-12 (a). The purpose of the metal plates is to prevent localized crushing at the supports due to perpendicular to grain bearing.

The loading was applied through a hydraulic jack, and the applied load was transferred via a distribution beam (Steel I-beam) to two line loads across the panel width at the third points of the clear span using load transfer beams (Figure 3-12 (b)). The applied load was obtained by means of a load cell that was connected to the hydraulic jack, while the mid-span deflection was measured using a wire gauge attached to the tension face of the specimen, as shown in Figure 3-12 (a). Strain gauges were glued at mid-span on the tension and compression faces. All test outputs were recorded using a data acquisition system (DAS) with a sampling rate of 10 samples per second.

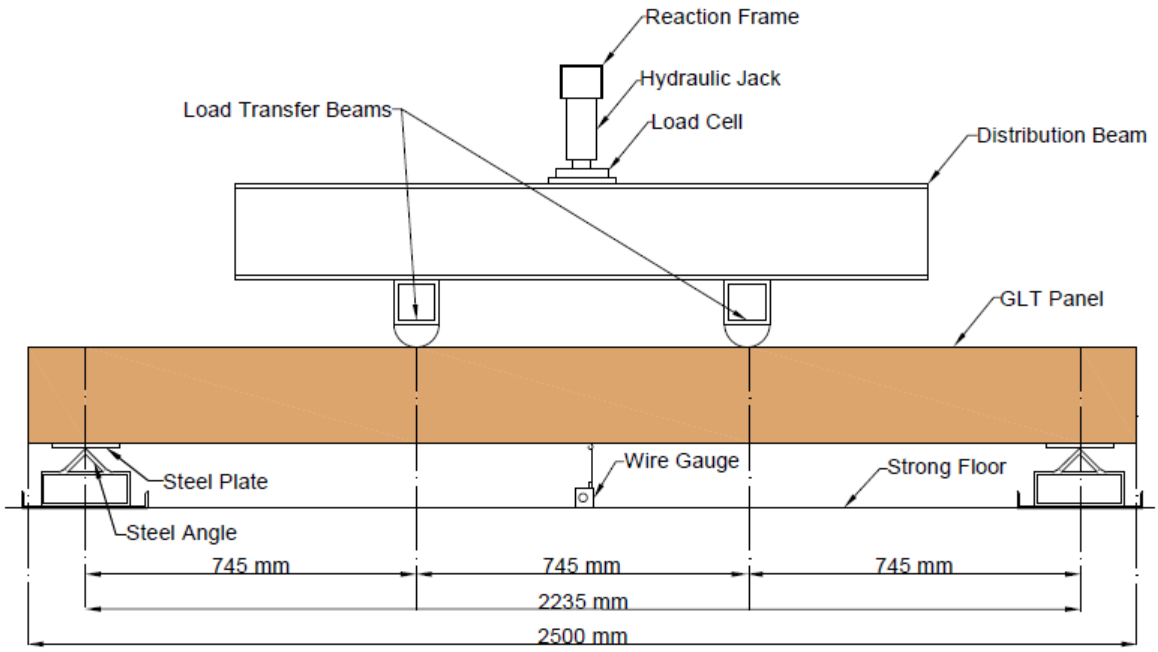

(a)

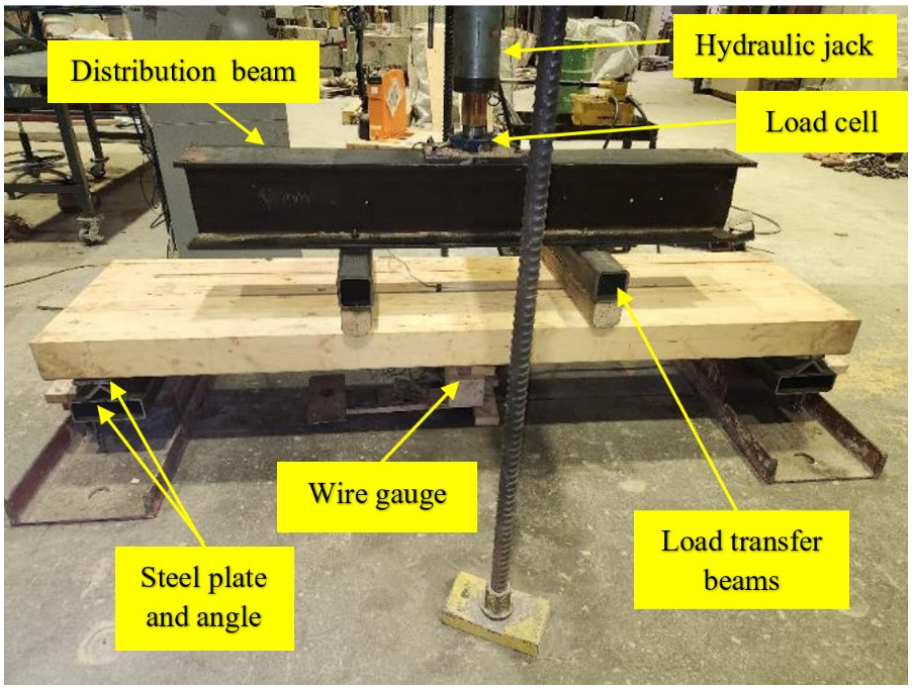

(b)

Figure 3-12 Static test Setups: (a) sketch, (b) Actual

3.7 Dynamic Test Setup

The dynamic test setup was constructed to mimic the static setup such that a direct comparison between the results can be made. This includes both the load application mechanism as well as the simply-supported boundary conditions. Dynamic testing was conducted using the University of Ottawa's Shock Tube facility.

The simulated blast waves are generated in Shock Tube by means of compressed air using a double diaphragm mechanism. The shock wave travels through the expansion section until interacting with the specimens at the end frame, which consists of an opening with dimensions of 2,032 x 2,032 mm, allowing for testing of large-scale specimens. The Shock Tube is capable of generating reflected pressure and impulse up to 100 kPa and 2200 kPa-ms, respectively. The positive phase of the shock wave can vary from 5 ms to 70 ms, depending on the length of the driver section used. The Shock Tube is shown in Figure 3-13.

The length of the driver section shown in Figure 3-13 (a) ranges between 305 mm and 5,185 mm, with increments of 305 mm. The driver length controls the shock wave's positive duration, which affects the wave impulse. The spool section (double diaphragm system) consists of two main parts separated by aluminum foils (see Figure 3-13 (b)). The desired pressure in the driver section can be determined by modifying the thickness and number of the aluminum foils. The combination of foils between each section must be greater than the estimated differential pressure to avoid early trigger. The expansion section (Figure 3-13 (c)) is 6,096 mm long and ensures smooth transition of the pressure between the diaphragm and end-frame. The load can be transferred directly to planar specimens or through a load transfer device (LTD) when testing beams or panels with reduced width compared to that of the end frame. Once the desired pressure in the driver section is reached, the control nozzle reduces the pressure in the spool section until the foils rupture. Once the foils rupture, the compressed air travels through the

expansion section, creating a shock front that interacts with the specimen mounted at the end frame.

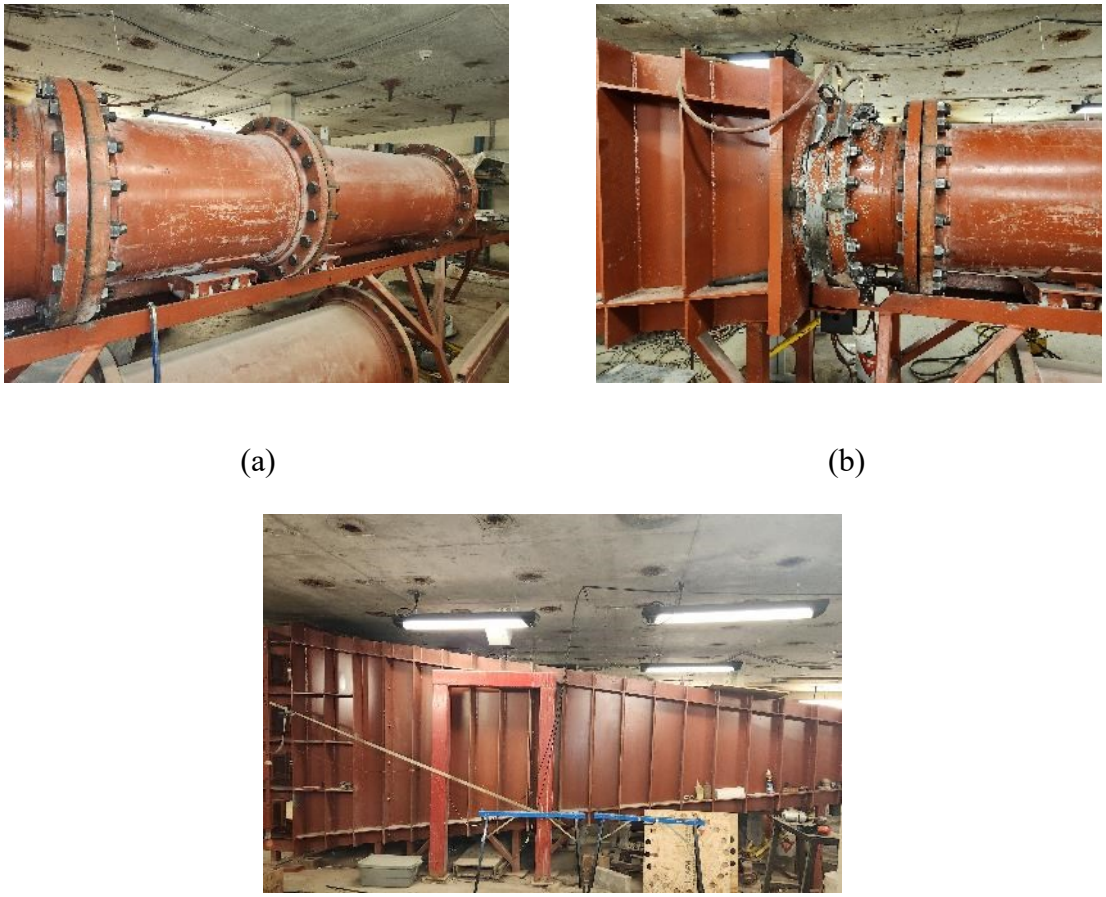

(a) (b)

(c)

Figure 3-13 Shock Tube Sections: (a) Driver section, (b) Spool section, and (c) Expansion section

In the present study, the chosen driver lengths were 2,743 mm (9ft) and 4,877 (16ft) to obtain the pressure and impulse required to fail the specimens. The shock wave was transferred to the specimens using an LTD and via a steel I-beam at the third points of the clear span of the specimens. The supports were free to rotate, and similar to the static test setup, metal plates were attached to the specimen under each support and load application point to prevent localized crushing effects due to bearing.

The dynamic reactions at supports were measured using load cells. The mid-span deflection was measured using a linear variable displacement transducer (LVDT), which was attached to an independent steel post placed in front of the Shock Tube and affixed to the ground and ceiling. Strain gauges were glued at mid-span to measure compression and tension strains.

The reflected pressure-time histories were recorded using two piezoelectric sensors (pressure gauges) installed near the opening of the frame end. All test outputs were recorded using a DAS with a sampling rate of 100,000 samples per second. Two cameras with a recording rate of 500 frames/sec were mounted on the sides of the Shock Tube to record the specimen failure behaviour. The sketch and actual dynamic test setup are shown in Figure 3-14 and Figure 3-15.

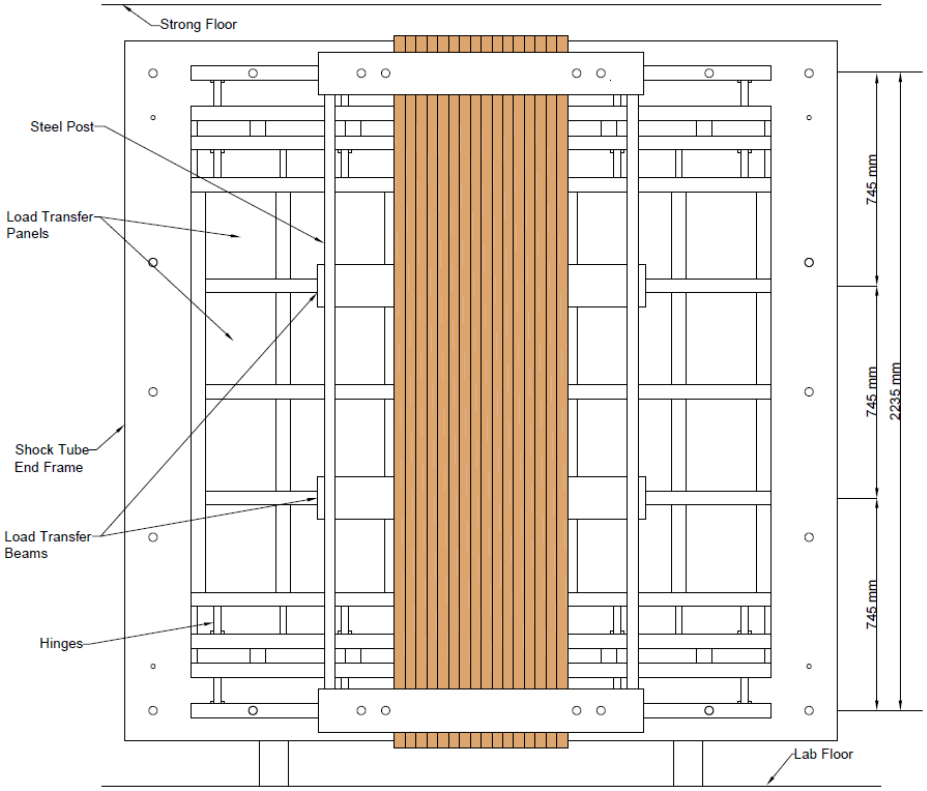

(a)

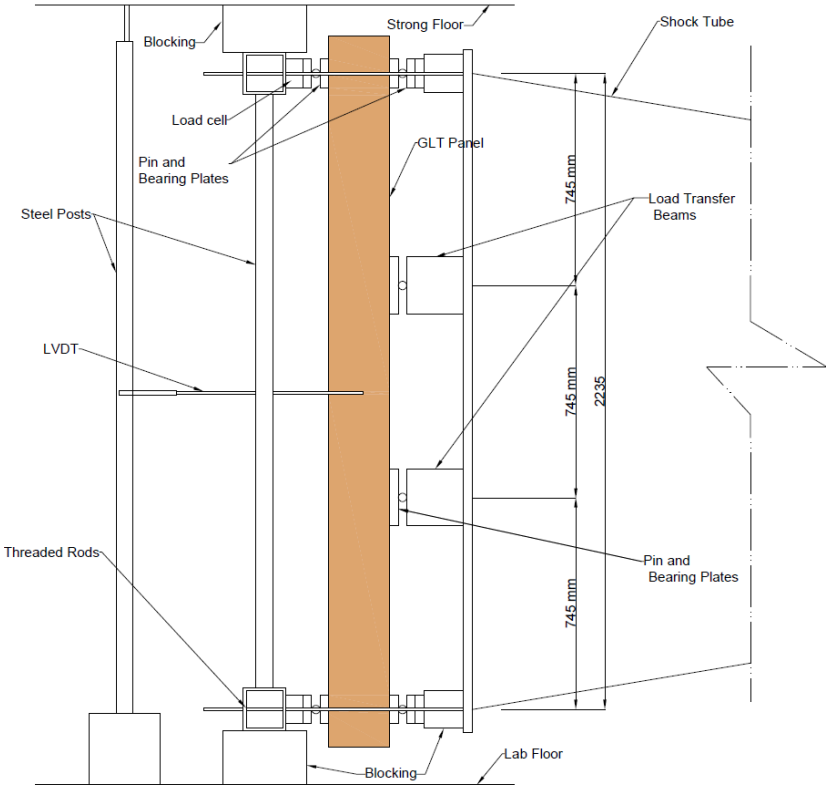

(b)

Figure 3-14 Dynamic test setup sketch: (a) front view (b) side view.

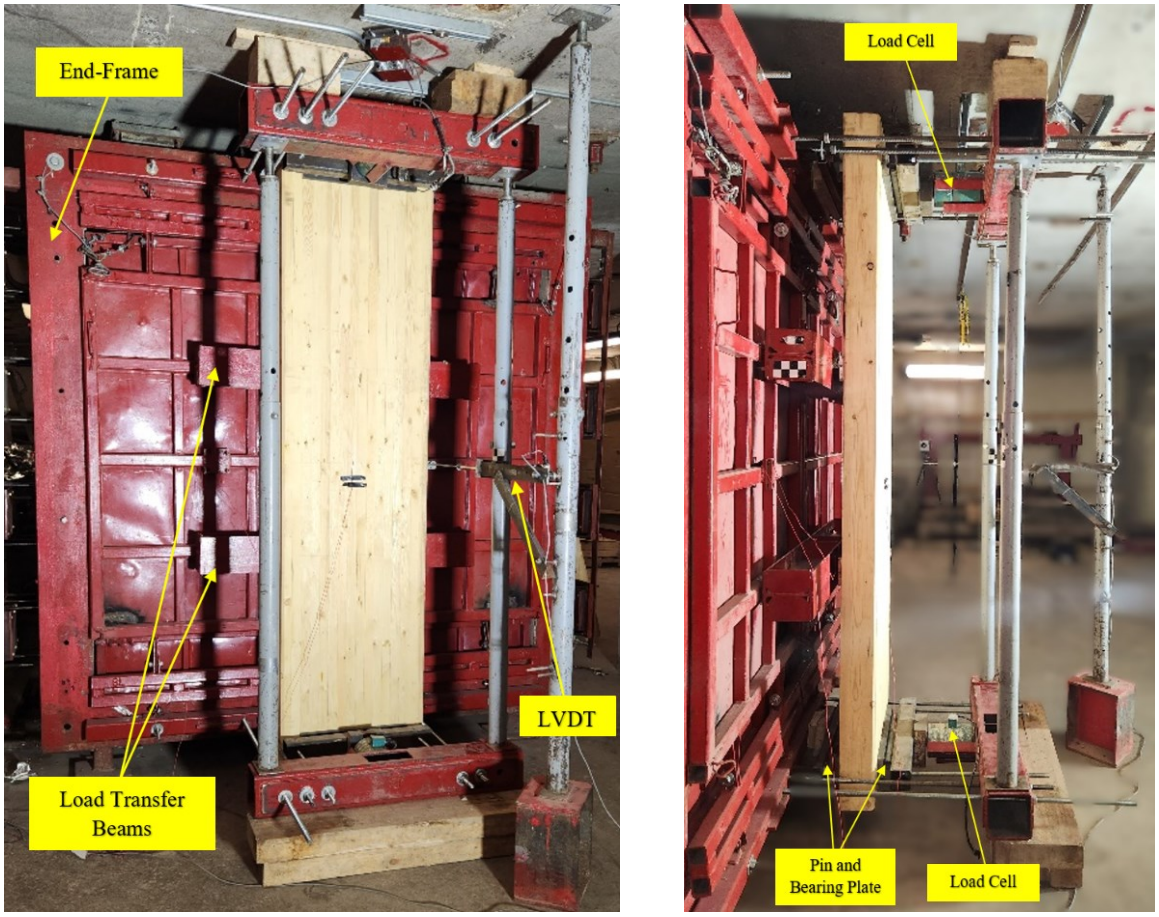

(a) (b)

Figure 3-15 Actual dynamic test setup: (a) front view (b) side view

Chapter 4 Experimental Results

4.1 General

This section includes the results obtained on char depth and charring rate, residual char and pyrolysis layer thickness, static and dynamic tests, as well as zero-strength layer thickness.

4.2 Char Depth and Charring Rate Results

Seven full-scale charred specimens were cleaned by removing the char layer in preparation for the static and dynamic tests, and the average char depth was recorded. Since the specimens were roof panels, they were all exposed to the fire from one side only. There was no charring on the two side edges of the panels. It is important to note that there were small fine cracks observed on the surface of the charred panels after char removal (see Figure 4-1).

Figure 4-1 An example of the small fine cracks on the surface after char removal

Table 4-1 summarizes the measurement results while the dimensions are illustrated in Figure 4-2. The reported average char depth (x_c) for each specimen is taken as the difference between the original estimated depth prior to fire exposure (d) and the average residual depth after char removal (d_r). Also included in the table are the dimensions of the specimens before and after char removal, where (d_i) is the average depth before char removal, (d_{rc}) is the thickness of the residual char layer attached to the specimen after the char has fallen off, (b) is the original

estimated width of the panel prior to fire exposure and (b_i) is the measured width of the panel after fire exposure. The average char depth obtained when considering all specimens was 20.0 mm (CV 7.9%), and the average width was 598 mm (CV 2.0%), which was on average 5 mm less than the original reported section width of 603 mm. As there was no char on the sides, the difference in the width could be attributed to shrinkage (i.e., loss of moisture during fire) and due to the panels' manufacturing variability. The average thickness of the residual char layer attached to the specimens was 5.6 mm (CV 22.3%), which means that the thickness of the char that fell off was on average 14.4 mm. It should be noted that the assessment of the residual char layer is outside the scope of the present study and it was only used for image analysis.

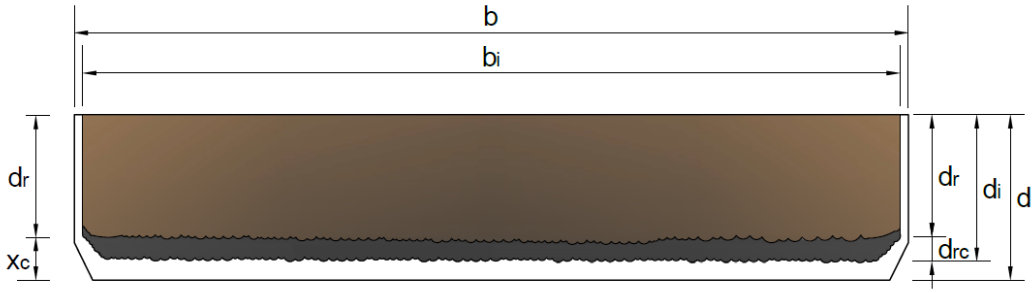

Figure 4-2 Charred Specimens dimensions before and after char removal

Table 4-1 Charred GLT Specimens measurements before and after char removal process

Specimen	d_i (mm)	d_r (mm)	d_{rc} (mm)	x_c (mm)	b_i (mm)
CGLT1 [215]	202.5	195.2	7.3	19.8	598
CGLT2 [215]	197.8	194.4	3.4	20.6	600
CGLT3 [215]	198.4	192.2	6.3	22.9	597
CGLT4 [215]	200.2	194.6	5.6	20.4	598
CGLT5 [215]	202.0	196.9	5.2	18.1	598
CGLT6 [215]	202.0	195.5	6.5	19.5	596
CGLT7 [215]	201.5	196.4	5.1	18.6	599
Avg.	200.6	195.0	5.6	20.0	598
SD	1.9	1.5	1.3	1.6	1.3
CV	0.009	0.008	0.223	0.079	0.002

A typical example is provided in Table 4-2, which shows detailed values of the individual measurements of specimen CGLT1 [215]. A total of 22 measurements were undertaken to obtain the average values in a manner consistent with the procedure described in Section 0. The average depth before and after removal of the char layer were 202.5 mm and 195.2 mm, respectively. Since the original depth of the member was reported to be 215 mm, the average char depth was calculated by subtracting the original member depth from the depth average measured after char removal, obtaining 19.8 mm (CV 8.6%). Further details on the measurement results for each specimen are provided in Appendix B.

Table 4-2 CGLT1 [215] Specimen depths measurements before and after char removal

Point #	d_i (mm)	d_r (mm)	d_{rc} (mm)	x_c (mm)
1	200.5	194.6	5.9	20.4
2	206.2	196.3	9.9	18.7
3	202.8	198.4	4.5	16.6
4	205.2	196.2	9.1	18.9
5	205.2	194.1	11.1	20.9
6	205.9	195.5	10.4	19.5
7	201.4	196.2	5.2	18.8
8	202.0	197.7	4.3	17.3
9	202.7	194.7	8.0	20.3
10	205.0	195.8	9.2	19.2
11	204.1	195.7	8.4	19.3
12	200.4	193.3	7.2	21.8
13	201.0	194.1	6.8	20.9
14	200.5	197.0	3.5	18.0
15	200.7	196.0	4.7	19.0
16	200.8	193.8	7.0	21.2
17	202.0	193.8	8.2	21.2
18	201.3	195.5	5.8	19.5
19	203.6	195.2	8.4	19.9
20	200.6	196.7	3.9	18.3
21	199.4	191.2	8.2	23.8
22	203.1	192.4	10.6	22.6
Avg.	202.5	195.2	7.3	19.8
SD	2.0	1.7	2.3	1.7
CV	0.010	0.009	0.316	0.086

The average one-dimensional charring rate (β) presented in Table 4-3 was obtained from the linear char depth relationship (Equation 4-1) found in Annex B of the CSA O86 (2024) standard, based on fire exposure duration (t).

$$x_c = \beta t \tag{4-1}$$

The fire exposure time was defined as the time period during which the measured gas temperature remained above 400 °C and ranged approximately from 25.7 and 43.5 min. As the exact location of the extracted panels in Bay 4 is not known, a conservative exposure time of 25.7 min was adopted and was deemed appropriate given that the primary objective of the charring rate comparison in this study is used for post-fire assessment. The average charring rate was found to be 0.78 mm/min (CV 7.9%).

Table 4-3 Charring rate of charred GLT specimens

Specimen	x_c (mm)	t (min)	β (mm/min)
CGLT1 [215]	19.8		0.77
CGLT2 [215]	20.6		0.80
CGLT3 [215]	22.9		0.89
CGLT4 [215]	20.4	25.7	0.79
CGLT5 [215]	18.1		0.70
CGLT6 [215]	19.5		0.76
CGLT7 [215]	18.6		0.72
Avg.	20.0		0.78
SD	1.6		0.06
CV	0.079		0.079

4.3 Digital Image Analysis Results

Image analysis tools like Fiji / ImageJ (Schneider et al., 2012) have previously been used for the evaluation of wood density and aging (e.g., Rzepecki & Thomas, 2017; Lachowicz & Bijak, 2025), and in charred wood analysis for aspects such as char depth and surface cracks (e.g.,

Kymäläinen et al., 2022; Pereira et al., 2024; Albert & Liew, 2025). One of the plugins available in the Fiji / ImageJ software is the Trainable Weka Segmentation (TWS) plugin, which employs machine learning techniques to create and classify segmentations of images (Arganda-Carreras et al., 2017). The plugin algorithm is obtained from Weka machine learning library (Witten et al., 2016). The use of the TWS plugin has primarily been limited to detecting natural defects in wood (e.g., Luo et al., 2021) or for identifying wood density profiles (e.g., De Mil et al., 2018). Based on the potential of the TWS plugin in identifying colour variations in wood cross-sections effectively, digital image analysis was conducted using the TWS plugin within Fiji (ImageJ v1.54p). The following steps summarize the image analysis process:

- Calibration of each image was undertaken with reference to the drawn frame measuring 150x150 mm within the image, and images were cropped to speed up the analysis time (Figure 4-3).

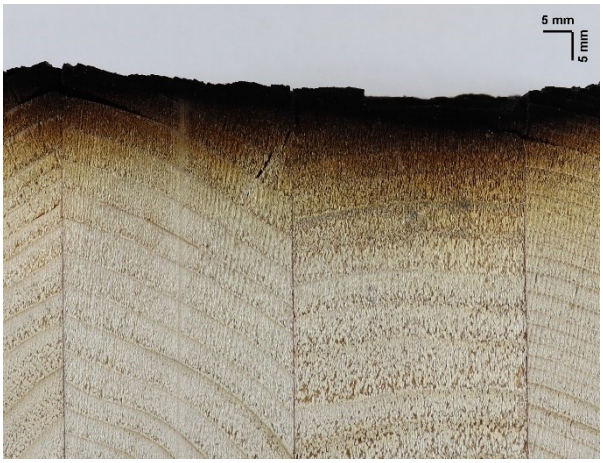

Figure 4-3 Example of calibrated and cropped image before segmentation (S5-3)

- Segmentation of the images was done by using the TWS plugin after configuring the settings as follows:
    - Selection of Gaussian blur (to smooth the image), Sobel filter (to emphasize image edges), Hessian (to enhance contrast), and Membrane projections (to enhance cell membranes such as wood grains).

- Selection of FastRandomForest algorithm (Supek, 2015) classifier due to its effectiveness in handling complex images.
- Addition of four class names to represent each layer, namely: white background, char, pyrolysis, and sound wood.
- Selection of the "Balance classes" option in the advanced settings to prevent the classifier from being biased toward the more common class.

- Selection of samples of different layers as part of training the classifier to recognize each layer based on colour variation. This step was an iterative process that was repeated using two different samples to enhance the accuracy, as shown in Figure 4-4. The decision to repeat this step was made based on checking the 32-bit probability map for each layer. The resulting hyper-stack images (Figure 4-5) provided a visual audit and the classifier's confidence in the outcomes as pixel values ranging from 0 (0% likelihood) to 1 (100% likelihood).

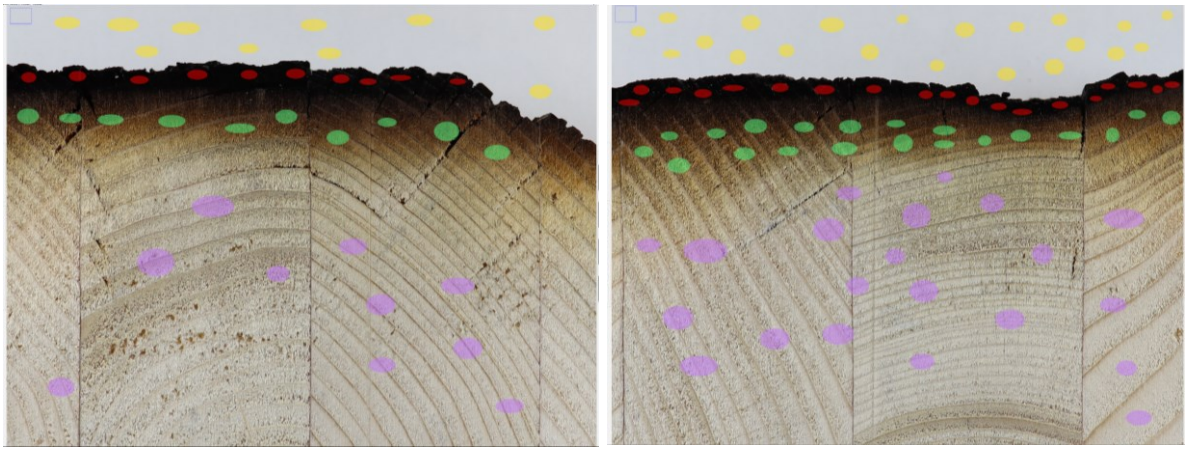

(a) (b)

Figure 4-4 Training the classifier in TWS plugin: (a) First sample (S1-5) (b) Second sample (S1-3)

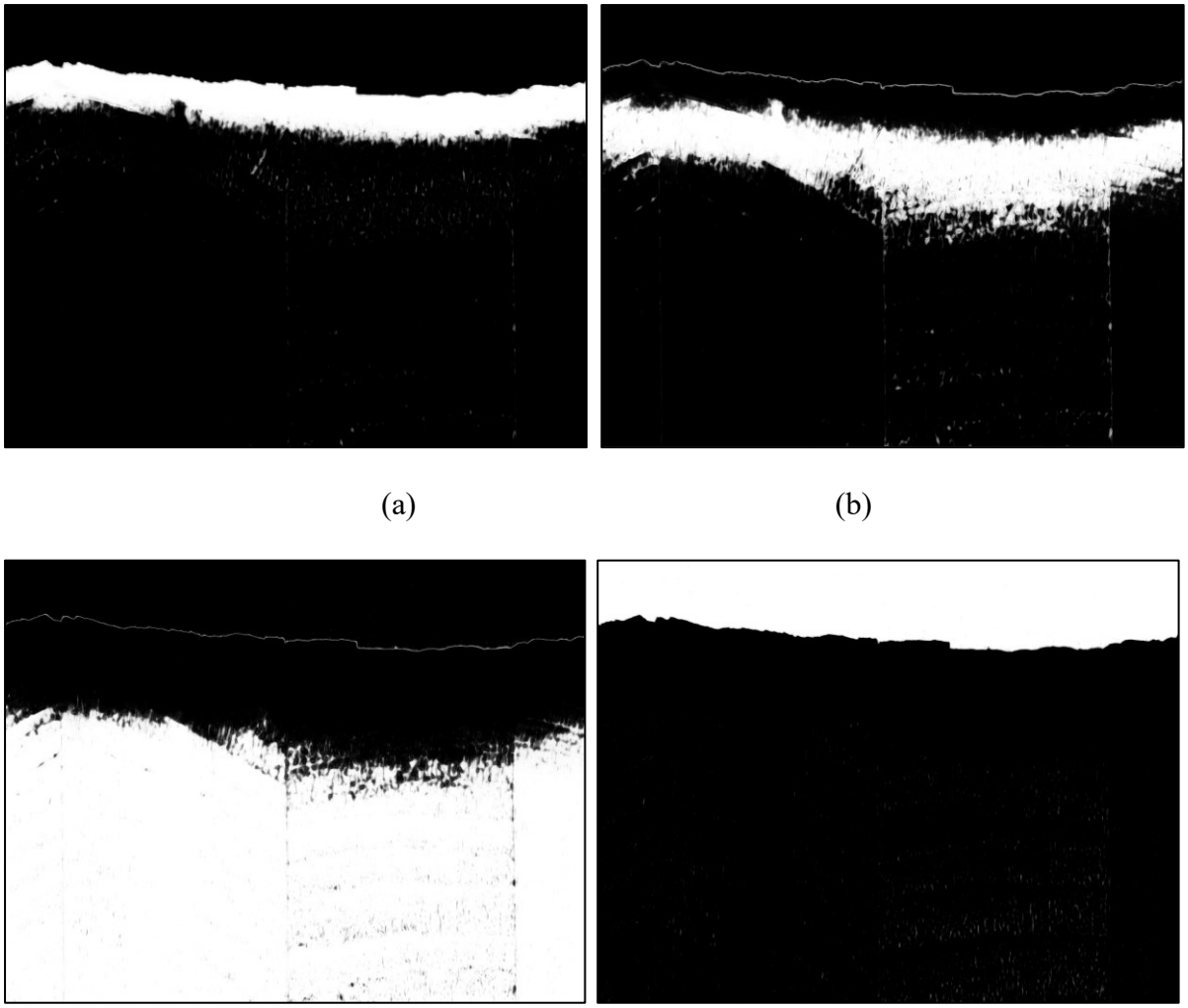

(a) (b)

(c) (d)

Figure 4-5 An example of Probability maps after segmentation (S5-3): (a) Char layer (b) Pyrolysis layer (c) Sound wood layer (d) White background layer

- Application of the classifier and training data to the entire image set to segment them into predefined classes based on the learned features (Figure 4-6).

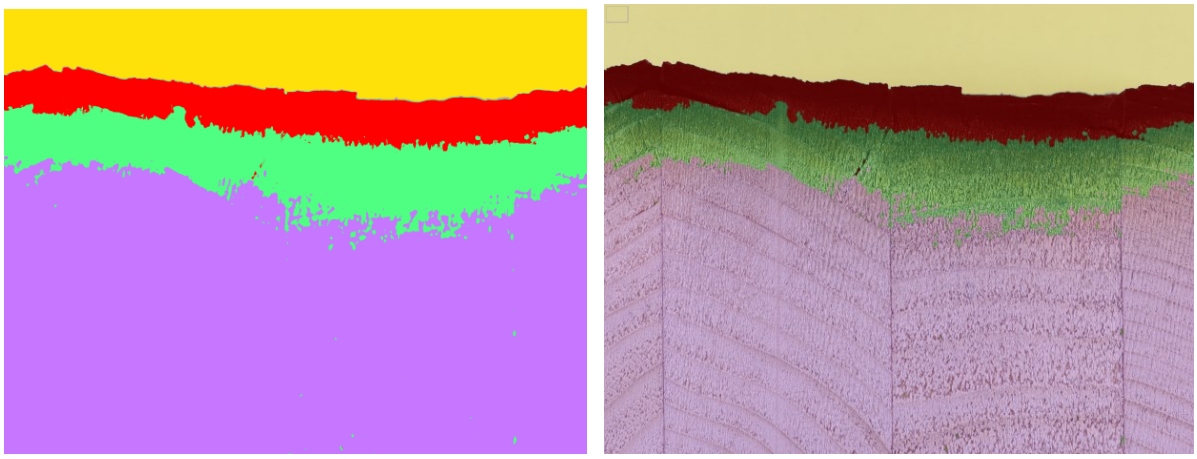

(a) (b)

Figure 4-6 An example of images after segmentation for sample S5-3: (a) Classified image (b) Toggle overlay image

- Definition of a grid with an area equal to 25 mm^2, and the location of points 1 to 6 on the grid lines using ROI Manager to speed up the process and ensure consistency, as shown in Figure 4-7.

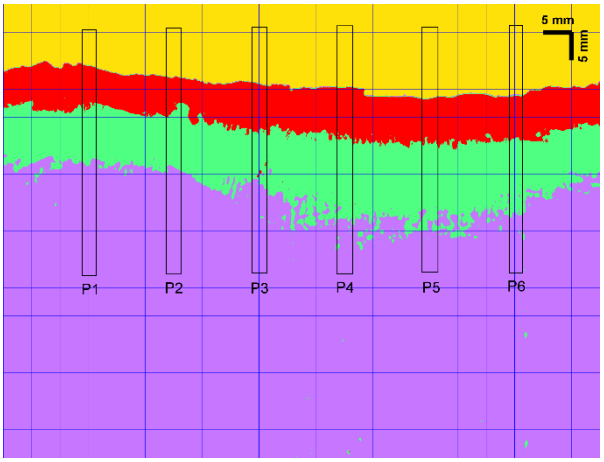

Figure 4-7 An example of images after segmentation (S5-3) with grids and points locations

- Measurement of residual char and pyrolysis layer thickness at each point, while excluding the first and last three points in corner samples due to corner rounding effects as well as very small char and pyrolysis layer thickness, as shown in Figure 4-8.

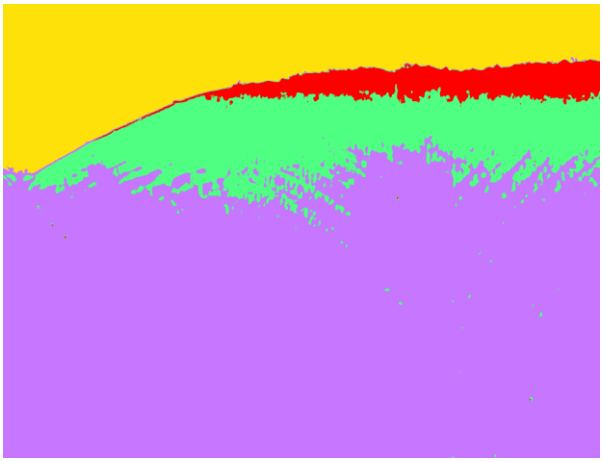

Figure 4-8 An example of corner sample Image (S3-1)

Further details on the image analysis results for each sample are provided in Appendix C. A total of 120 measurements were recorded for each layer thickness (pyrolysis and residual char), resulting in 240 measurements overall. A summary of the pyrolysis layer and residual char thickness results is presented in Table 4-4 and 4-5, respectively. For the investigated samples, an average thickness of residual char and pyrolysis layers were determined to be 7.1 mm (CV 23.5%) and 11.1 mm (CV 23.2%), respectively.

Table 4-4 Pyrolysis layer thickness results

Point # /Sample #	P1 (mm)	P2 (mm)	P5 (mm)	P4 (mm)	P5 (mm)	P6 (mm)	
S1-1	-	-	-	5.2	7.3	9.7	
S1-2	8.4	11.1	12.9	12.7	12.3	12.2	
S1-3	9.2	11.6	9.6	7.1	9.6	11.8	
S1-4	14.8	13.7	12.0	6.9	6.3	9.9	
S1-5	8.6	9.9	10.9	-	-	-	
S2-1	-	-	-	5.6	6.3	7.6	
S2-2	10.8	9.3	10.5	13.8	12.6	10.0	
S2-3	10.7	12.3	11.0	9.2	12.2	13.5	
S2-4	8.4	10.3	13.6	17.4	13.2	10.8	
S2-5	8.8	13.0	13.5	-	-	-	
S3-1	-	-	-	12.7	8.0	11.7	
S3-2	11.9	16.0	20.8	13.9	12.7	11.9	
S3-3	13.0	12.9	12.5	13.3	10.2	11.8	
S3-4	12.3	10.1	11.2	10.8	11.5	8.3	
S3-5	12.9	14.5	13.1	-	-	-	
S4-1	-	-	-	10.9	7.1	7.6	
S4-2	13.6	7.1	9.1	8.4	10.6	10.6	
S4-3	8.8	9.1	13.3	17.6	12.8	11.9	
S4-4	13.0	10.6	13.4	14.4	11.5	9.4	
S4-5	8.1	10.6	10.2	-	-	-	
S5-1	-	-	-	6.0	7.9	6.9	
S5-2	12.6	11.0	10.8	13.2	11.2	9.7	
S5-3	9.8	9.8	8.9	14.2	13.4	13.0	
S5-4	12.7	13.8	9.1	9.4	10.5	12.6	
S5-5	12.0	14.2	12.2	-	-	-	
						Avg.	11.1
						SD	2.6
						CV	0.232

* Fields with " - " refer to values that were excluded due to corner rounding and very small thickness values

Table 4-5 Residual char layer thickness results

Point # /Sample #	P1 (mm)	P2 (mm)	P5 (mm)	P4 (mm)	P5 (mm)	P6 (mm)	
S1-1	-	-	-	7.6	6.7	7.0	
S1-2	6.3	5.2	7.5	6.8	5.3	4.1	
S1-3	7.8	4.9	5.1	3.9	4.3	3.7	
S1-4	8.8	9.9	7.5	8.3	8.1	7.2	
S1-5	6.4	6.7	7.9	-	-	-	
S2-1	-	-	-	8.5	7.3	7.1	
S2-2	7.2	9.0	7.9	10.7	9.9	9.1	
S2-3	6.9	7.3	8.4	5.6	4.9	7.3	
S2-4	7.5	7.8	6.3	7.6	4.6	8.1	
S2-5	5.1	5.4	5.6	-	-	-	
S3-1	-	-	-	4.3	4.3	5.7	
S3-2	4.1	1.9	5.1	6.9	8.1	8.2	
S3-3	5.8	5.2	8.2	7.1	6.7	5.2	
S3-4	6.7	6.7	9.7	9.5	7.6	8.4	
S3-5	7.9	6.9	5.2	-	-	-	
S4-1	-	-	-	4.5	6.4	8.0	
S4-2	8.0	7.5	7.5	7.5	6.5	7.9	
S4-3	7.7	8.0	8.4	6.3	6.5	6.5	
S4-4	10.5	10.6	10.9	10.7	10.5	6.7	
S4-5	8.4	7.1	7.9	-	-	-	
S5-1	-	-	-	7.5	6.4	7.0	
S5-2	6.4	7.1	9.0	10.2	7.5	7.7	
S5-3	7.6	5.5	8.3	8.9	7.9	7.7	
S5-4	6.7	4.8	6.1	6.5	7.5	8.3	
S5-5	7.5	6.5	6.2	-	-	-	
						Avg.	7.1
						SD	1.7
						CV	0.235

* Fields with " - " refer to values that were excluded due to corner rounding and very small thickness values

Measurements of the pyrolysis layer $(x_{p,v})$ and residual char layer $(x_{rc,v})$ thickness were performed on a small subset of small-scale samples using a hand-held digital calliper and an overhead light for the purpose of comparison with the measurements obtained from Fiji

(ImageJ) for the pyrolysis layer $(x_{p,i})$ and residual char layer $(x_{rc,i})$. The results and absolute differences are presented in Table 4-6. The absolute differences were 5.7% and 12.8% for pyrolysis and residual char layers, respectively. The discrepancies in residual char layer results between image-based and calliper measurements are likely due to the fragile nature of char and the possibility of losing char during sample extraction and handling.

Table 4-6 Comparison results of pyrolysis and residual char thickness

Sample #	Point #	$x_{p,v}$ (mm)	$x_{p,i}$ (mm)	ABS difference (%)	$x_{rc,v}$ (mm)	$x_{rc,i}$ (mm)	ABS difference (%)
S1-3	P2	11.6	11	5.5	4.9	4.5	8.9
S1-4	P5	6.3	6.7	6.0	8.1	7.5	8.0
S2-1	P6	7.6	7.2	5.6	7.1	6.2	14.5
S2-3	P1	10.7	11.2	4.5	6.9	6.0	15.0
S2-3	P5	12.2	11.6	5.2	4.9	4.1	19.5
S2-4	P6	10.8	11	1.8	8.1	7.8	3.8
S2-5	P1	8.8	7.7	14.3	5.1	4.8	6.3
S3-5	P2	14.5	14.4	0.7	6.9	6.4	7.8
S4-3	P6	11.9	11.2	6.3	6.5	5.9	10.2
S4-4	P5	11.5	10.8	6.5	10.5	9.0	16.7
S5-4	P2	13.8	13	6.2	4.8	3.7	29.7
Avg.		10.9	10.5	5.7	6.7	6.0	12.8
SD		2.5	2.4		1.8	1.7	
CV		0.227	0.228		0.264	0.276	

4.4 Static Test Results

Seven uncharred GLT panels consisting of two different depths (130 mm and 215 mm) and four charred panels with an original depth prior to fire exposure equal to 215 mm were tested statically until failure. Table 4-7 and Table 4-8 summarize the destructive static tests results, while further details on the results obtained for each specimen can be found in Appendix D. The tests followed the flexural bending test requirements found in ASTM-D198-22 (ASTM International, 2022). In Table 4-7 and Table 4-8, the strain-rate ($\acute{\varepsilon}$) was obtained from Equation 4-2, as the ratio between the maximum tensile strain (ε_T) and the time to reach the maximum tensile strain ($t_{\varepsilon T}$).

$$\acute{\varepsilon} = \frac{\varepsilon_T}{t_{\varepsilon T}} \quad \text{4-2}$$

The *MOR* was obtained from Equation 4-3, where (b) and (d) are the width and depth of the panels, respectively, (L) is the clear span and (R_{max}) is the maximum resistance obtained from the load applied on the panel until failure. The stiffness (K) was obtained from the resistance - displacement curves by determining the slope of a line between the 10% and 40% of the maximum recorded resistance. Apparent *MOE* was obtained from Equation 4-4.

$$MOR = \frac{R_{max}\, l}{bd^2} \quad \text{4-3}$$

$$MOE = \frac{23\, K\, l^3}{108\, bd^3} \quad \text{4-4}$$

The maximum moment (M_{max}) can be calculated using Equation 4-5, where (I) is the moment of inertia of the panel and (c) is the distance from the neutral axis to the extreme fibre of the cross-section taken here at mid-depth.

$$M_{max} = \frac{MOR\, I}{c} \quad \text{4-5}$$

The MOR and MOE reported results for the charred specimens in Table 4-8 were obtained based on the residual cross-section dimensions reported in Section 4.2.

Table 4-7 Summary of destructive static tests results for uncharred panels

Panel Name	R_{max}[1] (kN)	Δ_{Rmax}[2] (mm)	t_{Rmax}[3] (s)	ε_T[6] x 10^{-4} (mm/mm)	$\Delta\varepsilon_T$[7] (mm)	$t\varepsilon_T$[8] (s)	ε_c[9] x 10^{-4} (mm/mm)	$\Delta\varepsilon_c$[10] (mm)	$t\varepsilon_c$[11] (s)	$\dot{\varepsilon}$[12] (s^{-1})	MOR[13] (MPa)	K[14] (kN/mm)	MOE[15] (MPa)	M_{max}[16] (kN.m)
GLT1 [130]	147.7	33.0	258.6	31.3	33.0	258.6	33.6	33.0	258.6	$1.21x10^{-5}$	32.1	5.8	10252.4	55.0
GLT2 [130]	187.8	32.6	178.8	32.2	32.6	178.9	36.7	35.0	179.8	$1.80x10^{-5}$	40.8	5.9	10323.6	70.0
GLT3 [130]	183.2	35.5	450.1	24.3	34.5	441.5	27.3	33.2	425.6	$5.50x10^{-6}$	39.9	5.8	10323.6	68.3
Avg.	172.9	33.7		29.3			32.6	33.7		$1.19x10^{-5}$	37.6	5.8	10299.9	64.4
SD	22.0	1.6		4.3			4.8	1.1		$6.25x10^{-6}$	4.8	0.1	41.1	8.2
CV	0.127	0.047		0.148			0.147	0.034		0.527	0.127	0.012	0.004	0.127
GLT4 [215]	438.8	36.1	1546.0	36.0	37.8	1590.0	26.9	36.56	1546.0	$2.26x10^{-6}$	34.9	19.4	7633.4	163.5
GLT5 [215]	413.6	28.4	624.0	27.1	23.7	548.0	19.7	23.13	538.0	$4.94x10^{-6}$	32.9	19.6	7712.1	154.1
GLT6 [215]	473.0	29.2	658.0	29.0	30.9	659.0	39.6	30.90	659.0	$4.40x10^{-6}$	37.6	21.4	8420.4	176.2
GLT7 [215]	452.7	27.6	630.0	38.5	27.6	630.0	31.8	28.17	630.0	$6.11x10^{-6}$	36.0	20.8	8175.6	168.6
Avg.	444.5	30.3		32.6			29.5	29.7		$4.43x10^{-6}$	35.4	20.3	7985.4	165.6
SD	24.9	3.9		5.5			8.4	5.6		$1.61x10^{-6}$	2.0	1.0	375.9	9.3
CV	0.056	0.128		0.167			0.283	0.189		0.363	0.056	0.047	0.047	0.056

[1] Maximum resistance
[2] Displacement at maximum resistance
[3] Time to maximum resistance
[4] Maximum displacement
[5] Time to maximum displacement
[6] Maximum tensile strain
[7] Displacement at maximum tensile strain
[8] Time to maximum tensile strain
[9] Maximum compressive strain
[10] Displacement at maximum compressive strain
[11] Time to maximum compressive strain
[12] Strain rate
[13] Modulus of rupture
[14] Stiffness
[15] Apparent Modulus of Elasticity
[16] Maximum bending moment

Table 4-8 Summary of destructive static tests results for charred panels

Panel Name	R_{max}[1] (kN)	Δ_{Rmax}[2] (mm)	t_{Rmax}[3] (s)	ε_T[6] x 10^{-4} (mm/mm)	$\Delta\varepsilon_T$[7] (mm)	$t\varepsilon_T$[8] (s)	ε_c[9] x 10^{-4} (mm/mm)	$\Delta\varepsilon_c$[10] (mm)	$t\varepsilon_c$[11] (s)	$\dot{\varepsilon}$[12] (s^{-1})	MOR[13] (MPa)	K[14] (kN/mm)	MOE[15] (MPa)	M_{max}[16] (kN.m)
CGLT1 [215]	300.4	24.8	299.1	24.6	26.3	299.2	-38.3	30.3	324.1	$8.22x10^{-6}$	29.5	13.2	7058.4	111.9
CGLT2 [215]	280.7	26.3	323.6	16.1	20.9	276.0	-28.7	26.3	323.7	$5.82x10^{-6}$	27.7	13.2	7119.8	104.6
CGLT3 [215]	280.3	24.9	288.9	19.1	22.4	254.1	-31.0	24.9	24.9	$7.50x10^{-6}$	28.4	11.6	6506.7	104.4
CGLT4 [215]	240.0	28.9	266.3	20.2	14.6	149.4	-36.1	32.8	266.4	$1.35x10^{-5}$	23.7	13.1	7073.1	89.4
Avg.	275.4	26.2		20.0			-33.6	28.6		$8.76x10^{-6}$	27.3	12.8	7073.2	102.6
SD	25.4	1.9		3.5			4.4	3.6		$3.32x10^{-6}$	2.5	0.8	444.7	9.5
CV	0.092	0.072		0.177			-0.132	0.126		0.379	0.092	0.062	0.063	0.092

[1] Maximum resistance

[2] Displacement at maximum resistance

[3] Time to maximum resistance

[4] Maximum displacement

[5] Time to maximum displacement

[6] Maximum tensile strain

[7] Displacement at maximum tensile strain

[8] Time to maximum tensile strain

[9] Maximum compressive strain

[10] Displacement at maximum compressive strain

[11] Time to maximum compressive strain

[12] Strain rate

[13] Modulus of rupture of residual cross-section

[14] Stiffness

[15] Apparent Modulus of elasticity of residual cross-section

[16] Maximum bending moment

4.4.1 Specimens GLT1 – GLT3 [130]

Three uncharred GLT panels with a depth equal to 130 mm were tested statically under four-point bending to obtain a representative resistance curves. The average weight of the panels was 92.0 kg (CV 1.3%) and the average moisture content (MC) was 14.8% (CV 1.9%).

The static resistance curves are shown in Figure 4-9. The static behaviour of the panels until maximum resistance was characterized to be linear elastic, with simple tension flexural failure initiated at the tension face of the panels, as shown in Figure 4-10 (a). Figure 4-10 (b) shows the failure of the outer tension lamination, followed by cracks propagating across the panel depth. The cracks on the tension side were located around the midspan, between the two loading points. There was no observed damage on the compression face or at supports. The failure was observed to be primarily initiated at knots and/or FJ, as indicated by the arrows in Figure 4-10 (b).

The average static resistance was 172.9 kN (CV 12.7%), and the average displacement until maximum resistance was 33.7 mm (CV 4.7%). The average stiffness was 5.8 kN/mm (CV 1.2%), and the average MOR was 37.6 MPa (12.7%). The average values of maximum tensile strain and maximum compressive strain were 29.3 x 10^{-4} mm/mm (CV 14.8%) and 32.6 x 10^{-4} mm/mm (CV 14.7%), respectively.

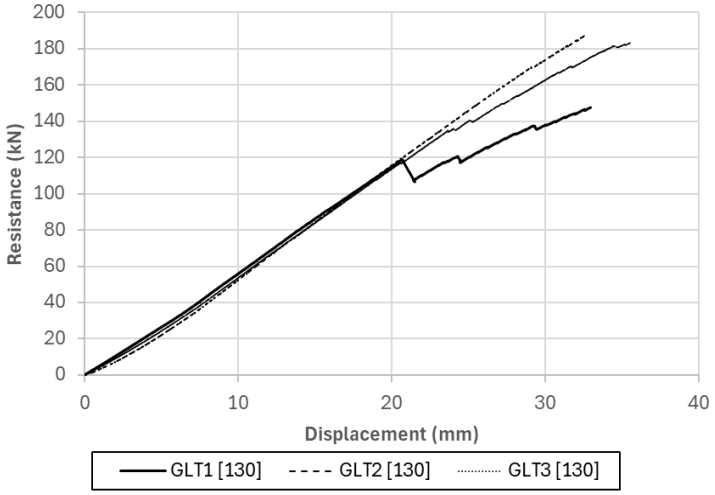

Figure 4-9 Static resistance curves of GLT1 [130] – GLT3 [130] panels

(a)

(b)

Figure 4-10 An example of static failure mode - GLT3 [130]: (a) side view (b) bottom view with FJ and knots locations

4.4.2 Specimens GLT4 – GLT7 [215]

Four uncharred GLT panels with depth equal to 215 mm were tested statically under four-point bending until failure. The average weight of the panels was 144.8 kg (CV 4.0%), and the average MC was 14.5% (CV 2.8%).

The static resistance curves are shown in Figure 4-11. The static behaviour of the panels until maximum resistance is characterized as linear elastic, which corresponds to a flexural failure in the tension lamination, where the failure mode was simple tension as shown in Figure 4-12 (a,b). The failure initiated near the mid-span of the specimen. This was followed by cracks propagating across the panel laminations, mostly limited to the region between the loading points, as shown in Figure 4-12 (c). Similar to GLT panels with 130 mm depth, the failures were initiated at knots or/and FJ, as indicated by the arrows (Figure 4-12 (c)).

The average static resistance was 444.5 kN (CV 5.6%) and the average displacement until maximum resistance was 30.3 mm (CV 12.8). The average stiffness was 20.3 kN/mm (CV 4.7%) and average MOR was 35.4 MPa (5.6%). The average value of maximum tensile strain and maximum compressive strain were 32.6 x 10^{-4} mm/mm (CV 16.7%) and 29.5 x 10^{-4} mm/mm (CV 28.3%), respectively.

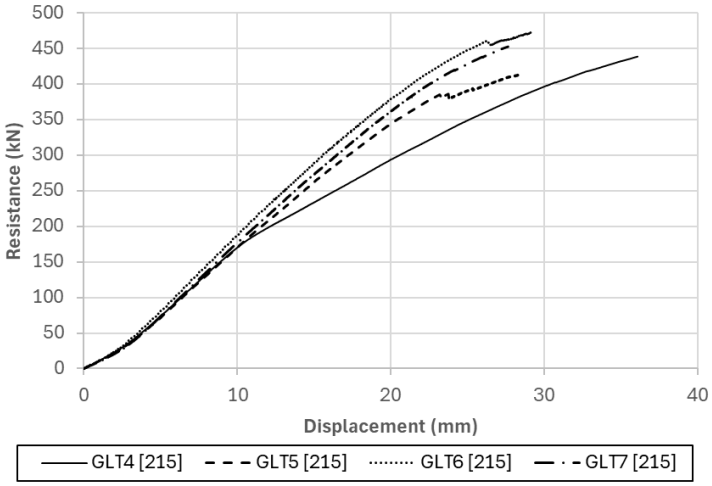

Figure 4-11 Static resistance curves of GLT4 [215] to GLT7 [215] panels

(a)

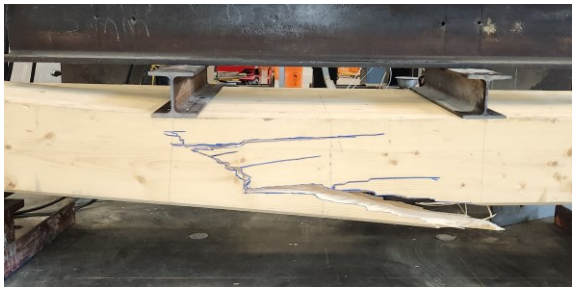

(b)

(c)

Figure 4-12 Examples of static failure mode of GLT [215] panels: (a) GLT4 [215] - side view (b) GLT6 [215] - side view (c) GLT7 [215] – bottom view

4.4.3 Specimens CGLT1 – CGLT4 [215]

Four charred GLT panels with an original depth of 215 mm prior to fire exposure were tested statically under four-point loading until failure. The average weight of the three panels was 119.8 kg (CV 2.7), and the average MC was 11.1% (1.5%). The average depth for these panels was 194.1 mm (char depth of 20.9 mm (CV 6.5%)), and the average width was 598.3 mm (CV 2.0%).

The static resistance curves are shown in Figure 4-13. The static behaviour of the panels until maximum resistance was characterized as linear elastic, which was consistent with the observation made for the uncharred panels. The specimens failed in flexure through failure of

the tension lamination. The failure mode was characterized as simple tension, as shown in Figure 4-14 (a). The failure initiated near the mid-span of the specimen. This was followed by cracks propagating across the GLT panel laminations mostly limited to the region between the loading points and the failures were initiated at knots and/or FJ as shown in Figure 4-14 (b). A notable difference compared to the uncharred specimens was visible separation between the individual laminations at the glue line (Figure 4-15).

The average static resistance was 275.4 kN (CV 9.2%) and the average displacement until maximum resistance was 26.2 mm (CV 7.2%). The average stiffness was 13.0 kN/mm (CV 8.2%). The average value of maximum tensile strain and maximum compressive strain were 20 x 10^{-4} mm/mm (CV 17.7%) and 33.6 x 10^{-4} mm/mm (CV 13.2%), respectively.

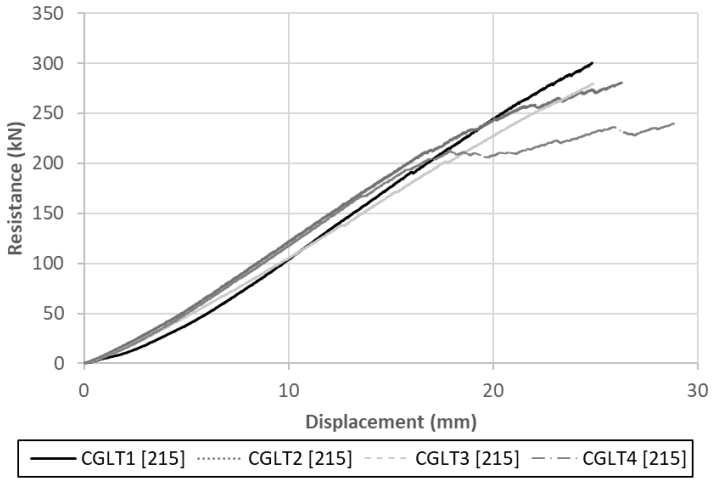

(c)

Figure 4-13 Static resistance curves of CGLT1 [215] – CGLT4 [215] panels

(a)

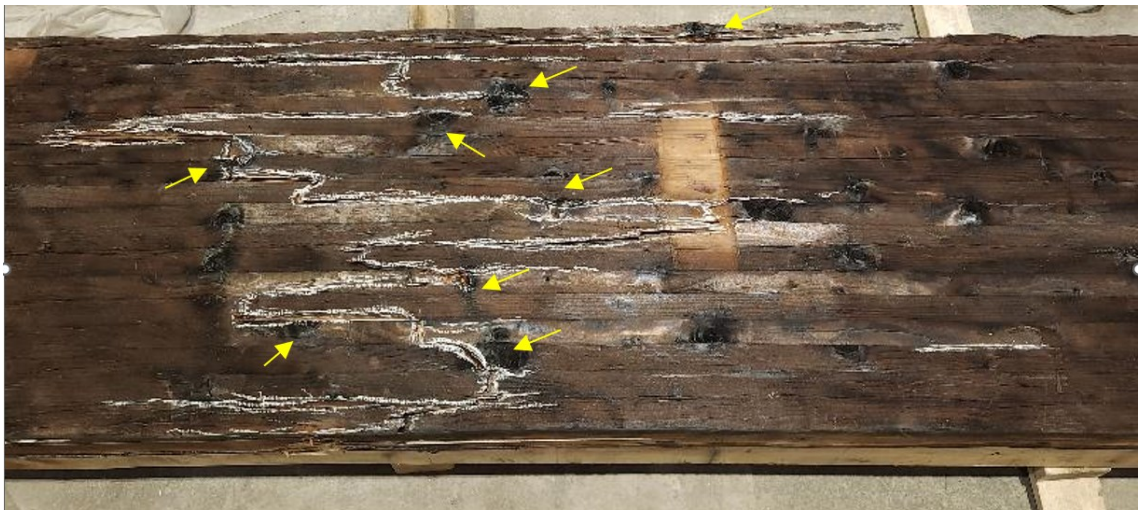

(b)

Figure 4-14 An example of static failure mode of charred panels - CGLT 1 [215]: (a) side view (b) bottom view with FJ and knots locations

Figure 4-15 The visible separation between the individual laminations at the glue line

4.5 Dynamic Test Results

Nine uncharred GLT panels with two different depths (130 mm and 215 mm), and three charred panels with original depth prior to fire exposure of 215 mm were tested dynamically until failure. The average weight of the 130 mm depth panels was 94.8 kg (CV 2.1), and the average MC was 14.3% (CV 2.8). The average weight of the 215 mm depth panels was 145.3 kg (CV 2.0%), and the average MC was 14.3% (CV 2.5%). The average weight of the charred panels was 115.4 kg (CV 3.0%), and the average MC was 11.1% (1.5%). The average depth for these panels was 196.3 mm (char depth of 18.7 mm (CV 3.8%)), and the average width was 597.7 mm (CV 3%).

Table 4-9 summarizes the destructive dynamic test results, and the presented data includes strain-rate, MOR, tension and compression strains, MOE and M_{max}, which was obtained based on the same approach adopted in Section 4.4. Figure 4-16 presents a typical example of the dynamic test results presented for specimen GLT12 [130]. Additional information and details on the results of each specimen can be found in Appendix E.

The dynamic resistance is not equal to the sum of measured dynamic reactions of the panel, as the system also includes inertia forces resulting from the mass of the LTD, which transfer the reflected pressure to the panel as two concentrated loads. The maximum dynamic resistance was obtained using Equations 4-6 and 4-7, assuming the inertia forces' distribution to follow that of the static deflected shape for a simply-supported panel subjected to four-point bending, and by considering the dynamic equilibrium of the idealized system at half-span. This method has been successfully used in other studies (e.g., Côté & Doudak, 2019; Jacques, 2016; D. Lacroix & Doudak, 2020; Poulin et al., 2018; Viau & Doudak, 2021a).

$$R(t) = \left\{\frac{6}{L}\right\}\{V(t)\, x_{eq} + 0.5\left[\frac{L}{3} - x_{eq}\right] F(t)\} \qquad 4\text{-}6$$

$$x_{eq} = \frac{0.102\ \overline{m}\ L^2 + 0.290\ m_c\ L}{0.319\ \overline{m}\ L + 0.870\ m_c} \quad \text{4-7}$$

Where ($R(t)$) and ($V(t)$) are the resistance and average dynamic reactions, respectively. (L) is the clear span and (x_{eq}) is the distance between the support and the point where the equivalent inertia force is applied. ($\overline{m}$) is the distributed mass of the panel and (m_c) is half of the LTD mass. The mass of the LTD was taken equal to 284 kg (Lacroix, 2017). The stiffness was obtained from the dynamic resistance-displacement curves. The dynamic resistance curves for uncharred and charred specimens are shown in Figure 4-17 to Figure 4-19. The reported MOR and MOE results for the charred specimens in Table 4-10 were obtained based on the residual cross-section dimensions reported in Section 4.2.

Table 4-9 Summary of destructive dynamic tests results for uncharred panels

Panel Name	P_R[1] (kPa)	I_R[2] (kPa.ms)	R_{max}[3] (kN)	Δ_{Rmax}[6] (mm)	t_{Rmax}[7] (ms)	ε_T[8] x 10^{-4} (mm/mm)	$\Delta\varepsilon_T$[9] (mm)	$t\varepsilon_T$[10] (ms)	ε_c[11] x 10^{-4} (mm/mm)	$\Delta\varepsilon_c$[12] (mm)	$t\varepsilon_c$[13] (ms)	$\dot{\varepsilon}$[14] (s^{-1})	MOR[15] (MPa)	K[16] (kN/mm)	MOE[17] (MPa)	M_{max}[18] (kN.m)
GLT8 [130]	74.6	634.3	185.9	40.8	15.4	37.0	44.6	16.6	39.5	49.31	17.9	0.2	40.4	4.9	8721.7	69.3
GLT9 [130]	59.8	659.8	182.8	36.2	19.6	42.8	35.2	22.4	32.6	35.2	22.4	0.2	39.8	5.1	9077.6	68.1
GLT10 [130]	69.7	753.7	179.6	41.4	16.0	52.7	44.4	22.6	33.8	44.42	22.6	0.2	39.1	5.0	8899.7	66.9
GLT11 [130]	69.2	1178.9	189.5	35.2	13.4	28.7	39.9	14.4	53.07	73.07	19.6	0.1	41.2	5.4	9611.6	70.6
GLT12 [130]	72.2	1080.9	205.4	40.3	19.6	34.29	40.88	20.00	47.93	45.39	25.0	0.1	44.7	5.2	9255.6	76.5
GLT13 [130]	68.2	1059.5	179.7	35.3	14.6	32.56	39.43	15.40	34.41	75.74	23.6	0.2	39.1	5.4	9611.6	67.0
GLT14 [130]	71.8	937.5	182.8	35.3	15.2	27.07	35.3	15.2	39.81	37.81	16.4	0.2	39.8	5.1	9077.6	68.1
Avg.			186.5	37.8		36.4			40.2	51.6		0.2	40.6	5.2	9179.4	69.5
SD			9.0	2.9		8.9			7.7	16.3		0.066	2.0	0.2	338.6	3.4
CV			0.048	0.076		0.243			0.192	0.316		0.387	0.048	0.037	0.037	0.048
GLT15 [215]	94.5	2405.2	455.1	24.2	15.4	26.21	24.6	16.2	29.06	24.6	16.2	0.2	36.2	19.1	7515.4	169.5
GLT16 [215]	112.8	2231.6	479.0	28.1	12.9	62.8	28.6	13.7	37.3	34.6	16.7	0.2	38.1	18.1	7121.9	178.4
Avg.			467.0	26.1		44.5			37.3	34.6		0.2	37.1	18.6	7318.6	174.0
SD			16.9	2.8		25.9			5.8	7.1		0.041	1.3	0.7	278.2	6.3
CV			0.036	0.106		0.582			0.157	0.204		0.214	0.036	0.038	0.038	0.036

[1] Peak reflected pressure
[2] Peak reflected impulse
[3] Maximum resistance
[4] Displacement at maximum resistance
[5] Time to maximum resistance
[6] Maximum recorded displacement
[7] Time to maximum recorded displacement
[8] Maximum tensile strain
[9] Displacement at maximum tensile strain
[10] Time to maximum tensile strain
[11] Maximum compressive strain
[12] Displacement at maximum compressive strain
[13] Time to maximum compressive strain
[14] Strain rate
[15] Modulus of rupture
[17] Apparent modulus of elasticity
[18] Maximum moment

Table 4-10 Summary of destructive dynamic tests results for charred panels

Panel Name	P_R[1] (kPa)	I_R[2] (kPa.ms)	R_{max}[3] (kN)	Δ_{Rmax}[6] (mm)	t_{Rmax}[7] (ms)	ε_T[8] x 10^{-4} (mm/mm)	$\Delta\varepsilon_T$[9] (mm)	$t\varepsilon_T$[10] (ms)	ε_c[11] x 10^{-4} (mm/mm)	$\Delta\varepsilon_c$[12] (mm)	$t\varepsilon_c$[13] (ms)	$\dot{\varepsilon}$[14] (s^{-1})	MOR[15] (MPa)	K[16] (kN/mm)	MOE[17] (MPa)	M_{max}[19] (kN.m)
CGLT5 [215]	94.4	1390.5	245.9	21.1	10.0	15.1	15.7	7.4	28.5	47.5	16.4	0.2	24.7	15.9	8281.2	91.6
CGLT6 [215]	100.9	1378.0	245.3	21.9	12.0	19.5	19.4	10.0	36.0	59.7	23.6	0.2	25.2	13.5	7207.5	91.4
CGLT7 [215]	71.7	1473.7	268.6	20.5	13.8	27.5	20.9	18.4	24.7	20.7	19.8	0.1	27.2	13.3	6968.5	100.1
Avg.			253.3	21.2		20.7			29.7	42.6		0.2	25.7	14.2	7485.7	94.3
SD			13.3	0.7		6.2			5.7	19.9		0.0	1.3	1.4	699.2	5.0
CV			0.053	0.033		0.302			0.193	0.467		0.162	0.051	0.102	0.093	0.053

[1] Peak reflected pressure

[2] Peak reflected impulse

[3] Maximum resistance

[4] Displacement at maximum resistance

[5] Time to maximum resistance

[6] Maximum recorded displacement

[7] Time to maximum recorded displacement

[8] Maximum tensile strain

[9] Displacement at maximum tensile strain

[10] Time to maximum tensile strain

[11] Maximum compressive strain

[12] Displacement at maximum compressive strain

[13] Time to maximum compressive strain

[14] Strain rate

[15] Modulus of rupture of residual cross-section

[16] Stiffness

[17] Apparent modulus of elasticity of residual cross-section

[18] Maximum moment

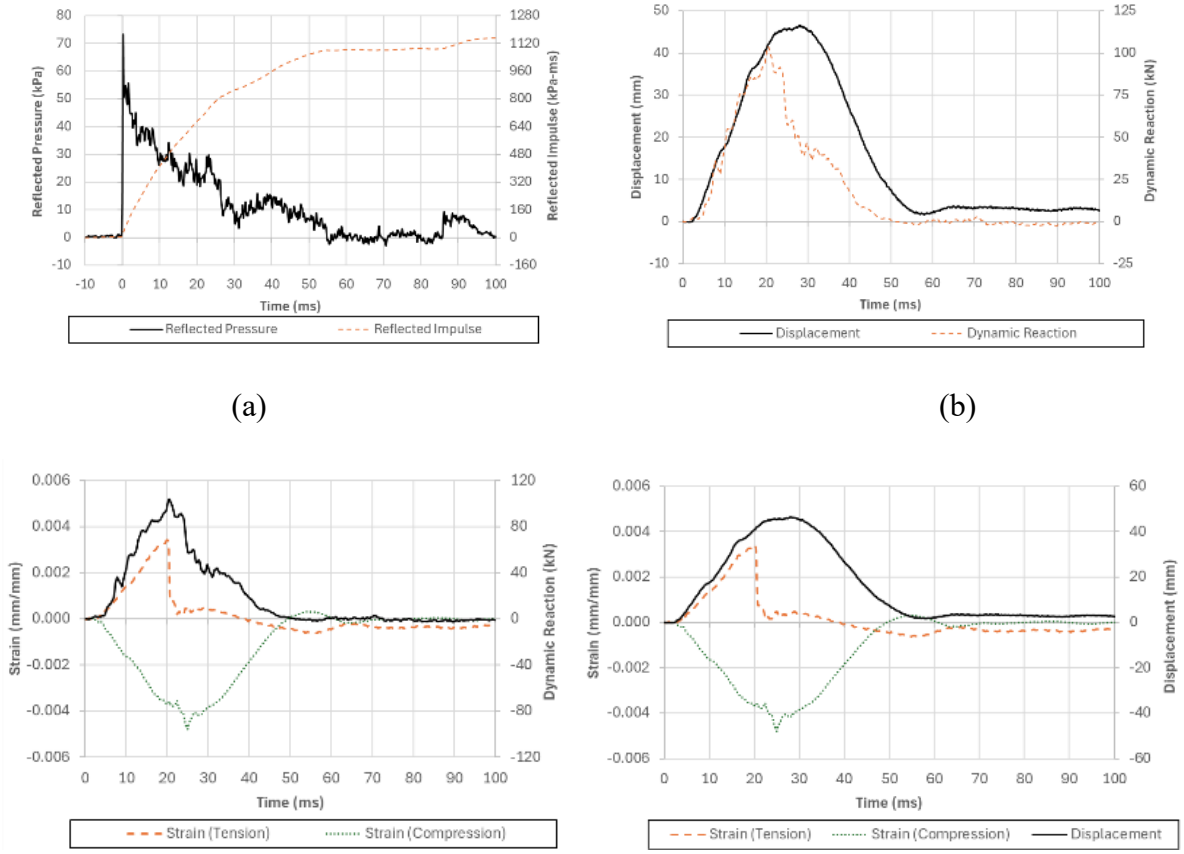

Figure 4-16 An example of dynamic test results of GLT panels (GLT12 [130]) results: (a) Pressure- and impulse-time histories; (b) Displacement- Dynamic reaction histories; (c) Dynamic reaction-strain histories; (d) Displacement-strain histories

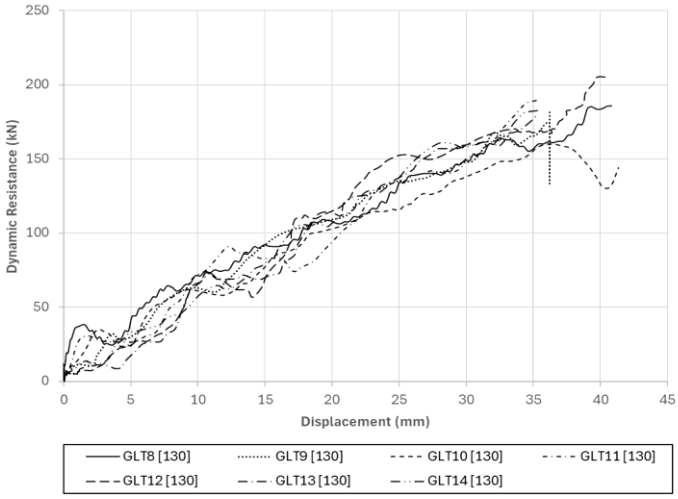

Figure 4-17 Dynamic resistance curves of GLT8 [130] – GLT14 [130] panels

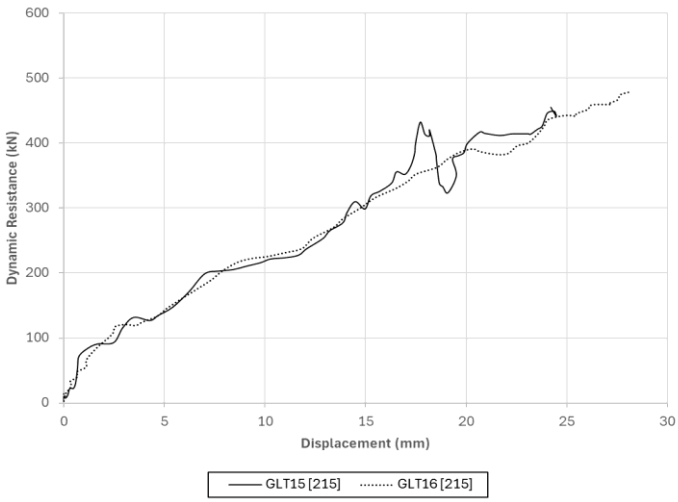

Figure 4-18 Dynamic resistance curves of GLT15 [215] – GLT16 [215] panels

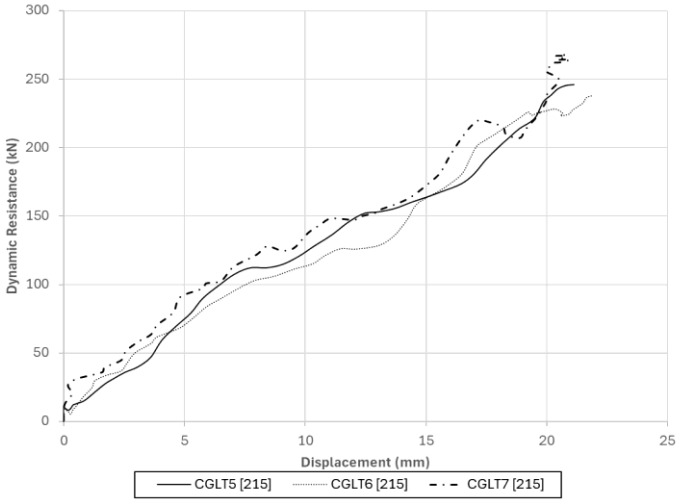

Figure 4-19 Dynamic resistance curves of CGLT5 [215] – CGLT7 [215] panels

4.5.1 Specimen GLT8 [130]

The specimen' s weight and MC were 95.0 kg and 14.0 %, respectively. There were three finger joints and several knots between the loading points, and an additional four FJ outside the shear-free region. The specimen before and after the test is shown in Figure 4-20. The driver pressure and length used were 413.7 kPa and 2,743 mm (9 ft), respectively. This resulted in a peak reflected pressure of 74.6 kPa and a peak reflected impulse of 634.3 kPa.ms over a positive duration of 21.9 ms. The maximum dynamic resistance was 185.9 kN with mid-span displacement of 40.8 mm at 15.4 ms. The specimen failed in flexural (simple tension) at mid-span in a consistent manner to the failure observed under static loading. Crack initiation and development occurred between the loading points with some cracks extending beyond this region. The failure occurred at FJ and knots.

(a) (b) (c)

Figure 4-20 Dynamic Failure of GLT8 [130]: (a) Before test; (b) After test - front view with FJ locations; (c) After test - side view

4.5.2 Specimen GLT9 [130]

Specimen GLT9 [130] weighed 96.2 kg and had a MC of 14.5%. There were no finger joints between the loading points, and only two finger joints were documented outside this region. However, several knots were distributed across the panel. The condition of the specimen before and after the test is shown in Figure 4-21. The driver pressure and length were 414.4 kPa and 2,743 mm (9 ft), respectively. This resulted a peak reflected pressure of 59.8 kPa and a peak reflected impulse 659.8 kPa.ms over a positive duration of 26.6 ms. The maximum dynamic resistance was 182.8 kN with mid-span displacement of 36.2 mm at 19.6 ms. Although the damage was relatively small, the failure mode was observed to be in flexure, which occurred at the element mid-span. The cracks were observed to initiate in the mid-span region between the loading points and little to no propagation across the specimen width was observed. The specimen exhibited almost full rebound with no residual deformation, but the cracks remained visible.

(a) (b) (c)

Figure 4-21 Dynamic Failure of GLT9 [130]: (a) Before test; (b) After test - front view; (c) After test - side view

4.5.3 Specimen GLT10 [130]

The weight and MC of specimen GLT10 [130] were determined to be 94.5 kg and 14%, respectively. Two finger joints were documented between the loading points and additional eight outside this zone, while several knots were distributed across the length. The specimen is shown in Figure 4-22. The driver pressure and length used in this test were 482.6 kPa and 2,743 mm (9 ft), respectively. This resulted in a peak reflected pressure of 69.7 kPa and a peak reflected impulse of 753.7 kPa.ms over a positive duration of 26.8 ms. The maximum dynamic resistance was 179.6 kN with mid-span displacement of 41.4 mm at 16 ms. Consistently with the previous two specimens, the failure was that of simple tension flexural failure at mid-span. The cracks were initiated in the region between the loading points. The specimen exhibited rebound after loading with relatively insignificant permanent deformation.

(a) (b) (c)

Figure 4-22 Dynamic Failure of GLT10 [130]: (a) Before test; (b) After test - front view with FJ locations; (c) After test - side view

4.5.4 Specimen GLT11 [130]

Specimen GLT11[130] weighted 96.2 kg and had a MC at the time of testing of 15%. There were three finger joints between the loading points and additional four outside this region. The specimen can be seen in Figure 4-23 before and after the testing. The driver pressure was 483.3 kPa and a driver length equal to 4,877 (16ft) was used. This resulted in a peak reflected pressure and a peak reflected impulse of 69.2 kPa and 1178.9 kPa.ms, respectively, over a positive duration of 50.2 ms. The maximum dynamic resistance was 189.5 kN with mid-span displacement of 35.2 mm at 13.4 ms. The specimen failure was flexural failure (brash) at mid-span, and the cracks were located in the middle region between the loading points.

(a) (b) (c)

Figure 4-23 Dynamic Failure of GLT11 [130]: (a) Before test; (b) After test - front view with FJ locations; (c) After test - side view

4.5.5 Specimen GLT12 [130]

The specimen weight and MC were 97.3 kg and 14.5% respectively. There were no finger joints between the loading points, while seven were outside this region. The specimen before and after the test is shown in Figure 4-24. The driver pressure and length used were 379.2 kPa and 4,877 (16ft), respectively. This resulted in a peak reflected pressure of 72.2 kPa and a peak reflected impulse 1080.9 kPa.ms over a positive duration of 54.6 ms. The maximum dynamic resistance was 205.4 kN with mid-span displacement of 40.3 mm at 19.6 ms. The specimen failure was a simple tension flexural failure at mid-span, and the cracks were located in the middle region between the loading points.

(a) (b) (c)

Figure 4-24 Dynamic Failure of GLT12 [130]: (a) Before test; (b) After test - front view with FJ locations; (c) After test - side view

4.5.6 Specimen GLT13 [130]

The specimen weight and MC were 92.5 kg and 14% respectively. There were three finger joints between the loading points, and five outside this region. The specimen before and after test is shown in Figure 4-25. The driver pressure and length used were 413.7 kPa and 4,877 (16ft), respectively. This resulted in a peak reflected pressure of 68.2 kPa and a peak reflected impulse 1059.5 kPa.ms over a positive duration of 45.4 ms. The maximum dynamic resistance was 179.7 kN with mid-span displacement of 35.3 mm at 14.6 ms. The specimen failure was simple tension flexural failure, and the cracks initiated at the mid-span.

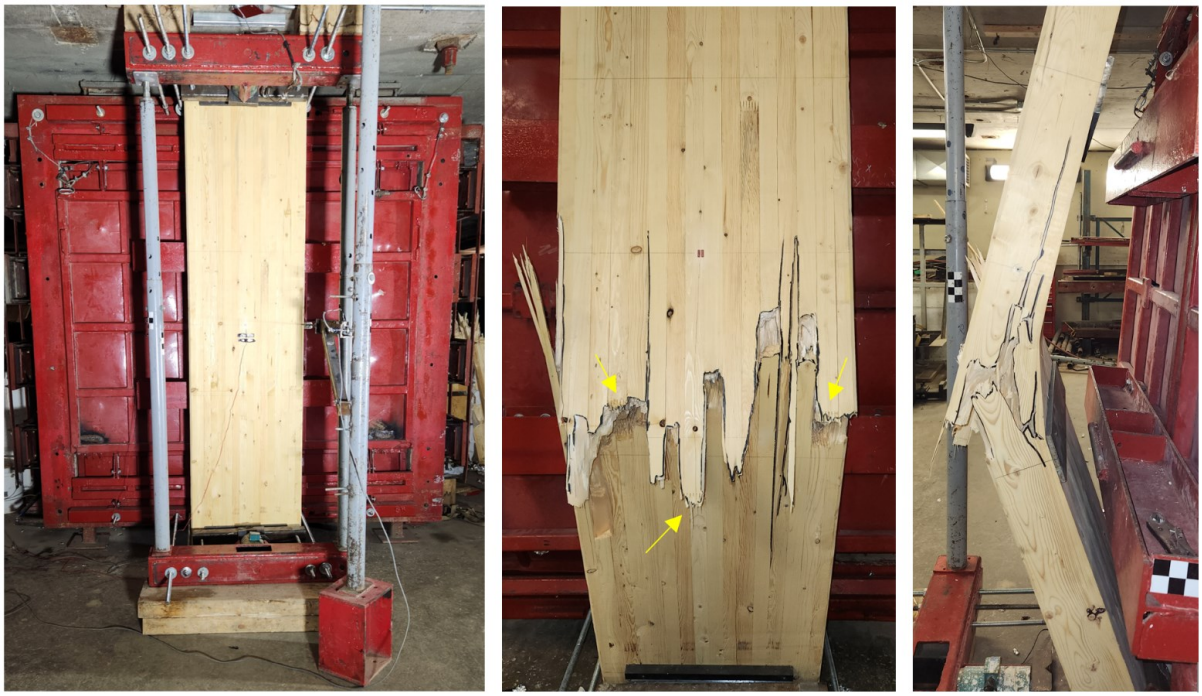

(a) (b) (c)

Figure 4-25 Dynamic Failure of GLT13 [130]: (a) Before test; (b) After test - front view with FJ locations; (c) After test - side view

4.5.7 Specimen GLT14 [130]

The specimen weight and MC were 92.0 kg and 14.0% respectively. There were three finger joints between the loading points, and three outside this region. The specimen before and after the test is shown in Figure 4-26. The driver pressure and length used were 386.1 kPa and 4,877

(16ft), respectively. This resulted a peak reflected pressure of 71.8 kPa and a peak reflected impulse of 937.5 kPa.ms over a positive duration of 38.8 ms. The maximum dynamic resistance was 182.8 kN with mid-span displacement of 35.3 mm at 15.2 ms. The specimen failure was simple tension flexural failure at mid-span. The cracks were located in the middle region between the loading points.

(a) (b) (c)

Figure 4-26 Dynamic Failure of GLT14 [130]: (a) Before test; (b) After test - front view with FJ locations; (c) After test - side view

4.5.8 Specimen GLT15 [215]

The specimen weight and MC were 145.0 kg and 14.0% respectively. There were two finger joints between the loading points, and another two outside this zone. The specimen before and after test is shown in Figure 4-27. The driver pressure and length used were 758.4 kPa and 4,877 (16ft), respectively. This resulted a peak reflected pressure of 94.5 kPa and a peak

reflected impulse of 2405.2 kPa.ms over a positive duration of 61.6 ms. The maximum dynamic resistance was 455.1 kN with mid-span displacement of 24.2 mm at 15.4 ms. The extent of failure in the specimen was low and represented only the initiation of the first crack. Only a small crack was observed at the side face and at the front face of the panel. Although the crack was visible through review of the video recording, when the specimen rebounded, the cracks were not very visible.

(a) (b) (c)

Figure 4-27 Dynamic Failure of GLT15 [215]: (a) Before test; (b) After test - front view with FJ locations; (c) After test - side view

4.5.9 Specimen GLT16 [215]

The specimen weight and MC were 145.2 kg and 14.5% respectively. There were two finger joints between the loading points, and another two outside this zone. The specimen before and after the test is shown in Figure 4-28. The driver pressure and length used were 827.4 kPa and 4,877 (16ft), respectively. This resulted a peak reflected pressure of 112.8 kPa and a peak

reflected impulse 2231.6 kPa.ms over a positive duration of 42.1 ms. The maximum dynamic resistance was 479.0 kN with mid-span displacement of 28.1 mm at 12.9 ms. The specimen failure was simple tension flexural failure closer to one of the loading points and the cracks were generally observed in the mid-span region.

(a) (b) (c)

Figure 4-28 Dynamic Failure of GLT16 [215]: (a) Before test; (b) After test - front view with FJ locations; (c) After test - side view

4.5.10 Specimen CGLT5 [215]

The specimen average depth and width were 197 mm and 598 mm, respectively, and the specimen weight was 115.2 kg. The average char depth was 18.1 mm. The specimen before and after test is shown in Figure 4-29. The driver pressure and length used were 651.6 kPa and 4,877 (16ft), respectively. This resulted in a peak reflected pressure of 94.4 kPa and a peak

reflected impulse of 1390.5 kPa.ms over a positive duration of 35.8 ms. The maximum dynamic resistance was 245.9 kN with mid-span displacement of 21.1 mm at 10.0 ms. The specimen failure was simple tension flexural failure closer to one of the loading points. The cracks were initiated at mid-span, and a separation between the laminations at the glue lines was observed.

(a) (b) (c)

Figure 4-29 Dynamic Failure of CGLT5 [215]: (a) Before test; (b) After test - front view; (c) After test - side view

4.5.11 Specimen CGLT6 [215]

The specimen average depth and width were 195.5 mm and 596 mm, respectively, and the specimen weight was 115.0 kg. The average char depth was 19.5 mm. The specimen before and after the test is shown in Figure 4-30. The driver pressure and length used were 551.6 kPa and 4,877 (16ft), respectively. This resulted a peak reflected pressure of 100.9 kPa and a peak

reflected impulse 1390.5 kPa.ms over a positive duration of 51.4 ms. The maximum dynamic resistance was 245.3 kN with mid-span displacement of 21.9 mm at 12.0 ms.

The specimen failure was simple tension flexural failure at mid-span. The cracks were located in the middle with a small ratio propagating beyond the load application points. There was separation between the laminations observed.

(a) (b) (c)

Figure 4-30 Dynamic Failure of CGLT6 [215]: (a) Before test; (b) After test - front view; (c) After test - side view

4.5.12 Specimen CGLT7 [215]

The specimen average depth and width were 196.4 mm and 599 mm, respectively, and the specimen weight was 115.5 kg. The average char depth was 18.6 mm. The specimen before and after the test is shown in Figure 4-31. The driver pressure and length used were 472.3 kPa and 4,877 (16ft), respectively. This resulted in a peak reflected pressure of 72.7 kPa and a peak

reflected impulse 1473.7 kPa.ms over a positive duration of 60 ms. The maximum dynamic resistance was 238.6 kN with mid-span displacement of 20.5 mm at 13.8 ms. The maximum displacement was 21.2 mm at 18.0 ms. The specimen failure was flexural failure at mid-span. This shot resulted in minor crack development, which were located between the mid-span and the loading points. The cracks did not propagate across the specimen width.

The specimen was subjected to a second shot to induce a higher level of damage, but the maximum dynamic resistance was observed in the first shot. The driver pressure and length used in the second shot were 524.0 kPa and 4,877 (16ft), respectively. The second shot resulted a peak reflected pressure of 77.4 kPa and a peak reflected impulse 1249.7 kPa.ms over a positive duration of 51.4 ms. The specimen after the second shot is shown in Figure 4-32. The specimen cracks were located between the mid-span and one of the loading points.

(a) (b) (c)

Figure 4-31 Dynamic Failure of CGLT7 [215] first shot: (a) Before test; (b) After test – front view; (c) After test – side view

(a) (b)

Figure 4-32 Dynamic Failure of CGLT7 [215] second shot: (b) After test - front view; (c) After test - side view

4.6 Zero-strength Layer Results

The ZSL can be obtained by equating the resistance of the actual residual cross-section in fire conditions with the resistance of the effective cross-section at ambient conditions, as RCSM assumes that material properties of the effective residual section remain unchanged (Schmid et al., 2015). The same approach was adopted to determine ZSL thickness post real fire in this study. The experimental moment resistance of the residual cross-section post real fire (M_{max}), which are summarized in Table 4-8 in Section 4.4 and Table 4-10 in Section 4.5, was considered equal to the experimental moment resistance of the effective cross-section at ambient temperature (M_{ef}), as presented in Equations 4-8 and 4-9.

$$M_{max} = M_{ef} \quad 4\text{-}8$$

$$M_{max} = S_{ef}\, MOR \quad 4\text{-}9$$

Where MOR is the experimental modulus of rupture of panels with the original cross-section dimensions at ambient temperature, and summarized in Table 4-7 in Section 4.4 and Table 4-10 in Section 4.5. The average MOR of uncharred panels with 215 mm depth was found equal to 35.4 MPa and 37.1 MPa, under static and dynamic loading, respectively. (S_{ef}) is the section modulus of the effective cross-section and replaced in Equation 4-10 with the effective depth (d_{ef}) and effective width (b_{ef}). The effective width is equal to (b_i) reported in Section 4.2. As panels were exposed to fire from one side only, the ZSL is removed from one side only as shown in Equation 4-11 and the thickness of ZSL (x_t) is presented in Equation 4-12.

$$M_{max} = \frac{b_i\, d_{ef}^2}{6}\, MOR \quad 4\text{-}10$$

$$M_{max} = \frac{b_i\, (d_r - x_t)^2}{6}\, MOR \quad 4\text{-}11$$

$$x_t = d_r - \sqrt{\frac{6\, M_{max}}{b_i\, MOR}} \quad 4\text{-}12$$

Table 4-11 summarizes the ZSL and effective depth results under static and dynamic loading. The results showed an average ZSL equal to 23.8 mm (CV 34.0%) and 36.5 mm (CV 10.9%) mm under static loading (0.9 x10^{-6} s^{-1}) and dynamic loading (0.2 s^{-1}), respectively. The average effective depth was found to be 170.4 mm (CV 4.7%) and 159.8 mm (2.5%) at strain rates of 0.9 x10^{-6} s^{-1} and 0.2 s^{-1}, respectively, after removal of the ZSL.

Table 4-11 ZSL and effective depth results under static and dynamic loads

Test Type	Specimen Name	b_i (mm)	d_r (mm)	M_{max} (MPa)	x_t (mm)	d_{ef} (mm)
Static	**CGLT1 [215]**	598	195.2	111.9	17.1	178.1
	CGLT2 [215]	600	194.4	104.6	22.5	171.9
	CGLT3 [215]	597	192.2	104.4	20.0	172.2
	CGLT4 [215]	598	194.6	89.4	35.4	159.2
	Avg.	598.3	194.1	102.6	23.8	170.4
	SD	1.3	1.3	9.5	8.1	8.0
	CV	0.002	0.007	0.092	0.340	0.047
Dynamic	**CGLT5 [215]**	598	196.9	91.6	39.5	157.4
	CGLT6 [215]	596	195.5	91.4	38.0	157.5
	CGLT7 [215]	599	196.4	100.1	32.0	164.4
	Avg.	597.7	196.3	94.4	36.5	159.8
	SD	1.5	0.7	5.0	4.0	4.0
	CV	0.003	0.004	0.053	0.109	0.025

Chapter 5 Analytical Modelling and Results

5.1 General

This section includes the method used to determine the strength increase factor and dynamic increase factor for charred and uncharred GLT panels. Further, the method used to develop the predictive model for the dynamic behaviour of the panels under simulated blast loads is included.

5.2 Determination of Strength Increase Factors (SIF)

The SIF results were determined by dividing the static strengths obtained from the current experimental campaign by the design-level strength obtained from CSA O86 (CSA, 2024) and CSA S850 (CSA, 2025). The design moment resistance (M_r) was obtained from Equation 5-1.

$$M_r = \varphi f_b (k_D k_H k_{Sb} k_T) S K_{zb} K_L \quad 5\text{-}1$$

Where the resistance factor (φ) was taken equal to 1.0 according to the Canadian blast design standard (CSA, 2025). The specified strength in bending (f_b) was taken equal to 11.8 MPa based on the manufacturer's specification (see Section 3.2), and the Canadian wood design standard (CSA, 2024). The load duration factor (k_D) for a short-term duration was taken equal to 1.25 (Doudak et al., 2022). The system factor (k_H) was taken equal to 1.1 according to the built-up beam provisions in CSA O86 (CSA, 2024). The service condition factor (k_{sb}) and treatment factor (k_T) were assumed equal to unity since the tested specimens were not treated, and they were conditioned to dry service conditions. The size factor (k_{Zb}) was obtained based on the depth of the panel and lamination thickness, and it was taken as 1.4 and 1.1 for panels with 130 mm and 215 mm depth, respectively. The lateral stability factor (K_L) was taken as unity since there is no possibility of such failure mechanism. The section modulus (S) was obtained from Equation 5-2, where (b) and (d) are the width and depth of the panel, respectively.

$$S = \frac{bd^2}{6} \quad 5\text{-}2$$

Table 5-1 summarizes the SIF results for uncharred panels, with an average of 1.6 (CV 12.7%) and 1.9 (CV 5.6%) for panels with depth of 130 mm and 215 mm, respectively.

Table 5-1 Strength increase factor results for uncharred GLT panels

Panel Name	K_{zb}	M_{max} (kN.m)	M_r (kN.m)	SIF
GLT1 [130]	1.4	55.0	40.0	1.4
GLT2 [130]		70.0		1.8
GLT3 [130]		68.3		1.7
Avg.		64.4		1.6
SD		8.2		0.2
CV		0.127		0.127
GLT4 [215]	1.1	163.5	87.1	1.9
GLT5 [215]		154.1		1.8
GLT6 [215]		176.2		2.0
GLT7 [215]		168.6		1.9
Avg.		165.6		1.9
SD		9.3		0.1
CV		0.056		0.056

The same approach as above was used to determine SIF for charred panels. The modification factors were kept identical to the ambient design case; only the section modulus was changed to reflect fire damage. The size factor for charred panels was taken based on the effective cross-section depth, i.e. after removal of experimental char depth and ZSL under static loading. Table 5-2 summarizes the SIF results for charred panels, with an average of 1.8 (CV 9.2%).

Table 5-2 Strength increase factor results for charred GLT panels

Panel Name	M_{max} (kN.m)	M_r (kN.m)	SIF
CGLT1 [215]	111.9	58.0	1.9
CGLT2 [215]	104.6	57.6	1.8
CGLT3 [215]	104.4	55.9	1.9
CGLT4 [215]	89.4	57.6	1.6
Avg.	102.6	57.2	1.8
SD	9.5	0.9	0.2
CV	0.092	0.016	0.092

5.3 Determination of Dynamic Increase Factors (DIF)

DIF was determined by comparing the resistance-displacement curves from dynamic and static tests, as shown in Figure 5-1. The comparison showed a slight increase in resistance for uncharred panels, whereas charred panels exhibited no increase, in fact, an apparent reduction in strength was observed. The DIF was calculated by dividing the maximum dynamic resistance by the average static resistance, and the results are summarized in Table 5-3. An average DIF of 1.1 (CV 4.4 %) was obtained for uncharred GLT panels, and DIF of 0.9 (CV 5.3%) for charred GLT panels. Since a reduction, rather than increase, in strength was observed in the dynamic tests of the charred specimens, the term dynamic "increase" factor is a misnomer. However, it is kept since the procedure used to obtain this ratio is consistent with that used to calculate the DIF for the uncharred specimens.

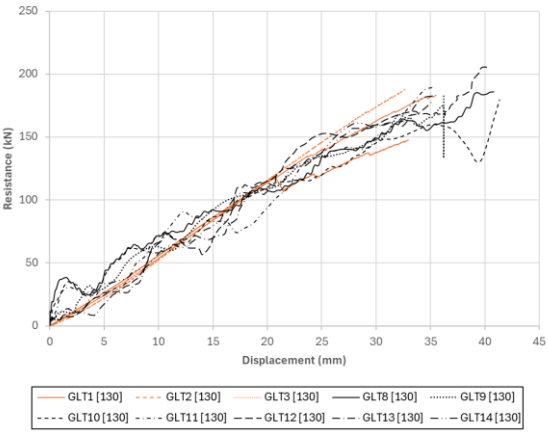

(a)

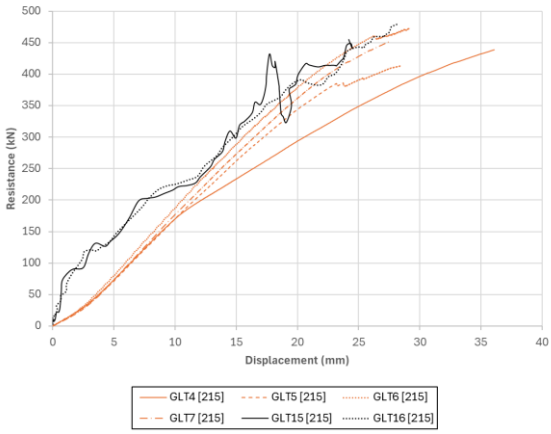

(b)

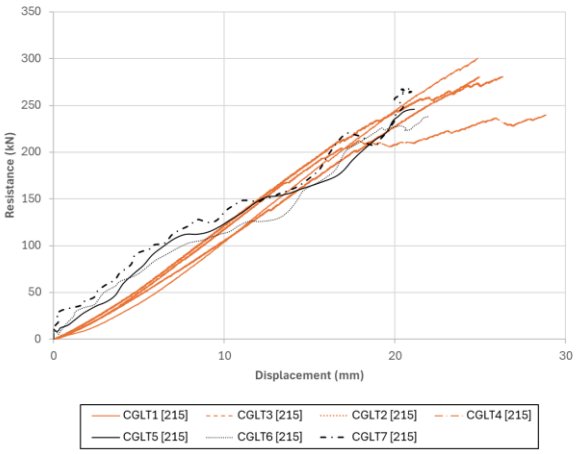

(c)

Figure 5-1 Static and dynamic resistance-displacement curves: (a) 130 mm depth (b) 215 mm depth (c) charred panels

Table 5-3 Dynamic increase factor results for charred and uncharred GLT panels

Panel Name	R_{max-d}[1] (kN.m)	R_{max-s}[2] (kN.m)	DIF
GLT8 [130]	185.9		1.08
GLT9 [130]	182.8		1.06
GLT10 [130]	179.6		1.04
GLT11 [130]	189.5	172.9	1.10
GLT12 [130]	205.4		1.19
GLT13 [130]	179.7		1.04
GLT14 [130]	182.8		1.06
GLT15 [215]	455.1	444.5	1.02
GLT16 [215]	479.0		1.08
Avg.			1.1
SD			0.05
CV			0.044
CGLT5 [215]	245.9		0.89
CGLT6 [215]	245.3	275.4	0.89
CGLT7 [215]	268.6		0.98
Avg.			0.9
SD			0.1
CV			0.053

[1] Maximum resistance from dynamic tests

[2] Average resistance from static tests

5.4 Material Predictive Model

A single-degree-of-freedom modelling approach was utilized to simulate the dynamic response of the GLT panels, which had proven to be effective in modelling various structural elements from different materials subjected to simulated planar blast loads (e.g., Aoude et al., 2015; Côté & Doudak, 2019a; Jacques et al., 2013; M. Poulin et al., 2018a). Further details of the dynamic analysis used are provided in Section 2.2.1. In this model, the structural system is simplified into SDOF system, where the mass of the GLT panel is distributed, and the mass of the LTD is treated as concentrated loads. In this SDOF system, the motion is described using a single generalized coordinate, represented as displacement at mid-span and reflecting the deflected

shape of a simply supported beam under four-point bending. Damping was neglected due to the short duration of blast loading and the focus on capturing the maximum dynamic displacement.

Flexural failure was the sole dominant failure mode observed during the full-scale dynamic testing for uncharred and charred panels. The resistance curves were developed to reflect a linear elastic behaviour up to maximum resistance. A load-mass factor of 0.87 was used in the model (Biggs, 1964; Department of Defense, 2014). The model was validated by using the dynamic experimental results as inputs in the blast analysis software RCBlast® (Jacques, 2024). This software is a blast analysis software tool capable of conducting equivalent SDOF simulations and has demonstrated accuracy in analyzing the dynamic responses of various structural systems. In addition to the model resistance curves, the experimental reflected pressure-time histories were used as inputs, along with the structural system mass. The total mass of the uncharred panels was taken as 378.8 kg and 429.5 kg for panels with depth 130 mm and 215 mm, respectively, while the total mass for charred panels was taken as 399.4 kg. The effective loaded area was taken equal to 3.55 mm^2, which is equal to the LTD effective tributary area. Model validation was performed by comparing the predicted displacement-time history curves with those obtained experimentally. Figure 5-2 presents an example of the comparison between the experimental and SDOF modelling results for uncharred panels, and Figure 5-3 presents an example of the comparison for charred GLT panels. Further details on the results of each specimen can be found in Appendix F.

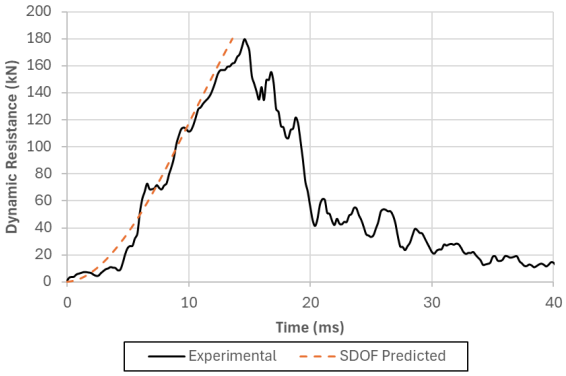

(a)

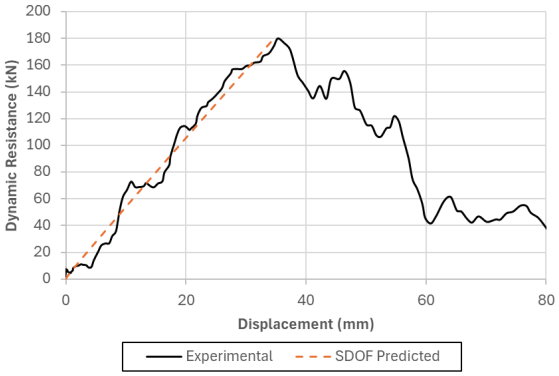

(b)

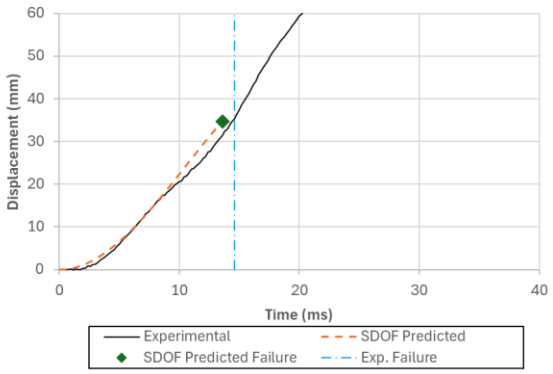

(c)

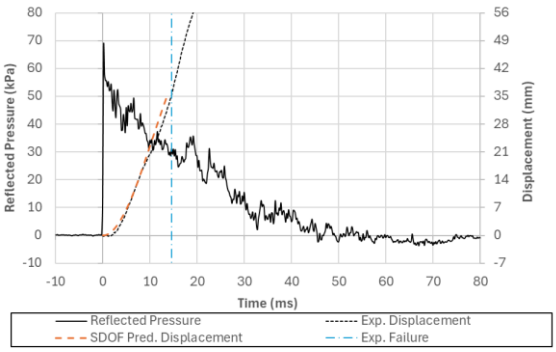

(d)

Figure 5-2 Uncharred panel SDOF Model results compared to experimental results, GLT13 [130]: (a) Dynamic resistance-time history; (b) Dynamic resistance curves; (c) Displacement-time histories; (d) Reflected pressure and displacement- time histories.

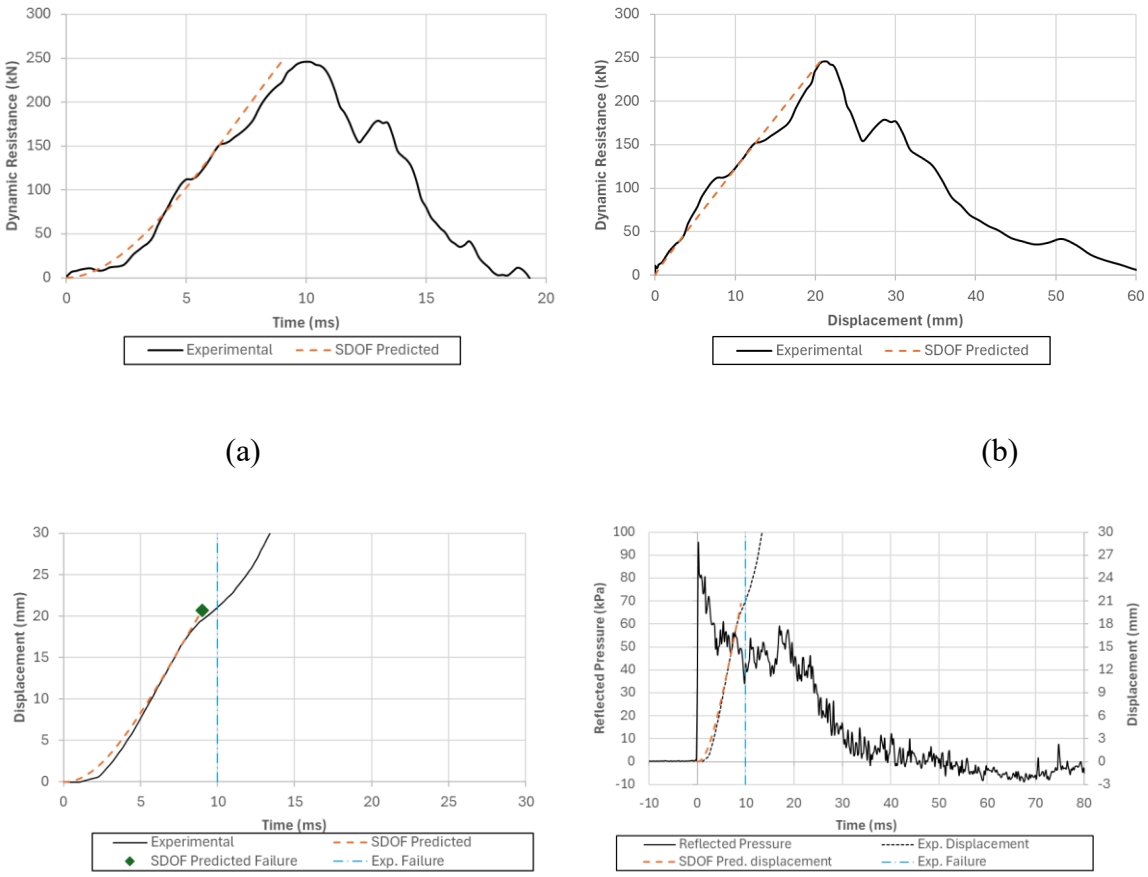

Figure 5-3 Charred panel SDOF Model results compared to experimental results, CGLT5 [215]: (a) Dynamic resistance-time history; (b) Dynamic resistance curves; (c) Displacement-time histories; (d) Reflected pressure and displacement- time histories.

Chapter 6 Discussion

6.1 General

The present study investigates scenarios involving a building with mass timber elements (with a focus on GLT) subjected to a blast caused by a fire incident that has potentially compromised the integrity of, for example, a gas tank. This loading condition is very rare yet probable, and the fact that encapsulated mass timber elements are designed to potentially self-extinguish and sustain some residual resistance makes this situation particularly relevant for tall buildings, where damage to a single element could lead to disproportional damage to the building. The approach taken during this investigation is to assess the condition of the elements during and after the fire (say 10 to 20 min), and blast loading is eminent thereafter.

Interesting questions to consider are:1) How do GLT elements behave structurally during and after real (rather than standard) fires when considering a cooling phase?, 2) How would such elements behave during a subsequent blast event, given their in-situ condition and potential damage beyond the surface char?, and 3) Assuming such elements have adequate dimensions to be cleaned, repaired, and reused as part of the structural system, how can a designer assess their residual resistance? None of these questions is trivial, given the complexity of the situation and the rare opportunity to investigate such scenarios. Such an opportunity was presented through the MTDFTP project conducted in Ottawa during the summer of 2022, where a mass timber building was subjected to real fires, and a total of seven GLT panels were selected after they self-extinguished and brought to the University of Ottawa's structural laboratory to be investigated statically and under simulated blast loading.

Due to the intricate nature of this investigation, which involves multiple load types and attempting to answer several design-related questions, the discussion chapter is divided into three sections. Section 6.2 discusses the characteristics of the charred specimens in terms of

charring rate, zero-strength layer, and fire resistance adjustment factor as well as evaluate the use of image analysis tools to obtain some of these parameters. Section 6.3 examines the blast-resisting performance of uncharred and charred GLT panels. Key parameters include DIF and SIF, which help establish the resistance curves needed for the dynamic analysis. Section 6.4 provides design implications for multiple stages, including the blast performance of uncharred GLT panels, charred panels immediately after the cooling phase of a real fire, as well as the performance during a subsequent loading is a decision is made to maintain the residual section.

6.2 Charring Behaviour of GLT panels

6.2.1 Char Depth and Charring Rate

The char depth was obtained as the difference between the original and residual cross-section depth after char layer removal. This was done in order to obtain the one-dimensional charring rate as part of the post-fire assessment. During this process, the char depth was obtained using a calliper, and it was determined to on average be equal to 20.0 mm (CV 7.9%) after an estimated 25.7 min of real fire exposure. This resulted in a measured char depth of around 1.2 times that obtained using the design charring rate of 0.65 mm/min according to CSA O86 (CSA, 2024) (i.e. 16.7 mm). A comprehensive evaluation of the MTDFTP building was undertaken by Su et al. (2023), and reported an average char depth of 24 mm for the ceiling panels overall and values of 15, 25, 30, and 40 mm at measured locations every 2.4 m spacing in Bay 4 (See Figure 3-4 in Section 3.2). While the exact location of the investigated specimens within Bay 4 is unknown, the measured average char depth (i.e., 20 mm) lies within that reported range and slightly below the overall average.

A key uncertainty in estimating the charring rate is the definition of the fire exposure duration. Video recordings and visual observations reported visible flames entering and exiting Bay 4 during approximately 12 min (Su et al. 2023), however, this duration does not necessarily

represent the thermal exposure relevant to charring, as high temperatures can persist beyond the period of visible flaming. Furthermore, compartment fires are highly variable, and ceiling gas temperatures were non-uniform due to the large open-plan compartment in this study. Therefore, the fire exposure time was taken as 25.7 min based on the measured gas temperature (400 °C threshold), which provides a conservative estimate of the charring rate by shortening the exposure duration and therefore resulting in a higher calculated charring rate, given that the primary objective here is post-fire assessment.

Based on the aforementioned estimated char depth and fire exposure duration, the average one-dimensional charring rate is estimated to be 0.78 mm/min (CV 7.9%), which, as mentioned earlier, exceeds that provided in the CSA O86 standard (CSA, 2024) for design purposes (0.65 mm/min). It should be noted, however, that this direct comparison may not be appropriate, since the design charring rate is developed based on an average value over a more substantial time duration (e.g., 30 min to 120 min), where the developed char provides an insulating layer that reduces the charring rate. Furthermore, standardized fire tests are not intended to reproduce specific real fires but to provide a consistent basis for comparison between various fire resisting systems by producing a total equivalent energy exposure representative of real fires. Figure 6-1 illustrates the difference between the time-temperature curves of the real fire and ISO 834 (2025). The higher charring rate of 0.78 mm/min observed in this study primarily reflects the short and initial intense heating phase of the real fire, when the wood is first exposed to fire.

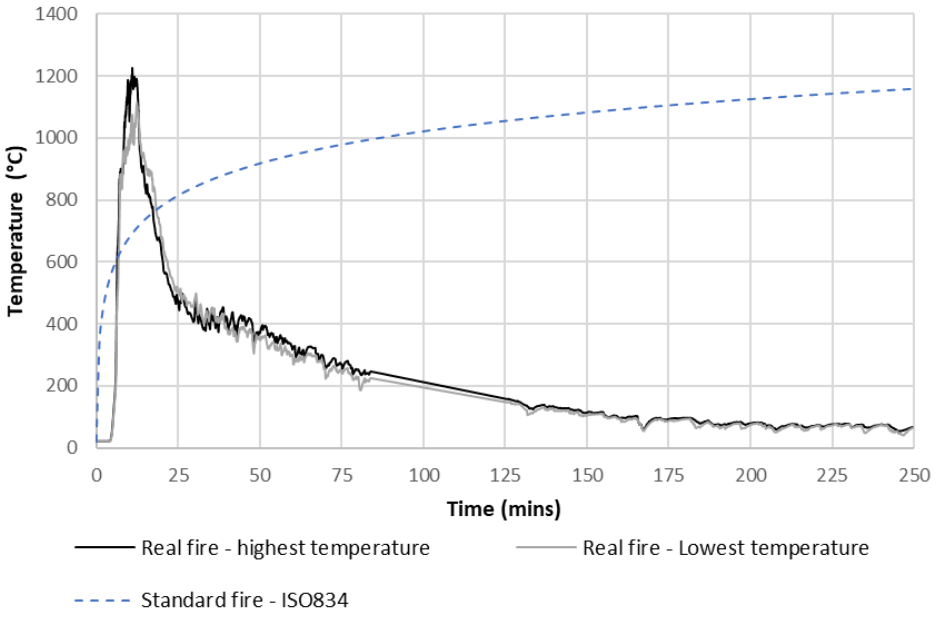

Figure 6-1 Time-temperature fire curves in Bay 4 - Test (5) of MTDFTP

In addition to initial intense heating phase temperature and duration of the real fire, it should be reminded that the MTDFTP test was representative of a worst-case fire scenario with high movable fuel load density (362 MJ/m²) and high ventilation through large openings that allowed significant airflow (Su et al. 2023), all of which can contribute to an increase in charring rate. Mitchell et al. (2023) reported that charring rates in compartment fires are influenced by ventilation, which increases oxygen supply, and by movable fuel load, which results in higher temperatures and higher heat fluxes incident on timber surfaces. As shown in Figure 6-1, the gas temperature measured at 150 mm below the ceiling surface in Bay 4, where the GLT panels were located, reached approximately 1200 °C in approximately 5 min, compared with about 550 °C in the standard-temperature-time fire curve (ISO 834 ,2025). Seyedrazavi & Viau (2025) also reported high charring rate of an average of 2.3 mm/min charring rate for a glulam column extracted from the same bay and story as the investigated charred GLT panels.

Current approach for encapsulated mass timber in compartment fires generally focuses on protection through an "encapsulation rating" or fall-off time obtained from standard fire tests, and mainly focuses on ensuring adequate encapsulation duration, limiting the area of exposed timber, and, in performance-based designs, demonstrating burnout or self-extinction (e.g., Wiesner et al., 2025), rather than modifying the charring rate after fire exposure. When encapsulation materials are used, they are found to substantially delay the charring and reduce the initial charring rate compared with unprotected members. However, once the encapsulation material falls off or crack, the exposed timber chars at an accelerated rate because it is exposed to the fire at a higher compartment temperature than at ignition. If the encapsulation remains intact, it behaves similar to a char insulation layer in unprotected timber, slowing the charring process and allowing the use of the standard design charring rate (Hasburgh et al., 2016; Schmid et al., 2019). While an initial charring rate is expected to be higher than those in the design standards, the higher charring rate, similar to those observed in this study for the unprotected GLT panels, should be used when evaluating post-fire residual capacity and potential reuse of structural mass-timber components.

6.2.2 Image Analysis Tool and Process

The objective of this section is to investigate the applicability of image analysis tool using a machine learning plugin, namely Fiji (ImageJ) (Schneider et al., 2012) and Trainable Weka Segmentation (TWS) plugin (Arganda-Carreras et al., 2017). The intent is to identify the discoloured layers in the charred specimens (i.e., residual char and pyrolysis layers shown in Figure 6-2) and confirm that fire-induced structural degradation extends beyond the visibly discoloured zones of charred wood by comparing the obtained pyrolysis layer thickness with the ZSL discussed in the following section as part of the post-fire assessment.

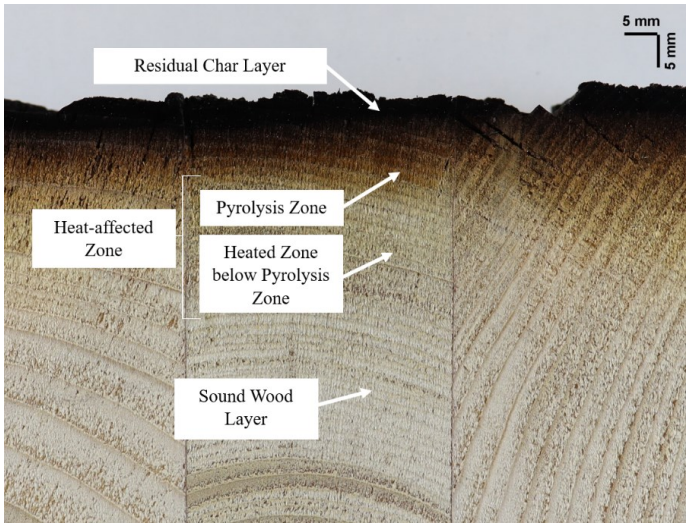

Figure 6-2 Residual char and pyrolysis layers in GLT panels (reproduced for convenience from Figure 2-9)

When considering all small-scale samples (120 measurements), the average thickness of the residual char layer from image analysis was 7.1 mm (CV 23.5%). This value falls within the range of the residual char layer thickness (3.4 mm - 7.3 mm) found in the full-scale specimens using a digital calliper, obtained as the difference between panel depth before and after char removal (Table 4-1, Section 4.2). On the same 120 samples investigated for the residual char layer, additional 120 measurements were taken of the pyrolysis layer and the average thickness from image analysis was 11.1 mm (CV 23.2%). A small subset of small-scale samples (11 measurements) was considered for a direct comparison between image analysis and the handheld digital calliper measurements. It was found that the absolute difference in the pyrolysis layer, between results obtained from image analysis and calliper was 5.7%. The 11.1 mm thickness of the pyrolysis layer is consistent with the findings reported by Seyedrazavi & Viau (2025), where the visually degraded layer thickness was reported to be 9.7 mm (using a calliper) for a glulam column extracted from the same test, bay, and story as the investigated charred GLT panels. The back-calculated ZSL post real fire exposure showed average values of 23.8 mm and 36.5 mm for specimens tested under static and blast-simulated dynamic

loading, respectively (Table 4-11 in Section 4.6). The findings show that the ZSL value is significantly greater than the pyrolysis layer by 2 to 3 times, which confirms that structural degradation extends beyond the visibly coloured layers, as highlighted by Schmid (2020).

The image analysis tool and workflow described in Section 4.3 proved to be fast, repeatable, and sufficiently accurate. The workflow was applied to 25 samples and produced a total of 240 measurements of the pyrolysis and residual char layers in a relatively short time, compared to handheld caliper measurements. Fiji (ImageJ) has previously been used in the analysis of charred wood to determine char depth (e.g., Albert & Liew, 2025), while TWS plugin has mainly been used in wood anatomy and density profiling applications (e.g., De Mil et al., 2018; Luo et al., 2021), and, to the best of the author's knowledge, has not been used to quantify char and pyrolysis layers in charred wood. Therefore, the present study, provided an opportunity to extend the use of TWS, which is based on machine learning segmentation, to a new application in post-fire assessment.

Image analysis tools, in general, have already been shown to enable more efficient and reproducible workflows resulting in an automated and semi-automated processes and allowing researchers to handle large datasets (e.g., von Arx et al., 2016). TWS has been shown to be a fast and accessible segmentation tool that can automate tasks that were previously carried out manually and considered time-consuming in fields other than wood and structural engineering (e.g., biomedical engineering) (e.g., Kataras et al., 2023). In the context of wood anatomy, TWS has enabled semi-automated processing where large amounts of images can be analysed quickly and accurately (Van den Bulcke et al., 2025). De Mil et al. (2018), for example, used TWS in combination with a block processing approach to derive wood density profiles from large number of images, substantially accelerating what is known to be a time-consuming analysis when performed without automated segmentation. Therefore, using the TWS plugin

for post-fire assessment shows promising opportunity for automating the quantification of char depth and pyrolysis layer, which could support research standardization, comparison of research findings, and design verification.

In terms of post-fire assessment, where a decision must be made on whether to reuse or replace a structural element, cross-section analysis using image processing before surface char cleaning, where access permits, could provide an indicator of the expected effective cross-section. Once a relationship is established between the ZSL and the pyrolysis layer, image analysis would provide a reasonable estimate of the effective cross-section before any invasive procedure is undertaken. Based on the present study, the thickness of ZSL was found to be twice that of the pyrolysis layer. However, this may not be generalized to all GLT, or other wood products and additional research is required to confirm these findings.

6.2.3 Zero-Strength Layer

Understanding the origin of the ZSL concept in design standards is important for this discussion. The ZSL was introduced as part of the Residual Cross-Section Method to account for the reduction of material strength under fire by deducting an additional layer beyond the char depth, which allows the use of ambient-temperature material properties in fire design. Schaffer (1984) proposed this method for simply supported glulam beams exposed on three or four sides to standard fires of 30 and 60 min and reported a ZSL of 7.6 mm, which was later adopted as 7 mm in various standards, including the CSA O86 (2024).

In the present study, the ZSL was back-calculated as part of the post-fire assessment and an average value of 23.8 mm (CV 34.0%) under static loading was found. In general, this value is consistent with those found in previous studies. For example, a study was undertaken by Schmid et al., (2015) and reported a range between 9.5 mm and 20.1 mm under standard fire. Quiquero et al. (2018) reported ZSL of approximately 23 mm for glulam beams exposed to

short-term real fire (3 to 15 min), and Huč et al. (2021) found values ranging between 8.4 and 30.5 mm for glulam beams exposed to parametric fire. Huč et al. (2025) reported a ZSL of 21.4 mm under simulated natural fire exposure. These examples show ranges that are consistent with the values found in the present study when specimens were tested statically.

To the author knowledge, no prior studies have addressed ZSL under dynamic loads, and as such the higher value obtained under the dynamic loading, which is 36.5 mm (CV 10.9%), is difficult to compare or verify. The increase in ZSL under dynamic loading observed in this study may suggest that high strain-rate effects could amplify the impact of the degradation zone, possibly due to the development of internal small cracks similar to the ones that were observed on the surface (described in Section 4.2). Due to the limited dataset in the current study, it is suggested that the observations related to rate-dependent post fire behaviour of mass timber elements be further investigated in future studies.

According to CSA O86 (2024), the ZSL thickness for fire exposure of 25.7 min is set to be 7 mm, which is 3.4 times lower than the ZSL of 23.8 mm found in this study. This finding suggests that current ZSL values in fire design standards may underestimate the actual extent of heat-affected zones under real fire, which aligns with recent studies reporting that existing ZSL values in standard may be non-conservative for both standard and non-standard fire exposures (e.g., Frangi et al., 2023). While Eurocode (2025) increased the ZSL to a fixed 10 mm value for bending members, this value is still smaller than the experimentally observed ZSL in the present study.

The difference between ZSL values obtained from standard fire and those measured after real fire can be attributed to the different heating and cooling rates, as reported by Lange et al., (2015). In the investigated GLT panels, ZSL was obtained post short-term real fire, where the specimens were subjected to a relatively rapid rise to high temperatures (approximately

1200°C) over a short duration followed by a slower cooling phase, where the temperature was maintained above 300°C for around 60 min during the cooling phase. It should be noted that due to the loading of specimens during fire in standard fire situation, the cooling phase does not enter into considerations. This extended cooling phase is expected to induce deeper thermal degradation (i.e. greater ZSL thickness) beyond the char layer compared with the standard fire exposure. The continuation of heat to penetrate into the wood during the cooling phase, extending the depth of the ZSL, has also been observed by Horio et al. (2016) and Huč et al. (2021).

Another important point is that fire design standards do not consider effects of fire type, duration, or member type when using the ZSL design value, even though these factors may significantly influence the actual ZSL. This generalization may not be appropriate for slabs exposed on one side only, as noted by Schmid et al., (2015), which is the case in the present study. Floor or roof panels in compartment fires exposed to fire from one side experience non-uniform in-depth and in-plane temperature penetration, which continue long after the fire exposure ends due to factors such as uneven burning, ventilation and long cooling phase, as reported by Wiesner et al. (2021). Furthermore, travelling fires in large open-office plan compartments, which is the case in the present study, produce deeper and more non-uniform internal temperature penetration, leading to greater zero-strength layer thickness in slabs compared to standard fire exposures, as observed by Richter et al. (2021).

Overall, the results indicate that ZSL in real fire conditions is significantly greater than the value adopted in current standards. Moreover, the large ZSL observed in this study implies that the effective residual cross-section of glulam panels after real fire exposure may be significantly smaller than that predicted by standard approaches, and consequently, post-fire capacity could be overestimated if standard ZSL values are used, particularly in design scenarios where short-duration real fire exposure occurs. Integrating experimentally derived

ZSL values into analytical or numerical models that evaluates structural member resistance under short fire exposure could improve prediction accuracy. This highlights the possible need to revisit design assumptions and residual resistance models for mass-timber structural elements.

6.2.4 Fire Resistance Adjustment Factor

The adjustment factor for fire resistance (K_{fi}) has the purpose to convert the specified strength to mean strength. The approach used to obtain the adjustment factor in Annex B of the CSA O86 standard (CSA, 2019) was simplified to determine a value that is independent of member size or grade. According to the CSA O86 commentary (Canadian Wood Council, 2020), the factor is estimated using the coefficient of variation (*CV*) of the mean strength by assuming a normal distribution, as shown in Equation 6-1.

$$K_{fi} = \frac{1}{1-(1.65)(CV)} \quad \text{6-1}$$

Where CV was taken to be 20% for solid lumber and 16% for glulam, yielding corresponding K_{fi} values of 1.5 and 1.35, respectively. The experimental *CV* for the *MOR*, obtained from the static bending test results, based on a pooled value from both panel depths, 130 mm and 215 mm, was found to be 9.1%, which corresponds to K_{fi} of 1.18. This result indicates that the obtained value is closer to the value for glulam (1.35) provided in Annex B of the CSA O86 standard, which is reasonable since GLT panels, similar to glulam beams, are made of MSR lumber laminations. The lower value obtained in the current study can be attributed to the fact that the GLT panels were produced by one manufacturer and came from the same batch. The higher value obtained in the standard reflects the larger variability found when glulam from different manufacturers, wood species, and grades are considered.

6.3 Static and Dynamic Behaviour of GLT panels Pre- and Post-fire

6.3.1 Failure Modes

The failure modes for charred and uncharred GLT panels under static and dynamic loading were consistent and characterized by flexural failure, which was initiated at the tension face of the panels, as shown in Figure 6-3 and Figure 6-4. The failure of the outer tension lamination was followed by cracks propagating across the GLT panel. The cracks on the tension face were located around the mid-span region, between the two loading points, and there was no observable damage on the compression face or at the supports. The failure was observed to be primarily initiated at knots and/or FJ, as indicated by the arrows in Figure 6-3 (c,d) and Figure 6-4 (b,d). The failure behaviour was consistent with that reported in previous studies on glulam beams and columns (D. Lacroix & Doudak, 2018).

(a)

(b)

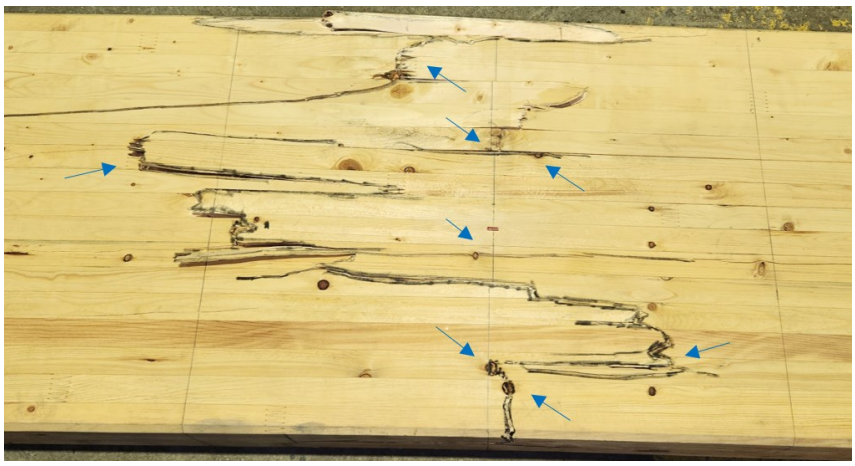

(c)

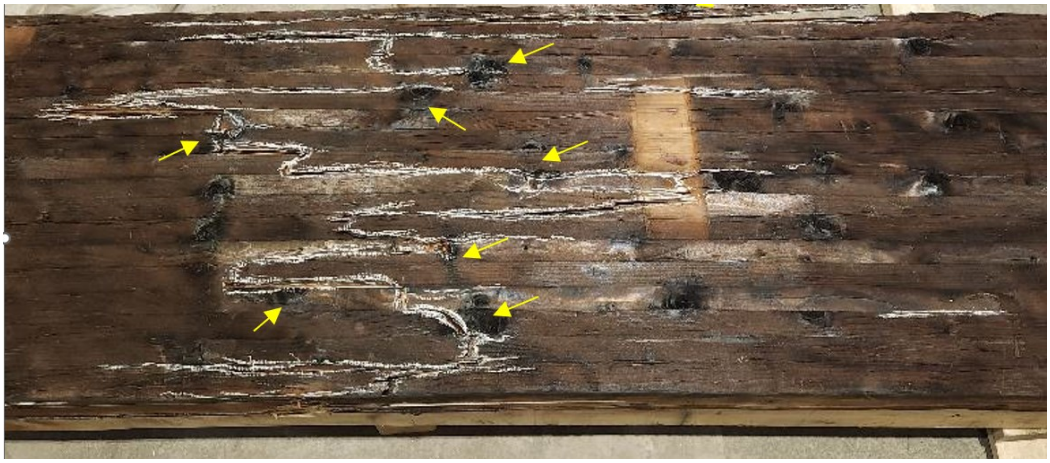

(d)

Figure 6-3 Typical static failure mode of GLT panels: (a) uncharred -side view, (b) charred - side view, (c) uncharred - bottom view with FJ and knots locations, (d) charred - bottom view with FJ and knots locations

(a) (b)

(c)

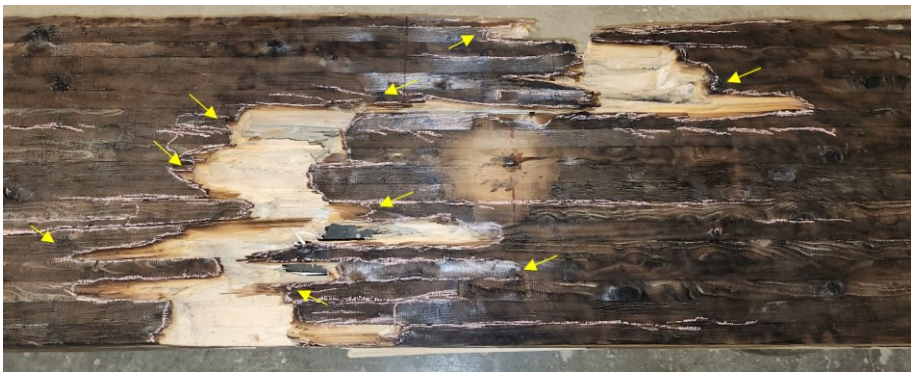

(d)

Figure 6-4 Typical dynamic failure mode of GLT panels: (a) uncharred -side view, (c) uncharred - bottom view with FJ and knots locations, (c) charred -side view, (d) charred - bottom view with FJ and knots locations

One key observation from the static and dynamic tests was that some of the charred specimens exhibited visible separation between individual laminations at the glueline locations, which was not observed in the uncharred specimens (Figure 6-5). The glueline separation in the charred panels suggests that the bond between laminations lost its integrity under fire exposure or subsequent exposure to the environment (i.e., possible wetting and drying). Delamination has been reported and observed when horizontally laminated glulam or CLT are exposed to fire, particularly when heat-sensitive polyurethane (PUR) adhesives were used, with individual lamellae falling off, even before the char layer reaches the bondline at adhesive temperatures estimated to be well below 300 °C (Hadden et al., 2017). The investigated GLT panels in this study were vertically laminated (parallel to the heat flow) and manufactured with an adhesive that complies with North American requirements, which require adhesives to resist fire-induced delamination. Therefore, whether the GLT panels investigated in this study exhibited delamination due to the weaker glueline cannot be confirmed.

(a) (b)

Figure 6-5 Visible separation between the individual laminations at the glue line locations: a) After static test; (b) After dynamic test.

Notwithstanding minor deviations, it was observed that the static and dynamic resistance curves were characterized by linear elastic response up to maximum resistance for both charred and uncharred panels, as shown in Figure 6-6 and Figure 6-7.

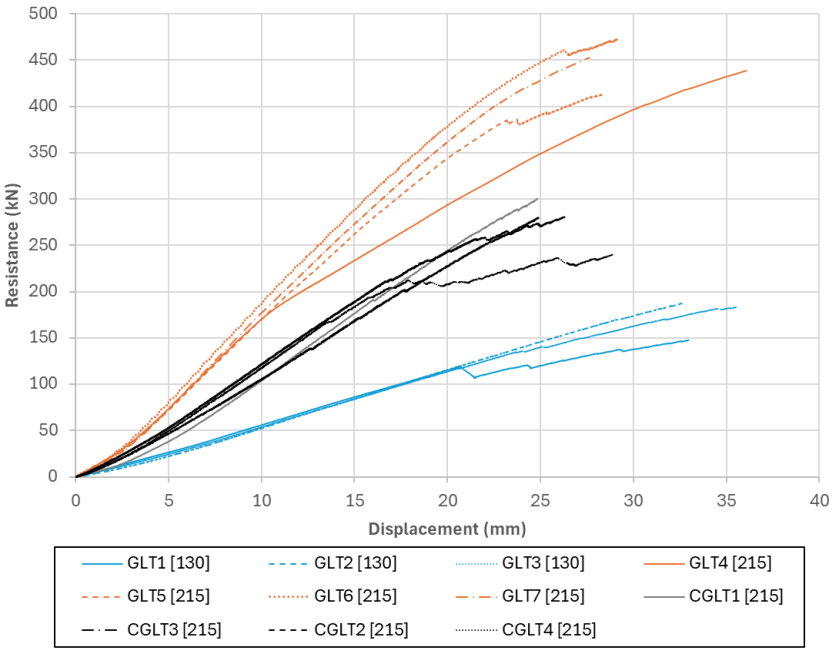

Figure 6-6 Comparison between the static resistance curves of charred and uncharred panels.

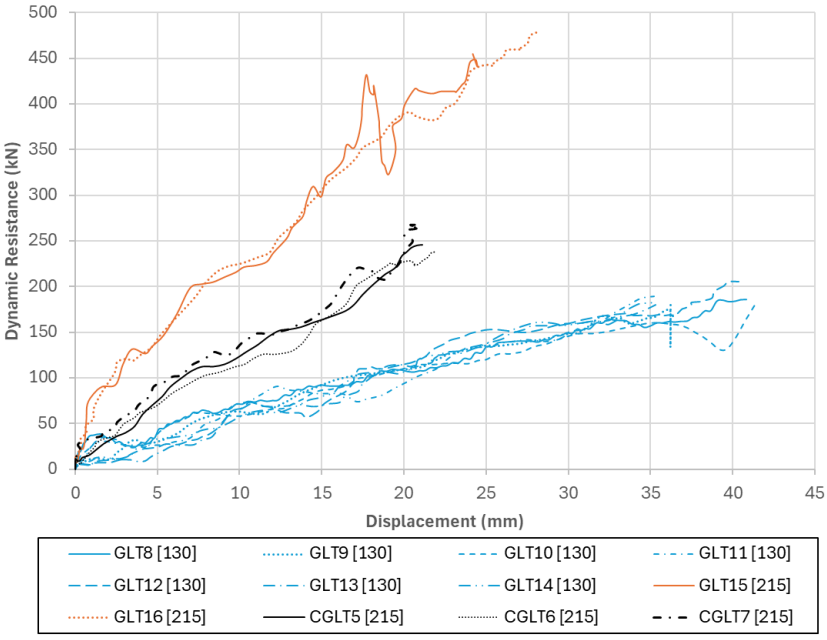

Figure 6-7 Comparison between the dynamic resistance curves of charred and uncharred panels.

6.3.2 Strength Increase Factors

The SIF results for uncharred panels resulted in an average value of 1.6 (CV 12.7%) and 1.9 (CV 5.6%) for panels with depths of 130 mm and 215 mm, respectively, while for the charred panels based on the effective cross-section, an average SIF was found equal to 1.8 (CV 9.2%). The difference between 1.6 and 1.9 values of SIF for the two depths of uncharred panels may be attributed to the size effect, which accounts for the probability of the presence of more defects in larger cross-section. Although such effects are present when a large sample size of specimens is evaluated, it is conceivable that given the small sample size, the fact that the specimens are of the same grade and came from the same manufacturer, the change in strength as a function of volume may not be evident. It is interesting to note that removing the size factor from the uncharred panels resistances results in a single SIF value equal to 1.4, independent of member depth. The obtained values for both charred and uncharred specimens align reasonably well with the range of values reported in CSA S850 (CSA, 2025) for visually-graded lumber and MSR, which are 1.9 and 1.5, respectively. This investigation confirms that the use of the values for SIF specified in the blast design standard seems valid and slightly conservative.

It is noteworthy to mention that SIF and K_{fi} in principle serve similar purposes in accounting for strength adjustments under blast loads and fire exposure, respectively. However, the approach used to obtain these factors differ between the blast design standard and Annex B of CSA O86 and as such a direct comparison is not possible.

6.3.3 Dynamic Increase Factors

The average DIF for uncharred GLT panels was found to be 1.1 (CV 4.5 %), which indicates that there was an increase in strength when wood subjected to high strain-rate loading. This finding is consistent with that reported in the literature for glulam (Daniel Lacroix & Doudak, 2018). It should be emphasized that although this number is significantly lower than that

anticipated value for visually-graded lumber and MSR (i.e. 1.4), the lower value obtained for GLT can be explained by the failure mode described in Section 6.3.1, where failure primarily occurred in a cluster of knots and FJs, as was also reported by D. Lacroix & Doudak (2018). This is an important finding that sheds light on the question of whether GLT panels should be considered as sawn lumber or glulam when it comes to blast analysis and design. The findings show that although in static design, it is reasonable to assume GLT panels as a built-up solid-sawn lumber elements, their dynamic response resembles that of glulam beams when subjected to high-strain rate effects.

A two tailed *t*-tests at a 95% confidence level, assuming unequal variances, were performed to assess whether statistically significant differences existed between the selected comparison groups, and the following statistics were reported in the form ($t(df) = t_{stat}$, p), where df is the degrees of freedom, t_{stat} is the *t*-statistic, and p is the probability value indicating the level of statistical significance. The comparison between uncharred statically and dynamically loaded elements indicated that the elements tested in the Shock Tube resulted in a higher strength compared to the static loading group ($t(10) = -2.4$, $p = 0.04$), indicating a statistically significant strain-rate effect for uncharred GLT specimens.

A factor of 0.9 (CV 5.3%) was determined when the ultimate capacity of the charred GLT panels under simulated blast loading was compared to that obtained from static testing. It is not clear if this could be attributed to the variability between the two material batches or wood in general or due to the small cracks observed on the surface of the wood after cleaning and before testing in addition to the changes in the material due to fire (e.g., possible damage to the adhesive) which could negate the beneficial strain-rate effect that usually leads to a higher strength under dynamic loading. A two-tailed t-test was performed on charred static and dynamic groups and the results indicated that the difference in strength is not statistically

significant ($t(5) = 1.88$, $p = 0.1$), and therefore the reduction cannot be conclusively attributed to changes in material properties at the tension face or dynamic effects.

Similar t-tests were performed for stiffness (MOE), and the results yielded no statistically significant increase. The comparison between the MOE for uncharred static vs. dynamic did not indicate significant change ($t(10) = 0.88$, $p = 0.40$). As well, the difference between charred static and dynamic MOE comparison was found to be insignificant ($t(3) = 0.64$, $p = 0.57$). These results confirm that stiffness is largely unaffected by strain-rate effects for both uncharred and charred GLT panels. These findings are consistent with other studies on both lumber and glulam (D. Lacroix & Doudak, 2015, 2018).

6.3.4 Predictive Model for GLT Panels Subjected to Blast Loading

The SDOF modelling approach was utilized to simulate the dynamic response of the GLT panels, reflective of the linear elastic behaviour up to maximum resistance described in Section 5.5. As shown in Figure 6-8 (a), the model proved to be relatively reasonable in predicting the maximum displacement for uncharred panels and the results demonstrated good correlation between analytical and experimental displacement with a coefficient of determination R^2=0.99, which is consistent with outcomes reported for glulam (D. Lacroix & Doudak, 2018). On the other hand, the model's predictability was less accurate when simulating the time to maximum displacement with a coefficient of determination R^2=0.58, as shown in Figure 6-8 (b). This outcome is not surprising since time to failure is notoriously more difficult to predict. Overall, the findings demonstrate that SDOF analysis with proper input (particularly characteristics of the dynamic resistance curves) can adequately predict the dynamic response of GLT panels to be used in blast design applications.

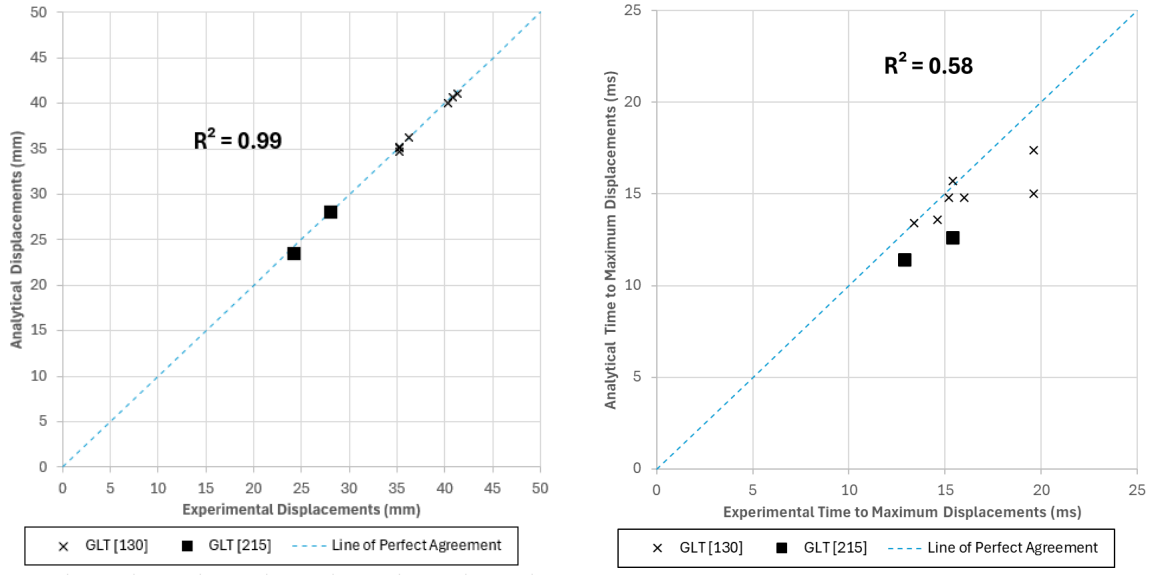

(a) (b)

Figure 6-8 Comparison between analytical and experimental results of uncharred panels: (a) maximum displacements, (b) time to maximum displacements

6.3.5 Predictive Model for Fire followed by Blast Loading

The same SDOF modelling approach used in the previous section was applied to simulate the dynamic response of the charred GLT panels under blast loading, representing the sequence of fire followed by blast. The model proved to be relatively reasonable in predicting the maximum displacement and time to maximum displacement of charred panels (Figure 6-9). The coefficients of determination are not shown in Figure 6-9 (a,b) (R^2 = 0.01 and R^2 = 1.00, respectively) and they are not used as formal measures of agreement in this study because the comparison is based on a very limited number of tests with a narrow range of values, which leads to clustered data and unstable R^2 estimates. Instead, the assessment of model performance is based on the absolute and relative differences between analytical and experimental results.

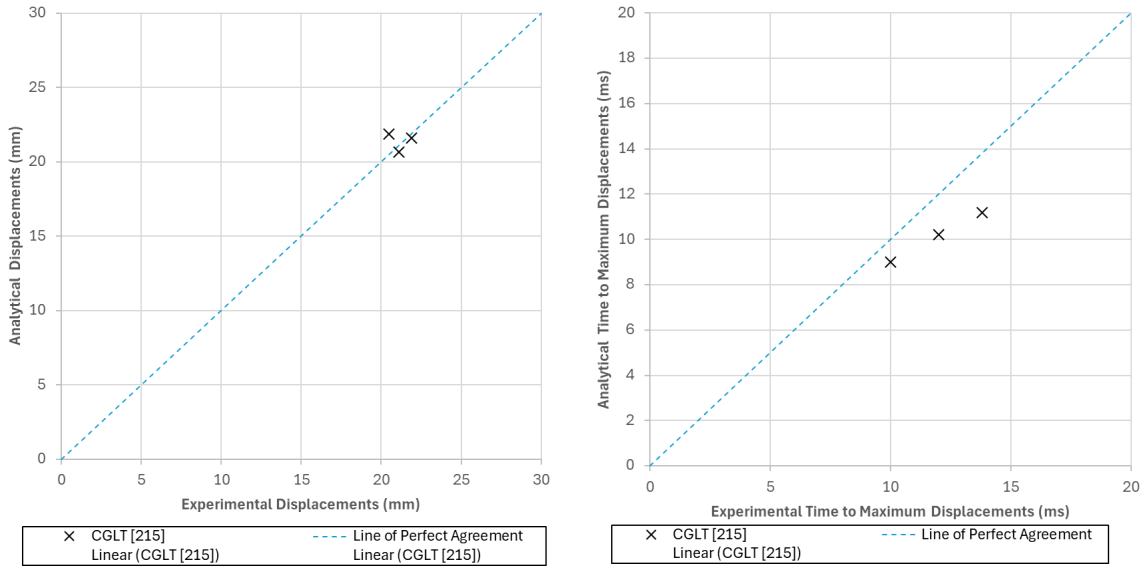

(b) (b)

Figure 6-9 Comparison between analytical and experimental results of charred panels: (a) maximum displacements, (b) time to maximum displacements

Following the validation of the model using the experimental results, six predictive SDOF cases were developed and evaluated (Table 6-1) to identify the most appropriate modelling assumptions and inputs for fire-damaged timber elements subjected to subsequent blast. All predictive cases used manufacturer ambient-temperature properties, consistent with the RCSM, and adjusted by SIF equal to 1.5 (in accordance with CSA S850 (2025)). The DIF was varied between 0.9 and 1.1, where DIF equal to 1.1 corresponds to value found experimentally for uncharred GLT panels, and is consistent with the value for glulam in CSA O86, a DIF of 0.9 reflects the experimentally derived value for the charred panels (although this reduction was statistically insignificant), and a DIF equal to 1.0 is proposed as the recommended design value for charred panels since no statistically significant reduction was reached for the tested charred specimens. The SDOF models were considered to systematically examine the influence of two key uncertainties that arise when timber elements are exposed to real fire conditions before experiencing blast loading and significantly affect stiffness and resistance: (1) the choice of

effective cross-section, and (2) the sensitivity of the assumed strain-rate effect of charred panels (DIF). Collectively, these models allow to identify which combination of assumptions best reproduces actual post-fire blast performance and therefore provides insight into how future design methods should treat ZSL and strain rate effects to achieve a conservative and safe assessment of fire-damaged mass timber elements. This comparison is also used to evaluate the conservatism of the recommended DIF value of 1.0.

Table 6-1 Fire followed by blast SDOF models cases

SDOF Case	Cross-section	DIF
SDOF 1	Effective cross-section (exp static ZSL + exp char depth)	1.1
SDOF 2	Effective cross-section (exp static ZSL + exp char depth)	1.0
SDOF 3	Effective cross-section (exp static ZSL + exp char depth)	0.9
SDOF 4	Effective cross-section (exp dynamic ZSL + exp char depth)	1.1
SDOF 5	Effective cross-section (exp dynamic ZSL + exp char depth)	1.0
SDOF 6	Effective cross-section (exp dynamic ZSL + exp char depth)	0.9

The experimental reflected pressure-time histories for the three charred panels were used as inputs, along with the structural system mass of charred panels. Bending moment resistance for each case was found using Equation 5-1 in Section 5.2. As the panels were dry, not treated, and with no possibility of lateral-torsional buckling failure, factors $k_{sb}, k_T,$ and K_L were taken equal to unity. The following modification factors were taken as: $\varphi = 1.0$, $k_H = 1.1$ and k_{Zb} was based on the effective cross-section dimensions (i.e. static vs dynamic ZSL), while k_D was taken 1.25 according to Doudak et al. (2022). Model predictions of maximum resistance $R_{\max}$, displacement at maximum resistance $\Delta_{R\max}$, and time to maximum displacement $t_{\max}$ were compared with experimental results as shown in Figure 6-10 and summarized in Table 6-2.

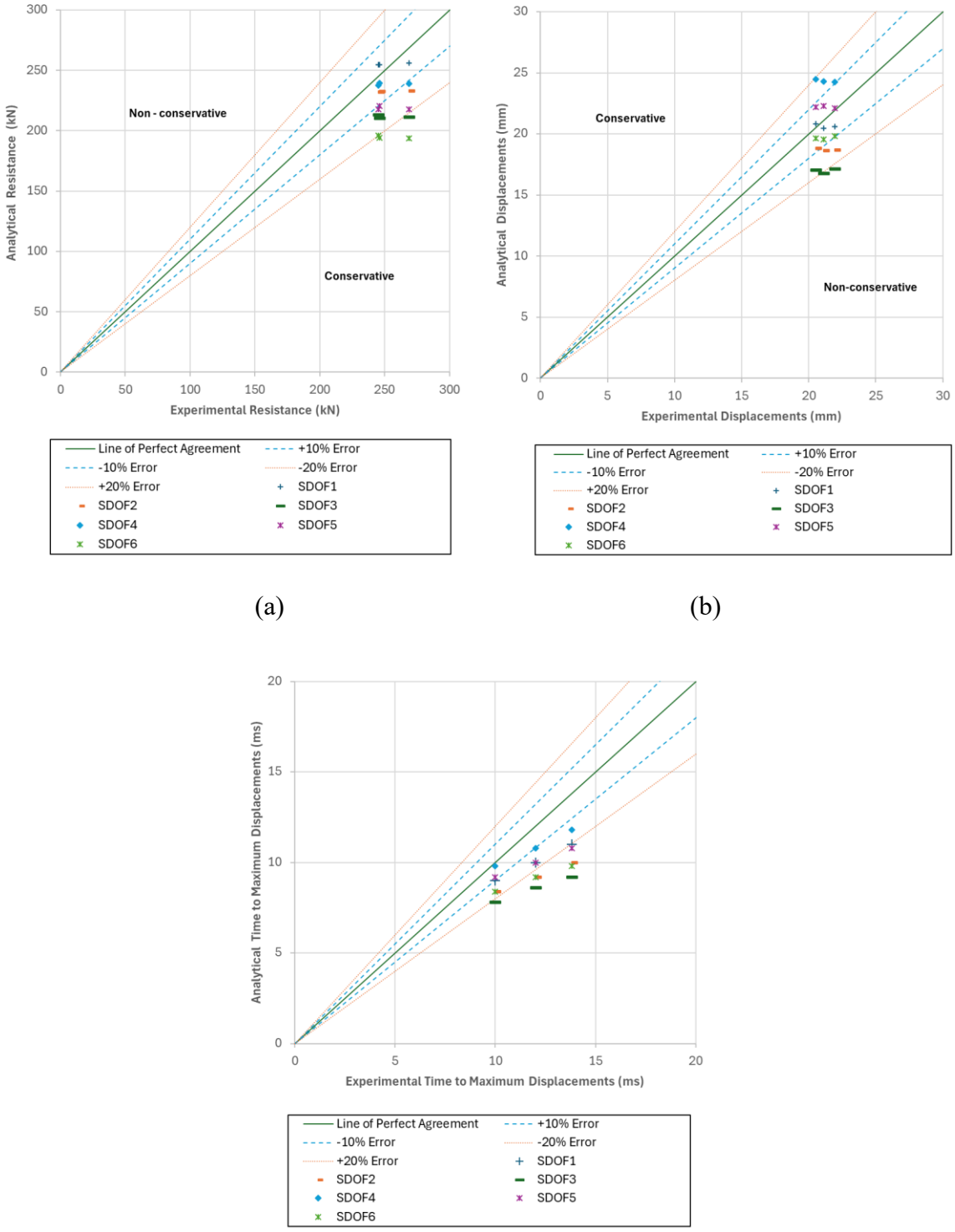

(a) (b)

(c)

Figure 6-10 Comparison between analytical and experimental results of SDOF models of charred panels: (a) maximum dynamic resistance, (b) maximum displacements, (c) time to maximum displacements

Table 6-2 Experimental and analytical results of SDOF models of charred panels

Case	Panel Name	R_{max}[1] (kN)	$\bar{e}_{Rmax}$[2] (%)	Δ_{Rmax}[3] (mm)	$\bar{e}_{\Delta Rmax}$[4] (%)	t_{Rmax}[5] (ms)	$\bar{e}_{tRmax}$[6] (%)
Experimental Results	CGLT5	245.9		21.1		10.0	
	CGLT6	245.3		21.9		12.0	
	CGLT7	268.6		20.5		13.8	
SDOF1	CGLT5	254.5 (**+3.5%**)	0.9%	20.4 (**−3.1%**)	-2.6%	9.0 (**−10.0%**)	-15.7%
	CGLT6	254.8 (**+3.9%**)		20.6 (**−6.0%**)		10.0 (**−16.7%**)	
	CGLT7	256.3 (**−4.6%**)		20.8 (**+1.4%**)		11.0 (**−20.3%**)	
SDOF2	CGLT5	232.7 (**−5.4%**)	-8.1%	18.6 (**−11.7%**)	-11.6%	8.4 (**−16.0%**)	-22.3%
	CGLT6	231.9 (**−5.5%**)		18.7 (**−14.8%**)		9.2 (**−23.3%**)	
	CGLT7	232.9 (**−13.3%**)		18.8 (**−8.3%**)		10.0 (**−27.5%**)	
SDOF3	CGLT5	210.2 (**−14.5%**)	-16.3%	16.8 (**−20.5%**)	-19.9%	7.8 (**−22.0%**)	-27.9%
	CGLT6	213.1 (**−13.1%**)		17.1 (**−22.0%**)		8.6 (**−28.3%**)	
	CGLT7	211.3 (**−21.3%**)		17.0 (**−17.2%**)		9.2 (**−33.3%**)	
SDOF4	CGLT5	239.3 (**−2.7%**)	-5.6%	24.3 (**+15.2%**)	15.0%	9.8 (**−2.0%**)	-8.8%
	CGLT6	237.6 (**−3.1%**)		24.3 (**+10.7%**)		10.8 (**−10.0%**)	
	CGLT7	239.0 (**−11.0%**)		24.5 (**+19.2%**)		11.8 (**−14.5%**)	
SDOF5	CGLT5	220.5 (**−10.3%**)	-13.5%	22.3 (**+5.6%**)	4.8%	9.2 (**−8.0%**)	-15.5%
	CGLT6	217.9 (**−11.2%**)		22.1 (**+0.8%**)		10.0 (**−16.7%**)	
	CGLT7	217.5 (**−19.0%**)		22.2 (**+8.0%**)		10.8 (**−21.7%**)	
SDOF6	CGLT5	194.3 (**−21.0%**)	-23.0%	19.5 (**−7.4%**)	-7.2%	8.4 (**−16.0%**)	-22.8%
	CGLT6	195.8 (**−20.2%**)		19.8 (**−9.7%**)		9.2 (**−23.3%**)	
	CGLT7	193.5 (**−28.0%**)		19.6 (**−4.4%**)		9.8 (**−29.0%**)	

[1] Maximum dynamic resistance
[2] Mean error in maximum dynamic resistance
[3] Displacement at maximum resistance
[4] Mean error in displacement at maximum resistance
[5] Time to maximum dynamic resistance
[6] Mean error in time to maximum resistance

In terms of resistance predictions (Figure 6-10 (a)) and according to Table 6-2, the negative sign in the error value indicate that the prediction is conservative, i.e. underpredicts resistance. SDOF 1 (static ZSL & DIF 1.1) overpredicts the resistance slightly (+0.9%), whereas SDOF 4

(dynamic ZSL & DIF 1.1) and SDOF2 (static ZSL & DIF 1.0) underpredict the resistance by 5.6% and 8.1%, respectively, all remain within ±10%. Remaining SDOFs models underpredict resistance by 13.5% to 23% on average, which is clearly very conservative. Among the predictive models, SDOF1 provides the closest resistance.

In terms of maximum displacement predictions (Figure 6-10 (b)), where positive error values means the prediction is conservative, both, SDOF 1 (static ZSL & DIF 1.1) and SDOF 6 (dynamic ZSL & DIF 0.9) underpredicted displacement by 2.6% and 7.2%, respectively, and falls within the 10% error. SDOF 5 (dynamic ZSL & DIF 1.0) slightly overpredicts displacement (+4.8%), while SDOF4 (dynamic ZSL & DIF 1.1) overpredicts displacement by 15.0%. SDOF2 and SDOF3, which is based on the static ZSL, significantly underpredicts displacement by 11.6% and 19.9%, respectively. SDOF1 remains the closest match, but SDOF5 seems to be the most appropriate and conservative choice for design, because the model slightly overestimates displacement while remaining conservative for resistance. It is also the model that is based on the recommended DIF.

In terms of time to maximum displacement predictions (Figure 6-10 (c)), all predictive models underestimate time to maximum resistance. Only SDOF4 (dynamic ZSL & DIF 1.1) predicts time within ±10%, while the remaining SDOFs underestimate time by 16% to 34%. As time to maximum resistance is governed mainly by stiffness and mass, the better performance of SDOF 4 suggests that dynamic ZSL more accurately captures post-fire stiffness.

Overall, these comparisons show that no single predictive case uniformly matches resistance, displacement, and time to maximum resistance. SDOF1 provides a reasonable overall agreement, particularly for maximum resistance and displacement, despite the slight displacement underprediction. In blast design where conservative displacement estimates are preferred, SDOF5 (dynamic ZSL & DIF = 1.0) offers the safest balanced assumption because

it remains conservative for both resistance and displacement. As dynamic ZSL results have not yet been exhaustively investigated, a more robust and transferable approach is to use a higher static ZSL value. In this study, a factor of approximately 1.5 can be used to estimate dynamic ZSL from the measured static ZSL. This value may not be generalized before being confirmed by other studies. Overall, the findings emphasize that the SDOF approach can be a reliable predictive tool with proper inputs.

6.4 Code Consideration and Design Implications

The design recommendations in this section address four key areas: 1) structural resistance immediately after the fire, 2) post-fire assessment and potential reuse, 3) blast design and 4) multi-hazard design (more specifically fire followed by blast).

Structural performance immediately after a fire is critical because life-safety decisions at this stage depend on the in-situ strength and stability of the member. In Canada, the fire design resistance of mass timber elements is governed by Annex B in the CSA O86 (CSA, 2024), where the resistance is determined based on the effective cross-section and after adjusting the specified strength by an adjustment factor (K_{fi}), as well as other modification factors, including: $\varphi = 1.0$, $k_D = 1.15$, $k_H = 1.0$, k_Z is based on the original cross-section dimensions, while k_L and S are based on the effective cross-section dimensions.

The effective cross-section is obtained from the original dimension by removing both the char depth and the ZSL. For slabs and walls, the char layer depth (Equation 6-2 in Section 4.2) can be found using the one-dimensional design charring rate, which is unified for different products and equal to 0.65 mm/min in Annex B in the CSA O86 (CSA, 2024). Although the present study results showed a char depth of 20.0 mm and a charring rate of 0.78 mm/min, these values are reflective of the brevity of fire exposure and the intensity of real fire during the initial

stages. Based on the results from this study, the author is not recommending any changes to the charring rate for fire design.

However, with regards to the ZSL, the experimentally observed ZSL thickness (23.8 under static loading) is significantly greater than the value provided in the CSA O86 standard. This may indicate that the current ZSL design value is non-conservative and may not be appropriate. It is therefore recommended that design committees consider revising the current ZSL values based on findings from this study and other studies (e.g., Huč et al., 2025; Quiquero et al., 2018), which suggest that fire severity and duration could impact the heat affected zone and thereby the ZSL value. In particular, for real fires, the current design value seems non-conservative and consideration for revisions should be discussed. The 2nd generation of the Eurocode (2025) increased the ZSL to a fixed value of 10 mm for bending and tension member and 14 mm for compression, which were chosen based on reliability-based calibration to ensure safety for standard fire-resistance design (Frangi et al., 2023, 2025), however, CSA O86 (CSA, 2024) ZSL design value have a maximum value of 7 mm regardless of member type (Equation 6-3).

$$\left.\begin{array}{ll} x_t = \left(\frac{t}{20}\right) * 7 & for\ t\ < 20\ min \\ x_t = 7 & for\ t\ \geq\ 20\ min \end{array}\right\} \quad \text{6-3}$$

Structural performance post-fire for potential reuse or retrofitting focus on evaluating the residual resistance, serviceability, and suitability of the member for reuse after char removal. As such, it may be recommended that a higher charring rate, similar to the experimentally obtained value in this study (i.e., 0.78 mm/min), and a greater ZSL thickness (23.8 mm under static loading) be used for post-fire assessment and reuse.

Structural performance under blast loading focuses on the dynamic response of the GLT panels, with particular emphasis on their resistance, deflection, and damage control to prevent collapse.

In Canada, blast design is governed by in CSA S850 (CSA, 2025) and the dynamic design strength (S_D) of GLT panels can be determined, as outlined in Equation 6-4, using the static strength (S_S) provided in CSA O86 (CSA, 2024), where the following modification factors are used, $\varphi = 1.0$ and $k_D = 1.15$.

$$S_D = SIF\ x\ DIF\ x\ S_s \qquad 6\text{-}4$$

Currently, the design standard assigns SIF values for visually-graded lumber and MSR of 1.9 and 1.5, respectively. As discussed in Section 6.3.2, the size factor selected for each section could have played a role and the fact that there were fewer panels with 215 mm depth could allude to a possible overestimation of the factor of 1.9. In light of the fact that both factors obtained in the experimental study are similar or higher than that provided in the design standard, it is recommended that the (conservative) value found in the design standard (1.5) be used in the design of GLT panels made of MSR lumber. Although it seems logical to also use a factor of 1.9 for GLT panels comprised of visually graded solid-sawn boards, further studies are needed to support this recommendation. The average DIF for uncharred GLT panels was found to be 1.1, which is similar to value reported for glulam in the blast design standard, and as such, it is recommended that GLT panels be treated as glulam for the purpose of blast design.

Structural performance under multi-hazard scenario, specifically fire followed by blast, requires integrating both the residual post-fire properties and the dynamic response under blast loading. For the multi-hazard design of fire followed by blast scenario, Equation 6-4 is adapted to determine the strength based on the RCSM and a DIF of 1.0. The effective cross-section should be based on the higher charring rate (e.g., 0.78 mm/min) and the ZSL value (e.g., 36.5 mm) obtained from the dynamic testing results.

The following design example evaluates the structural performance of the GLT panels in each of the four key areas of the design recommendations discussed earlier in this section. The

investigated GLT panels used in this study were roof panels with a slope of 2%, a clear span of 7,300 mm, cross-section of 600 x 215 mm, and originally designed for the following loads: dead (D) = 2.2 kPa (Assuming permanent mechanical equipment), snow (S) = 2.4 kPa and live (L) = 1.0 kPa, as illustrated in the structural drawings (Appendix A). According to the manufacturer specifications, the specified bending strength and modulus of elasticity of the GLT panels are 11.8 MPa and 9,500 MPa, respectively. The panels density was assumed to be 450 kg/m^3, based on the manufacturer's specifications.

The design bending moment resistance of the reference uncharred panel (59.7 kN·m) was obtained using Equation 5-1 in Section 5.2, and as the panels were dry, not treated, and with no possibility of lateral-torsional buckling failure, factors $k_{sb}, k_T,$ and K_L were taken equal to unity. Other modification factors include: $\varphi = 0.9$, $k_D = 1.0$, $k_H = 1.1$ and k_{Zb} was taken based on the cross-section dimensions (i.e. 1.1). The factored bending moment resistance was 25.5 kN·m, which was governed by the ultimate limit state (ULS) combination (1.25D + 1.5S), resulting in a strength utilisation ratio of 0.43. Under the serviceability limit state (SLS) combination (1.0D + 1.0S), the deflection was 21.7 mm, which is below the allowable limit of 40.6 mm, resulting in a utilisation ratio of 0.53.

1) Fire resistance immediately after the fire

The design bending moment resistance was found equal to 59.4 kN.m, where the following modification factors were taken as $\varphi = 1.0$, $k_D = 1.15$, $k_H = 1.0$, while the specified bending strength was modified by the design fire adjustment factor, $k_{fi} = 1.35$. The section modulus was determined using the effective cross-section dimensions after 25.7 min fire exposure, i.e. after removal of 20 mm char depth and 23.8 mm static ZSL. The factored moment demand under the governing fire load combination (1.0D + 1.0S) was 18.1 kN.m, yielding a utilisation ratio of 0.31, which indicates adequate strength. There is no allowable deflection limit to be

used immediately post-fire, as fire design focuses on achieving life safety and collapse prevention, and since resistance exceeded the demand, the GLT panels meets the design requirements.

In case the proposed experimental ZSL is unknown and the designer has to rely on two available information, namely field investigation and design standard, they may be tempted to use the pyrolysis layer thickness, based on observed discolored zone (i.e. 11.1 mm) combined with the char depth based on the design charring rate after 25.7 min of fire exposure. This yields a bending moment resistance that is significantly higher (i.e. 71.0 kN.m), which leads to overestimate post-fire resistance. An assessment with these variables can only be undertaken once a relationship is established between the pyrolysis layer and ZSL as mentioned in Section 6.2.3.

2) Post-fire assessment and potential reuse

The bending moment resistance was found equal to 41.3 kN.m using the original design modification factors ($\phi = 0.9$, $k_D = 1.0$, $k_H = 1.1$) except k_{Zb} was based on the effective cross-section while using the ambient temperature specified strength. The section modulus was found using the effective cross-section. The factored moment demand remained 25.1 kN·m, yielding a utilization ratio of 0.61, which meet ULS strength requirements. However, under the serviceability load combination (1.0D + 1.0S), the deflection was found to be 42 mm, slightly above the allowable limit 40.6 mm (utilization ratio of 1.04). This means that even after only 25.7 min exposure to fire, and although the panel is not expected to collapse, an intervention may be required in order to meet the deflection criterion. In other words, the panel is structurally "safe" (in terms of ULS) for future use due to the original over design but is no longer in conformance with the design provisions for its intended use because its deformation is incompatible with the performance expected of the roof and attached non-structural systems.

Retrofit options to enhance the panels' stiffness may include adding timber or steel elements or FRP sheets if access permits, or by adding additional supports to reduce the span (e.g., intermediate columns or a wall). These interventions primarily target serviceability (i.e., deflection), while also potentially increasing strength, and are consistent with common retrofit strategies for timber members that have experienced either fire damage or long-term excessive deflection (e.g. McLain, 2023).

3) Blast design

Assuming that a risk assessment was conducted for the structure and the design basis threat analysis indicated a likelihood of an explosion in front of the building equivalent to 100 kg of TNT detonated at a distance of 10 m (Figure 6-11). This threat corresponds to a far-field explosion, i.e. $Z \geq 1.2$ m/kg$^{1/3}$, and resulted an incident pressure and positive phase duration equal to 239.7 kPa and 9.7 ms, respectively. The blast wave length corresponding to duration of overpressure was 5.8 m, which resulted in an effective overpressure coefficient of 0.45 for 7.3 m span. The drag coefficient was -0.3 for the roof. This resulted in an averaged overpressure equal to 60.8 kPa. The shock front velocity was found equal to 596.5 m/s and the rise time was equal to 1.7 ms. The total duration of blast load on the roof was found equal to 11.4 ms.

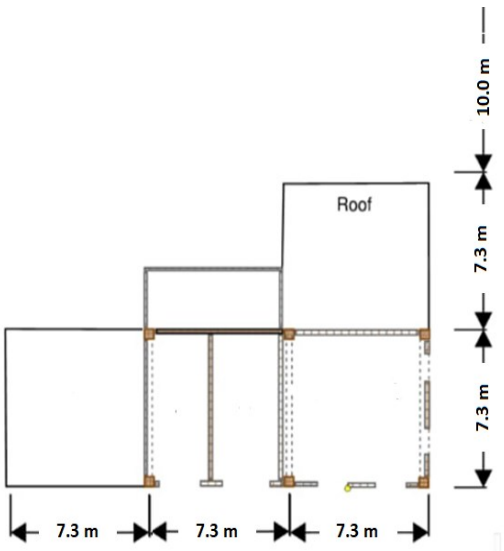

Figure 6-11 Floor plan with explosion location

The dynamic resistance was found equal to 137.9 kN using the following modification factors ($\varphi = 1.0,\ k_D = 1.15$), and the equivalent stiffness was found equal to 0.9 kN/mm. The factored moment demand was found equal to 14.9 kN·m under blast load combination (1.0D + 1.0L + 0.2S). The remaining dynamic resistance was 111.0 kN which resulted an ultimate displacement equal to 118.5 mm for the resistance curve. The total mass, including the GLT panel self-weight and permanent dead loads, was found equal to 987 kg and the loading area was taken equal to the individual GLT panel surface, i.e. 0.6 x 7.3. The SDOF analysis with RCBlast (Figure 6-12) yielded a maximum midspan displacement of 53.55 mm. This value is lower than the elastic limit displacement of the resistance curve, corresponding to a ductility ratio of μ = 0.45, which is below the CSA S850 ductility limit (μ = 1). Since the displacement demand remains within the elastic range, the panel is expected to safely withstand this blast scenario.

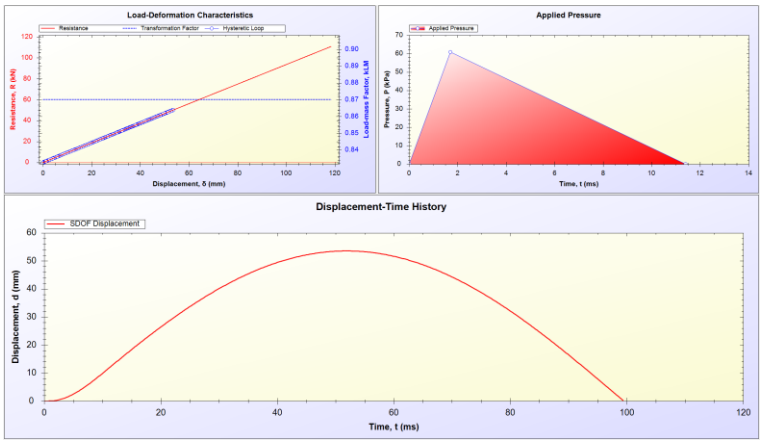

Figure 6-12 SDOF analysis of the GLT roof panel under blast load only

4) Multi-hazard design (more specifically fire followed by blast).

Assuming the GLT roof panels were first exposed to a 25.6 min fire and following this fire event, the building was subjected to a far-field explosion originating outside the building or from an adjacent structure, which is consistent with a design basis threat scenario explained in the previous section.

The dynamic post-fire resistance was found equal to 45.1 kN using the recommended multi-hazard modification factors ($\phi = 1.0$, $k_D = 1.15$, $k_H = 1.1$) in addition to DIF $= 1.0$ and SIF $= 1.5$. The section modulus and size factor ($k_{Zb} = 1.2$) were found based on the effective cross-section utilising the experimental char depth and dynamic ZSL (i.e. 20 mm and 36.5 mm, respectively). The equivalent stiffness was found equal to 0.4 kN/mm. The factored moment demand was found equal to 14.9 kN.m using blast load combination. The remaining dynamic resistance was 49.6 kN which resulted in an ultimate displacement equal to 132.8 mm for the resistance curve. The total mass was adjusted to account for the char depth and was found equal to 947 kg and the loading area did not change. The SDOF analysis with RCBlast (Figure 6-13) yielded a maximum midspan displacement of 90.7 mm, corresponding to a ductility ratio of μ= 0.0.68, which is still below CSA S850 ductility elastic limit, therefore, the panel is expected to safely withstand this fire followed by blast scenario.

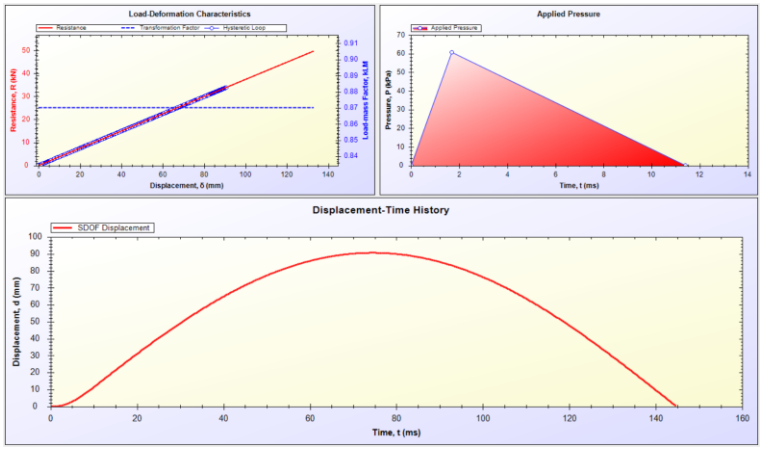

Figure 6-13 SDOF analysis of the GLT roof panel after fire exposure and blast loads.

Chapter 7 Conclusions and Recommendations

7.1 Conclusions

The following conclusions can be drawn from the work undertaken during this research study:

- A char depth and charring rate of 20.0 mm and 0.78 mm/min was found, respectively, after fire exposure of approximately 25.7 min. No changes are recommended to the design charring rate in Annex B of CSA O86 (2024) for fire design. However, it may be recommended to use a higher charring rate for post-fire assessment and reuse depending on the severity of the fire.
- Image analysis proved to be a fast, repeatable, and sufficiently accurate method to quantify residual char and pyrolysis layer thickness. Based on the image analysis, the residual char thickness averaged 7.1 mm, while the pyrolysis layer averaged 11.1 mm.
- An average ZSL value of 23.8 mm and 36.5 mm was found under static and dynamic loading, respectively. This may indicate that the current ZSL design value is non-conservative and therefore, it is recommended to revise the current ZSL values in Annex B of CSA O86 (2024) and to use a greater ZSL for post-fire assessment and reuse.
- The failure modes for charred and uncharred GLT panels under static and dynamic loading were consistent and characterized by flexural failure (simple tension or brash), where the failure of the outer tension lamination was followed by cracks propagating across the GLT panel. Both static and dynamic resistance curves were characterized by linear elastic response up to maximum resistance for both charred and uncharred panels. One key observation was that some of the charred panels exhibited visible separation between individual laminations at the glueline locations, which was not observed in the uncharred panels.

- An average SIF value of 1.6 and 1.9 was found for uncharred panels with depths of 130 mm and 215 mm, respectively, and an average value of 1.8 was found for charred panels. These results confirm that the use of the values for SIF specified in CSA S850 (CSA, 2025) for MSR seems valid and slightly conservative.
- An average DIF on the flexural strength for uncharred GLT panels was found to be 1.1 under high-strain rates (0.2 s^{-1}), representing far-field explosion. This finding is consistent with the glulam values currently recommended in the blast design standard and published literature. No statistically significant increase was found in the charred specimens. Further, no increase was observed in the panel stiffness when the dynamic and static results were compared. The findings also show that although in static design, it is reasonable to assume GLT panels as a built-up solid sawn lumber elements, their dynamic response resembles that of glulam beams when subjected to high-strain rate effects.
- The findings demonstrate that SDOF analysis can adequately predict the dynamic response of charred and uncharred GLT panels to be used in blast design applications.
- Six predictive SDOF cases were developed to evaluate and identify the most appropriate modelling assumptions and inputs for multi-hazard scenario of fire followed by blast. The results indicate that using dynamic ZSL and DIF of 1.0 offers the safest balanced assumption.
- The SDOF approach combined with RCSM can be a reliable predictive tool for fire followed by blast scenario with proper inputs.
- Code consideration and design recommendations were provided in four key areas: 1) structural resistance immediately after the fire; 2) post-fire assessment and potential reuse; 3) blast design and 4) multi-hazard design (more specifically fire followed by blast).

7.2 Recommendations for Future Work

Based on the findings of this research, the following future investigations are recommended:

- Establishing a relationship between the visually discoloured zone (pyrolysis layer thickness) and the ZSL for various EWP. If validated, such relationships could support more reliable post-fire assessment by allowing designers to estimate ZSL from non-invasive measurements of the discoloured zone prior to char removal.
- The effect of high strain-rates on ZSL thickness using a wider range of loading rates should be investigated. It is suggested that this investigation could include systematic comparison of ZSL determined under static and dynamic testing for the same fire exposure so that a rate-dependent "dynamic ZSL" can be established. The goal would be to derive a relationship linking static and dynamic ZSL values for multi-hazard scenarios.
- Although the current study showed no significant increase on the dynamic resistance, additional studies on GLT as well as other EWPs are recommended, especially for scenarios involving short and long fire exposure and including a cooling phase. Such studies would help quantify how prior fire damage and cooling rate influence strain-rate sensitivity and dynamic strength.
- A system-level investigation of the response of mass timber building subjected to sequential fire followed by blast is recommended. This will help to evaluate load redistribution and collapse prevention and will inform practical guidelines for assessing, repairing, and reusing of such structural elements.

References

Albert, C. M., & Liew, K. C. (2025). Influence of Short-Duration Densification on the Temperature Profile of Cross-Laminated Timber during an Open Burning Test. *Journal of the Korean Wood Science and Technology*, *53*(2), 119–128. https://doi.org/10.5658/WOOD.2025.53.2.119

Aoude, H., Dagenais, F. P., Burrell, R. P., & Saatcioglu, M. (2015). Behavior of ultra-high performance fiber reinforced concrete columns under blast loading. *International Journal of Impact Engineering*, *80*, 185–202. https://doi.org/10.1016/J.IJIMPENG.2015.02.006

Arganda-Carreras, I., Kaynig, V., Rueden, C., Eliceiri, K. W., Schindelin, J., Cardona, A., & Sebastian Seung, H. (2017). Trainable Weka Segmentation: a machine learning tool for microscopy pixel classification. *Bioinformatics*, *33*(15), 2424–2426. https://doi.org/10.1093/bioinformatics/btx180

Ashworth, T., Ibrahimli, V., Scherf, D., & Jalbert, N. (2025). *Guide to Encapsulated Mass Timber Construction in the Ontario Building Code*.

ASTM International. (2022). *ASTM D198-22: Test Methods of Static Tests of Lumber in Structural Sizes*. ASTM International. https://doi.org/10.1520/D0198-22A

ASTM International. (2023). *ASTM E119 - Standard Test Methods for Fire Tests of Building Construction and Materials*.

Barrett, D. L., & Lau, W. (1994). *Canadian lumber properties*.

Bérubé, A., & Doudak, G. (2023). Investigation of energy-absorbing connections for application in mass timber structures [Article]. *Engineering Structures*, *297*, 117018. https://doi.org/10.1016/j.engstruct.2023.117018

Bérubé, A., & Doudak, G. (2024). Enhancing energy dissipation in glued-laminated timber assemblies using boundary connections [Article]. *Structures (Oxford)*, *65*, 106744. https://doi.org/10.1016/j.istruc.2024.106744

Biggs, J. M. (1964). *Introduction to structural dynamics.* McGraw-Hill,.

Bragov, A., & Lomunov, A. K. (1997). Dynamic properties of some wood species. *Journal De Physique. IV : JP*, *7*(3). https://doi.org/10.1051/jp4:1997384

Brandon, D., Sjöström, J., Hallberg, E., Temple, A., & Kahl, F. (2021). *Fire Safe implementation of visible mass timber in tall buildings – compartment fire testing*.

Canadian Board for Harmonized Construction Codes (CBHCC). (2025). *National Building Code of Canada 2025* (Numbers 978-0-660-37913–5). National Research Council Canada. https://doi.org/10.4224/26fz-gg26

Canadian Wood Council. (2020). *Wood Design Manual* (2020th ed., Vol. 1). Canadian Wood Council.

Chen, C. kun, Yang, J., Chen, J., Zeng, J. wei, Wang, W. yu, & Zhao, X. long. (2017). Fire resistance performance of glulam beam. *Journal of Central South University*, *24*(4). https://doi.org/10.1007/s11771-017-3495-8

Chorlton, B., & Gales, J. (2020). Mechanical performance of laminated veneer lumber and Glulam beams after short-term incident heat exposure [Article]. *Construction & Building Materials*, *263*, 120129. https://doi.org/10.1016/j.conbuildmat.2020.120129

Choudhary, N. S., Goel, M. D., & Panchal, S. (2024). Multi-hazard analysis of a reinforced concrete structure under blast and post-blast fire. *Proceedings of the Institution of Civil Engineers - Structures and Buildings*, *177*(2), 147–158. https://doi.org/10.1680/jstbu.22.00164

Collier, P. C. R. (1992). *Charring Rates of Timber*.

Côté, D., & Doudak, G. (2019). Experimental investigation of cross-laminated timber panels with realistic boundary conditions subjected to simulated blast loads. *Engineering Structures*, *187*, 444–456. https://doi.org/0.1016/j.engstruct.2019.02.009

CSA. (2024). *Engineering Design in Wood. CSA O86.* (12th ed.). CSA Group.

CSA. (2025). *Design and assessment of buildings subjected to blast loads. CSA S850.* CSA Group.

D'Arenzo, G., & Seim, W. (2023). Experimental characterisation of glulam shear walls under lateral cyclic loading. *World Conference on Timber Engineering (WCTE 2023)*, 2070–2076. https://doi.org/10.52202/069179-0274

D'Arenzo, G., & Seim, W. (2024). Cyclic behaviour of Glulam, LVL and GLVL shear walls and their base connections. *Engineering Structures*, *315*, 118493. https://doi.org/10.1016/J.ENGSTRUCT.2024.118493

De Mil, T., Tarelkin, Y., Hahn, S., Hubau, W., Deklerck, V., Debeir, O., Van Acker, J., De Cannière, C., Beeckman, H., & Van den Bulcke, J. (2018). Wood Density Profiles and Their Corresponding Tissue Fractions in Tropical Angiosperm Trees. *Forests*, *9*(12), 763. https://doi.org/10.3390/f9120763

Department of Defense. (2014). *Unified Facilities Criteria (UFC) 3-340-02: Structures to Resist the Effects of Accidental Explosions (Change 2).* (Number UFC 03-0340-02). https://www.wbdg.org/ffc/dod/unified-facilities-criteria-ufc/ufc-3-340-02

Doudak, G., Viau, C., & Lacroix, D. N. (2022). Proposed Design Methods for Timber Members Subjected to Blast Loads. *Journal of Performance of Constructed Facilities*, *36*(3). https://doi.org/10.1061/(asce)cf.1943-5509.0001723

Drysdale, D. (2011). An Introduction to Fire Dynamics [Bookitem]. In *An Introduction to Fire Dynamics*. John Wiley & Sons, Incorporated.

Ebadi, M. M., Doudak, G., & Smith, I. (2017). Finite-Element Modeling and Parametric Study of Glulam Beam-and-Deck Floors [Article]. *Journal of Structural Engineering (New York, N.Y.)*, *143*(9). https://doi.org/10.1061/(ASCE)ST.1943-541X.0001844

Ebadi, M. M., Doudak, G., & Smith, I. (2018). Vibration responses of glulam beam-and-deck floors. *Engineering Structures*, *156*, 235–242. https://doi.org/10.1016/j.engstruct.2017.11.051

Ebadi, M. M., Doudak, G., & Smith, I. (2019). Evaluation of floor vibration caused by human walking in a large glulam beam and deck floor. *Engineering Structures*, *196*, 109349. https://doi.org/10.1016/j.engstruct.2019.109349

European Committee for Standardization. (2004). *Eurocode 5: Design of timber structures - Part 1-2: General -Structural fire design (EN 1995-1-2)*.

Fahrni, R., Klippel, M., Just, A., Ollino, A., & Frangi, A. (2019). Fire tests on glued-laminated timber beams with specific local material properties. *Fire Safety Journal*, *107*, 161–169. https://doi.org/10.1016/j.firesaf.2017.11.003

Fink, G., Jockwer, R., Šušteršič, I., Stepinac, M., Palma, P., Bedon, C., Casagrande, D., Franke, S., D'Arenzo, G., Brandon, D., & Viau, C. (2023). HOLISTIC DESIGN OF TALLER TIMBER BUILDINGS - COST ACTION HELEN (CA20139). *World Conference on Timber Engineering (WCTE 2023)*, 1001–1008. https://doi.org/10.52202/069179-0137

Forest Products Laboratory. (2021). *Wood Handbook: Wood as an Engineering Material*. General Technical Report FPL-GTR-282, WI: U.S. Department of Agriculture, Forest Service, Forest Products Laboratory.

Frangi, A., & Fontana, M. (2005). Fire performance of timber structures under natural fire conditions. *Fire Safety Science*, 279–290. https://doi.org/10.3801/IAFSS.FSS.8-279

Frangi, A., Just, A., Hakkarainen, J., Schmid, J., & Werther, N. (2023). Eurocode 5 Revision – Fire Design of Timber Structures. In R. Görlacher (Ed.), *0th International Network on Timber Engineering Research (INTER 2023)*. Timber Scientific Publishing, KIT Holzbau und Baukonstruktionen.

Frangi, A., Just, A., Krenn, H., Schmid, J., Werther, N., Hakkarainen, J., Blondeau, R., & Stapf, G. (2025). *THE SECOND GENERATION OF EUROCODE 5 – FIRE DESIGN*. 11–18. https://doi.org/10.52202/080513-0002

Gerhards, C. C. (1977). Effect of duration and rate of loading on strength of wood and wood-based materials. *US For Prod Lab Res Pap FPL 283*.

Gernay, T., Zehfuß, J., Brunkhorst, S., Robert, F., Bamonte, P., McNamee, R., Mohaine, S., & Franssen, J. (2023). Experimental investigation of structural failure during the cooling phase of a fire: Timber columns [Article]. *Fire and Materials*, *47*(4), 445–460. https://doi.org/10.1002/fam.3110

Gilbertson, C. G., & Bulleit, W. M. (2013). Load Duration Effects in Wood at High Strain Rates. *Journal of Materials in Civil Engineering*, *25*(11). https://doi.org/10.1061/(asce)mt.1943-5533.0000708

Hadden, R. M., Bartlett, A. I., Hidalgo, J. P., Santamaria, S., Wiesner, F., Bisby, L. A., Deeny, S., & Lane, B. (2017). Effects of exposed cross laminated timber on compartment fire dynamics [Article]. *Fire Safety Journal*, *91*, 480–489. https://doi.org/10.1016/j.firesaf.2017.03.074

Hasburgh, L., Bourne, K., Dagenais, C., Ranger (Osborne), L., & Roy-Poirier, A. (2016, August). Fire performance of mass-timber encapsulation methods and the effect of encapsulation on char rate of cross-laminated timber. *WCTE 2016: World Conference on Timber Engineerng*.

Hegazi, M., & Salem, O. (Sam). (2024). Fire behaviour of damaged wood–steel–wood beam connections retrofitted with self-tapping screws — experimental study [Article]. *Canadian Journal of Civil Engineering*, *51*(7), 812–827. https://doi.org/10.1139/cjce-2023-0442

Horio, T., Saito, K., Kinjo, H., Katakura, Y., Hirashima, T., & Yusa, S. (2016). Deflection behavior and load-bearing period of structural glued laminated timber beams in fire including cooling phase: Study on fire performance of structural glued laminated timber beams Part 2 [Article]. *Journal of Structural and Construction Engineering (Transactions of AIJ)*, *81*(726), 1355–1361. https://doi.org/10.3130/aijs.81.1355

Huč, S., Hozjan, T., & Pečenko, R. (2023). Thickness of zero-strength layer in timber beam exposed to fuel-controlled parametric fires [Article]. *Wood Science and Technology*, *57*(4), 929–944. https://doi.org/10.1007/s00226-023-01480-8

Huč, S., Hozjan, T., & Pečenko, R. (2025). Effective cross-section of a timber beam exposed to natural fires [Article]. *European Journal of Wood and Wood Products*, *83*(2), 71–71. https://doi.org/10.1007/s00107-025-02202-6

Huč, S., Pečenko, R., & Hozjan, T. (2021). Predicting the thickness of zero-strength layer in timber beam exposed to parametric fires. *Engineering Structures*, *229*, 111608. https://doi.org/10.1016/j.engstruct.2020.111608

International Organization for Standardization. (2025). *ISO 834-1:2025- Fire-resistance tests - Elements of building construction - Part 1: General requirements*.

Jacques, E. (2016). *Characteristics of Reinforced Concrete Bond at High Strain Rates* (M. Saatcioglu & University of Ottawa. Department of Civil Engineering., Eds.).

Jacques, E. (2024). *Overpressure*. https://www.ericjacques.com/courses/research/overpressure/

Jacques, E., Lloyd, A., Braimah, A., Saatcioglu, M., Doudak, G., & Abdelalim, O. (2014). Influence of high strain-rates on the dynamic flexural material properties of spruce-pine-

fir wood studs. *Canadian Journal of Civil Engineering*, *41*(1). https://doi.org/10.1139/cjce-2013-0141

Jacques, E., Lloyd, A., & Saatcioglu, M. (2013). Predicting reinforced concrete response to blast loads [Article]. *Canadian Journal of Civil Engineering*, *40*(5), 427–444. https://doi.org/10.1139/L2012-014

Janssens, M. L., & White, R. H. (1994). Short communication: Temperature profiles in wood members exposed to fire [Article]. *Fire and Materials*, *18*(4), 263–265. https://doi.org/10.1002/fam.810180410

Kataras, T. J., Jang, T. J., Koury, J., Singh, H., Fok, D., & Kaul, M. (2023). ACCT is a fast and accessible automatic cell counting tool using machine learning for 2D image segmentation [Article]. *Scientific Reports*, *13*(1), 8213–12. https://doi.org/10.1038/s41598-023-34943-w

Kimbell, R. G., & Fies, J. (1953). *Two Typical Wood Frame Houses Exposed to Energy Released by Nuclear Fission*. National Lumber Manufacturers Association.

Lachowicz, H., & Bijak, S. (2025). Tree Age and Size Affect Selected Fiber Parameters in Black Locust (Robinia pseudoacacia L.) Wood [Article]. *Forests*, *16*(1), 111. https://doi.org/10.3390/f16010111

Lacroix, D., & Doudak, G. (2015). Investigation of Dynamic Increase Factors in Light-Frame Wood Stud Walls Subjected to Out-of-Plane Blast Loading. *Journal of Structural Engineering*, *141*(6), 04014159. https://doi.org/10.1061/(asce)st.1943-541x.0001139

Lacroix, Daniel, & Doudak, G. (2018). Determining the Dynamic Increase Factor for Glued-Laminated Timber Beams. *Journal of Structural Engineering (New York, N.Y.)*, *144*(9), 4018160. https://doi.org/10.1061/(ASCE)ST.1943-541X.0002146

Lacroix, D., & Doudak, G. (2018). Effects of High Strain Rates on the Response of Glulam Beams and Columns. *Journal of Structural Engineering*, *144*(5), 04018029. https://doi.org/10.1061/(asce)st.1943-541x.0002020

Lacroix, D., & Doudak, G. (2020). Towards enhancing the post-peak performance of glued-laminated timber beams using multi-directional fibre reinforced polymers. *Engineering Structures*, *215*, 110680.

Lacroix, D. N. (2017). *Investigating the Behaviour of Glulam Beams and Columns Subjected to Simulated Blast Loading*. Université d'Ottawa / University of Ottawa.

Lacroix, D. N., & Doudak, G. (2018). Experimental and Analytical Investigation of FRP Retrofitted Glued-Laminated Beams Subjected to Simulated Blast Loading. *Journal of Structural Engineering*, *144*(7), 4018089. https://doi.org/10.1061/(ASCE)ST.1943-541X.0002084

Lacroix, D. N., & Doudak, G. (2019). Design and Analysis of Unretrofitted and Retrofitted Glulam Beams and Columns under Blast Loading. *Structures Congress 2019: Blast, Impact Loading, and Research and Education - Selected Papers from the Structures Congress 2019*, 137–146. https://doi.org/10.1061/9780784482247.013

Lacroix, D. N., Doudak, G., & El-Domiaty, K. (2014). Retrofit Options for Light-Frame Wood Stud Walls Subjected to Blast Loading. *Journal of Structural Engineering*, *140*(4), 04013104. https://doi.org/10.1061/(asce)st.1943-541x.0000885

Lange, D., Boström, L., Schmid, J., & Albrektsson, J. (2015). The Reduced Cross Section Method Applied to Glulam Timber Exposed to Non-standard Fire Curves [Article]. *Fire Technology*, *51*(6), 1311–1340. https://doi.org/10.1007/s10694-015-0485-y

Le, V. T., Ghazlan, A., Nguyen, T., & Ngo, T. D. (2021). Performance of bio-inspired cross-laminated timber under blast loading – A numerical study. *Composite Structures*, *260*, 113524. https://api.semanticscholar.org/CorpusID:233628484

Li, H., Chen, W., & Hao, H. (2024). Performance of reinforced concrete slabs subjected to simultaneous fire and blast loads. *Engineering Structures*, *311*, 118133. https://doi.org/10.1016/j.engstruct.2024.118133

Lie, T. T. (1977). METHOD FOR ASSESSING THE FIRE RESISTANCE OF LAMINATED TIMBER BEAMS AND COLUMNS. *Canadian Journal of Civil Engineering*, *4*(2). https://doi.org/10.1139/l77-021

Liska, J. A. (1950). *Effect of rapid loading on the compressive and flexural strength of wood*. USDA, Forest Service, Forest Products Laboratory.

Lopez-Molina, A., & Doudak, G. (2019). Retrofit techniques for Cross-Laminated Timber (CLT) elements subjected to blast loads. *Engineering Structures*, *197*. https://doi.org/10.1016/j.engstruct.2019.109450

Luo, D., Gattas, J. M., & Tan, P. S. S. (2021). Real-Time Defect Recognition and Optimized Decision Making for Structural Timber Jointing. In *Proceedings of the 2020 DigitalFUTURES* (pp. 36–45). Springer Singapore. https://doi.org/10.1007/978-981-33-4400-6_4

Marchand, K. A. (2002). *BAIT, BASS & RODS Testing Results*. Applied Research Associates, Prepared for the USAF Force Protection Battlelab.

McLain, R. (2023). *Repair of Fire-Damaged Mass Timber* .

Mikkola, E. (1991). Charring Of Wood Based Materials. *Fire Safety Science*, *3*. https://doi.org/10.3801/iafss.fss.3-547

Mindess, S., & Madsen, B. (1986). The fracture of wood under impact loading. *Materials and Structures*, *19*(1). https://doi.org/10.1007/BF02472310

Mitchell, H., Kotsovinos, P., Richter, F., Thomson, D., Barber, D., & Rein, G. (2023). Review of fire experiments in mass timber compartments: Current understanding, limitations, and research gaps. *Fire and Materials*, *47*(4), 415–432. https://doi.org/10.1002/fam.3121

Neumann, M., Herter, J., Droste, B. O., & Hartwig, S. (2011). Compressive behaviour of axially loaded spruce wood under large deformations at different strain rates. *European Journal of Wood and Wood Products*, *69*(3). https://doi.org/10.1007/s00107-010-0442-x

Okunrounmu, O., Salem, O. (Sam), & Hadjisophocleous, G. (2024). Effects of Bolt Number and Pattern on the Failure Time of Minimally Fire-Protected Glulam Beam Connections Reinforced with Self-tapping Screws [Article]. *Fire Technology*, *60*(5), 3209–3241. https://doi.org/10.1007/s10694-023-01477-6

Oliveira, D., Viau, C., & Doudak, G. (2023). Modelling the behaviour of heavy and mass timber members subjected to blast loads. *Engineering Structures*. https://api.semanticscholar.org/CorpusID:259291053

Ontario Building Code, Pub. L. O. Reg. 332/24, Government of Ontario (2024). https://www.ontario.ca/page/2024-ontario-building-code

Oswald, C. J. (2005). *Component Explosive Damage Assessment Workbook (CEDAW) Methodology Manual V1.0.* Prepared for the Protective Design Center, US Army Corps of Engineers.

Phillips, E. E., Murphy, R., Connors, J., McMullen, K. F., Jacques, E., & Bruhl, J. C. (2021). Experimental evaluation of OSB-faced structural insulated panels subject to blast loads. *Engineering Structures*, *229*, 111597. https://doi.org/10.1016/J.ENGSTRUCT.2020.111597

Poulin, M., Viau, C., Lacroix, D. N., & Doudak, G. (2018). Experimental and Analytical Investigation of Cross-Laminated Timber Panels Subjected to Out-of-Plane Blast Loads. *Journal of Structural Engineering*, *144*, 4017197. https://api.semanticscholar.org/CorpusID:116116284

Quiquero, H., Chorlton, B., & Gales, J. (2018). Performance of adhesives in Glulam after short term fire exposure. *International Journal of High-Rise Buildings*, *7*(4). https://doi.org/10.21022/IJHRB.2018.7.4.299

Radzi, N. A. M., Hamid, R., Mutalib, A. A., & Kaish, A. B. M. A. (2021). A review of the structural fire performance testing methods for beam-to-column connections. In *Advances in Civil Engineering* (Vol. 2021). https://doi.org/10.1155/2021/5432746

Randall, P. A. (1961). *Damage to conventional and special types of residences exposed to nuclear effects*. U.S. Atomic Energy Commission, Wt-1194.

Ranger, L., Dagenais, C., & Bénichou, N. (2019). *Solutions for upper mid-rise and high-rise mass timber construction: fire resistance of mass timber laminated elements*.

Richter, F., Kotsovinos, P., Rackauskaite, E., & Rein, G. (2021). Thermal Response of Timber Slabs Exposed to Travelling Fires and Traditional Design Fires [Article]. *Fire Technology*, *57*(1), 393–414. https://doi.org/10.1007/s10694-020-01000-1

Roy, T., & Matsagar, V. (2021). Mechanics of damage in reinforced concrete member under post-blast fire scenario. *Structures*, *31*, 740–760. https://doi.org/10.1016/j.istruc.2021.02.005

Roy, T., & Matsagar, V. (2022). A probabilistic framework for assessment of reinforced concrete wall panel under cascaded post-blast fire scenario. *Journal of Building Engineering*, *45*, 103506. https://doi.org/10.1016/j.jobe.2021.103506

Ruan, Z., Chen, L., & Fang, Q. (2015). Numerical investigation into dynamic responses of RC columns subjected for fire and blast. *Journal of Loss Prevention in the Process Industries*, *34*, 10–21. https://doi.org/10.1016/j.jlp.2015.01.009

Rzepecki, A., & Thomas, F. M. (2017). A new Fiji-plugin for visualizing intra-annual density fluctuations and analyzing intra-annual theoretical volumetric flow rate fluctuations along wood cross-sections [Article]. *Dendrochronologia (Verona)*, *44*, 58–65. https://doi.org/10.1016/j.dendro.2017.03.002

Safarikrch, D., Elbrecht, J., & Miranda, W. (2022). State of Tall Timber 2022. *CTBUH Journal*, (I).

Schaffer, E. L. (1966). *Review of information related to the charring rate of wood*. Forest Products Laboratory.

Schaffer, E. L. (1967). *Simplified test for adhesive behavior in wood sections exposed to fire.* (E. L. Schaffer, Ed.) [Book].

Schaffer, E. L. (1984). *Structural fire design: wood.* (E. L. Schaffer, Ed.) [Book].

Schaffer, E. L., Marx, C. M., Bender, D. A., & Woeste, F. E. (1999). *Strength Validation and Fire Endurance of Glued-Laminated Timber Beams*.

Schindelin, J., Arganda-Carreras, I., Frise, E., Kaynig, V., Longair, M., Pietzsch, T., Preibisch, S., Rueden, C., Saalfeld, S., Schmid, B., Tinevez, J.-Y., White, D. J., Hartenstein, V., Eliceiri, K., Tomancak, P., & Cardona, A. (2012). Fiji: an open-source platform for biological-image analysis. *Nature Methods*, *9*(7), 676–682. https://doi.org/10.1038/nmeth.2019

Schmid, J. (2020). *Natural Fire Exposure of Structural Timber-Contribution to Determine the Influence in the Fully Developed and the Decay Phase*. ETH Zurich.

Schmid, J., Just, A., Klippel, M., & Fragiacomo, M. (2015). The Reduced Cross-Section Method for Evaluation of the Fire Resistance of Timber Members: Discussion and Determination of the Zero-Strength Layer. *Fire Technology*, *51*(6), 1285–1309. https://doi.org/10.1007/s10694-014-0421-6

Schmid, J., Klippel, M., Just, A., & Frangi, A. (2014). Review and analysis of fire resistance tests of timber members in bending, tension and compression with respect to the Reduced Cross-Section Method. *Fire Safety Journal*, *68*, 81–99. https://doi.org/10.1016/j.firesaf.2014.05.006

Schmid, J., Werther N, Klippel M, & Frangi A. (2019). Structural Fire Design-Statement on the Design of Cross-Laminated Timber (CLT). *Civil Engineering Research Journal*, *7*(5). https://doi.org/10.19080/CERJ.2019.07.555721

Schneider, C. A., Rasband, W. S., & Eliceiri, K. W. (2012). NIH Image to ImageJ: 25 years of image analysis. *Nature Methods*, *9*(7), 671–675. https://doi.org/10.1038/nmeth.2089

Seyedrazavi, S., & Viau, C. (2025). Post-fire structural performance of glued-laminated timber columns subjected to real fires [Article]. *Structures (Oxford)*, *75*, 108772. https://doi.org/10.1016/j.istruc.2025.108772

Šliseris, J., Gaile, L., & Pakrastiņš, L. (2017). Numerical analysis of behaviour of cross laminated timber (CLT) in blast loading [Article]. *IOP Conference Series. Materials Science and Engineering*, *251*(1), 12105. https://doi.org/10.1088/1757-899X/251/1/012105

Su, J., Gibbs, E., Weinfurter, M., Lafrance, P.-S., Gratton, K., Frade, A., & Leroux, P. (2023). Large-scale fire tests of a mass timber building structure for MTDFTP. In *Client Report (National Research Council of Canada. Construction); no. A1-018329.1/A1-018487.1*. National Research Council of Canada. https://doi.org/10.4224/40003036

Sukontasukkul, P., Lam, F., & Mindess, S. (2000). Fracture of Parallel Strand Lumber (PSL) under impact loading. *Materials and Structures/Materiaux et Constructions*, *33*(7). https://doi.org/10.1007/bf02480664

Supek, F. (2015). *FastRandomForest: A fast implementation of the Random Forest algorithm for WEKA* (2.0). Google Code Archive.

Tang, Z., Yue, K., Lu, D., Shi, X., Chu, Y., Tian, Z., & Lu, W. (2022). Experimental investigation into fire performance of mixed species glulam beams under three-side fire exposure. *European Journal of Wood and Wood Products*, *80*(1). https://doi.org/10.1007/s00107-021-01746-7

ULC Standards. (2014). *CAN/ULC-S101: Standard methods of fire endurance tests of building construction and materials*.

USACE. (2008). *Single-Degree-of-Freedom Blast Effects Design Spreadsheets (SBEDS)*.

USACE Protective Design Center Omaha District. (2018). *Analysis Guidance for Cross-Laminated Timber Construction Exposed to Airblast Loading*.

Vairo, M., Pignatta Silva, V., & Hideyoshi Icimoto, F. (2023). Behavior of cross-laminated timber panels during and after an ISO-fire: An experimental analysis. *Results in Engineering*, *17*, 100878. https://doi.org/10.1016/J.RINENG.2023.100878

Van den Bulcke, J., Verschuren, L., De Blaere, R., Vansuyt, S., Dekegeleer, M., Kibleur, P., Pieters, O., De Mil, T., Hubau, W., Beeckman, H., Van Acker, J., & wyffels, F. (2025). Enabling high-throughput quantitative wood anatomy through a dedicated pipeline [Article]. *Plant Methods*, *21*(1), 11–11. https://doi.org/10.1186/s13007-025-01330-7

Van Le, T., Ghazlan, A., Ngo, T., Remennikov, A., Kalubadanage, D., & Chern Jinn Gan, E. (2020). Dynamic increase factors for Radiata pine CLT panels subjected to simulated out-of-plane blast loading. *Engineering Structures*, *225*. https://doi.org/10.1016/j.engstruct.2020.111299

Van Le, T., Ghazlan, A., Nguyen, T., & Ngo, T. (2021). Performance of bio-inspired cross-laminated timber under blast loading – A numerical study. *Composite Structures*, *260*, 113524. https://doi.org/10.1016/j.compstruct.2020.113524

Viau, C., & Doudak, G. (2016a). Investigating the Behavior of Light-Frame Wood Stud Walls Subjected to Severe Blast Loading. *Journal of Structural Engineering*, *142*(12), 04016138. https://doi.org/10.1061/(asce)st.1943-541x.0001622

Viau, C., & Doudak, G. (2016b). Investigating the behaviour of typical and designed wall-to-floor connections in light-frame wood stud wall structures subjected to blast loading. *Canadian Journal of Civil Engineering*, *43*(6). https://doi.org/10.1139/cjce-2015-0452

Viau, C., & Doudak, G. (2019a). Behaviour and modelling of cross-laminated timber panels with boundary connections subjected to blast loads. *Engineering Structures*. https://api.semanticscholar.org/CorpusID:199656718

Viau, C., & Doudak, G. (2019b). Effect of high strain-rates on heavy timber connections. *Proceedings, Annual Conference - Canadian Society for Civil Engineering*, *2019-June*.

Viau, C., & Doudak, G. (2021a). Behavior and Modeling of Glulam Beams with Bolted Connections Subjected to Shock Tube–Simulated Blast Loads. *Journal of Structural Engineering*, *147*(1). https://doi.org/10.1061/(asce)st.1943-541x.0002876

Viau, C., & Doudak, G. (2021b). Energy-Absorbing Connection for Heavy-Timber Assemblies Subjected to Blast Loads–Concept Development and Application. *Journal of Structural Engineering*, *147*(4). https://doi.org/10.1061/(asce)st.1943-541x.0002975

Viau, C., & Doudak, G. (2021c). Energy-Absorbing Connection for Heavy-Timber Assemblies Subjected to Blast Loads–Concept Development and Application [Article]. *Journal of Structural Engineering (New York, N.Y.)*, *147*(4). https://doi.org/10.1061/(ASCE)ST.1943-541X.0002975

Viau, C., Lacroix, D. N., & Doudak, G. (2017). Damage level assessment of response limits in light-frame wood stud walls subjected to blast loading. *Canadian Journal of Civil Engineering*, *44*(2). https://doi.org/10.1139/cjce-2015-0418

von Arx, G., Crivellaro, A., Prendin, A. L., Čufar, K., & Carrer, M. (2016). Quantitative Wood Anatomy—Practical Guidelines [Article]. *Frontiers in Plant Science*, *7*, 781. https://doi.org/10.3389/fpls.2016.00781

Vural, M., & Ravichandran, G. (2003). Dynamic response and energy dissipation characteristics of balsa wood: Experiment and analysis. *International Journal of Solids and Structures*, *40*(9). https://doi.org/10.1016/S0020-7683(03)00057-X

Weaver, M. K., Newberry, C. M., Podesto, L., & O'Laughlin, C. (2018). Blast Testing of Loaded Cross-Laminated Timber Structures. *Structures Congress 2018: Blast, Impact Loading, and Response; and Research and Education - Selected Papers from the Structures Congress 2018*, *2018-April*. https://doi.org/10.1061/9780784481349.039

Western Archrib. (2025). https://www.westernarchrib.com/

White, R. H. (1988). *Charring rates of different wood species*.

White, R. H. (2024). Analytical methods for determining fire resistance of timber members. In *SFPE Handbook of Fire Protection Engineering, Fifth Edition* (pp. 1979–2011). Springer New York. https://doi.org/10.1007/978-1-4939-2565-0_55

White, R. H., & Nordheim, E. V. (1992). Charring rate of wood for ASTM E 119 exposure. *Fire Technology*, *28*(1), 5–30. https://doi.org/10.1007/BF01858049

Wiesner, F., Bartlett, A., Mohaine, S., Robert, F., McNamee, R., Mindeguia, J.-C., & Bisby, L. (2021). Structural Capacity of One-Way Spanning Large-Scale Cross-Laminated Timber

Slabs in Standard and Natural Fires [Article]. *Fire Technology*, *57*(1), 291–311. https://doi.org/10.1007/s10694-020-01003-y

Wiesner, F., Xu, H., Lange, D., Gupta, V., Pope, I., Torero, J. L., & Hidalgo, J. P. (2025). Large-scale compartment fires to develop a self-extinction design framework for mass timber-Part 2: Results, analysis and design implications. *Fire Safety Journal*, *152*, 104346. https://doi.org/10.1016/J.FIRESAF.2025.104346

Wight, N., Viau, C., & Heffernan, P. (2024). Behaviour of glued-laminated timber beams under impact loading. *Canadian Journal of Civil Engineering*, *51*(7), 753–768. https://doi.org/10.1139/cjce-2023-0298

Witten, I. H., Frank, E., Hall, M. A., & Pal, C. J. (2016). *Data Mining, Fourth Edition: Practical Machine Learning Tools and Techniques* (4th ed.). Morgan Kaufmann Publishers Inc.

Wouts, J., Haugou, G., Oudjene, M., Coutellier, D., & Morvan, H. (2016). Strain rate effects on the compressive response of wood and energy absorption capabilities - Part A: Experimental investigations. *Composite Structures*, *149*. https://doi.org/10.1016/j.compstruct.2016.03.058

Wrzesniak, D., & Fragiacomo, M. (2016). Cyclic behaviour of glulam shear walls with bolted connections [Article]. *European Journal of Wood and Wood Products*, *74*(3), 393–405. https://doi.org/10.1007/s00107-016-1020-7

Xing, Z., Wang, Y., Zhang, J., & Ma, H. (2021). Comparative study on fire resistance and zero strength layer thickness of CLT floor under natural fire and standard fire. *Construction and Building Materials*, *302*. https://doi.org/10.1016/j.conbuildmat.2021.124368

Zhang, S., Chen, Z., Liu, Y., Tao, Q., Wu, D., & Zou, P. (2025). Multi-Criteria Analysis of Steel–Concrete–Steel Slab Performance: Dynamic Response Assessment Under Post-Fire Explosion [Article]. *Buildings (Basel)*, *15*(8), 1340. https://doi.org/10.3390/buildings15081340

Zhang, Y., Zhang, X., & Wang, L. (2022). Experimental validation and simplified design of an energy-based time equivalent method applied to evaluate the fire resistance of the glulam exposed to parametric fire [Article]. *Engineering Structures*, *272*, 115051. https://doi.org/10.1016/j.engstruct.2022.115051

Appendix A: MTDFTP Structure and Related Drawings

The CWC Fire Test CAD Drawings (ISL Engineering and Land Services, 2022) were obtained from the original project documentation for the MTDFTP structure and are included for the purpose of illustrating the loading, GLT panels' location and sizes in addition to fire-test layout referenced in this thesis.

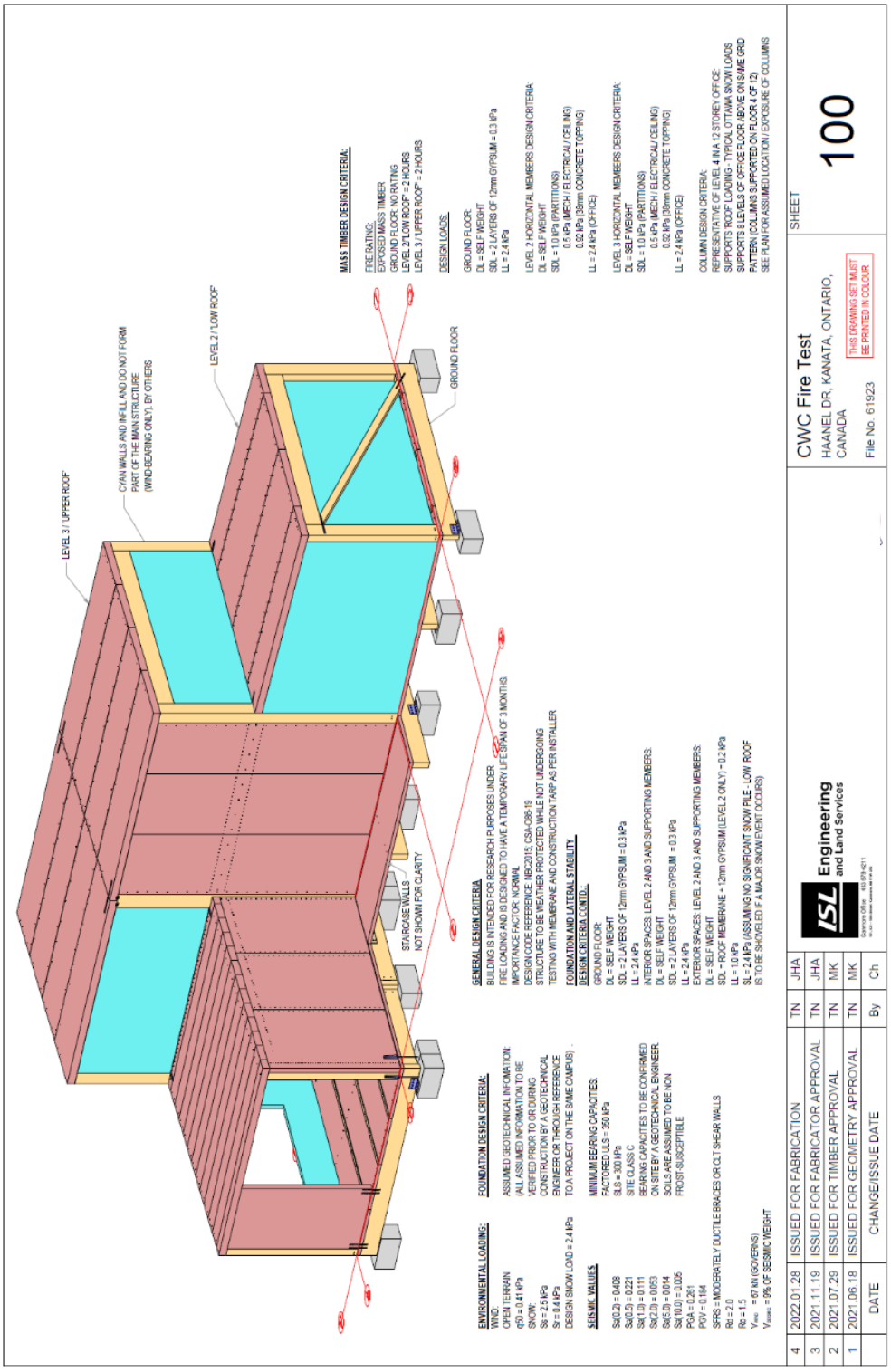

GLULAM MEMBERS SCHEDULE

Name	Quantity	Width	Height	Length	Grade Stress	Finish	Manufacturer	Sides Finished
B101	1	175	494	7300	SPRUCE-PINE 20f-E	INDUSTRIAL FINISH	WESTERN ARCHRIB	
B102	1	219	494	7300	D.Fir-L 24f-E	INDUSTRIAL FINISH	STRUCTURLAM	
B103	1	219	494	9300	D.Fir-L 24f-E	INDUSTRIAL FINISH	STRUCTURLAM	
B104	1	219	494	9300	D.Fir-L 24f-E	INDUSTRIAL FINISH	STRUCTURLAM	
B105	1	265	490	7300	SPRUCE-PINE 20f-EX	INDUSTRIAL FINISH	ELEMENT 5	
B106	1	175	494	7168	SPRUCE-PINE 20f-E	INDUSTRIAL FINISH	WESTERN ARCHRIB	
B107	1	215	490	7168	SPRUCE-PINE 20f-E	INDUSTRIAL FINISH	ELEMENT 5	
B108	1	215	490	7168	SPRUCE-PINE 20f-E	INDUSTRIAL FINISH	ELEMENT 5	
B109	1	215	495	7475	24F-ES/NPG	INDUSTRIAL FINISH	NORDIC	
B110	1	184	495	7475	24F-ES/NPG	INDUSTRIAL FINISH	NORDIC	
B111	2	175	494	3431	SPRUCE-PINE 20f-E	INDUSTRIAL FINISH	WESTERN ARCHRIB	
B111A	1	175	494	3407	SPRUCE-PINE 20f-E	INDUSTRIAL FINISH	WESTERN ARCHRIB	
B112	1	175	494	3663	SPRUCE-PINE 20f-E	INDUSTRIAL FINISH	WESTERN ARCHRIB	
B113	1	175	494	3543	SPRUCE-PINE 20f-E	INDUSTRIAL FINISH	WESTERN ARCHRIB	
B114	1	175	494	3359	SPRUCE-PINE 20f-E	INDUSTRIAL FINISH	WESTERN ARCHRIB	
B201	1	265	495	6386	SPRUCE-PINE 20f-E	INDUSTRIAL FINISH	ELEMENT 5	EXPOSED 2 SIDES (FIRE)
B202	1	346	578	6488	24F-ES/NPG	INDUSTRIAL FINISH	NORDIC	
B203	1	346	546	6369	24F-ES/NPG	INDUSTRIAL FINISH	NORDIC	
B204	1	263	489	6852	D.Fir-L 24f-E	INDUSTRIAL FINISH	STRUCTURLAM	EXPOSED 2 SIDES (FIRE)
B205	1	260	494	6542	SPRUCE-PINE 20f-E	INDUSTRIAL FINISH	WESTERN ARCHRIB	EXPOSED 2 SIDES (FIRE)
B206	1	263	494	6852	D.Fir-L 24f-E	INDUSTRIAL FINISH	STRUCTURLAM	EXPOSED 2 SIDES (FIRE)
B301	1	265	494	6499	SPRUCE-PINE 20f-E	INDUSTRIAL FINISH	WESTERN ARCHRIB	EXPOSED 2 SIDES (FIRE)
B302	1	346	574	6382	24F-ES/NPG	INDUSTRIAL FINISH	NORDIC	
B303	1	215	490	6553	SPRUCE-PINE 20f-E	INDUSTRIAL FINISH	ELEMENT 5	EXPOSED 2 SIDES (FIRE)
BR401	1	215	210	6995	SPRUCE-PINE 20f-EX	INDUSTRIAL FINISH	ELEMENT 5	
C101	1	265	455	3946	SPRUCE-PINE 12c-E	INDUSTRIAL FINISH	ELEMENT 5	2 SIDES EXPOSED
C102	1	265	455	3946	SPRUCE-PINE 12c-E	INDUSTRIAL FINISH	ELEMENT 5	2 SIDES EXPOSED
C103	2	395	395	4300	24F-ES/NPG	INDUSTRIAL FINISH	NORDIC	3 SIDES EXPOSED
C104	1	406	413	7137	D.Fir-L 16c-E	INDUSTRIAL FINISH	STRUCTURLAM	3 SIDES EXPOSED
C105	1	314	298	7247	D.Fir-L 16c-E	INDUSTRIAL FINISH	STRUCTURLAM	2 SIDES EXPOSED
C106	1	530	532	7139	SPRUCE-PINE 12c-E	INDUSTRIAL FINISH	WESTERN ARCHRIB	4 SIDES EXPOSED
C107	1	265	455	3938	SPRUCE-PINE 12c-E	INDUSTRIAL FINISH	ELEMENT 5	2 SIDES EXPOSED
C108	1	430	456	7110	SPRUCE-PINE 12c-E	INDUSTRIAL FINISH	WESTERN ARCHRIB	3 SIDES EXPOSED
C109	1	265	455	3938	SPRUCE-PINE 12c-E	INDUSTRIAL FINISH	ELEMENT 5	2 SIDES EXPOSED
C201	1	395	395	2972	24F-ES/NPG	INDUSTRIAL FINISH	NORDIC	3 SIDES EXPOSED
C202	1	395	395	2972	24F-ES/NPG	INDUSTRIAL FINISH	NORDIC	3 SIDES EXPOSED

PANEL SCHEDULE

Name	Size	Quantity	Width	Height	Length	Grade Stress	Finish	Manufacturer
P101	105 THK. CLT	1	1247	105	7299	SPF V2	INDUSTRIAL FINISH	ELEMENT 5
P102	105 THK. CLT	2	2400	105	7299	SPF V2	INDUSTRIAL FINISH	ELEMENT 5
P103	105 THK. CLT	1	1247	105	7299	SPF V2	INDUSTRIAL FINISH	ELEMENT 5
P104	105 THK. CLT	1	1998	105	7233	SPF V2M1.1	INDUSTRIAL FINISH	STRUCTURLAM
P105	105 THK. CLT	1	1247	105	7299	SPF V2	INDUSTRIAL FINISH	ELEMENT 5
P106	105 THK. CLT	2	2400	105	7299	SPF V2	INDUSTRIAL FINISH	ELEMENT 5
P107	105 THK. CLT	1	1247	105	7299	SPF V2	INDUSTRIAL FINISH	ELEMENT 5
P108	DLT4 PANEL	1	1822	89	7071	SPF No.2 OR BETTER	INDUSTRIAL FINISH	STRUCTURECRAFT
P109	DLT4 PANEL	2	1824	89	7071	SPF No.2 OR BETTER	INDUSTRIAL FINISH	STRUCTURECRAFT
P110	DLT4 PANEL	1	1824	89	7071	SPF No.2 OR BETTER	INDUSTRIAL FINISH	STRUCTURECRAFT
P111	DLT4 PANEL	1	1824	89	7527	SPF No.2 OR BETTER	INDUSTRIAL FINISH	STRUCTURECRAFT
P112	DLT4 PANEL	2	1824	89	7527	SPF No.2 OR BETTER	INDUSTRIAL FINISH	STRUCTURECRAFT
P113	DLT4 PANEL	1	1999	89	7527	SPF No.2 OR BETTER	INDUSTRIAL FINISH	STRUCTURECRAFT
P201	7-LAYER 213-7I	1	1247	213	7305	SPF E1	INDUSTRIAL FINISH	NORDIC
P202	7-LAYER 213-7I	2	2400	213	7305	SPF E1	INDUSTRIAL FINISH	NORDIC
P203	7-LAYER 213-7I	1	1247	213	7305	SPF E1	INDUSTRIAL FINISH	NORDIC
P204	245 THK. CLT	1	1056	245	7298	SPF E1M4	INDUSTRIAL FINISH	STRUCTURLAM
P205	245 THK. CLT	2	2400	245	7298	SPF E1M4	INDUSTRIAL FINISH	STRUCTURLAM
P206	245 THK. CLT	1	1247	245	7298	SPF E1M4	INDUSTRIAL FINISH	STRUCTURLAM
P207	L-245 THK. CLT	1	1247	245	7299	SPF E1	INDUSTRIAL FINISH	ELEMENT 5
P208	L-245 THK. CLT	2	2400	245	7299	SPF E1	INDUSTRIAL FINISH	ELEMENT 5
P209	L-245 THK. CLT	1	1247	245	7299	SPF E1	INDUSTRIAL FINISH	ELEMENT 5
P210	215 THK. WESTDEK	11	603	215	7475	SPF No.2 OR BETTER	INDUSTRIAL FINISH	WESTERN ARCHRIB
P211	215 THK. WESTDEK	1	371	215	7475	SPF No.2 OR BETTER	INDUSTRIAL FINISH	WESTERN ARCHRIB
P212	215 THK. WESTDEK	1	302	215	7475	SPF No.2 OR BETTER	INDUSTRIAL FINISH	WESTERN ARCHRIB
P301	DLT10 PANEL	4	1822	230	7299	SPF No.2 OR BETTER	INDUSTRIAL FINISH	STRUCTURECRAFT
P302	7-LAYER 213-7I	4	1822	213	7502	SPF E1	INDUSTRIAL FINISH	NORDIC
P401	175 THK. CLT	1	2024	191	7133	SPF V2.1	INDUSTRIAL FINISH	STRUCTURLAM
P402	175 THK. CLT	2	2400	191	7133	SPF V2.1	INDUSTRIAL FINISH	STRUCTURLAM
P403	175 THK. CLT	1	2398	175	4075	SPF V2M1.1	INDUSTRIAL FINISH	STRUCTURLAM
P404	175 THK. CLT	1	2400	175	4027	SPF V2M1.1	INDUSTRIAL FINISH	STRUCTURLAM
P405	175 THK. CLT	1	2495	175	3979	SPF V2M1.1	INDUSTRIAL FINISH	STRUCTURLAM
P406	175 THK. CLT	1	2400	175	3933	175-5s	INDUSTRIAL FINISH	NORDIC

	DATE	CHANGE/ISSUE DATE	By	Ch
4	2022.01.28	ISSUED FOR FABRICATION	TN	JHA
3	2021.11.19	ISSUED FOR FABRICATOR APPROVAL	TN	JHA
2	2021.07.29	ISSUED FOR TIMBER APPROVAL	TN	MK
1	2021.06.18	ISSUED FOR GEOMETRY APPROVAL	TN	MK

ISL Engineering and Land Services
Canmore Office 403-678-4211

CWC Fire Test
HAANEL DR, KANATA, ONTARIO, CANADA
File No. 61923
THIS DRAWING SET MUST BE PRINTED IN COLOUR

SHEET
100A

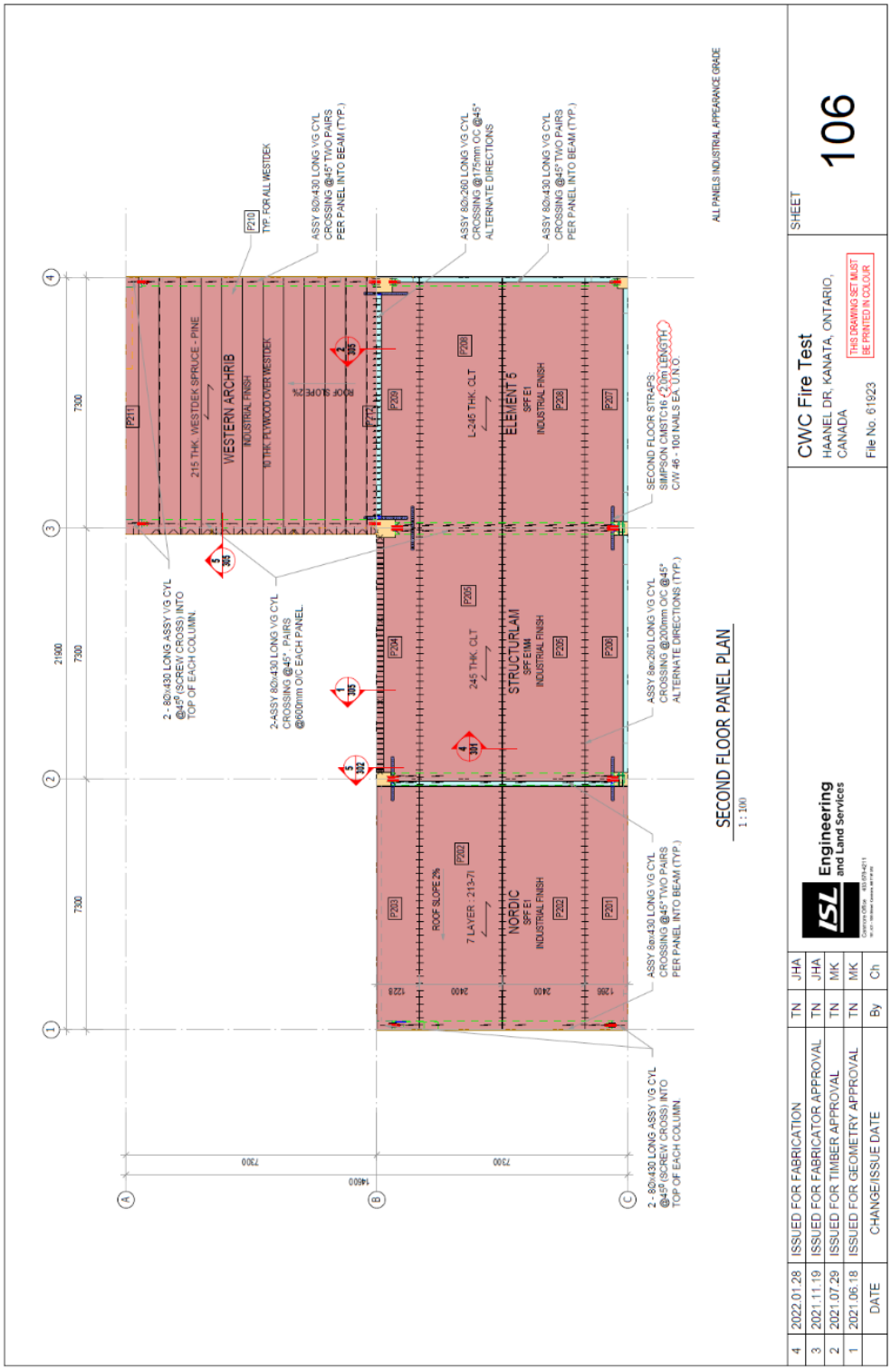
SECOND FLOOR PANEL PLAN
1 : 100
ALL PANELS INDUSTRIAL APPEARANCE GRADE
WESTERN ARCHRIB
INDUSTRIAL FINISH
215 THK. WESTDEK SPRUCE - PINE
10 THK. PLYWOOD OVER WESTDEK
ROOF SLOPE 2%
ELEMENT 6
SPF E1
INDUSTRIAL FINISH
L-245 THK. CLT
STRUCTURLAM
SPF E1 NM
INDUSTRIAL FINISH
245 THK. CLT
NORDIC
SPF E1
INDUSTRIAL FINISH
7 LAYER - 213+7i
ROOF SLOPE 2%
P210 TYP. FOR ALL WESTDEK
ASSY 80x430 LONG VG CYL CROSSING @45° TWO PAIRS PER PANEL INTO BEAM (TYP.)
ASSY 80x260 LONG VG CYL CROSSING @175mm O/C @45° ALTERNATE DIRECTIONS
2 - 80x430 LONG ASSY VG CYL @45° (SCREW CROSS) INTO TOP OF EACH COLUMN.
2-ASSY 80x430 LONG VG CYL CROSSING @45° - PAIRS @600mm O/C EACH PANEL
SECOND FLOOR STRAPS: SIMPSON CMSTC16 - 2.0m LONG C/W 46 - 100 NAILS EA. U.N.O.
ASSY 8ea260 LONG VG CYL CROSSING @200mm O/C @45° ALTERNATE DIRECTIONS (TYP.)
ASSY 8ea430 LONG VG CYL CROSSING @45° TWO PAIRS PER PANEL INTO BEAM (TYP.)
2 - 80x430 LONG ASSY VG CYL @45° (SCREW CROSS) INTO TOP OF EACH COLUMN
7300
14600
21900
1228
1256
2400
4 2022.01.28 ISSUED FOR FABRICATION TN JHA
3 2021.11.19 ISSUED FOR FABRICATOR APPROVAL TN JHA
2 2021.07.29 ISSUED FOR TIMBER APPROVAL TN MK
1 2021.06.18 ISSUED FOR GEOMETRY APPROVAL TN MK
DATE CHANGE/ISSUE DATE By Ch
Engineering and Land Services
CWC Fire Test
HAANEL DR, KANATA, ONTARIO, CANADA
File No. 61923
THIS DRAWING SET MUST BE PRINTED IN COLOUR
SHEET
106

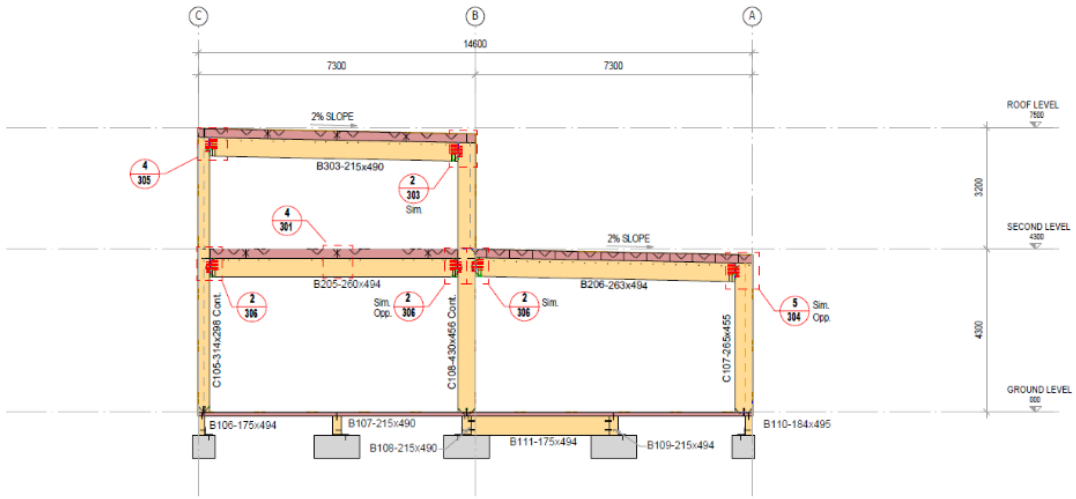

Section Along Gridline 4

1 : 100

4	2022.01.28	ISSUED FOR FABRICATION	TN	JHA
3	2021.11.19	ISSUED FOR FABRICATOR APPROVAL	TN	JHA
2	2021.07.29	ISSUED FOR TIMBER APPROVAL	TN	MK
1	2021.06.18	ISSUED FOR GEOMETRY APPROVAL	TN	MK
	DATE	CHANGE/ISSUE DATE	By	Ch

ISL Engineering and Land Services

CWC Fire Test

HAANEL DR, KANATA, ONTARIO, CANADA

File No. 61923

THIS DRAWING SET MUST BE PRINTED IN COLOUR

SHEET

204

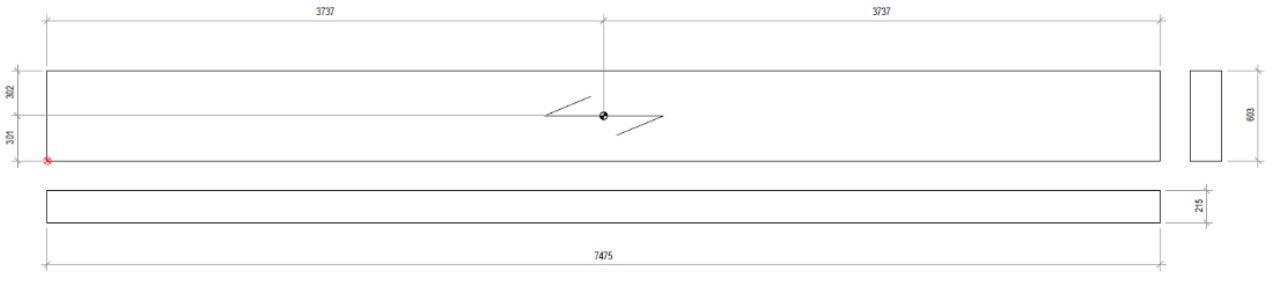

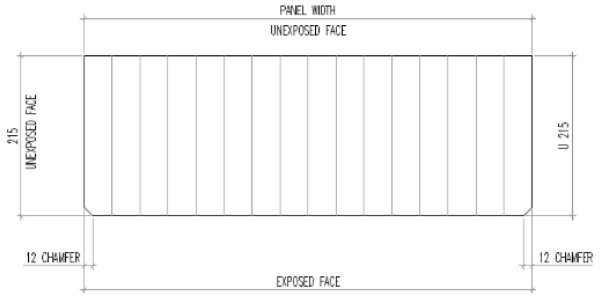

1 WESTDEK PROFILE & COATING DIAGRAM
1:5

1	2021.11.19	ISSUED FOR FABRICATOR APPROVAL	CWC Fire Test	SHOP APPLIED SEALER (AS PER QUOTE): FACE SEAL: NO COATINGS EDGE SEAL: NO COATINGS	**STRESS GRADE:** SPF No.2 OR BETTER **FINISH:** INDUSTRIAL FINISH **SIDES FINISHED:** **MANUFACTURER:** WESTERN ARCHRIB	**P210**	Western Archrib Structural Wood Systems
2	2022.01.28	ISSUED FOR FABRICATION					
			File No:61923	**WEIGHT:** 1369 lb		11 REQ'D	

Appendix B: Full-Scale Charred GLT Specimens Descriptions and Measurements

Specimen CGLT1 [215]

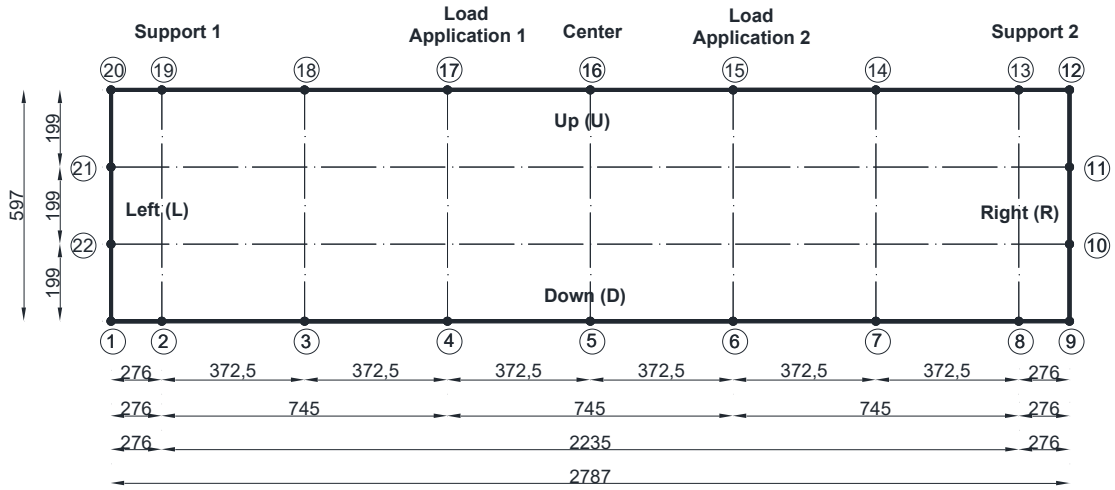

Figure B-1 Specimen CGLT1 [215] Dimensions

Figure B-2 Charred Specimen CGLT1 [215] before and after char removal

Table B-1 CGLT1 [215] Panel depth before and after char removal process

Point #	d_i (mm)	d_r (mm)	d_{rc} (mm)	x_c (mm)
1	200.5	194.6	5.9	20.4
2	206.2	196.3	9.9	18.7
3	202.8	198.4	4.5	16.6
4	205.2	196.2	9.1	18.9
5	205.2	194.1	11.1	20.9
6	205.9	195.5	10.4	19.5
7	201.4	196.2	5.2	18.8
8	202.0	197.7	4.3	17.3
9	202.7	194.7	8.0	20.3
10	205.0	195.8	9.2	19.2
11	204.1	195.7	8.4	19.3
12	200.4	193.3	7.2	21.8
13	201.0	194.1	6.8	20.9
14	200.5	197.0	3.5	18.0
15	200.7	196.0	4.7	19.0
16	200.8	193.8	7.0	21.2
17	202.0	193.8	8.2	21.2
18	201.3	195.5	5.8	19.5
19	203.6	195.2	8.4	19.9
20	200.6	196.7	3.9	18.3
21	199.4	191.2	8.2	23.8
22	203.1	192.4	10.6	22.6
Avg.	202.5	195.2	7.3	19.8
SD	2.0	1.7	2.3	1.7
CV	0.010	0.009	0.316	0.086

Specimen CGLT2 [215]

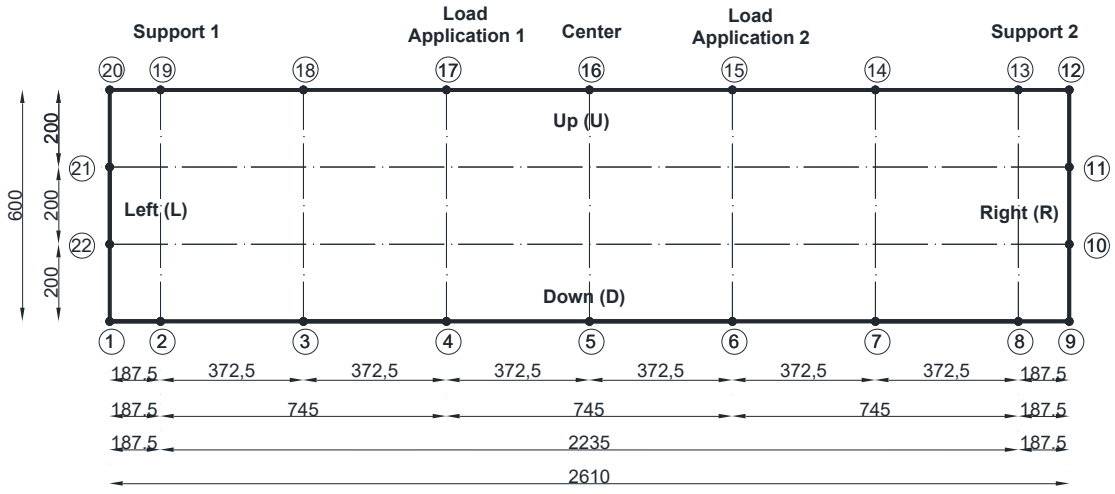

Figure B-3 Specimen CGLT2 [215] Dimensions

Figure B-4 Charred Specimen CGLT2 [215] before and after char removal

Table B-2 CGLT2 [215] Panel depth before and after char removal process

Point #	d_i (mm)	d_r (mm)	d_{rc} (mm)	x_c (mm)
1	197.3	195.6	1.7	19.4
2	199.4	196.2	3.2	18.8
3	197.0	195.6	1.5	19.4
4	199.3	195.9	3.5	19.1
5	197.5	193.1	4.5	21.9
6	195.0	194.6	0.4	20.4
7	192.2	191.3	0.9	23.7
8	193.0	191.5	1.6	23.6
9	193.0	191.6	1.3	23.4
10	198.3	192.6	5.7	22.4
11	201.3	195.6	5.7	19.4
12	198.9	194.8	4.1	20.2
13	200.5	194.1	6.4	20.9
14	199.5	196.3	3.3	18.8
15	199.5	194.8	4.7	20.2
16	199.6	194.6	5.0	20.4
17	200.4	196.3	4.1	18.7
18	198.9	195.8	3.0	19.2
19	198.7	195.4	3.3	19.6
20	196.3	196.1	0.1	18.9
21	199.3	191.8	7.5	23.2
22	195.9	193.3	2.6	21.7
Avg.	197.8	194.4	3.4	20.6
SD	2.6	1.7	2.0	1.7
CV	0.013	0.009	0.593	0.084

Specimen CGLT3 [215]

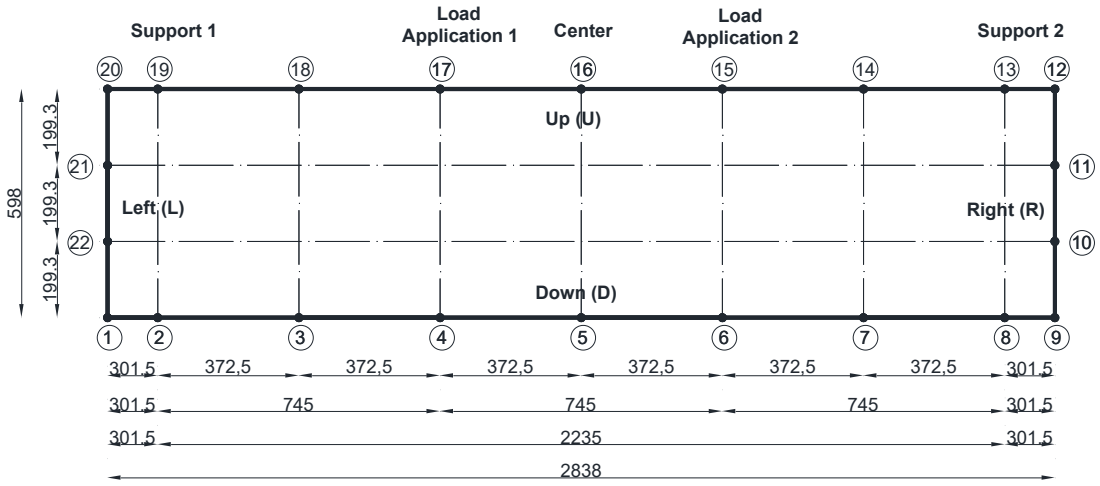

Figure B-5 Specimen CGLT2 [215] Dimensions

Figure B-6 Charred Specimen CGLT3 [215] before and after char removal

Table B-3 CGLT3 [215] Panel depth before and after char removal process

Point #	d_i (mm)	d_r (mm)	d_{rc} (mm)	x_c (mm)
1	195.6	188.6	7.0	26.4
2	201.3	193.8	7.5	21.2
3	199.5	193.9	5.5	21.1
4	200.0	196.8	3.2	18.3
5	203.6	194.3	9.3	20.7
6	203.4	193.7	9.8	21.3
7	202.6	195.4	7.1	19.6
8	199.5	194.0	5.5	21.0
9	201.1	195.9	5.2	19.1
10	197.2	192.5	4.7	22.5
11	196.9	188.4	8.5	26.6
12	195.3	188.4	6.9	26.6
13	199.9	198.7	1.2	16.3
14	200.5	191.1	9.3	23.9
15	200.8	190.6	10.1	24.4
16	189.8	183.2	6.6	31.8
17	195.2	189.2	6.1	25.9
18	196.3	191.2	5.1	23.9
19	196.3	192.0	4.3	23.0
20	190.6	190.0	0.6	25.0
21	200.3	193.6	6.7	21.4
22	199.4	192.2	7.3	22.9
Avg.	198.4	192.1	6.3	22.9
SD	3.7	3.4	2.5	3.4
CV	0.018	0.018	0.402	0.150

Specimen CGLT4 [215]

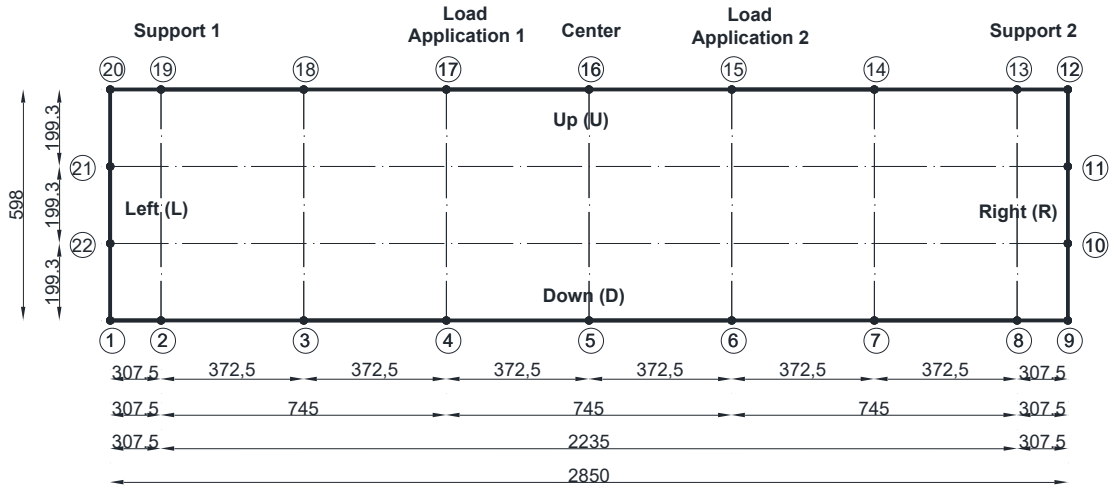

Figure B-7 Specimen CGLT4 [215] Dimensions

Figure B-8 Charred Specimen CGLT4 [215] before and after char removal

Table B-4 CGLT4 Panel depth before and after char removal process

Point #	d_i (mm)	d_r (mm)	d_{rc} (mm)	x_c (mm)
1	202.3	194.0	8.3	21.0
2	198.3	194.9	3.5	20.1
3	202.4	200.4	2.0	14.6
4	204.4	196.2	8.2	18.8
5	202.3	196.7	5.7	18.3
6	201.6	196.8	4.8	18.2
7	202.6	196.3	6.3	18.7
8	200.2	193.2	7.0	21.8
9	195.8	192.0	3.8	23.0
10	200.2	195.6	4.6	19.4
11	202.7	198.5	4.1	16.5
12	196.7	194.9	1.8	20.1
13	203.4	197.4	6.0	17.6
14	201.0	194.7	6.3	20.3
15	199.8	194.1	5.7	20.9
16	198.8	191.9	6.9	23.1
17	203.0	196.8	6.2	18.2
18	197.0	189.4	7.6	25.6
19	199.0	192.3	6.7	22.7
20	196.8	192.2	4.7	22.8
21	200.5	191.5	9.0	23.5
22	196.5	191.4	5.1	23.6
Avg.	200.2	194.6	5.6	20.4
SD	2.5	2.7	1.9	2.7
CV	0.013	0.014	0.338	0.132

Specimen CGLT5 [215]

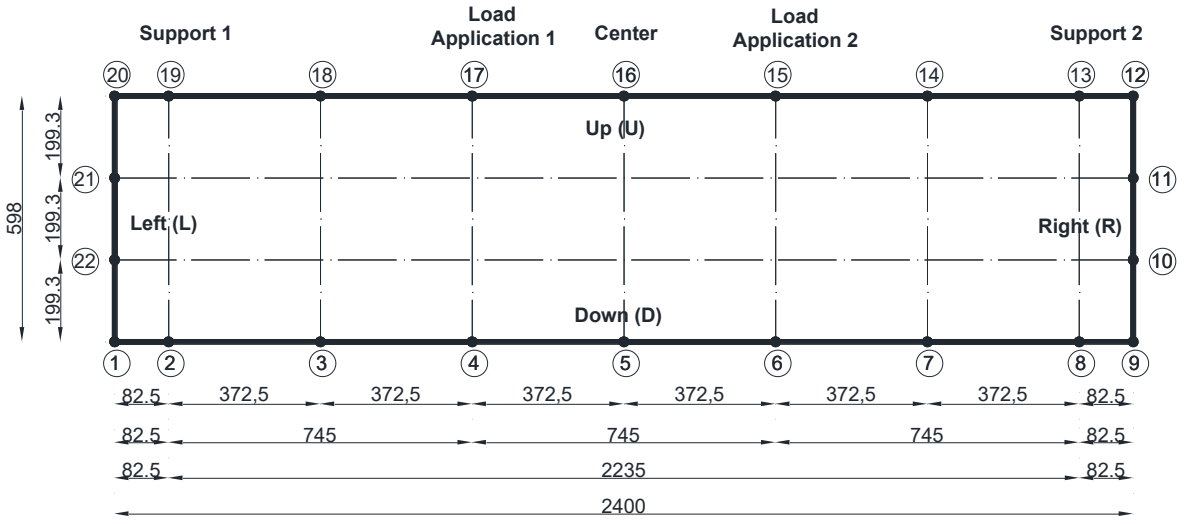

Figure B-9 Specimen CGLT5 [215] Dimensions

Figure B-10 Charred Specimen CGLT5 before and after char removal

Table B-5 CGLT5 [215] Panel depth before and after char removal process

Point #	d_i (mm)	d_r (mm)	d_{rc} (mm)	x_c (mm)
1	199.8	198.2	1.6	16.8
2	199.5	196.9	2.6	18.1
3	199.9	195.0	4.9	20.0
4	202.5	196.2	6.3	18.8
5	203.5	196.3	7.2	18.8
6	200.2	195.2	5.0	19.8
7	200.6	195.7	4.9	19.3
8	198.4	192.4	5.9	22.6
9	198.0	194.3	3.7	20.7
10	198.8	194.0	4.9	21.0
11	201.2	197.7	3.5	17.3
12	202.2	198.7	3.6	16.3
13	204.1	202.6	1.4	12.4
14	200.6	195.5	5.1	19.5
15	205.5	195.5	10.0	19.5
16	203.9	197.0	6.9	18.0
17	205.2	199.9	5.4	15.1
18	208.7	199.8	8.9	15.2
19	203.3	198.9	4.5	16.2
20	201.3	197.6	3.7	17.4
21	206.4	199.2	7.2	15.8
22	201.2	194.7	6.5	20.3
Avg.	202.0	196.9	5.2	18.1
SD	2.8	2.4	2.1	2.4
CV	0.014	0.012	0.414	0.131

Specimen CGLT6 [215]

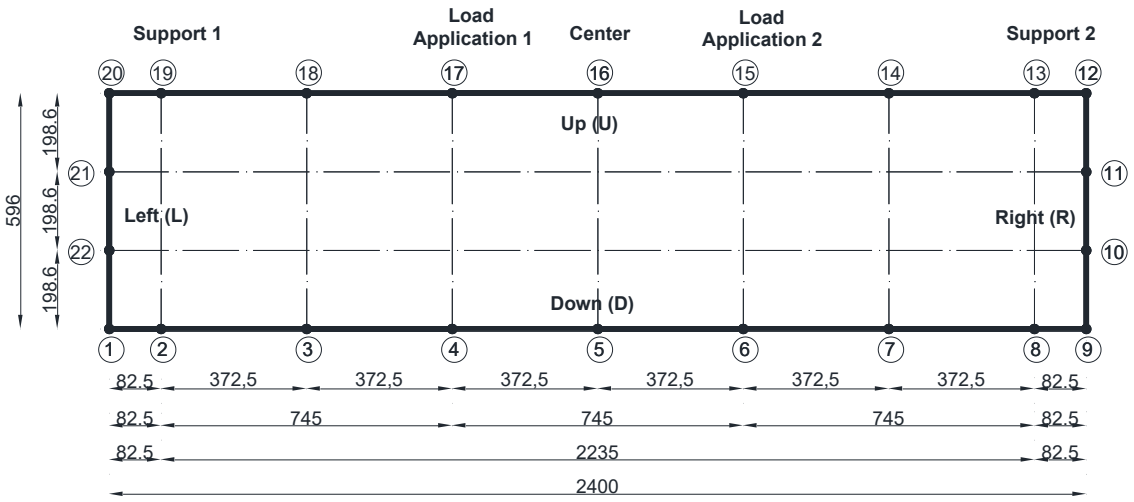

Figure B-11 Specimen CGLT6 [215] Dimensions

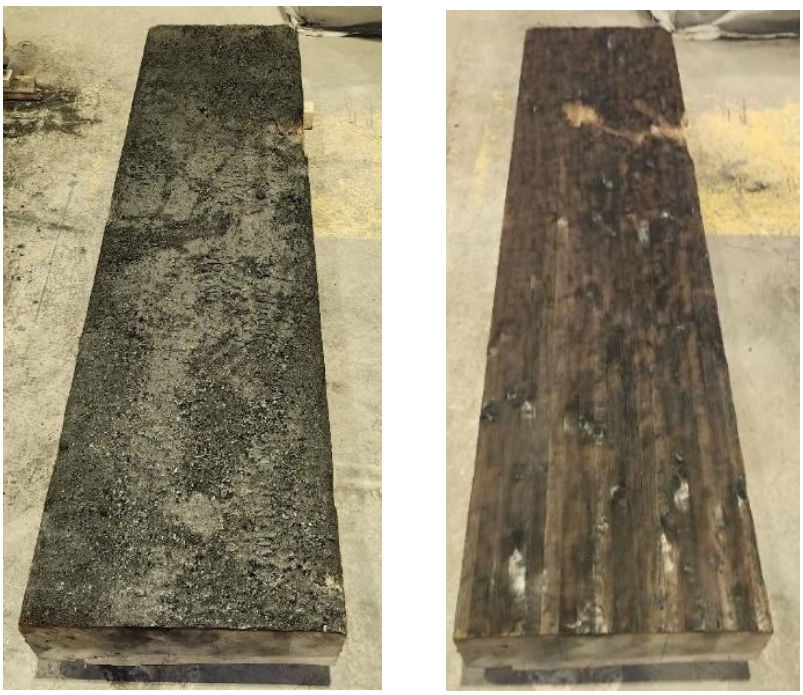

Figure B-12 Charred Specimen CGLT6 [215] before and after char removal

Table B-6 CGLT6 [215] Panel depth before and after char removal process

Point #	d_i (mm)	d_r (mm)	d_{rc} (mm)	x_c (mm)
1	203.5	196.1	7.4	18.9
2	206.1	197.4	8.6	17.6
3	208.6	196.7	11.9	18.3
4	208.8	195.7	13.1	19.3
5	204.8	194.7	10.0	20.3
6	196.0	195.3	0.7	19.7
7	204.5	200.6	3.9	14.4
8	202.1	195.3	6.9	19.7
9	202.2	198.1	4.1	16.9
10	201.2	196.5	4.7	18.5
11	197.3	188.1	9.3	27.0
12	198.8	195.5	3.4	19.5
13	198.9	193.3	5.5	21.7
14	200.0	194.2	5.8	20.8
15	207.1	195.7	11.4	19.3
16	199.3	196.0	3.3	19.1
17	202.5	194.5	8.0	20.5
18	199.5	193.4	6.1	21.6
19	199.8	194.7	5.0	20.3
20	197.9	194.4	3.4	20.6
21	201.3	197.1	4.2	18.0
22	202.8	197.6	5.2	17.4
Avg.	202.0	195.5	6.5	19.5
SD	3.6	2.4	3.1	2.358
CV	0.018	0.012	0.495	0.121

Specimen CGLT7 [215]

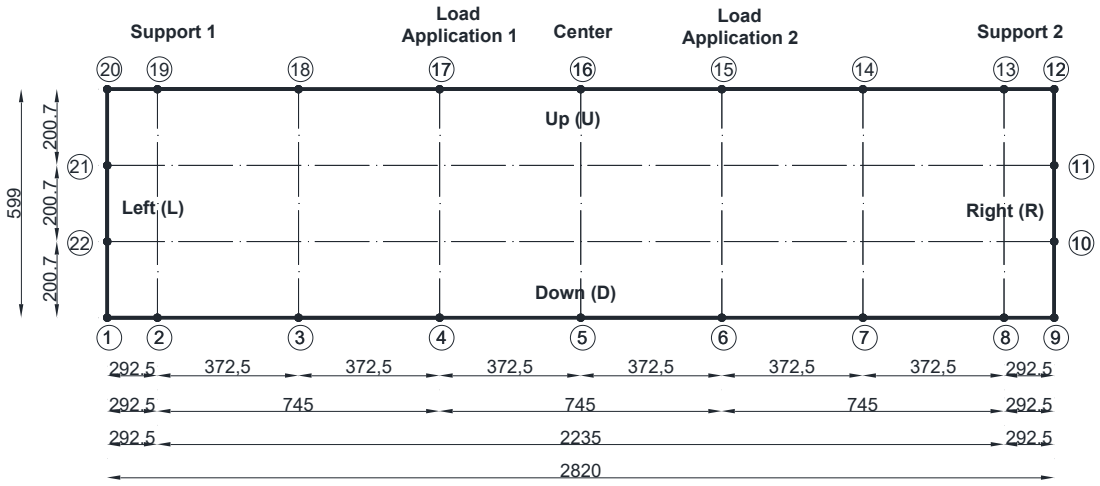

Figure B-13 Specimen CGLT7 [215] Dimensions

Figure B-14 Charred Specimen CGLT7 [215] before and after char removal

Table B-7 CGLT7 [215] Panel depth before and after char removal process

Point #	d_i (mm)	d_r (mm)	d_{rc} (mm)	x_c (mm)
1	205.5	196.9	8.7	18.1
2	202.4	196.3	6.1	18.7
3	198.7	196.9	1.8	18.1
4	199.0	194.1	5.0	20.9
5	201.3	199.7	1.6	15.4
6	200.8	197.2	3.6	17.8
7	199.9	194.8	5.0	20.2
8	198.3	194.7	3.6	20.3
9	198.9	194.6	4.3	20.4
10	203.7	193.5	10.2	21.5
11	204.1	196.0	8.2	19.0
12	202.2	193.9	8.3	21.1
13	202.1	198.5	3.6	16.5
14	202.6	198.6	3.9	16.4
15	202.4	198.0	4.5	17.1
16	200.0	197.1	3.0	17.9
17	203.2	194.6	8.6	20.4
18	206.5	196.9	9.5	18.1
19	203.2	197.5	5.8	17.6
20	200.0	196.7	3.3	18.3
21	201.1	198.5	2.6	16.5
22	198.3	196.6	1.7	18.4
Avg.	201.5	196.4	5.1	18.6
SD	2.3	1.7	2.7	1.7
CV	0.011	0.009	0.521	0.092

Appendix C Digital Image Analysis Results of Small-Scale Charred GLT Samples

Specimen Slice S1

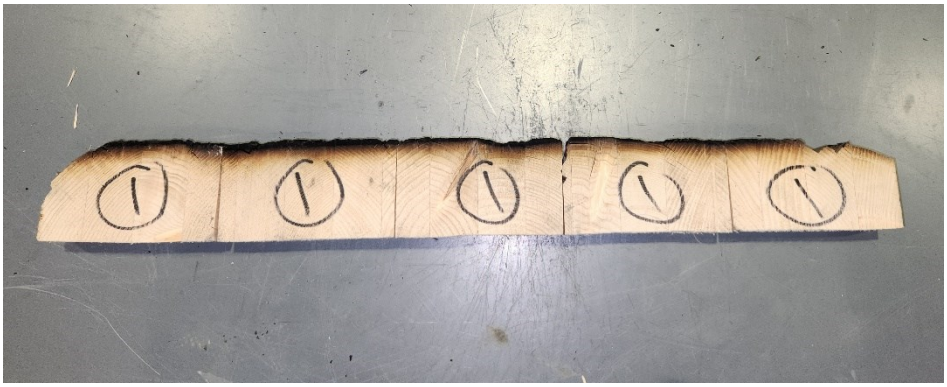

Figure C-1 Specimen slice S1

Sample S1-1

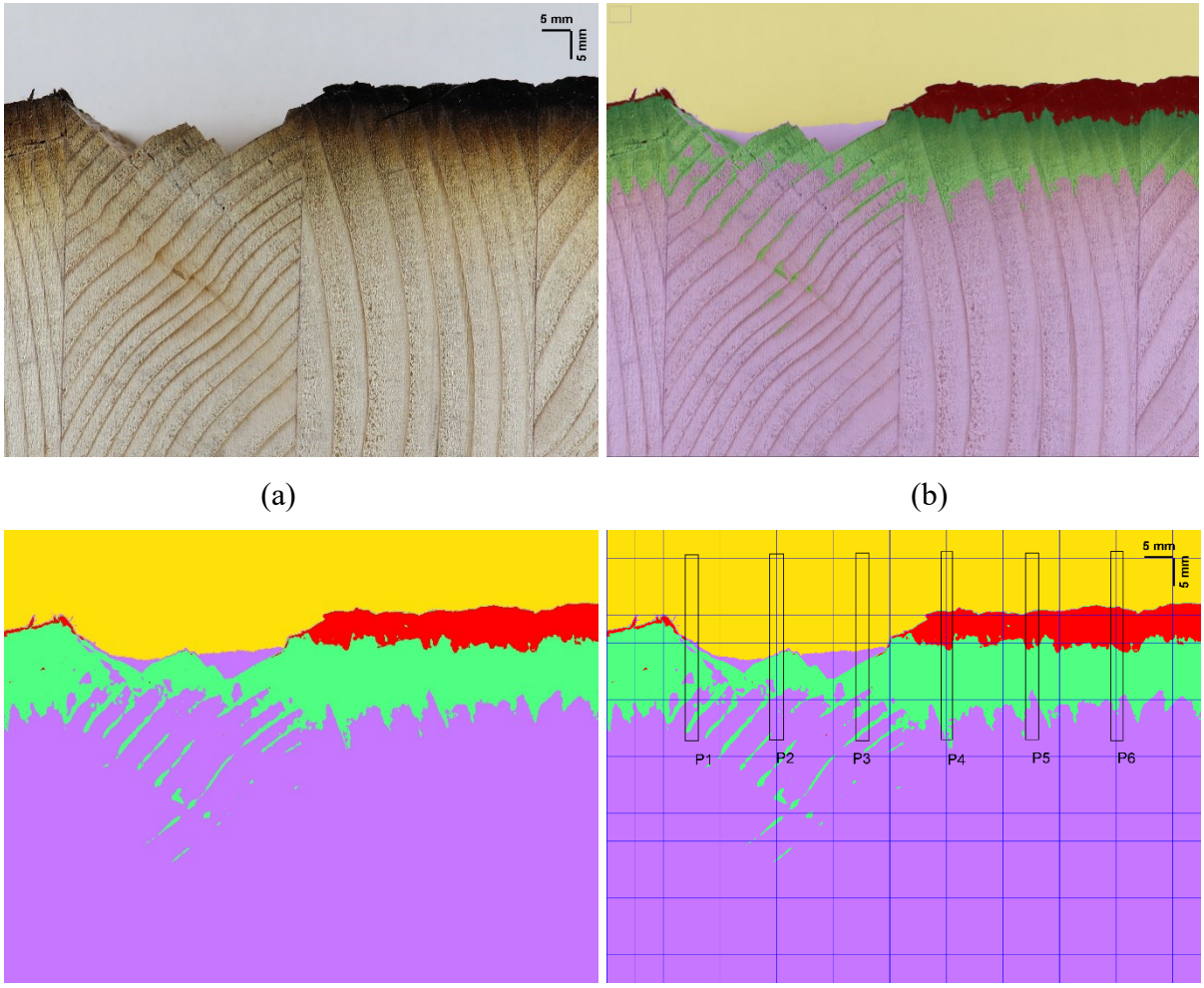

(a) (b)

(c) (d)

Figure C-2 Images of S1-1 prior and after segmentation: (a) Original image (b) Classified image (c) Toggle overlay image (d) Classified Image with grid and points

Sample S1-2

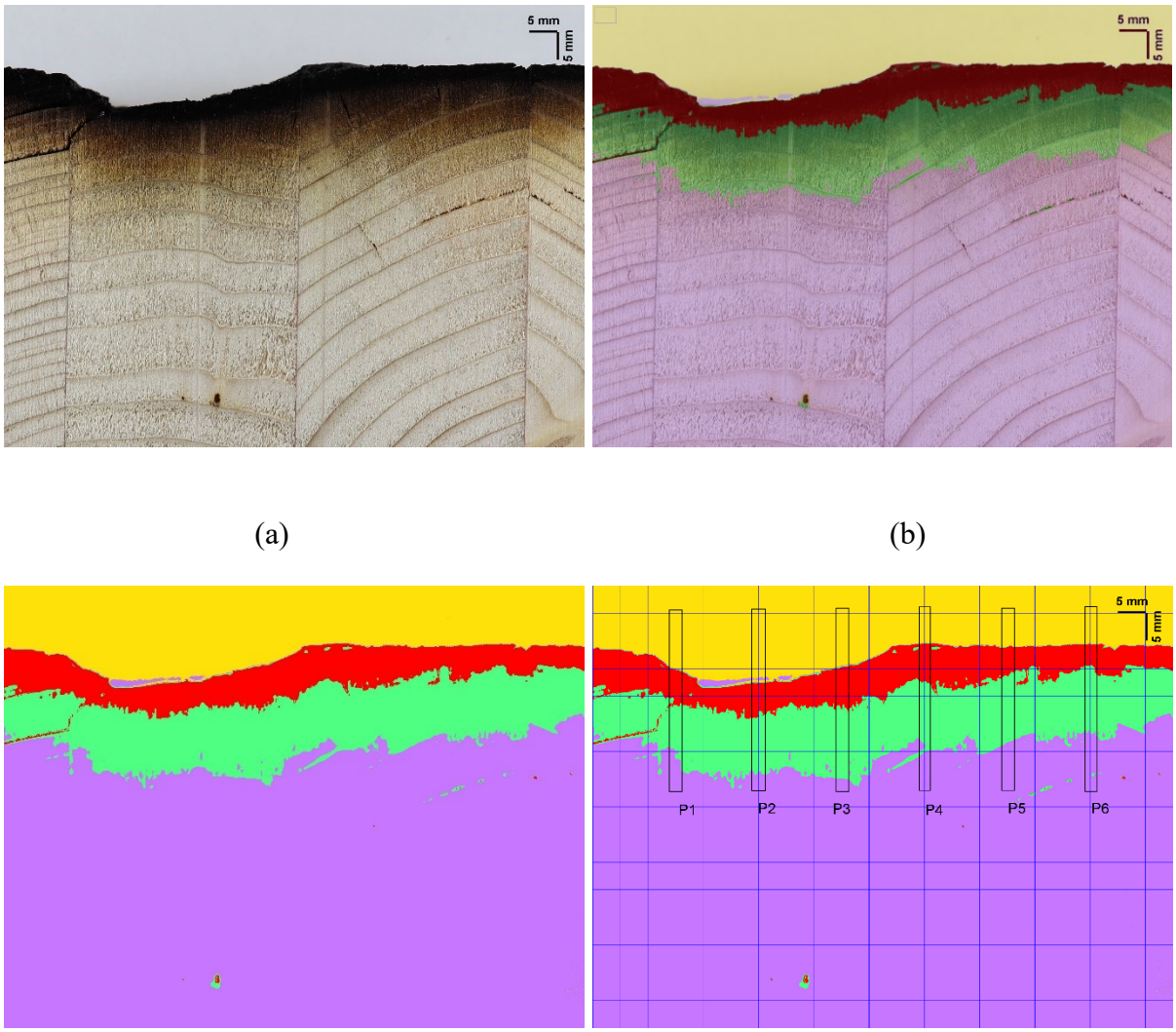

(a) (b)

(c) (d)

Figure C-3 Images of S1-2 prior and after segmentation: (a) Original image (b) Classified image (c) Toggle overlay image (d) Classified Image with grid and points

Sample S1-3

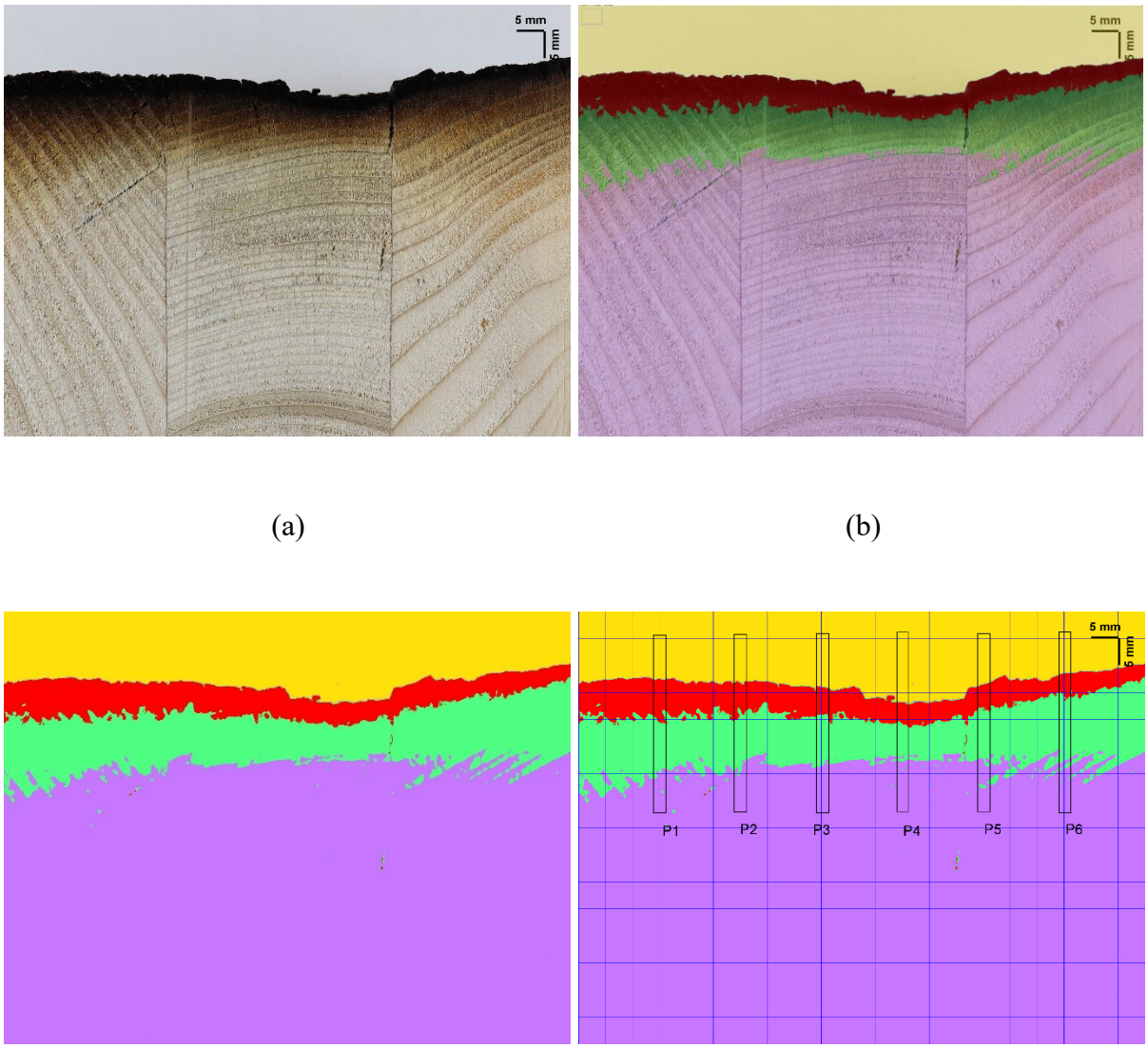

(a) (b)

(c) (d)

Figure C-4 Images of S1-3 prior and after segmentation: (a) Original image (b) Classified image (c) Toggle overlay image (d) Classified Image with grid and points

Sample S1-4

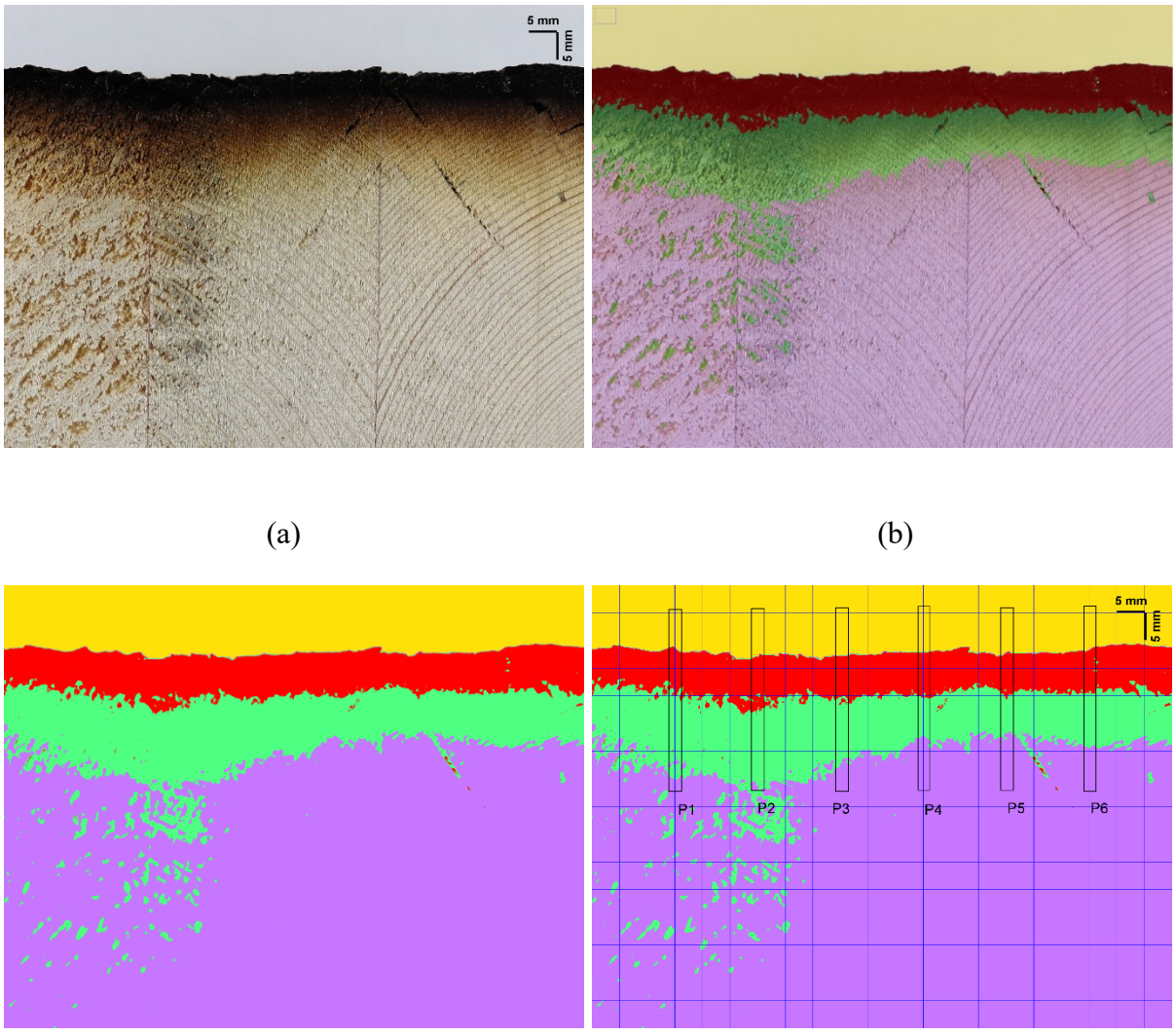

(a) (b)

(c) (d)

Figure C-5 Images of S1-4 prior and after segmentation: (a) Original image (b) Classified image (c) Toggle overlay image (d) Classified Image with grid and points

Sample S1-5

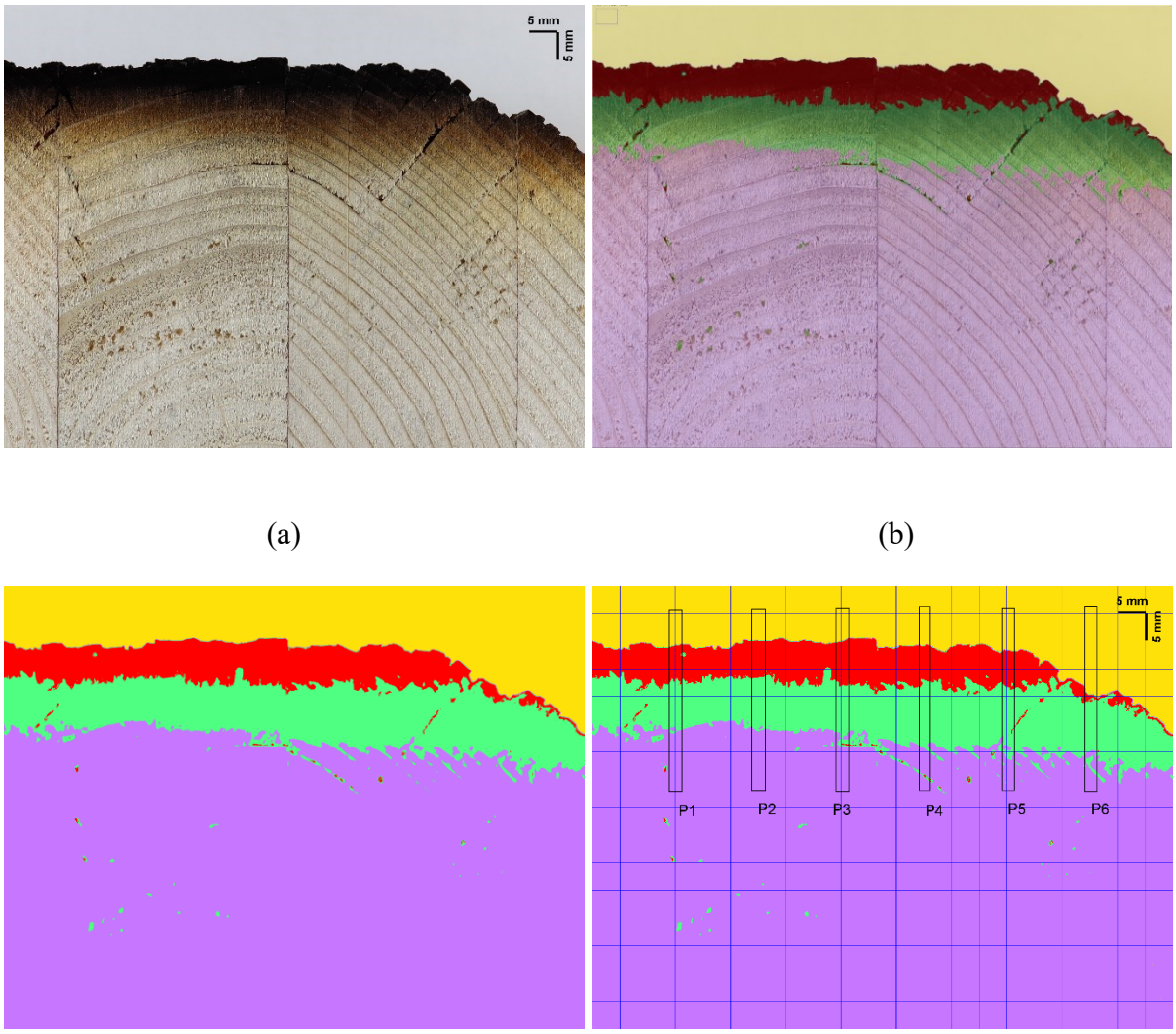

(a) (b)

(c) (d)

Figure C-6 Images of S1-5 prior and after segmentation: (a) Original image (b) Classified image (c) Toggle overlay image (d) Classified Image with grid and points

Specimen Slice S2

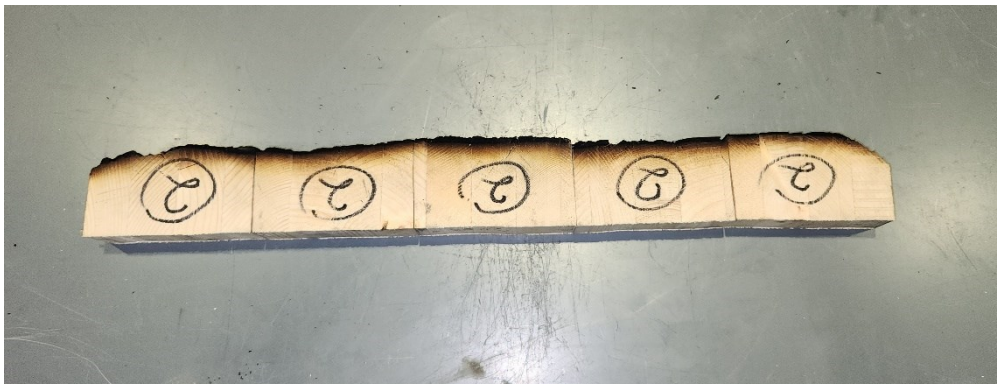

Figure C-7 Specimen slice S2

Sample S2-1

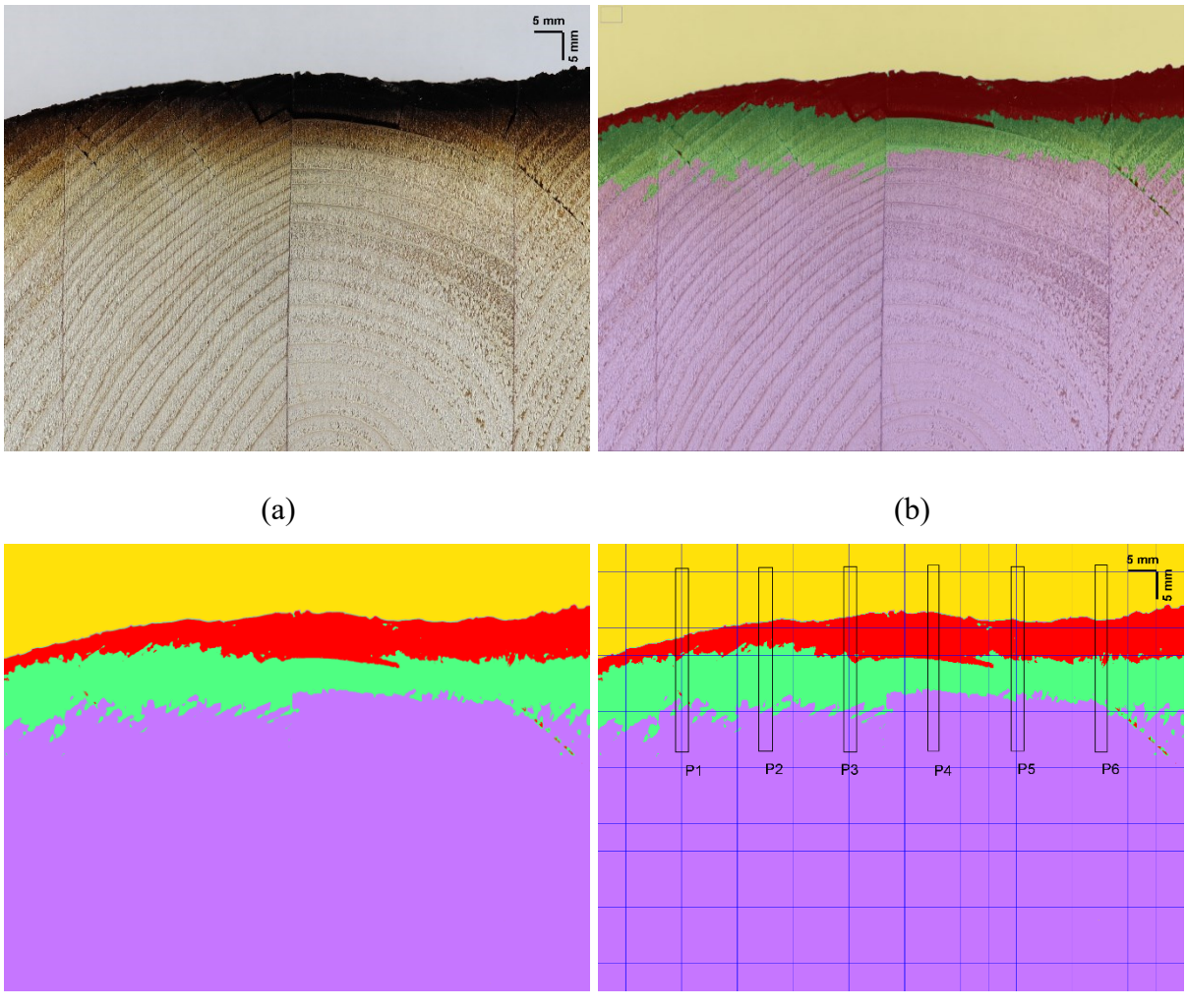

(a) (b)

(c) (d)

Figure C-8 Images of S2-1 prior and after segmentation: (a) Original image (b) Classified image (c) Toggle overlay image (d) Classified Image with grid and points

Sample S2-2

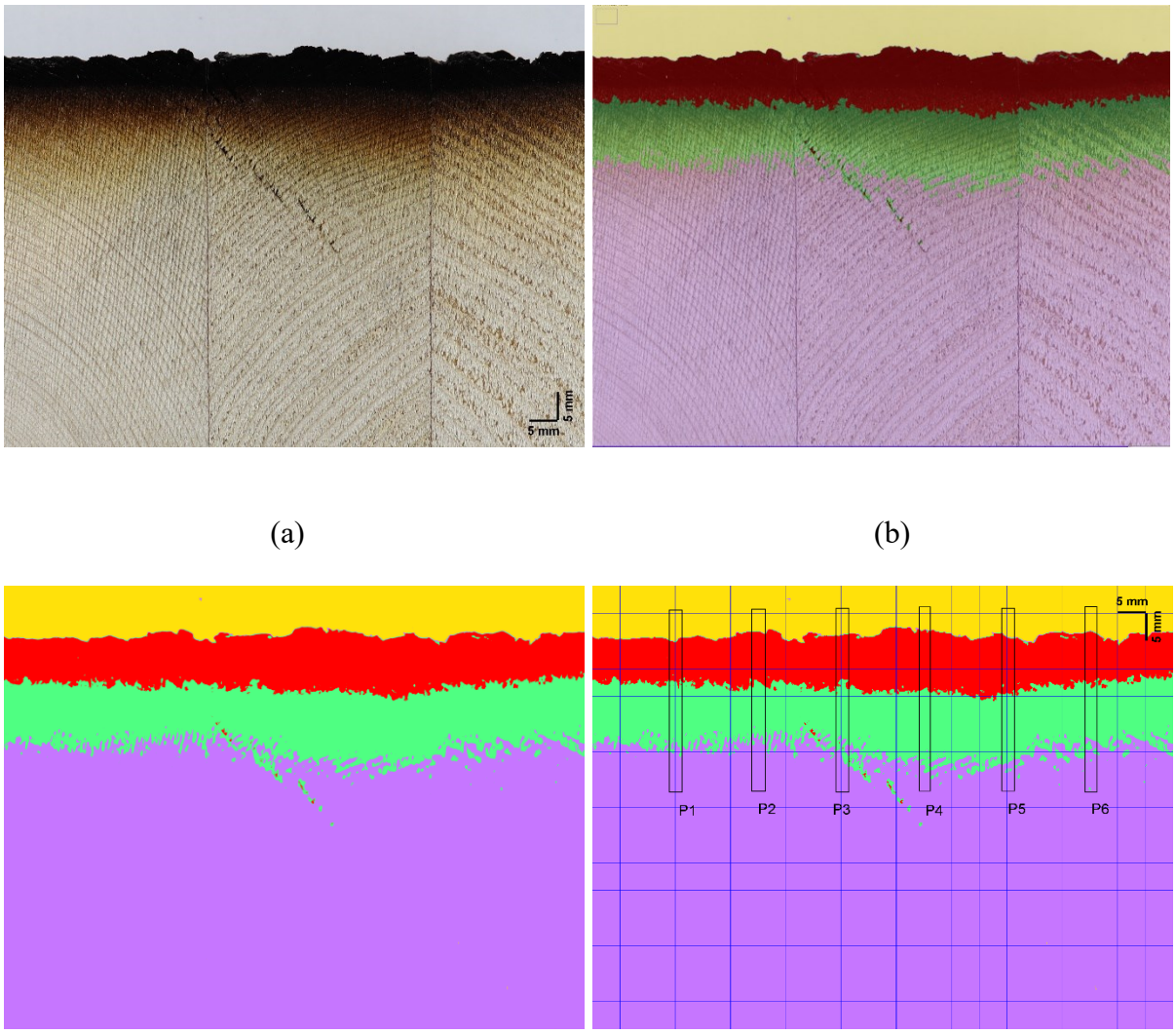

(a) (b)

(c) (d)

Figure C-9 Images of S2-2 prior and after segmentation: (a) Original image (b) Classified image (c) Toggle overlay image (d) Classified Image with grid and points

Sample S2-3

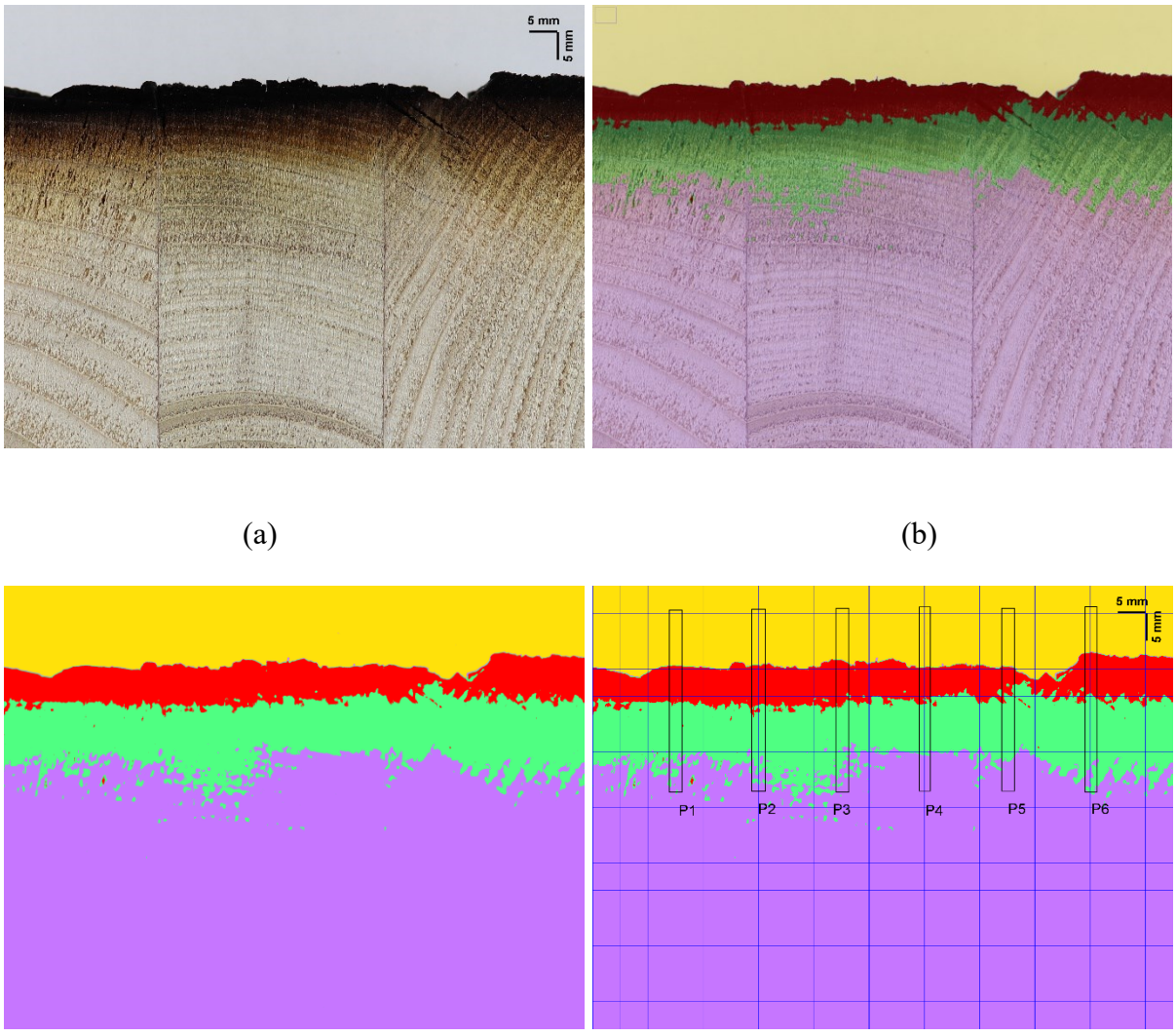

(a) (b)

(c) (d)

Figure C-10 Images of S2-3 prior and after segmentation: (a) Original image (b) Classified image (c) Toggle overlay image (d) Classified Image with grid and points

Sample S2-4

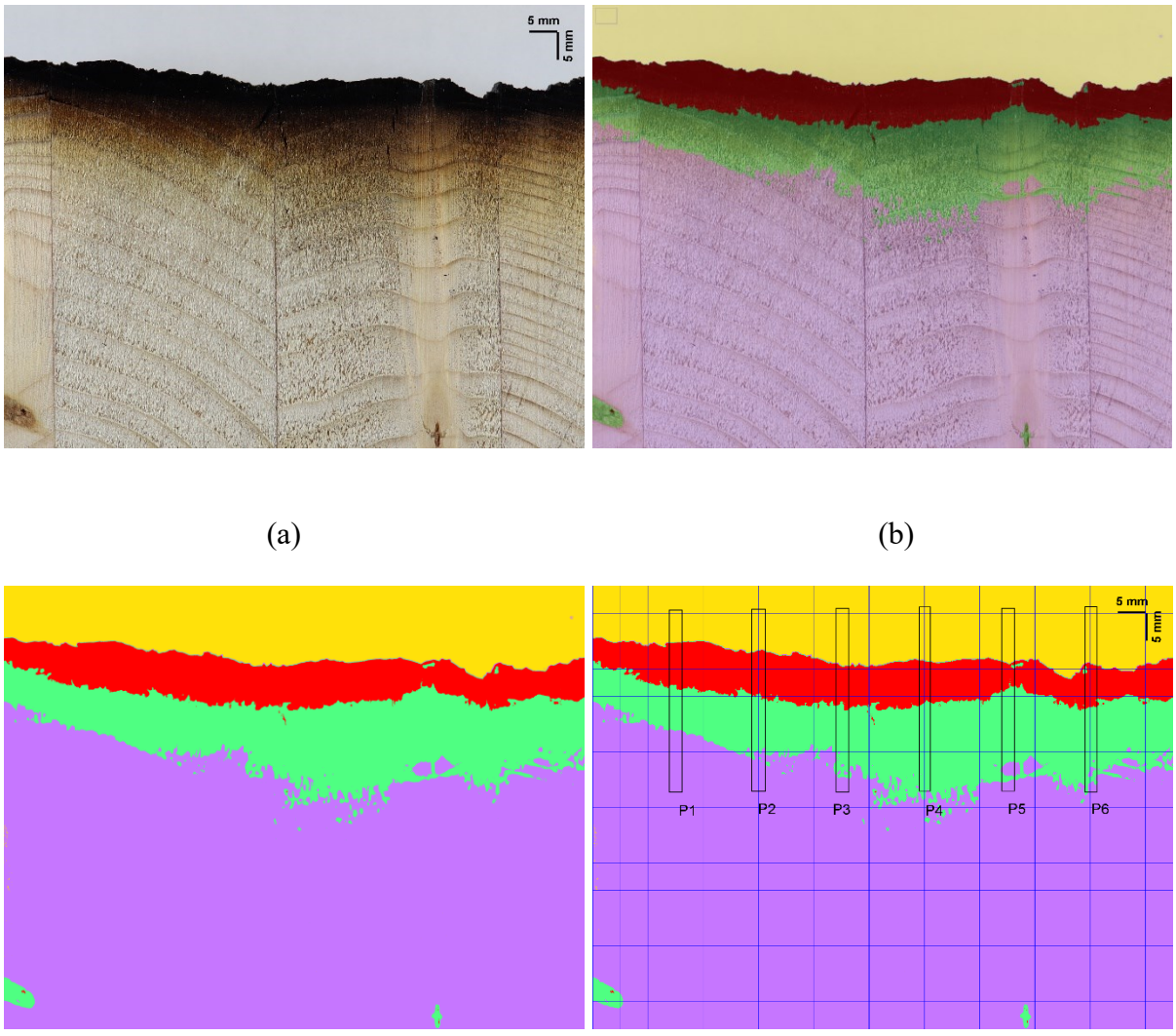

(a) (b)

(c) (d)

Figure C-11 Images of S2-4 prior and after segmentation: (a) Original image (b) Classified image (c) Toggle overlay image (d) Classified Image with grid and points

Sample S2-5

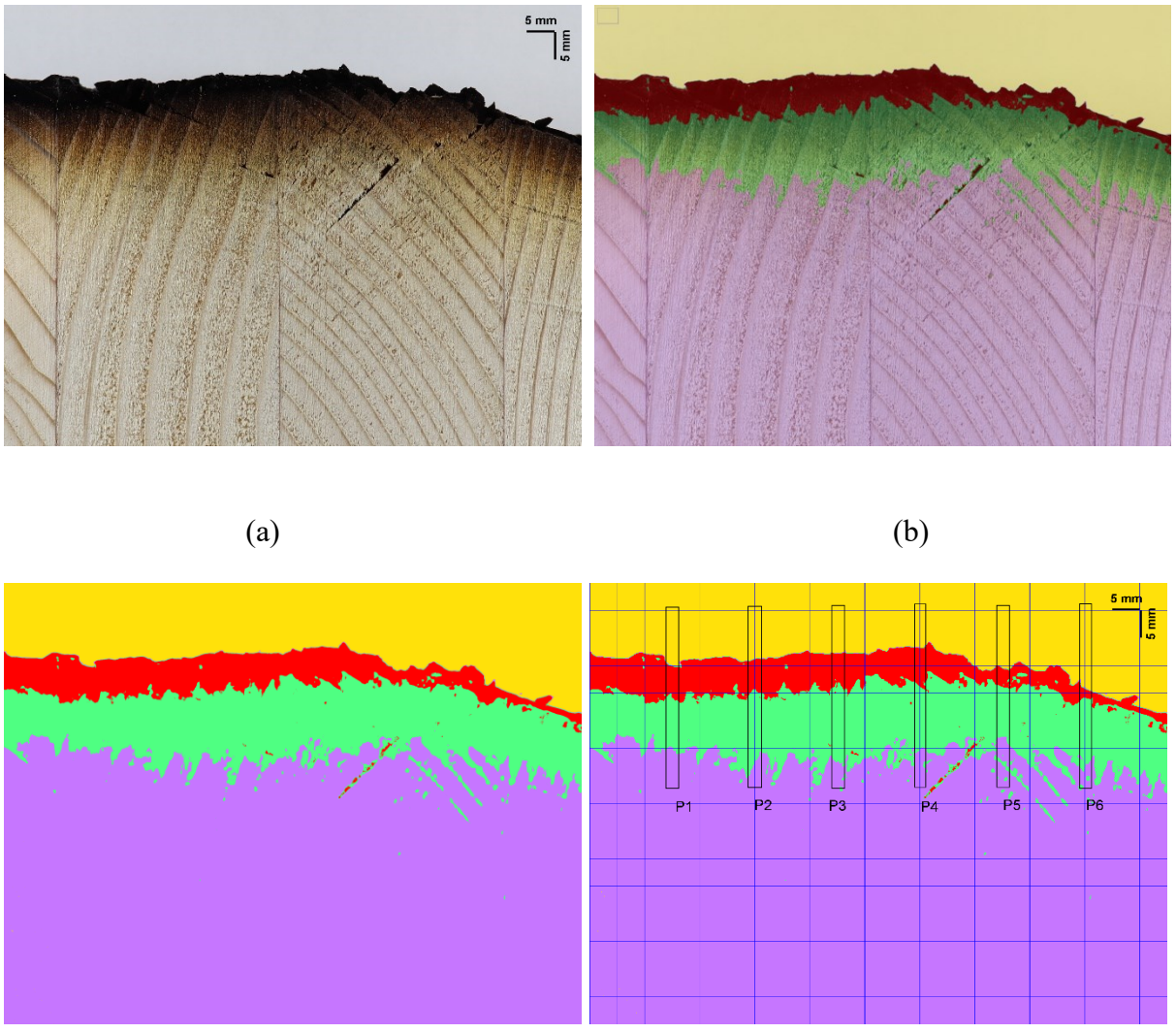

(a) (b)

(c) (d)

Figure C-12 Images of S2-5 prior and after segmentation: (a) Original image (b) Classified image (c) Toggle overlay image (d) Classified Image with grid and points

Specimen Slice S3

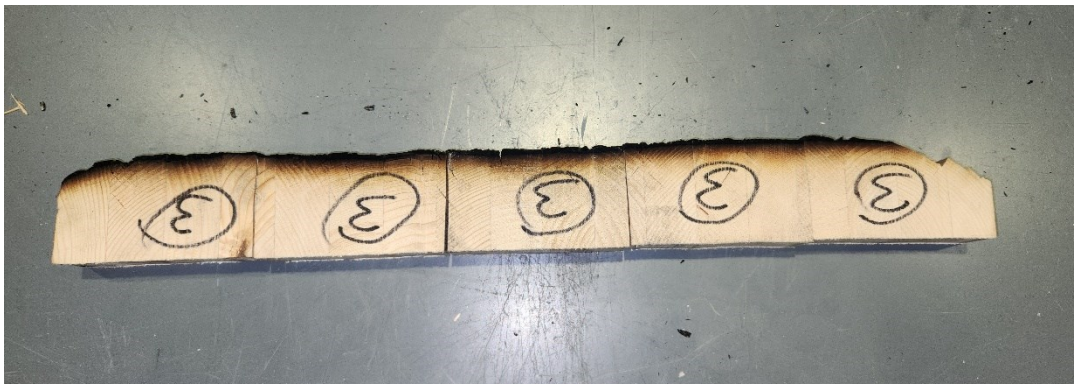

Figure C-13 Specimen slice S3

Sample S3-1

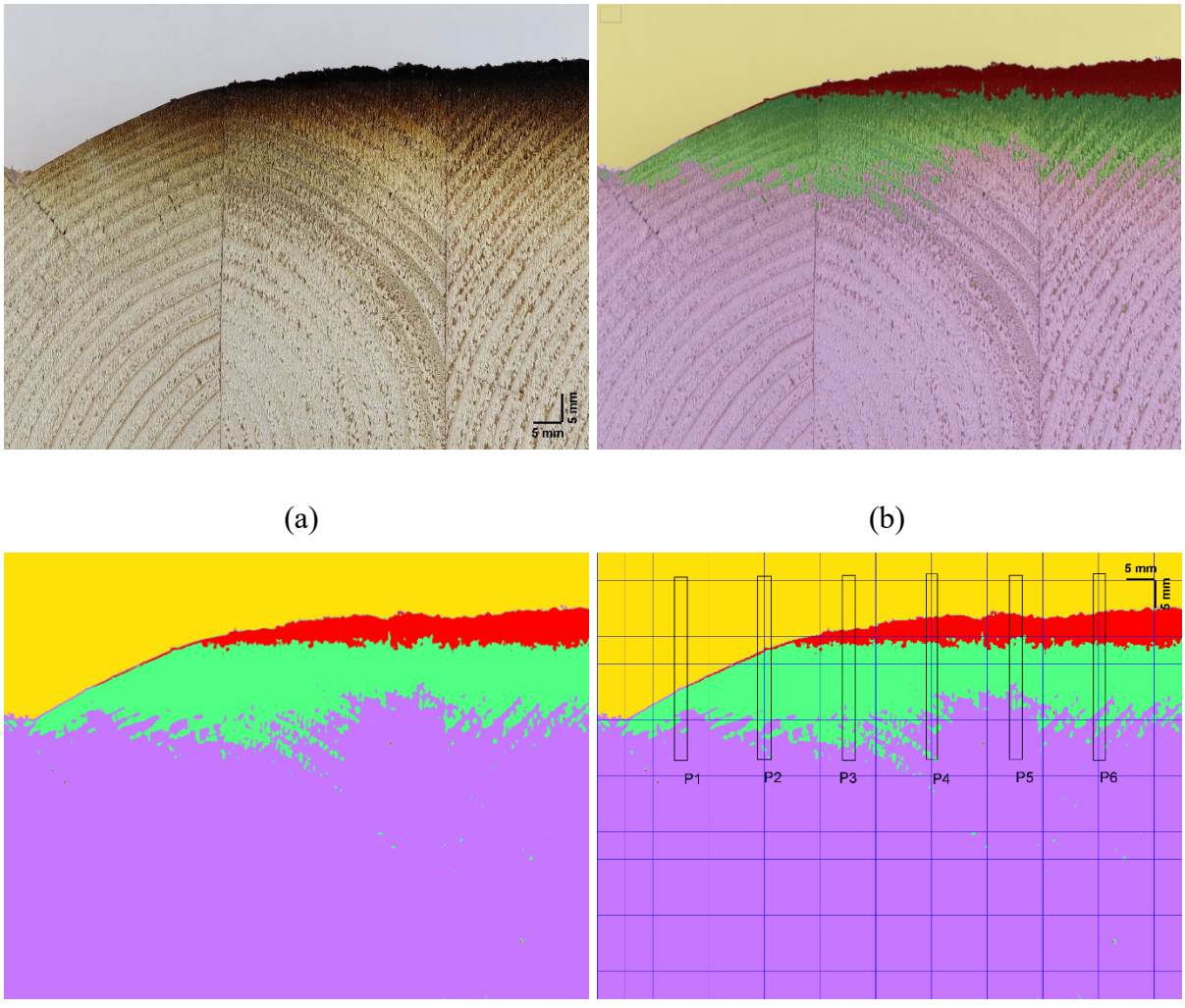

(a) (b)

(c) (d)

Figure C-14 Images of S3-1 prior and after segmentation: (a) Original image (b) Classified image (c) Toggle overlay image (d) Classified Image with grid and points

Sample S3-1

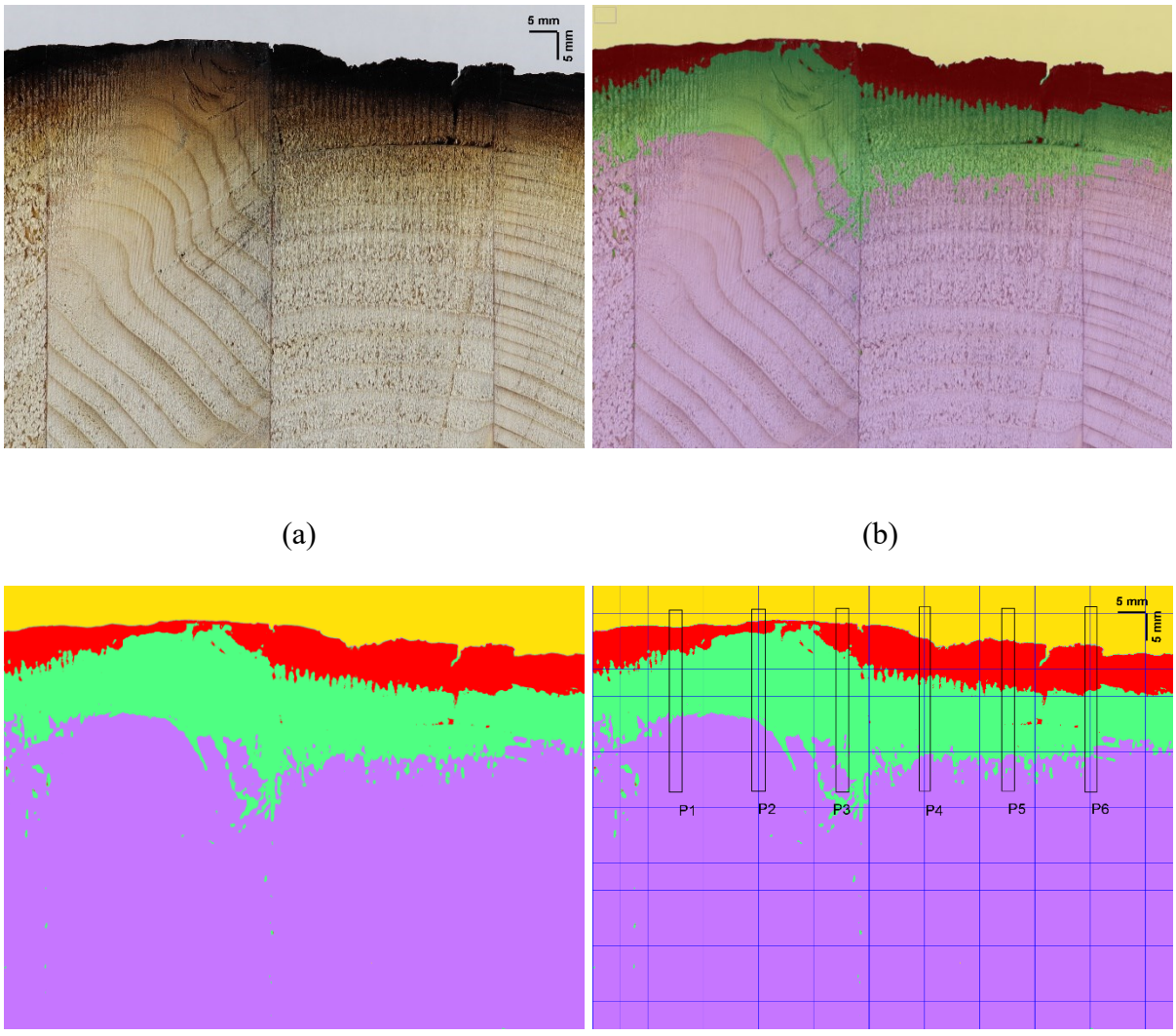

(a) (b)

(c) (d)

Figure C-15 Images of S3-2 prior and after segmentation: (a) Original image (b) Classified image (c) Toggle overlay image (d) Classified Image with grid and points

Sample S3-3

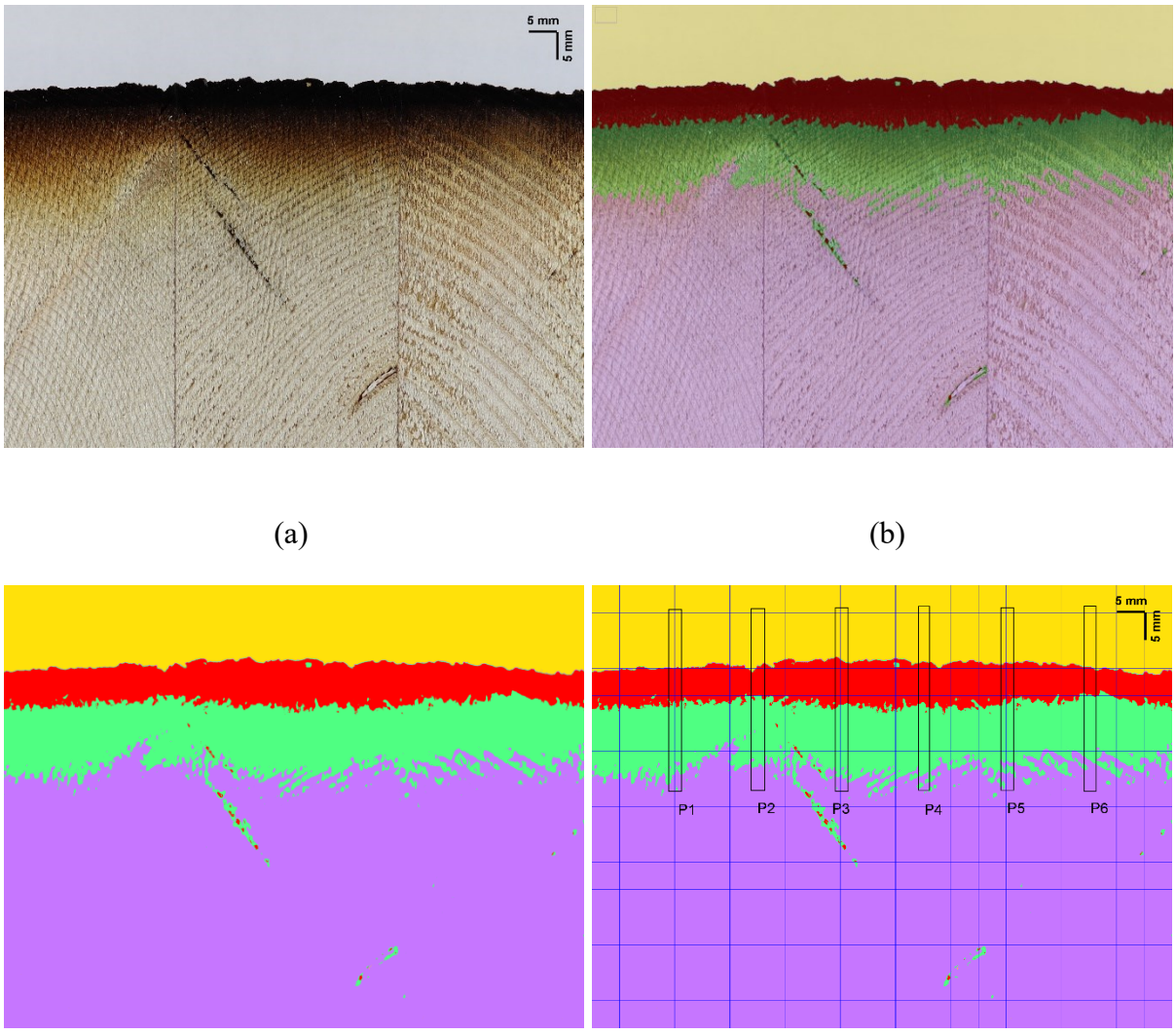

(a) (b)

(c) (d)

Figure C-16 Images of S3-3 prior and after segmentation: (a) Original image (b) Classified image (c) Toggle overlay image (d) Classified Image with grid and points

Sample S3-4

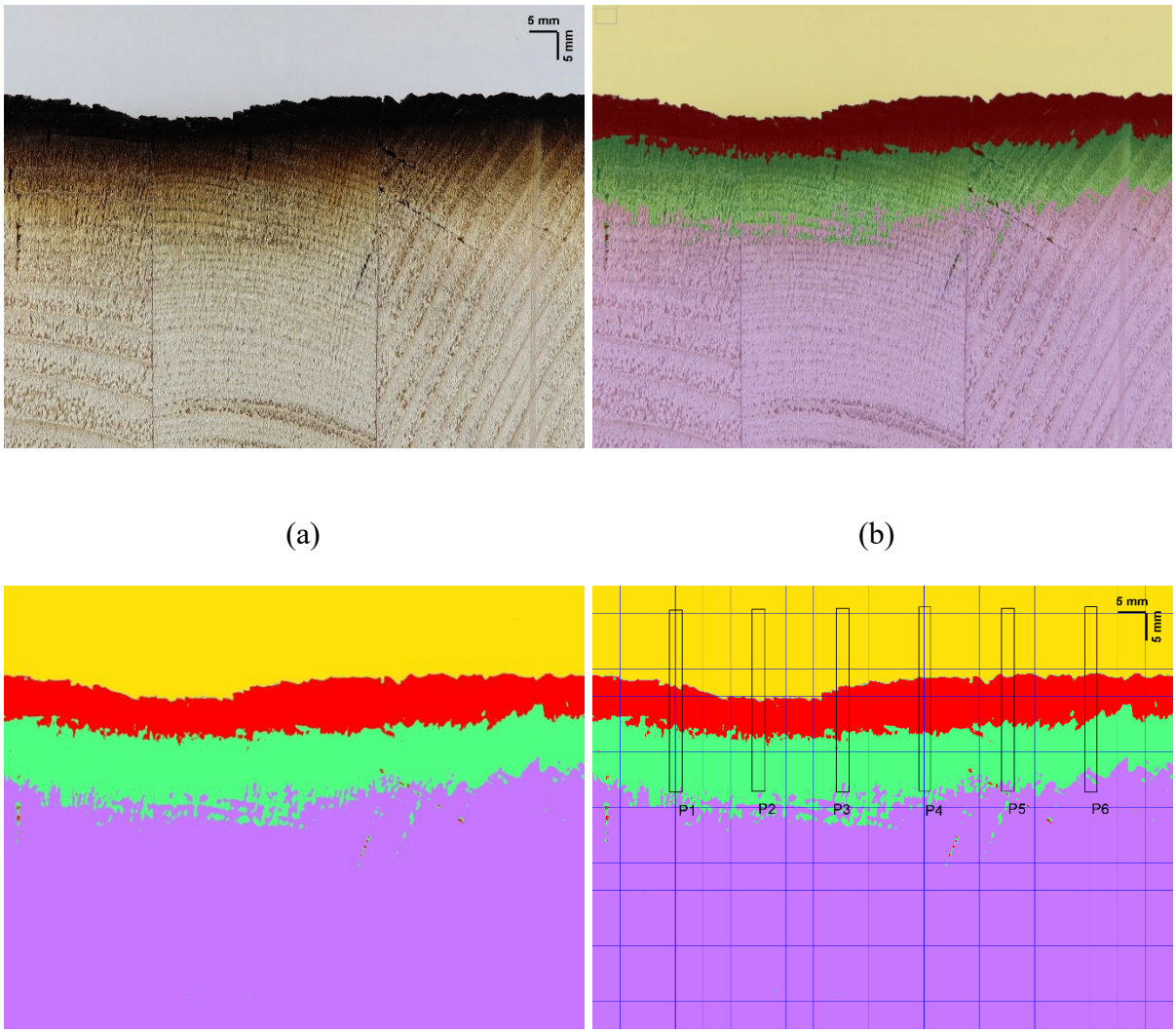

(a) (b)

(c) (d)

Figure C-17 Images of S3-4 prior and after segmentation: (a) Original image (b) Classified image (c) Toggle overlay image (d) Classified Image with grid and points

Sample S3-5

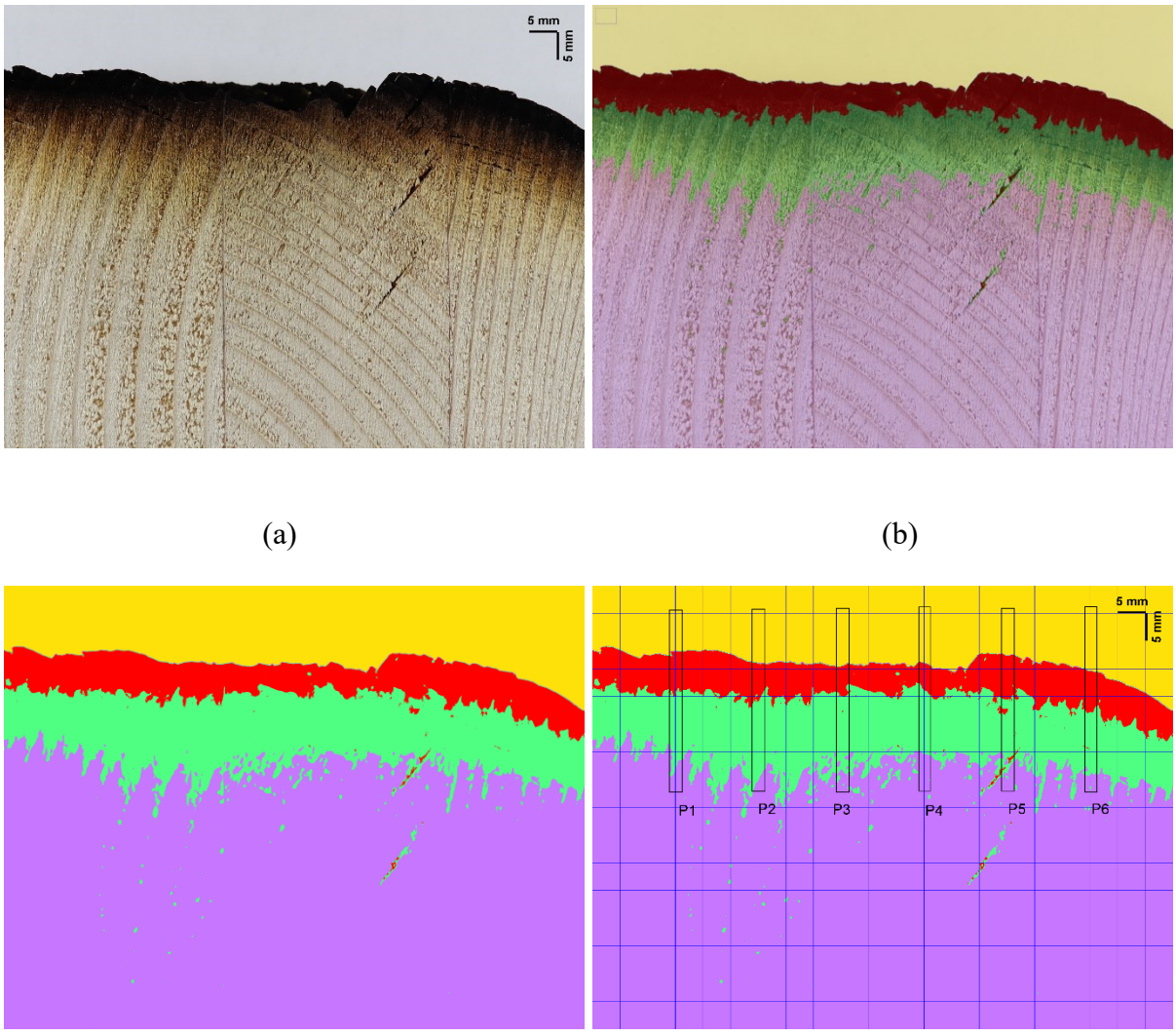

(a) (b)

(c) (d)

Figure C-18 Images of S3-5 prior and after segmentation: (a) Original image (b) Classified image (c) Toggle overlay image (d) Classified Image with grid and points

Specimen Slice S4

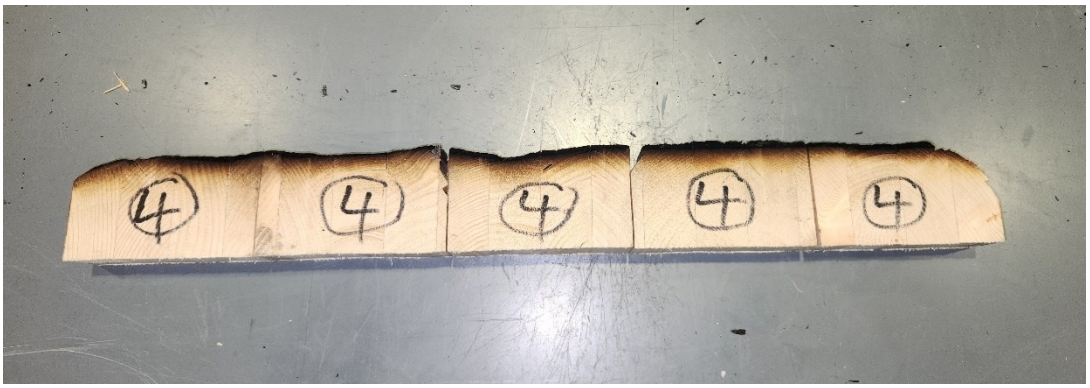

Figure C-19 Specimen slice S4

Sample S4-1

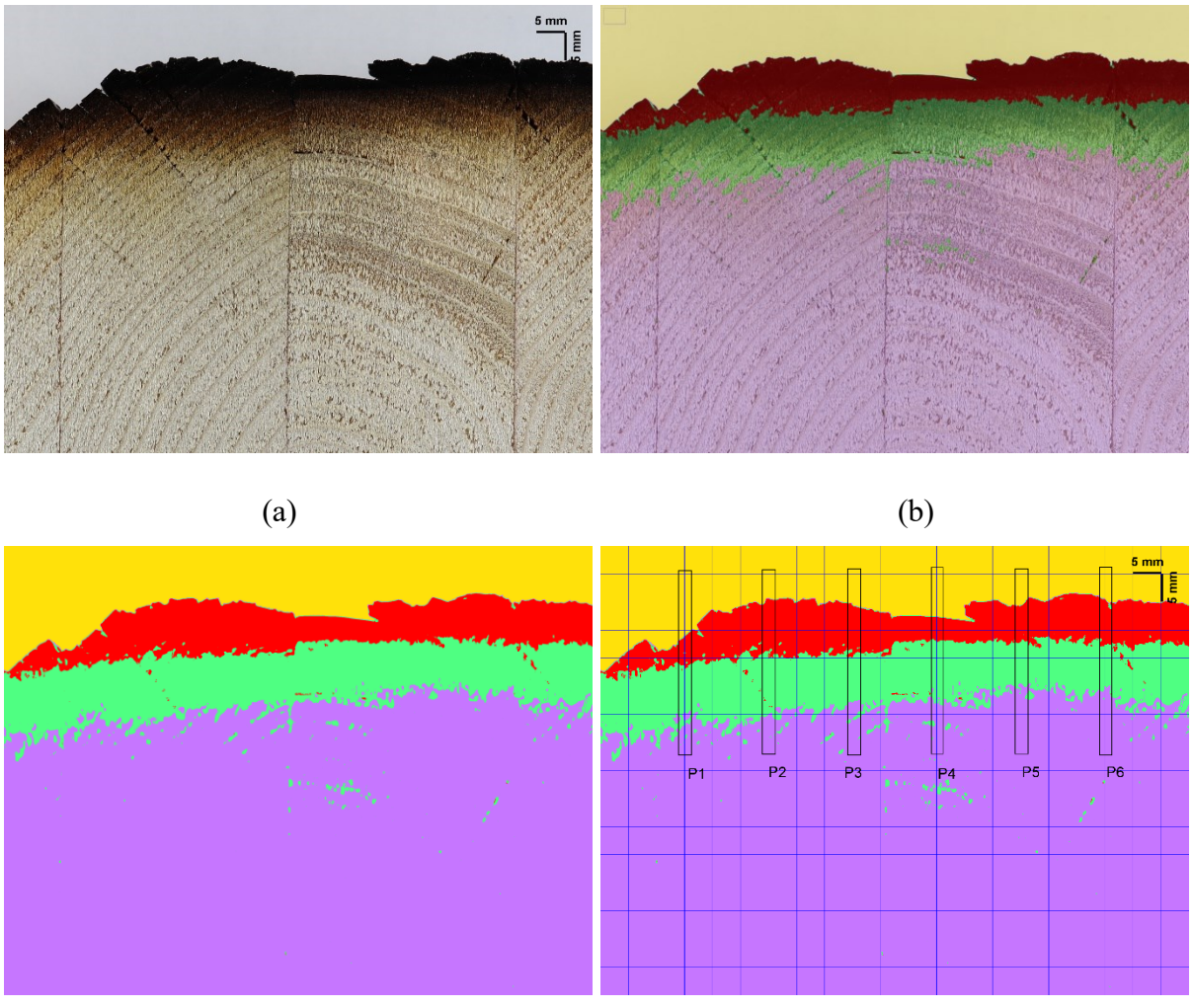

(a) (b)

(c) (d)

Figure C-20 Images of S4-1 prior and after segmentation: (a) Original image (b) Classified image (c) Toggle overlay image (d) Classified Image with grid and points

Sample S4-2

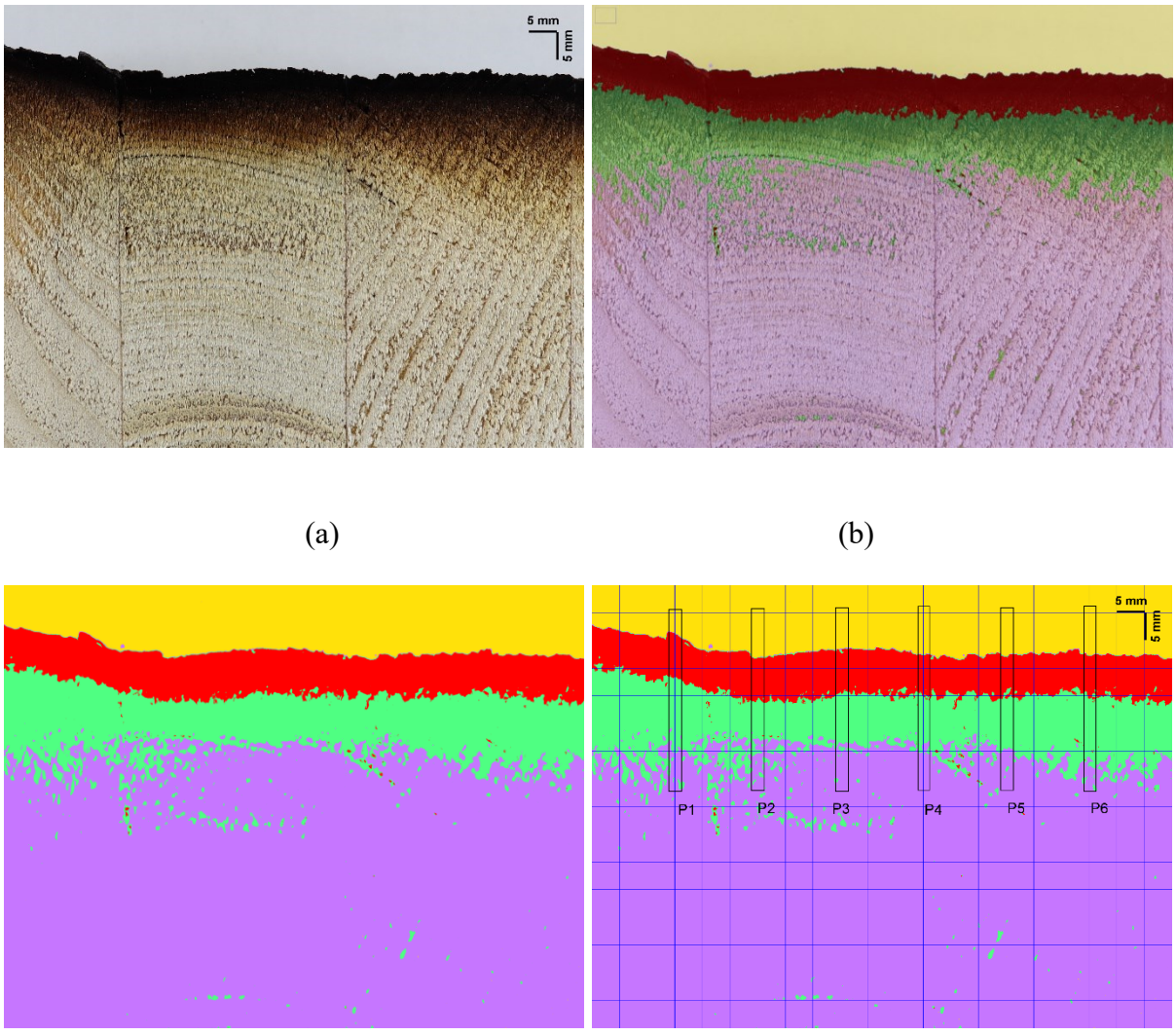

(a) (b)

(c) (d)

Figure C-21 Images of S4-2 prior and after segmentation: (a) Original image (b) Classified image (c) Toggle overlay image (d) Classified Image with grid and points

Sample S4-3

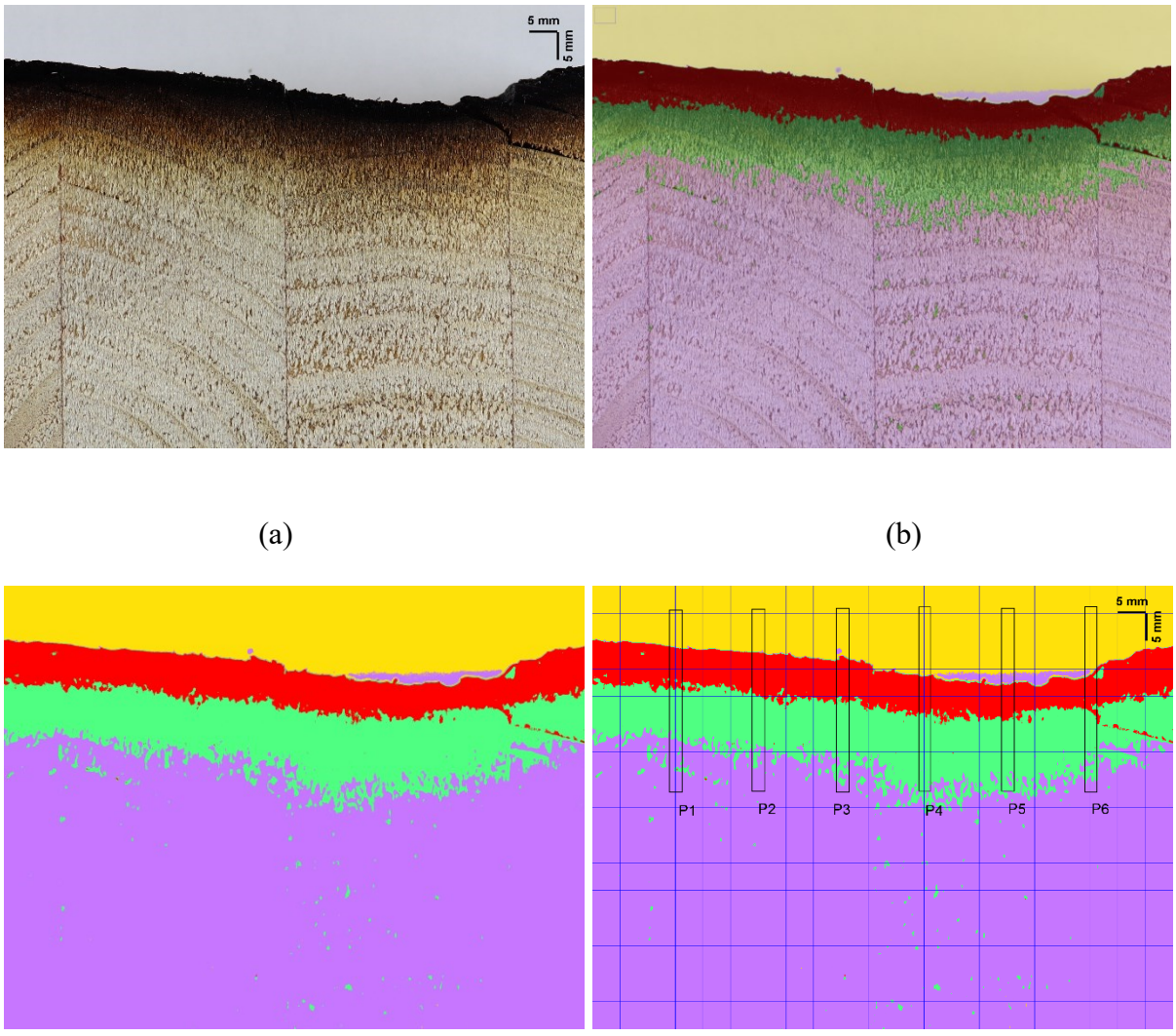

(a) (b)

(c) (d)

Figure C-22 Images of S4-3 prior and after segmentation: (a) Original image (b) Classified image (c) Toggle overlay image (d) Classified Image with grid and points

Sample S4-4

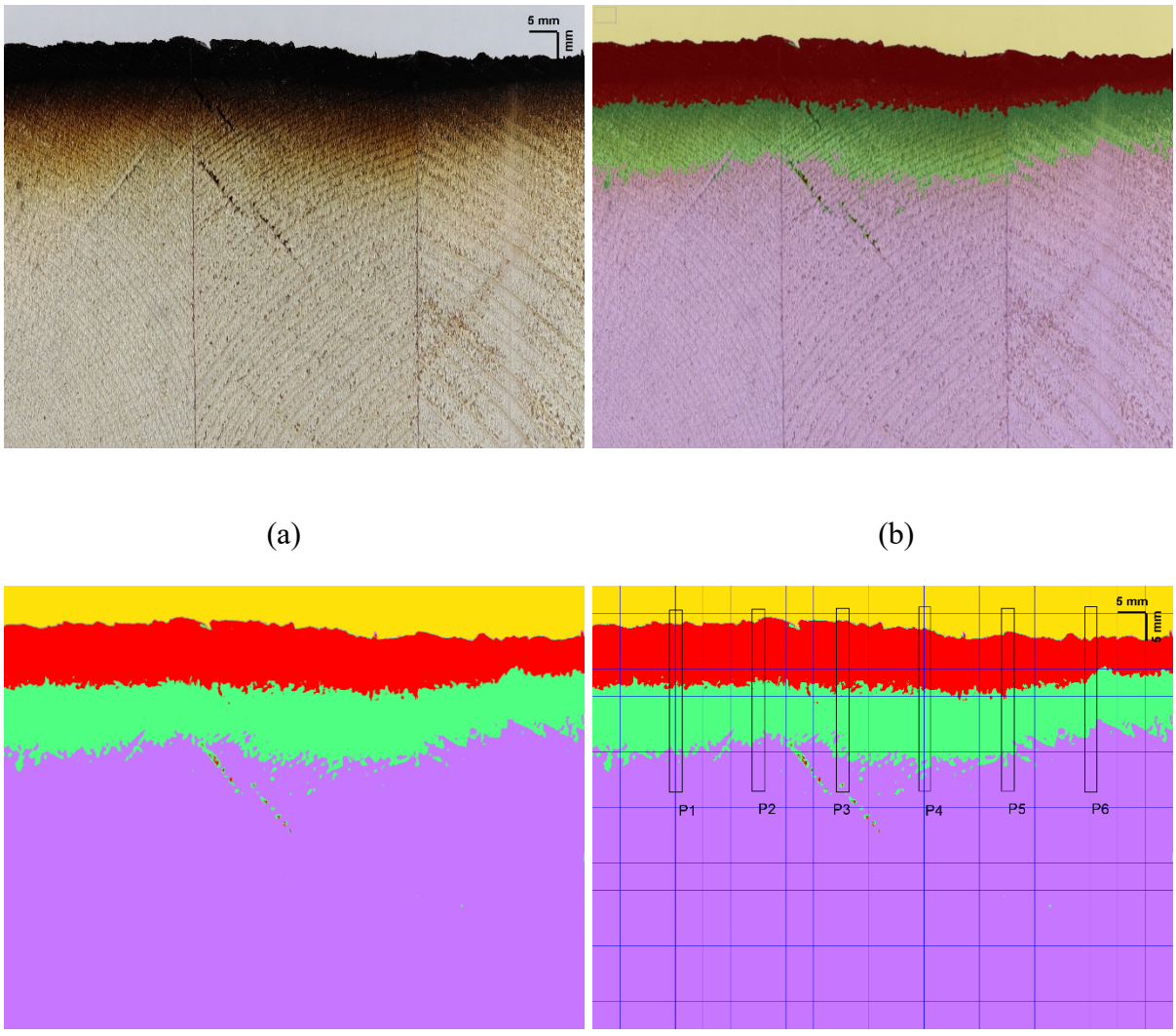

(a) (b)

(c) (d)

Figure C-23 Images of S4-4 prior and after segmentation: (a) Original image (b) Classified image (c) Toggle overlay image (d) Classified Image with grid and points

Sample S4-5

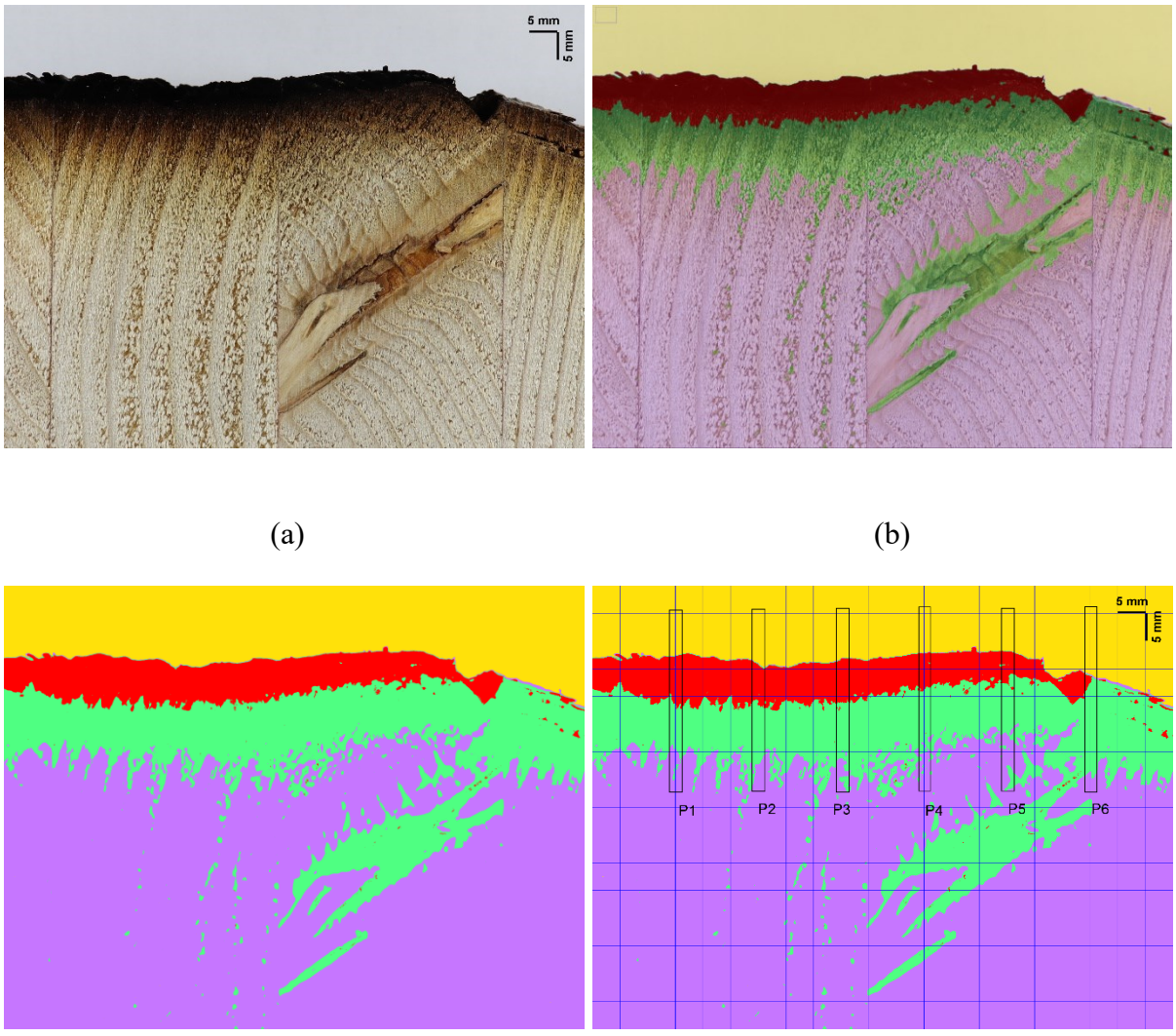

(a) (b)

(c) (d)

Figure C-24 Images of S4-5 prior and after segmentation: (a) Original image (b) Classified image (c) Toggle overlay image (d) Classified Image with grid and points

Specimen Slice S5

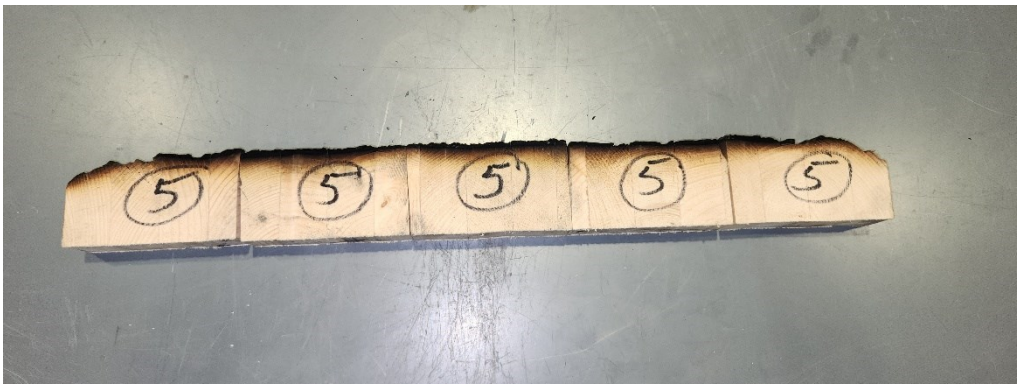

Figure C-25 Specimen slice S5

Sample S5-1

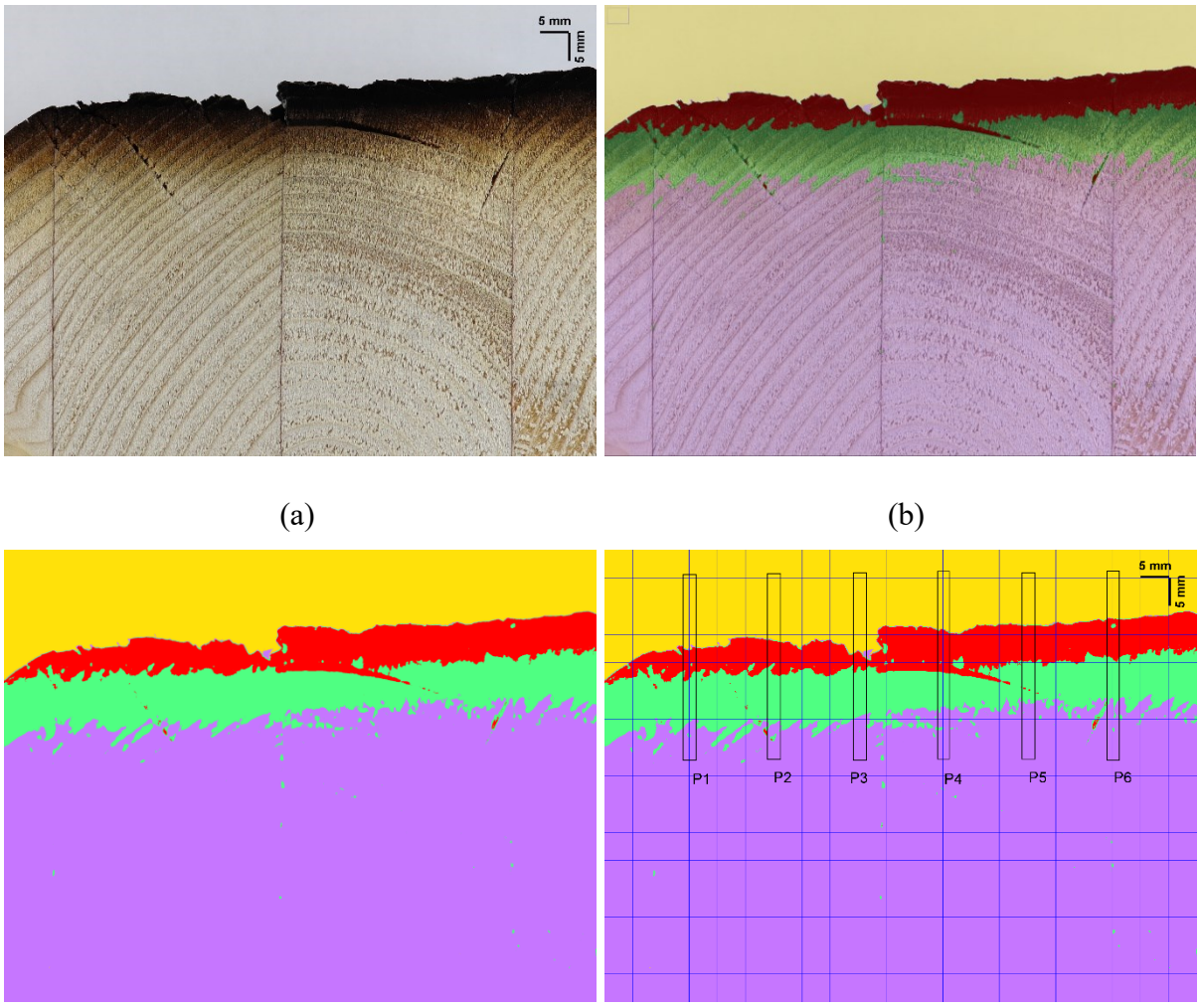

(a) (b)

(c) (d)

Figure C-26 Images of S5-1 prior and after segmentation: (a) Original image (b) Classified image (c) Toggle overlay image (d) Classified Image with grid and points

Sample S5-2

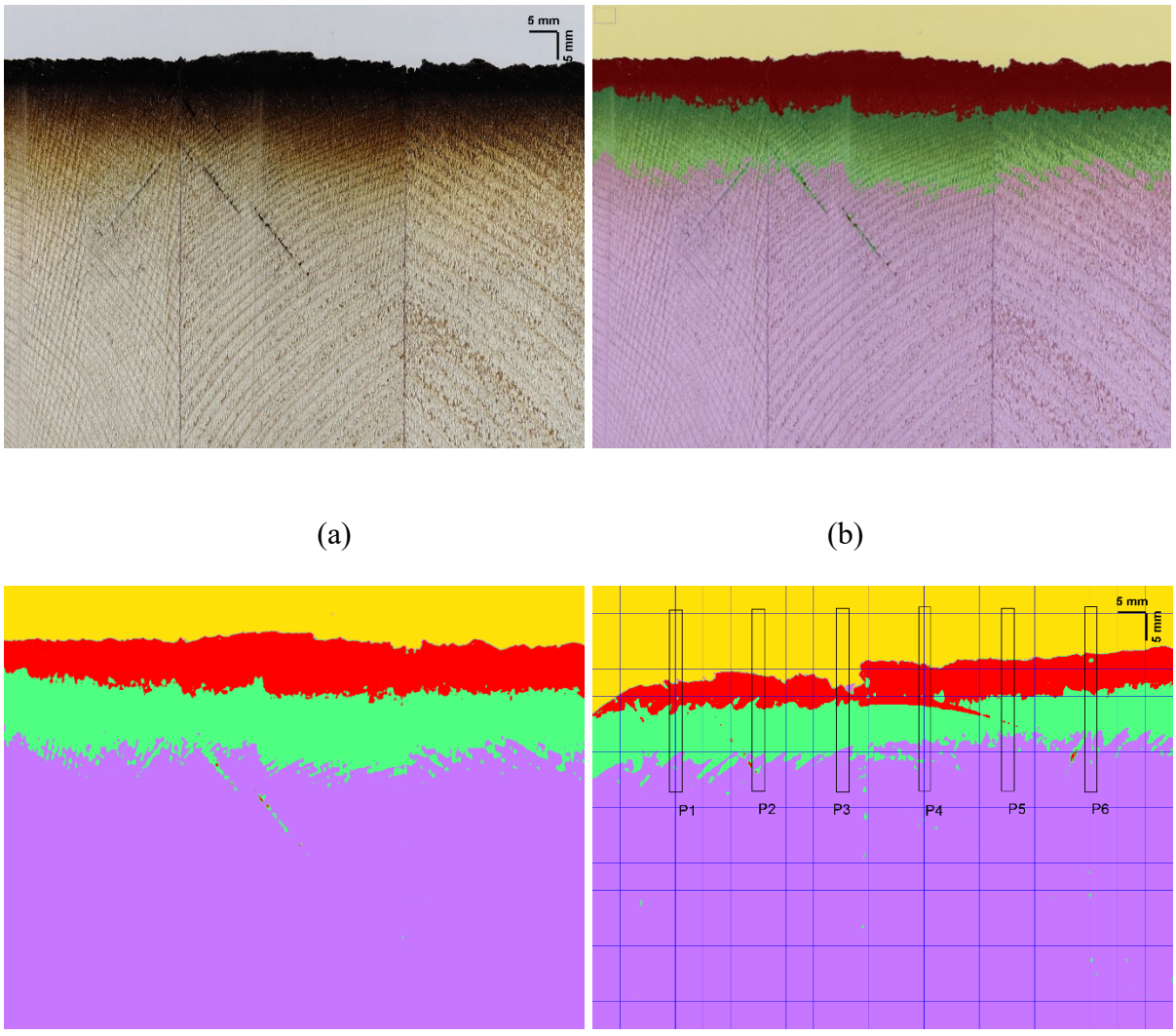

(a) (b)

(c) (d)

Figure C-27 Images of S5-2 prior and after segmentation: (a) Original image (b) Classified image (c) Toggle overlay image (d) Classified Image with grid and points

Sample S5-3

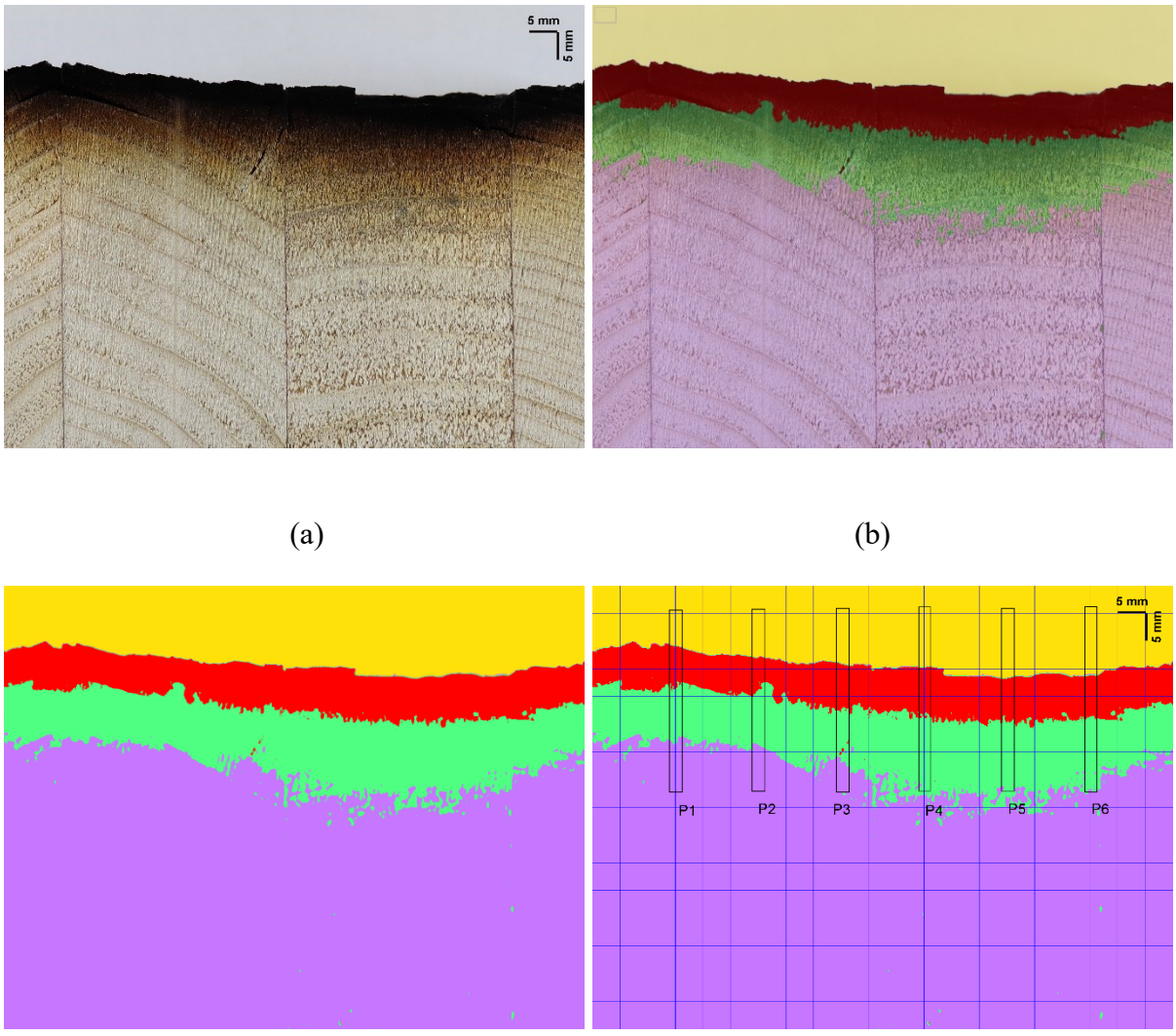

(a) (b)

(c) (d)

Figure C-28 Images of S5-3 prior and after segmentation: (a) Original image (b) Classified image (c) Toggle overlay image (d) Classified Image with grid and points

Sample S5-4

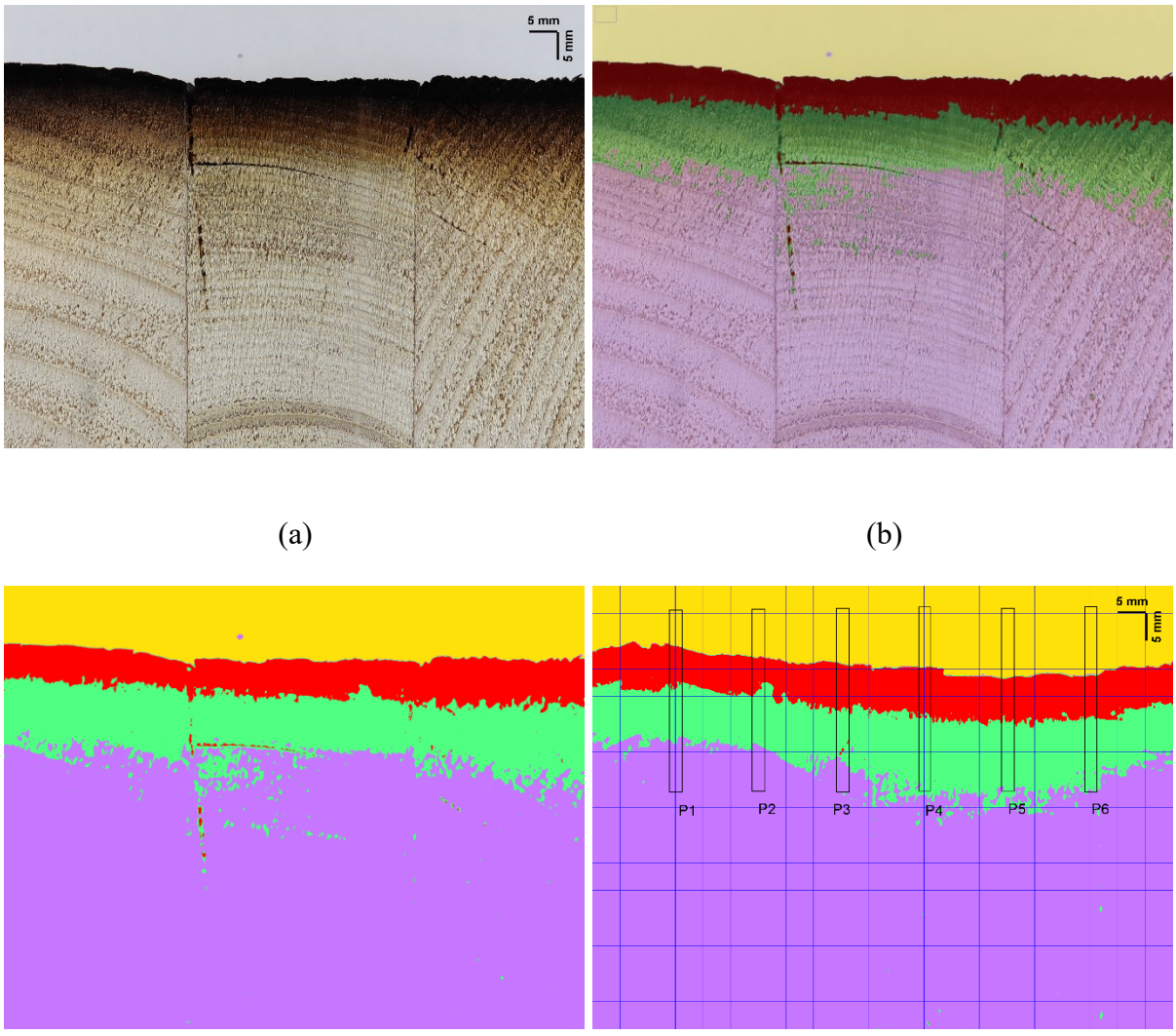

(a) (b)

(c) (d)

Figure C-29 Images of S5-4 prior and after segmentation: (a) Original image (b) Classified image (c) Toggle overlay image (d) Classified Image with grid and points

Sample S5-5

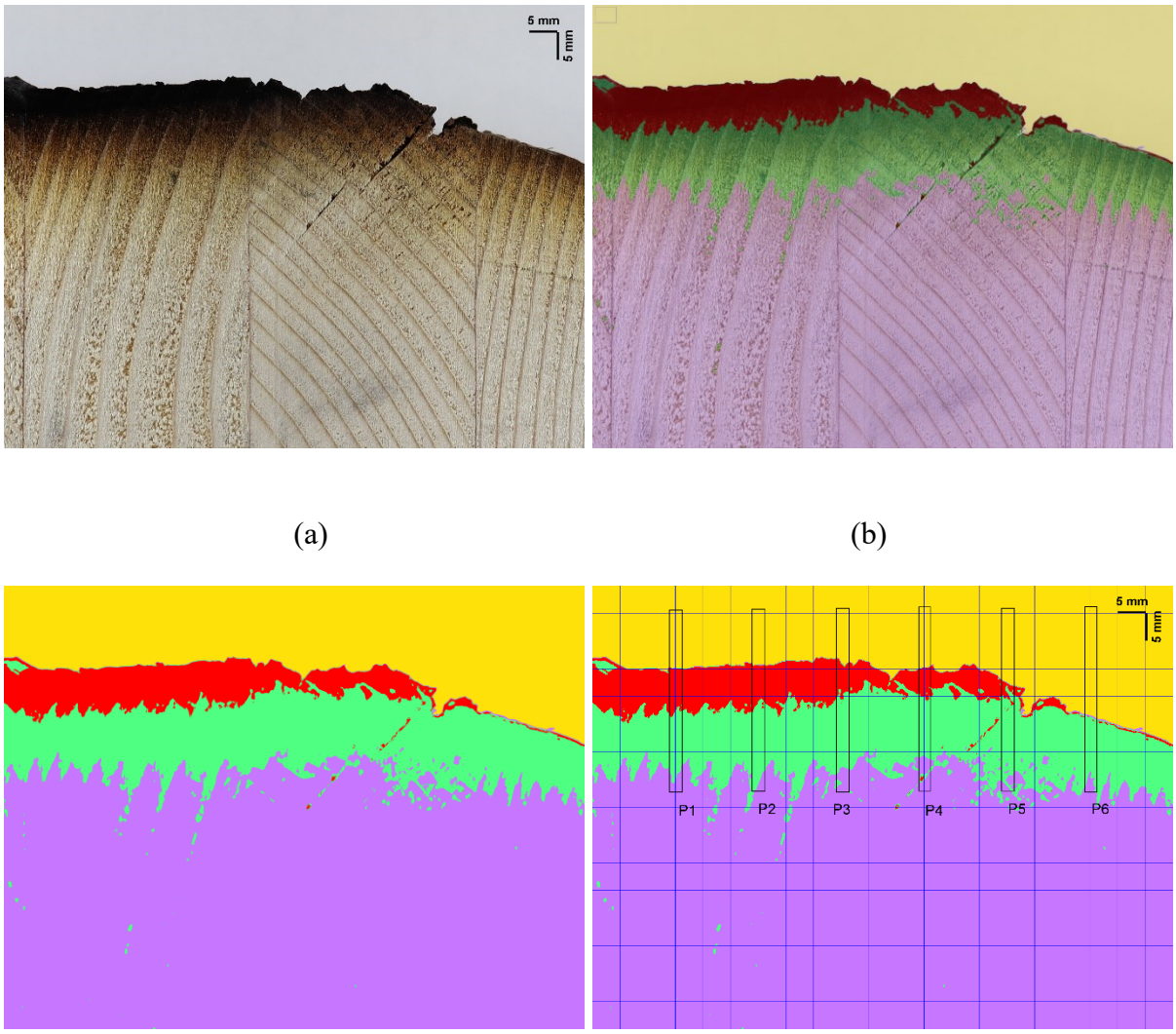

(a) (b)

(c) (d)

Figure C-30 Images of S5-5 prior and after segmentation: (a) Original image (b) Classified image (c) Toggle overlay image (d) Classified Image with grid and points

Appendix D: Static Tests Results

Specimen GLT1 [130]

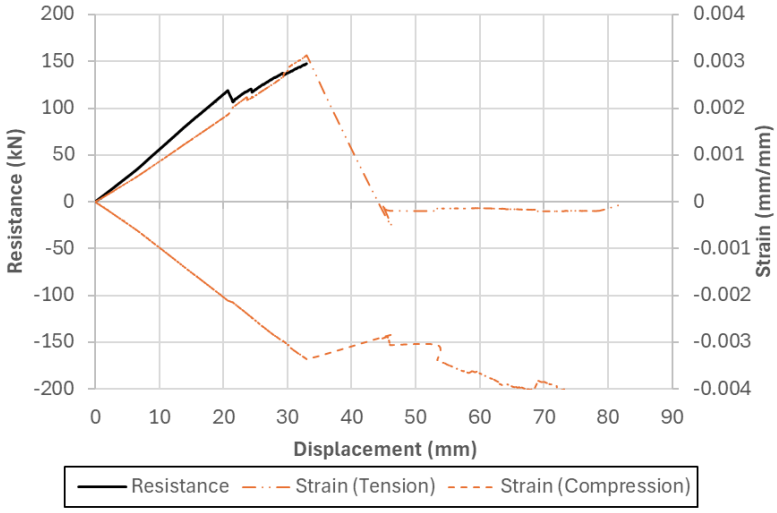

Figure D-1 GLT1 [130] resistance- and strain-displacement results

(a)

(b)

Figure D-2 GLT1 [130] static failure mode: (a) side view (b) bottom view

Specimen GLT2 [130]

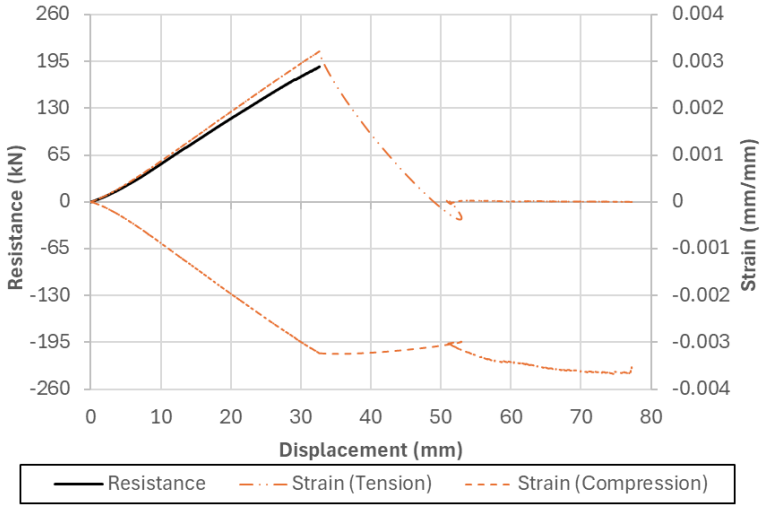

Figure D-3 GLT2 [130] resistance- and strain-displacement results

(a)

(b)

Figure D-4 GLT2 [130] static failure mode: (a) side view (b) bottom view

Specimen GLT3 [130]

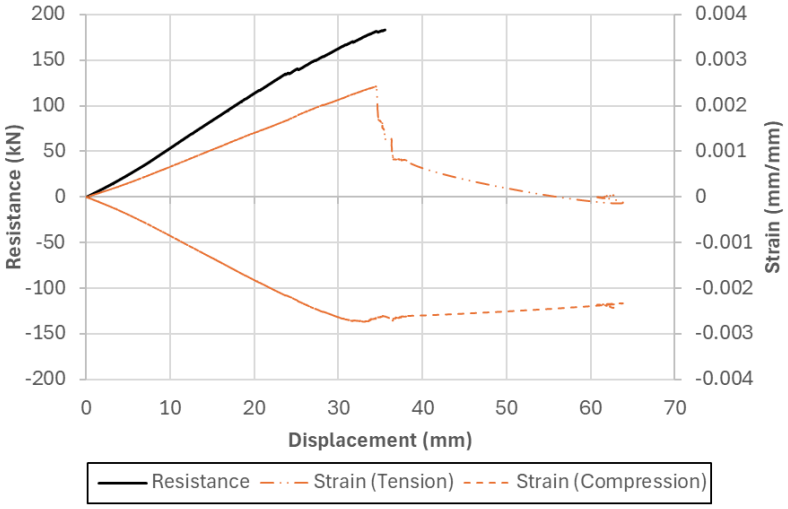

Figure D-5 GLT3 [130] resistance- and strain-displacement results

(a)

(b)

Figure D-6 GLT3 [130] static failure mode: (a) side view (b) bottom view

Specimen GLT4 [215]

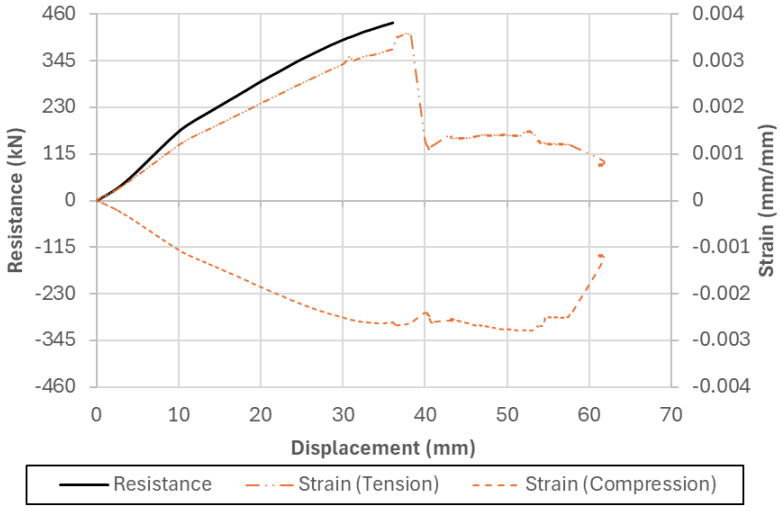

Figure D-7 GLT4 [215] resistance- and strain-displacement results

(a)

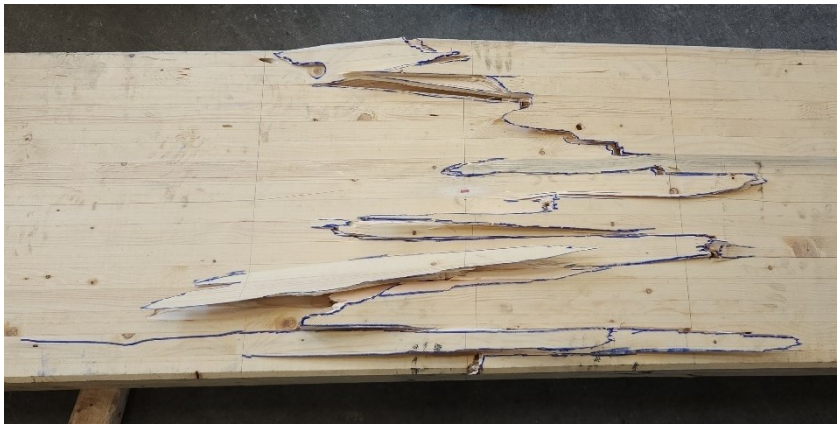

(b)

Figure D-8 GLT4 [215] static failure mode: (a) side view (b) bottom view

Specimen GLT5 [215]

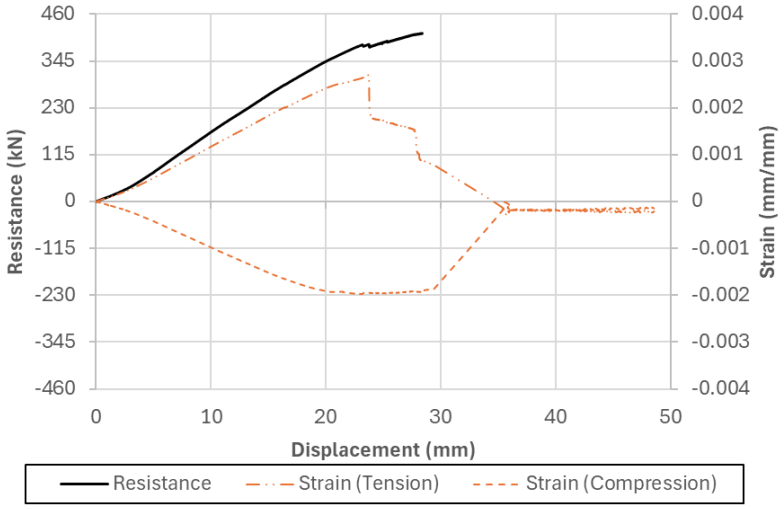

Figure D-9 GLT5 [215] resistance- and strain-displacement results

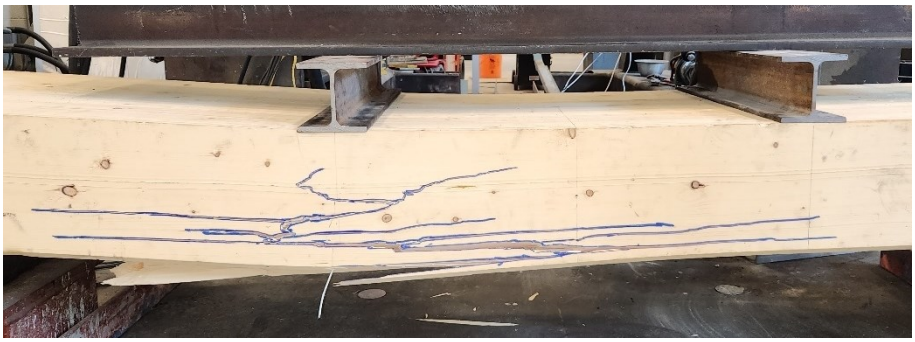

(a)

(b)

Figure D-10 GLT5 [215] static failure mode: (a) side view (b) bottom view

Specimen GLT6 [215]

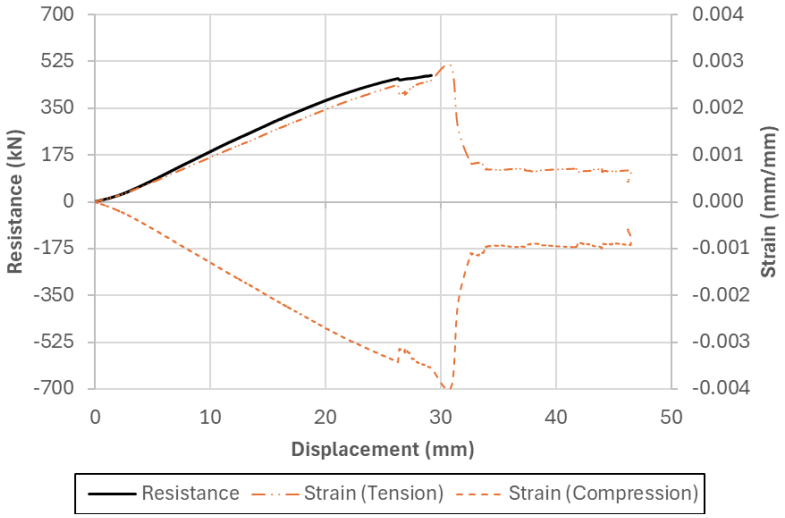

Figure D-11 GLT6 [215] resistance- and strain-displacement results

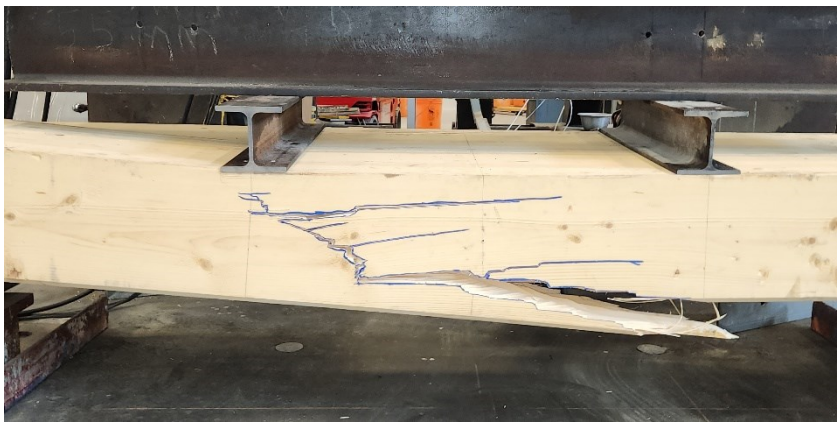

(a)

(b)

Figure D-12 GLT6 [215] static failure mode: (a) side view (b) bottom view

Specimen GLT7 [215]

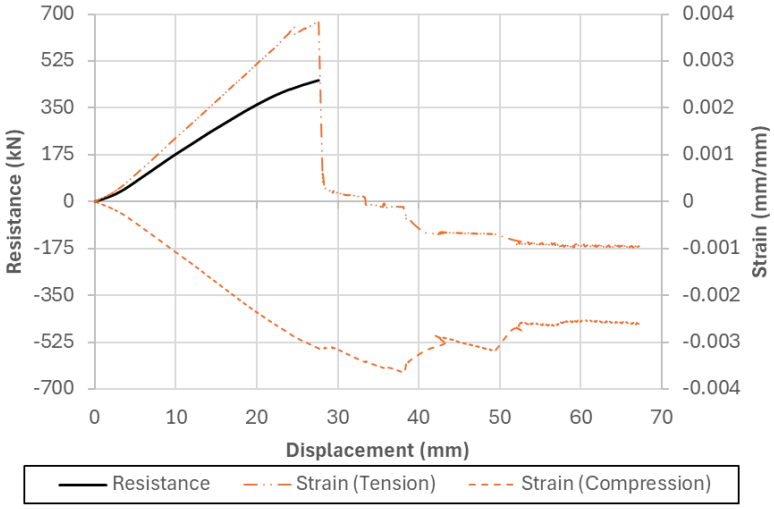

Figure D-13 GLT7 [215] resistance- and strain-displacement results

(a)

(b)

Figure D-14 GLT7 [215] static failure mode: (a) side view (b) bottom view

Specimen CGLT1 [215]

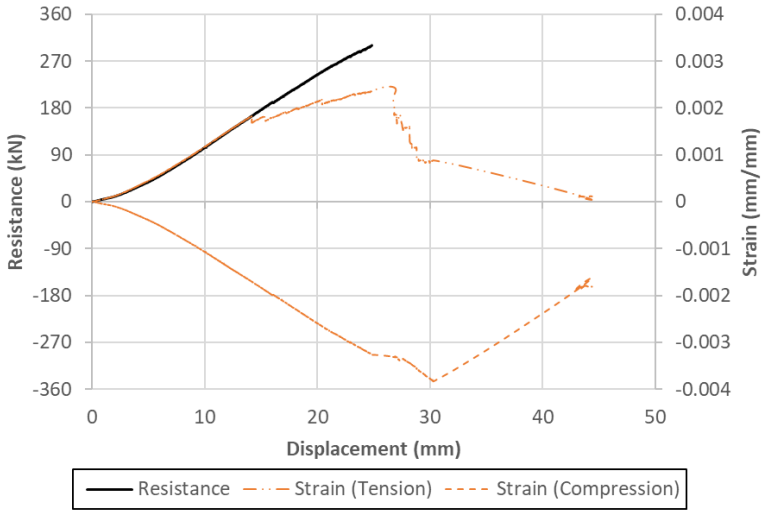

Figure D-15 CGLT1 [215] resistance- and strain-displacement results

(a)

(b)

Figure D-16 CGLT1 [215] static failure mode: (a) side view (b) bottom view

Specimen CGLT2 [215]

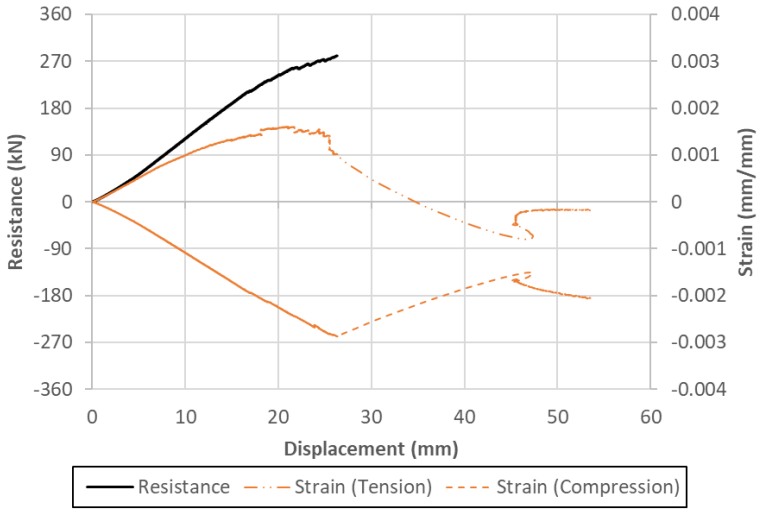

Figure D-17 CGLT2 [215] resistance- and strain-displacement results

(a)

(b)

Figure D-18 CGLT2 [215] static failure mode: (a) side view (b) bottom view

Specimen CGLT3 [215]

Figure D-19 CGLT3 [215] resistance- and strain-displacement results

(a)

(b)

Figure D-20 CGLT3 [215] static failure mode: (a) side view (b) bottom view

Specimen CGLT4 [215]

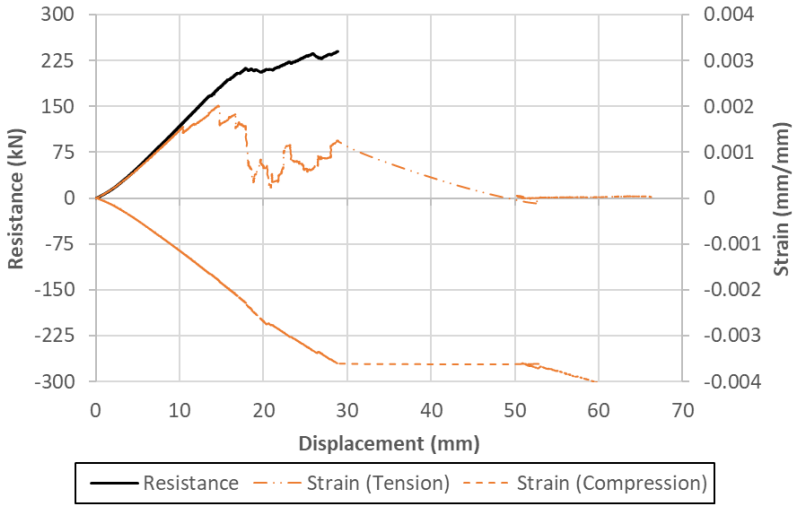

Figure D-21 CGLT4 [215] resistance- and strain-displacement results

(a)

(b)

Figure D-22 CGLT4 [215] static failure mode: (a) side view (b) bottom view

Appendix E: Dynamic Tests Results

Specimen GLT8 [130]

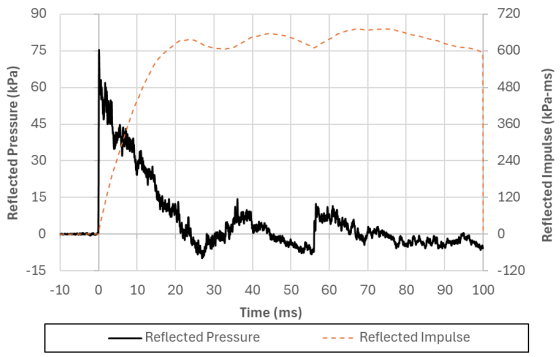

(a)

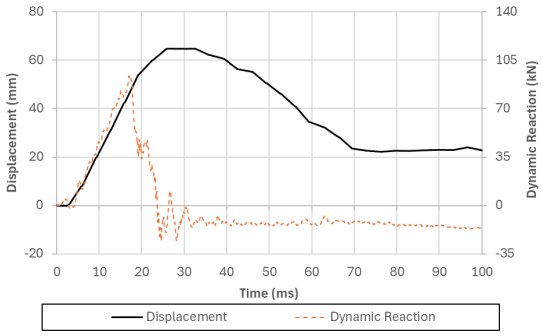

(b)

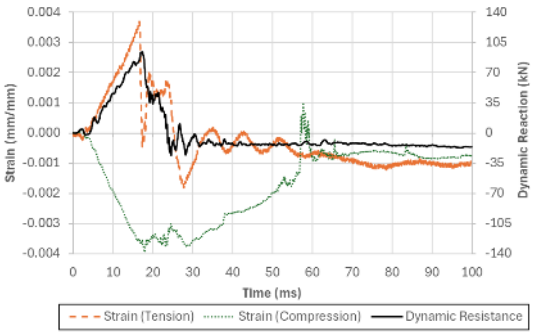

(c)

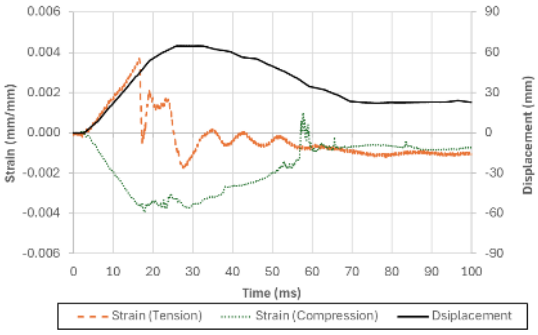

(d)

Figure E-1 Dynamic test results of GLT8 [130]: (a) Pressure- and impulse-time histories; (b) Displacement- Dynamic reaction histories; (c) Dynamic reaction-strain histories; (d) Displacement-strain histories

Specimen GLT9 [130]

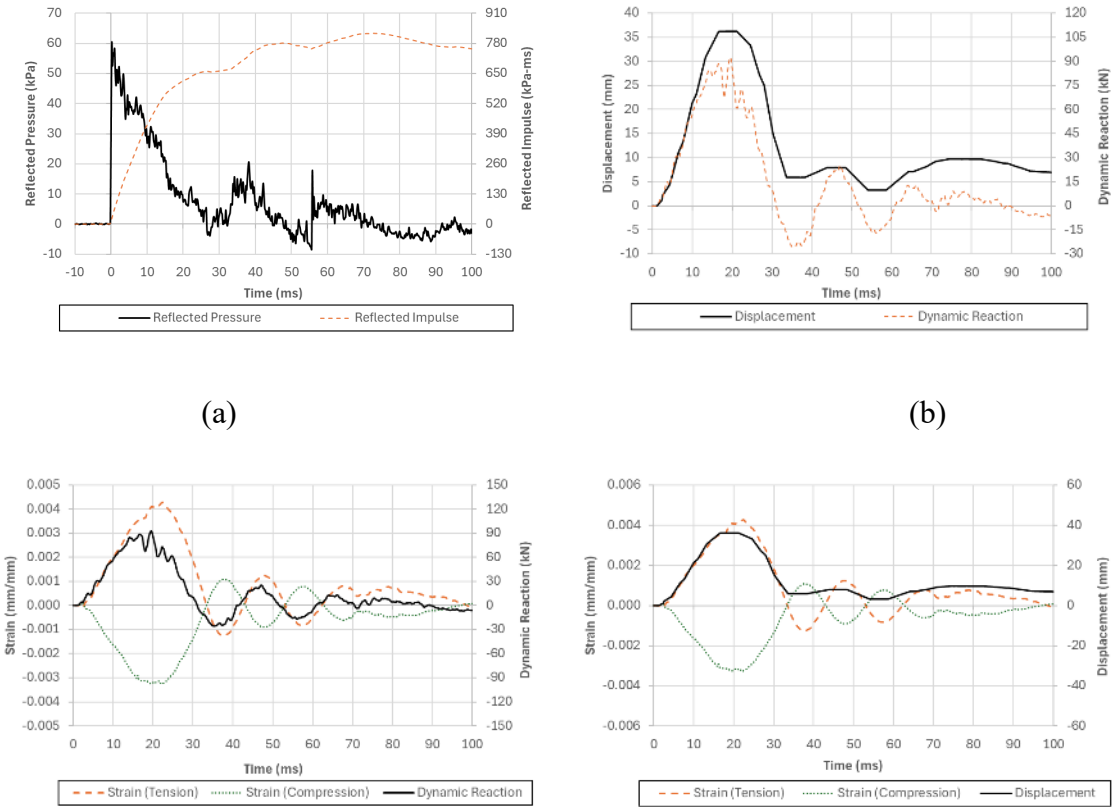

Figure E-2 Dynamic test results of GLT9 [130]: (a) Pressure- and impulse-time histories; (b) Displacement- Dynamic reaction histories; (c) Dynamic reaction-strain histories; (d) Displacement-strain histories

Specimen GLT10 [130]

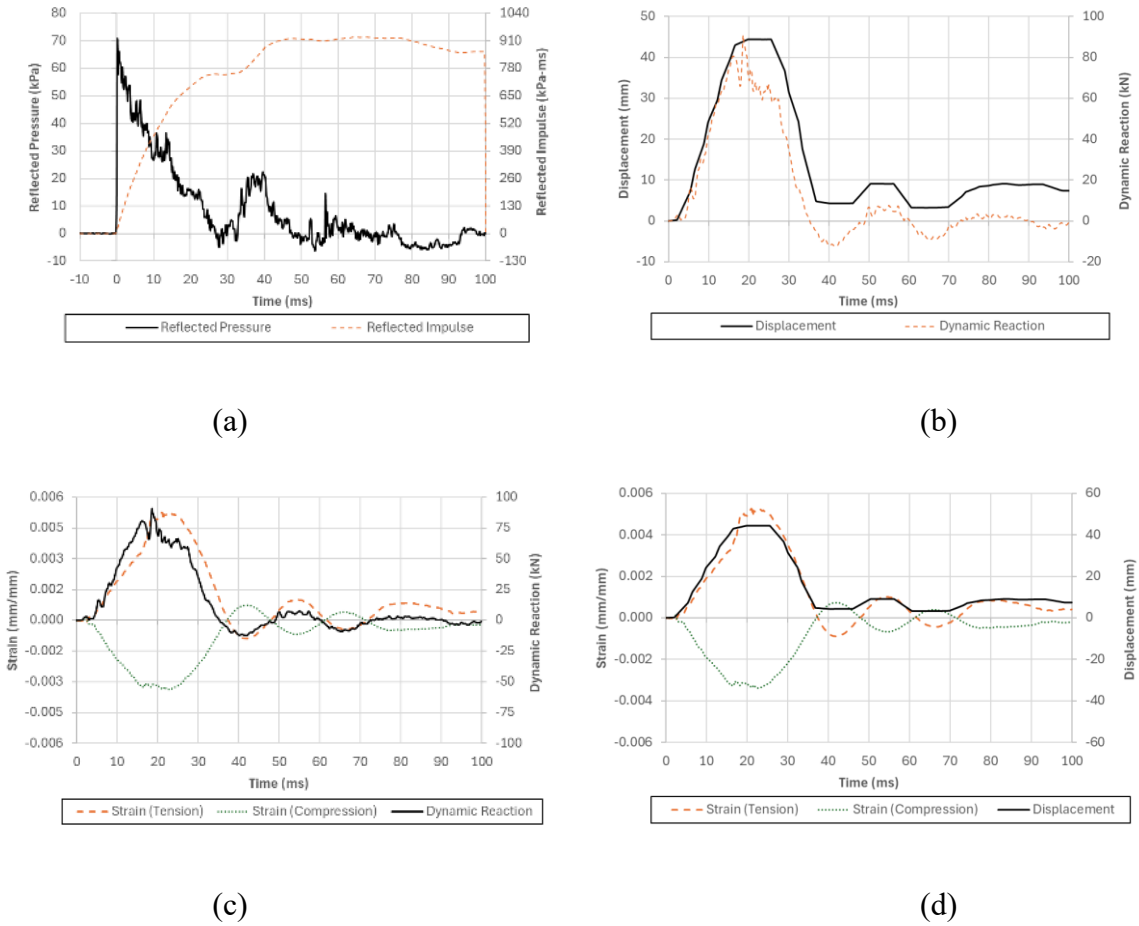

Figure E-3 Dynamic test results of GLT10 [130]: (a) Pressure- and impulse-time histories; (b) Displacement- Dynamic reaction histories; (c) Dynamic reaction-strain histories; (d) Displacement-strain histories

Specimen GLT11 [130]

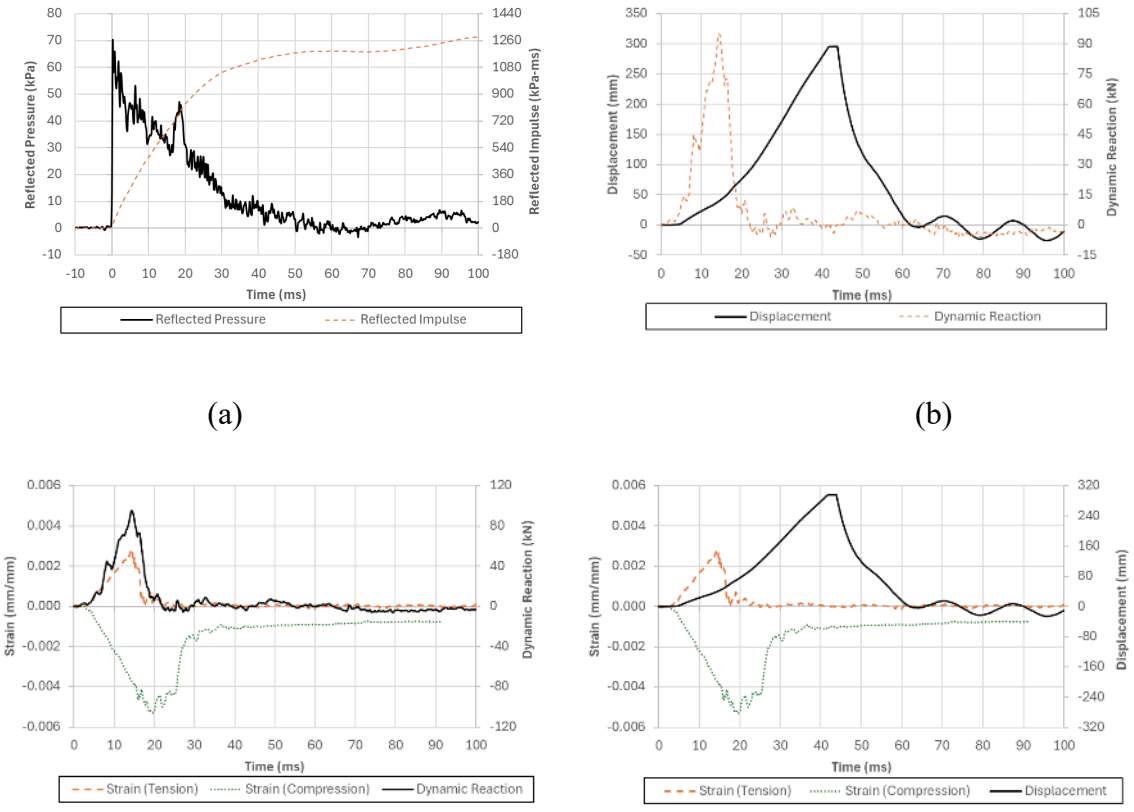

Figure E-4 Dynamic test results of GLT11 [130]: (a) Pressure- and impulse-time histories; (b) Displacement- Dynamic reaction histories; (c) Dynamic reaction-strain histories; (d) Displacement-strain histories

Specimen GLT12 [130]

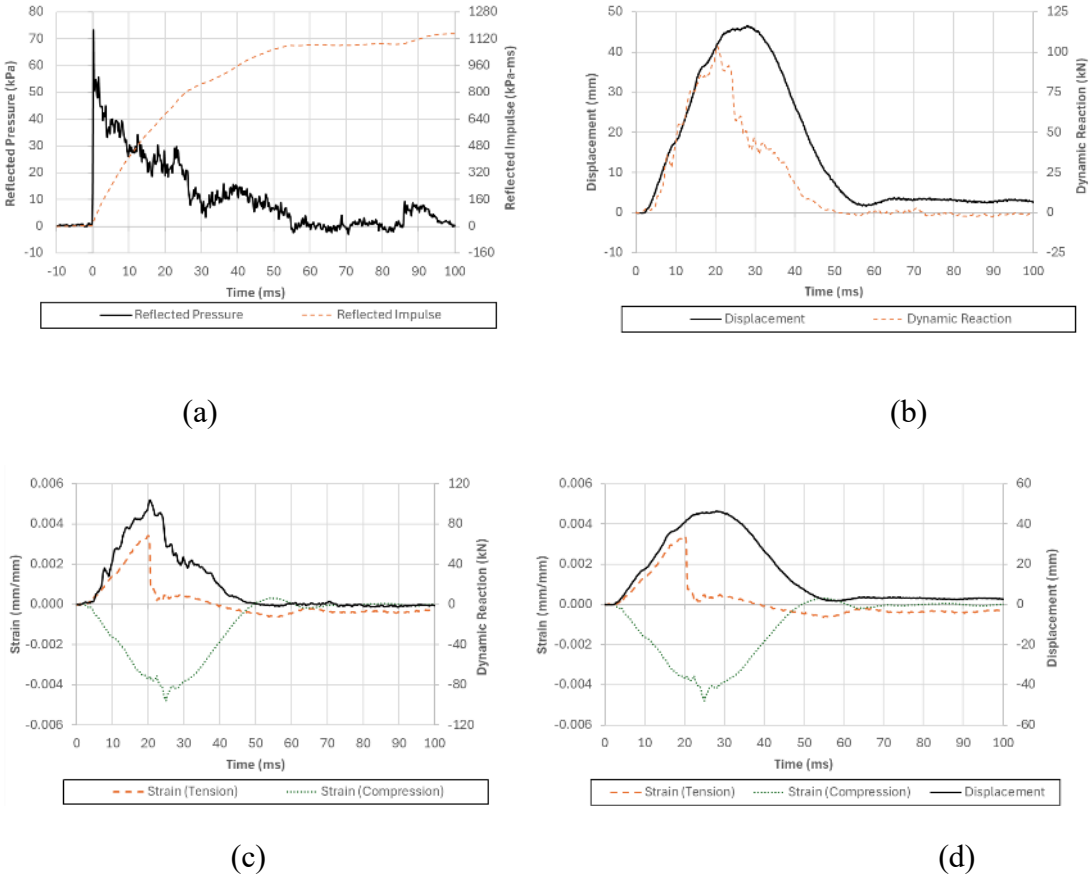

Figure E-5 Dynamic test results of GLT12 [130]: (a) Pressure- and impulse-time histories; (b) Displacement- Dynamic reaction histories; (c) Dynamic reaction-strain histories; (d) Displacement-strain histories

Specimen GLT13 [130]

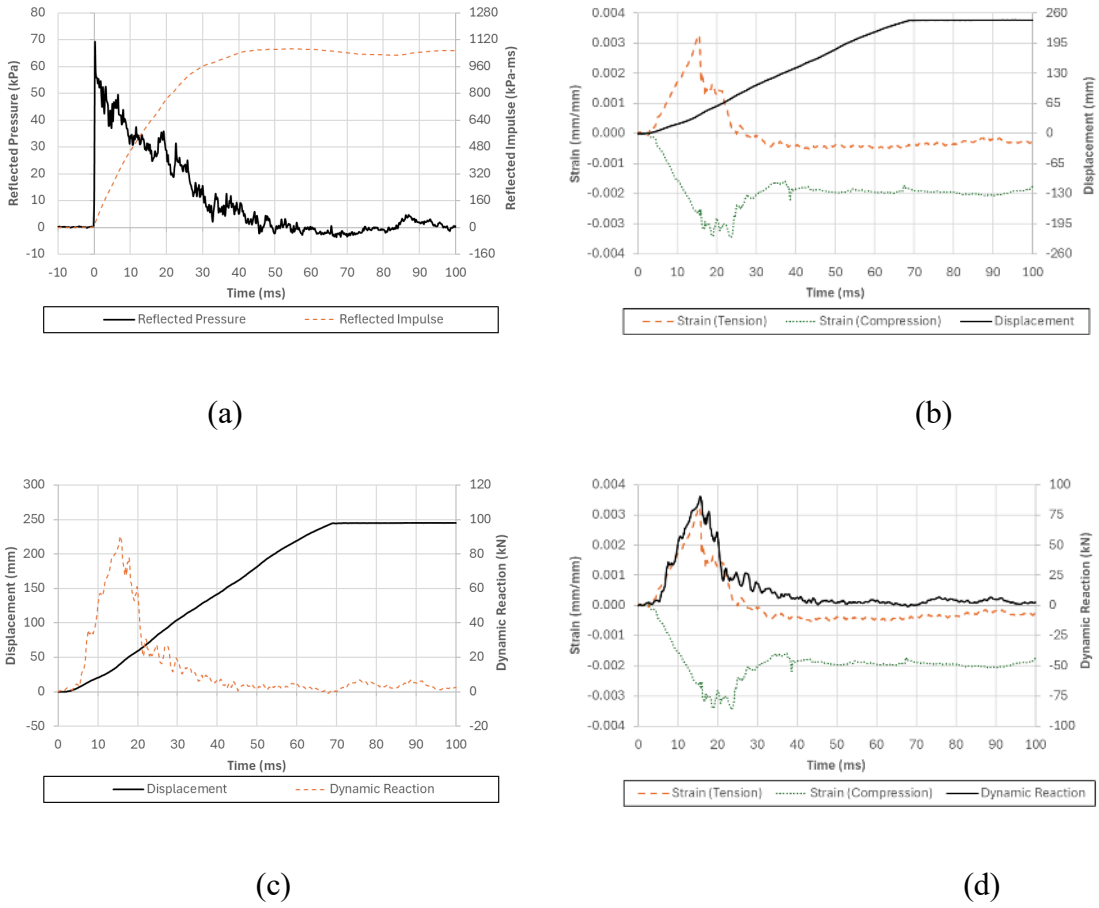

Figure E-6 Dynamic test results of GLT13 [130]: (a) Pressure- and impulse-time histories; (b) Displacement- Dynamic reaction histories; (c) Dynamic reaction-strain histories; (d) Displacement-strain histories

Specimen GLT14 [130]

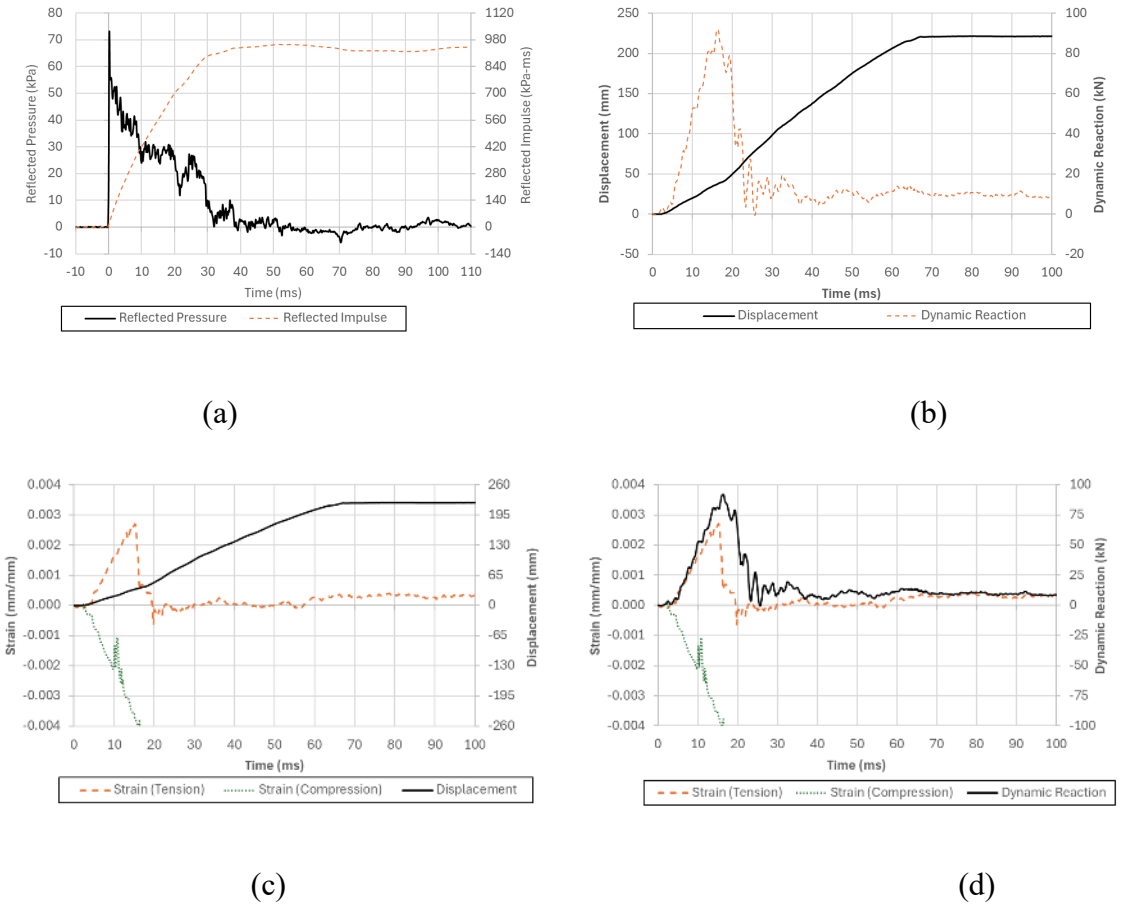

Figure E-7 Dynamic test results of GLT14 [130]: (a) Pressure- and impulse-time histories; (b) Displacement- Dynamic reaction histories; (c) Dynamic reaction-strain histories; (d) Displacement-strain histories

Specimen GLT15 [215]

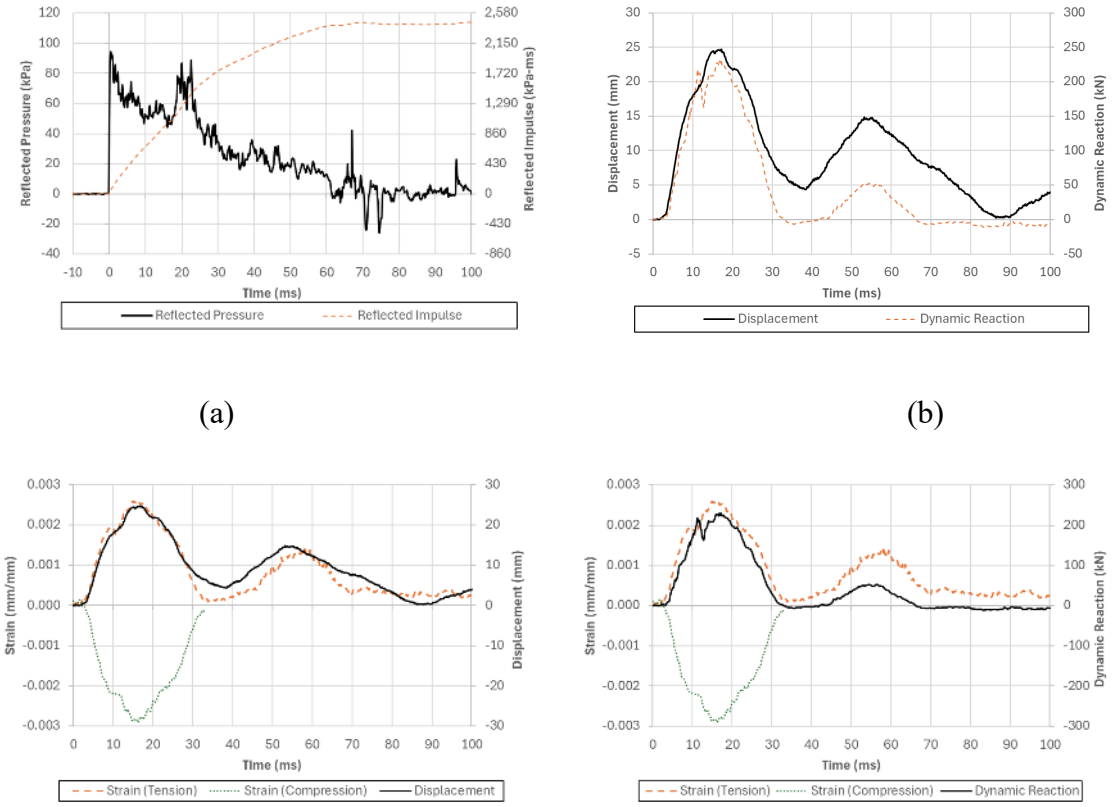

Figure E-8 Dynamic test results of GLT15 [215]: (a) Pressure- and impulse-time histories; (b) Displacement- Dynamic reaction histories; (c) Dynamic reaction-strain histories; (d) Displacement-strain histories

Specimen GLT16 [215]

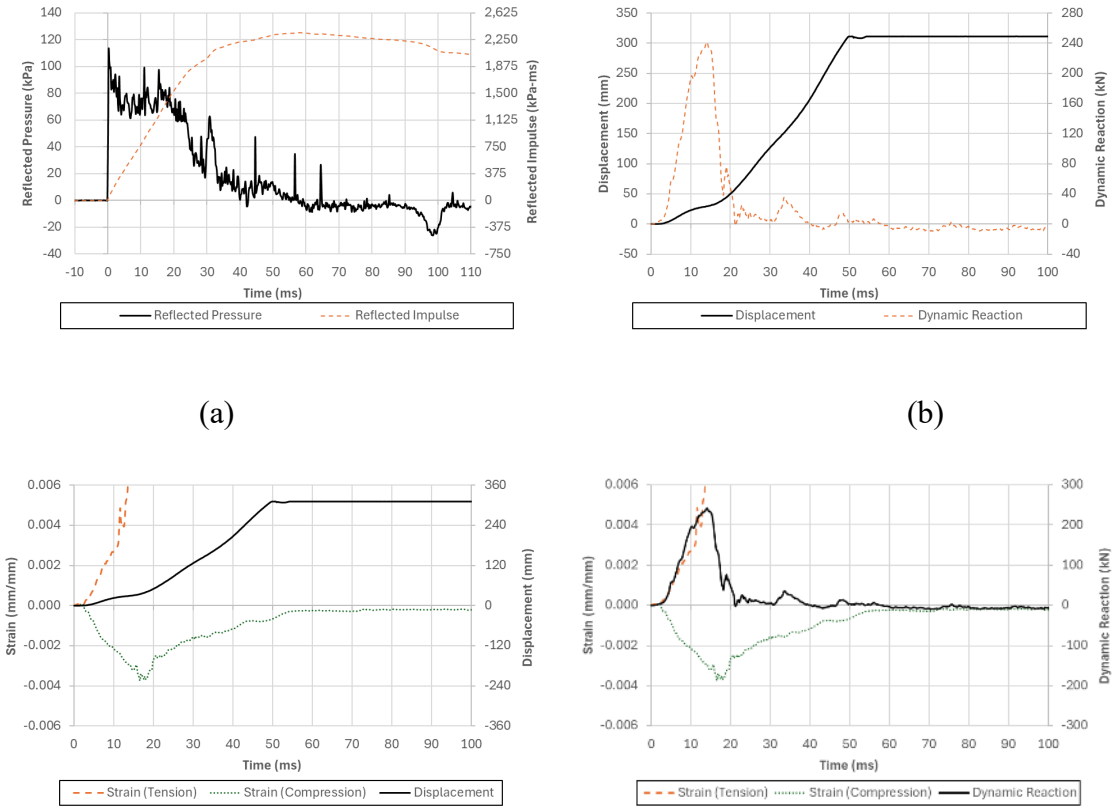

Figure E-9 Dynamic test results of GLT16 [215]: (a) Pressure- and impulse-time histories; (b) Displacement- Dynamic reaction histories; (c) Dynamic reaction-strain histories; (d) Displacement-strain histories

Specimen CGLT5 [215]

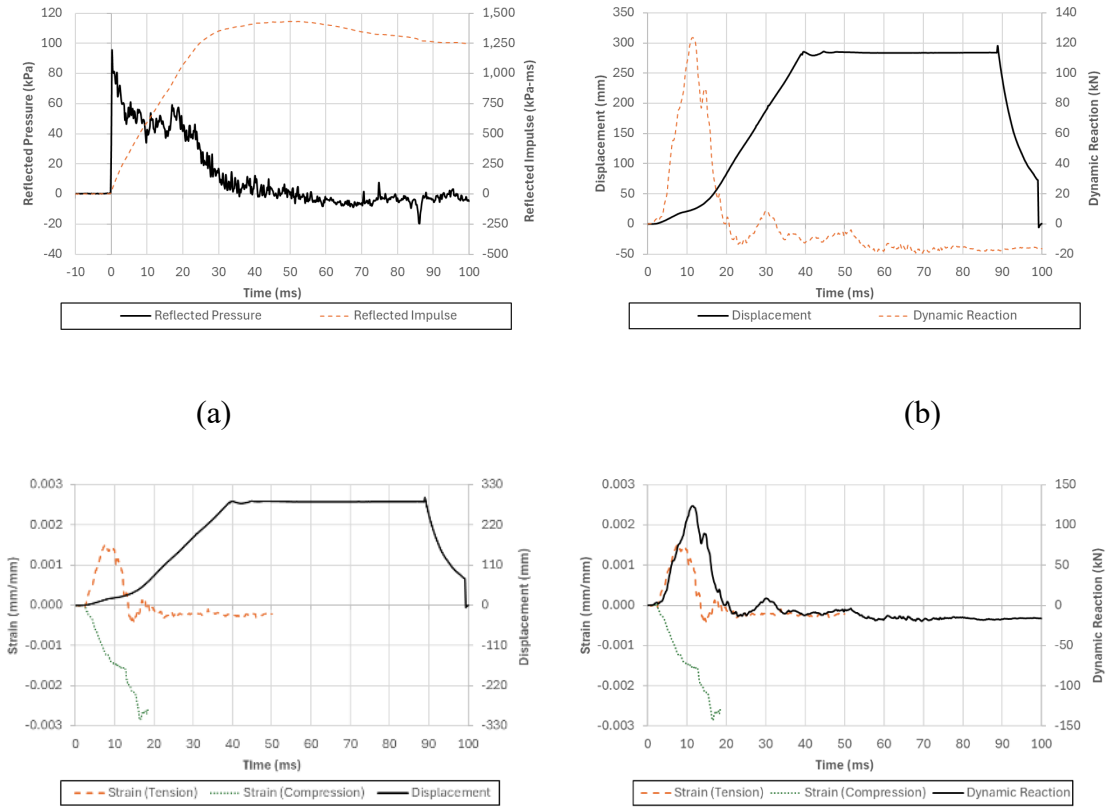

Figure E-10 Dynamic test results of CGLT15 [215]: (a) Pressure- and impulse-time histories; (b) Displacement- Dynamic reaction histories; (c) Dynamic reaction-strain histories; (d) Displacement-strain histories

Specimen CGLT6 [215]

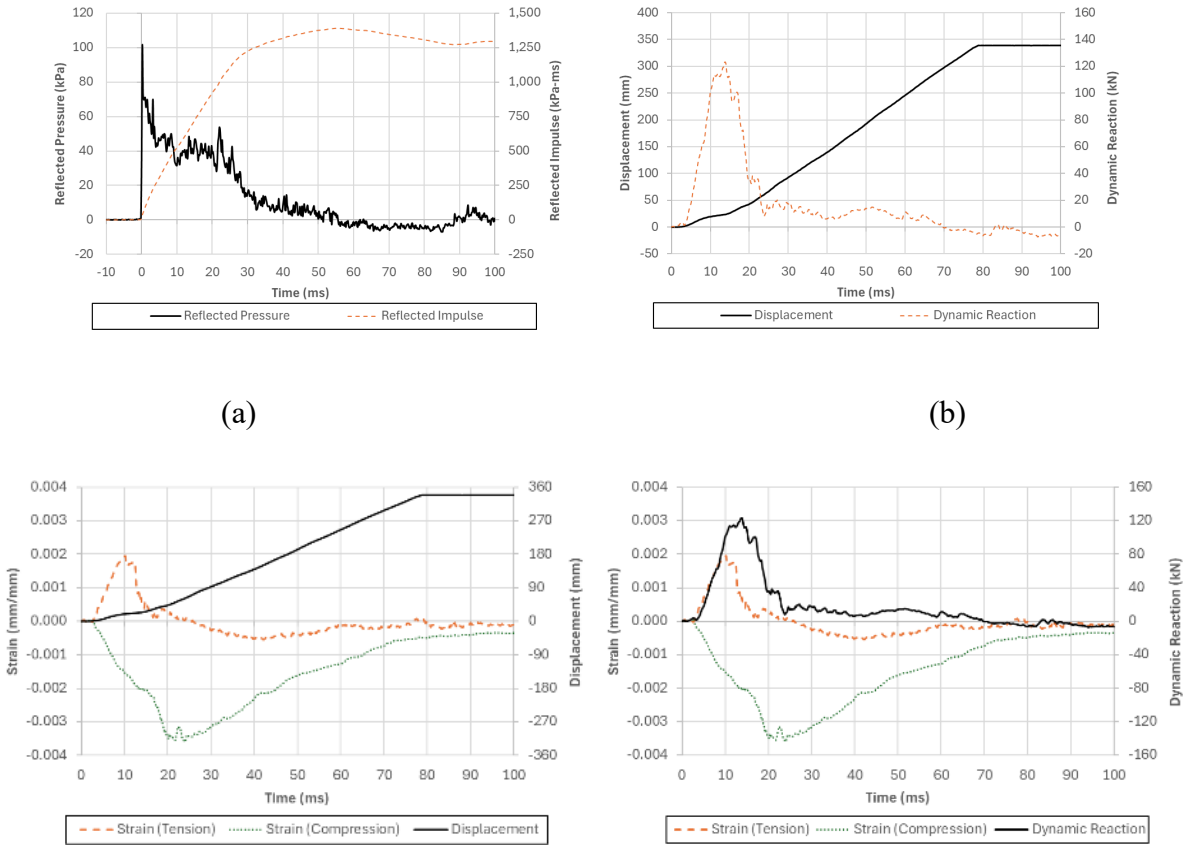

Figure E-11 Dynamic test results of CGLT16 [215]: (a) Pressure- and impulse-time histories; (b) Displacement- Dynamic reaction histories; (c) Dynamic reaction-strain histories; (d) Displacement-strain histories

Specimen CGLT7 [215]

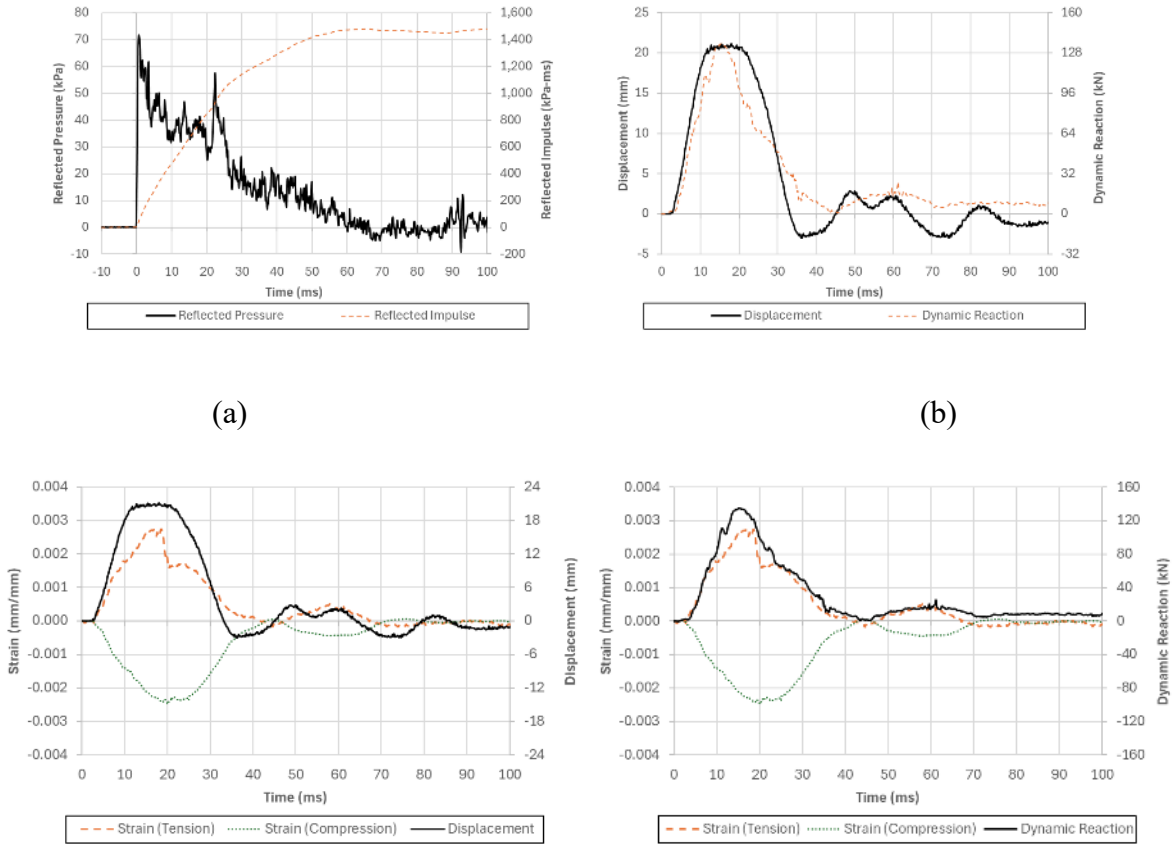

Figure E-12 Dynamic test results of CGLT17 [215]: (a) Pressure- and impulse-time histories; (b) Displacement- Dynamic reaction histories; (c) Dynamic reaction-strain histories; (d) Displacement-strain histories

Appendix F: SDOF Modelling Results

Specimen GLT8 [130]

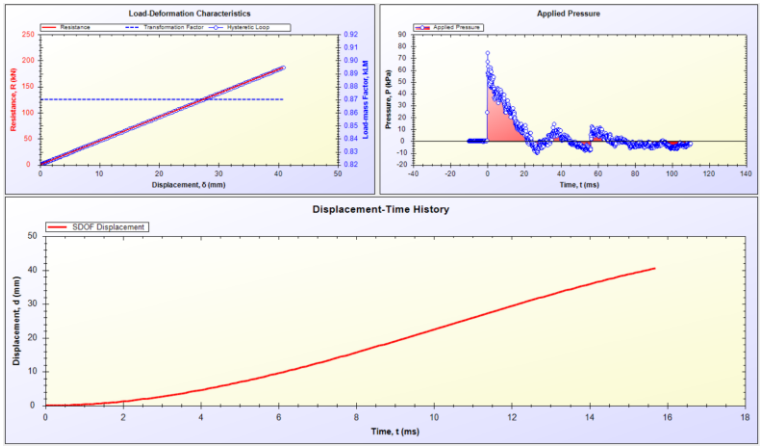

Figure F-1 SDOF Results - GLT8 [130]

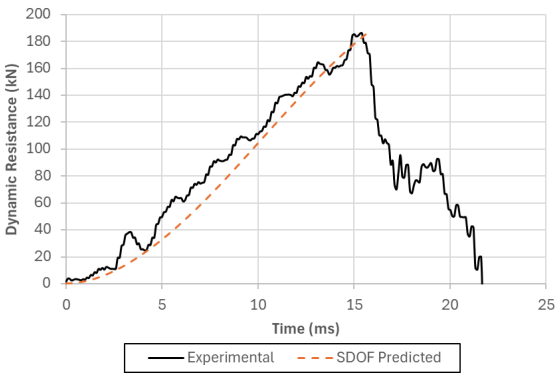

(a)

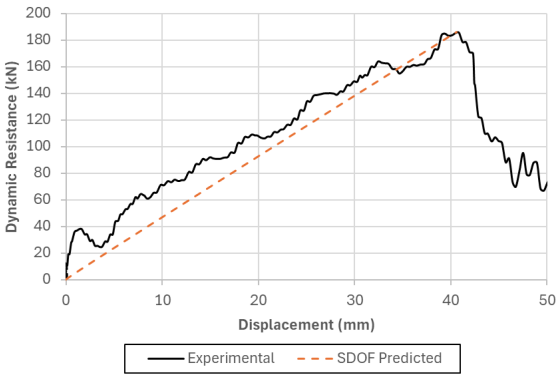

(b)

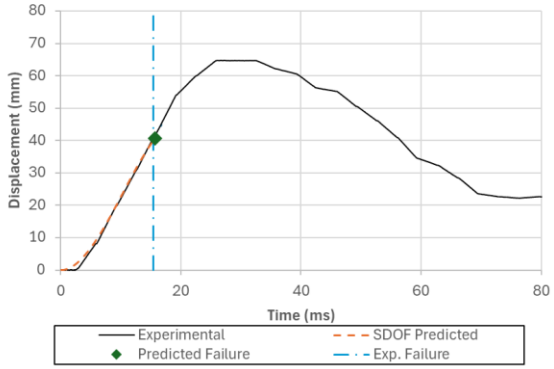

(c)

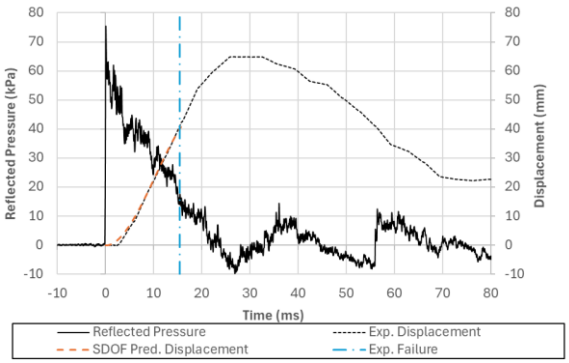

(d)

Figure F-2 Uncharred panel SDOF Model results compared to experimental results, GLT8 [130]: (a) Dynamic resistance-time history; (b) Dynamic resistance curves; (c) Displacement- time histories; (d) Reflected pressure and displacement- time histories.

Specimen GLT9 [130]

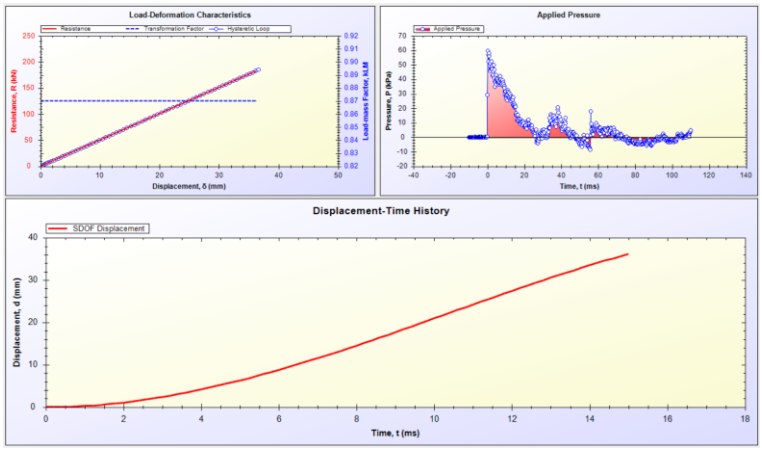

Figure F-3 SDOF Results – GLT9 [130]

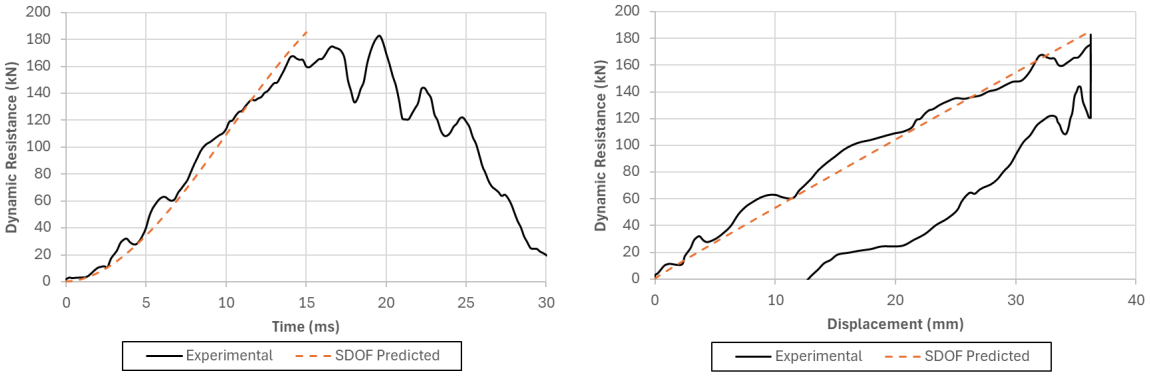

(a) (b)

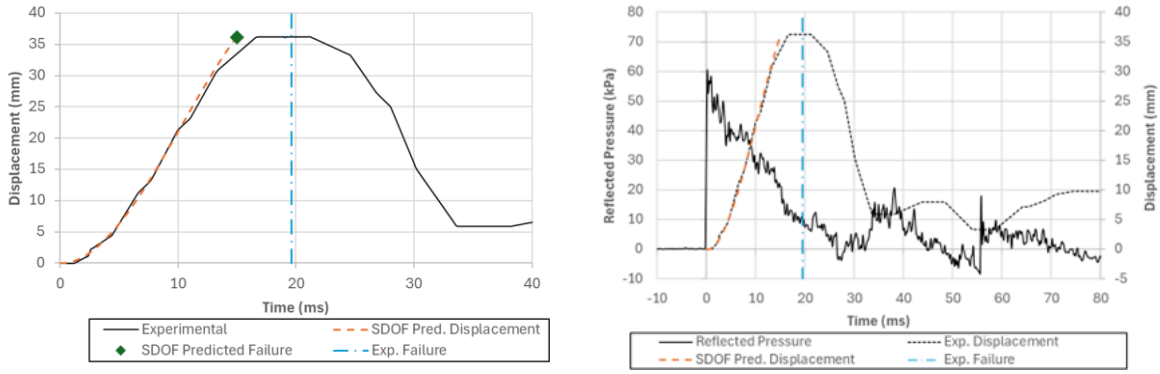

(c) (d)

Figure F-4 Uncharred panel SDOF Model results compared to experimental results, GLT9 [130]: (a) Dynamic resistance-time history; (b) Dynamic resistance curves; (c) Displacement- time histories; (d) Reflected pressure and displacement- time histories.

Specimens GLT10 [130]

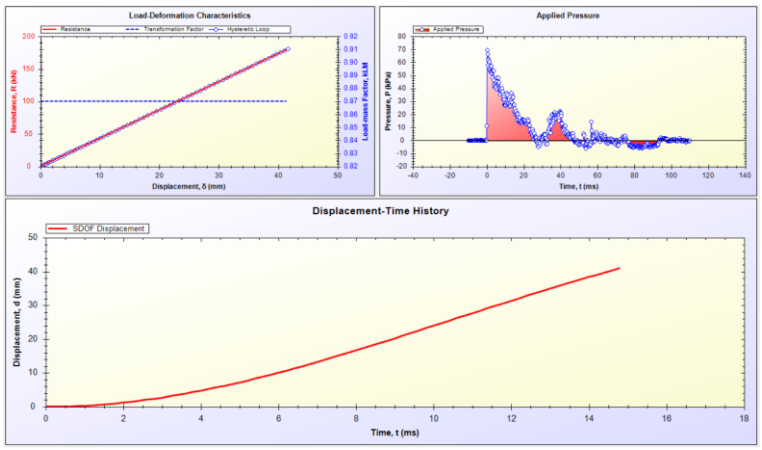

Figure F-5 SDOF Results – GLT10 [130]

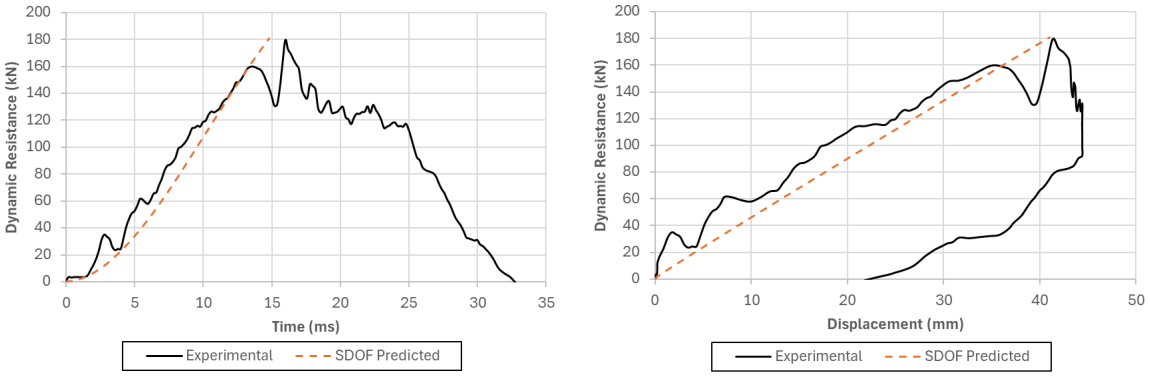

(a) (b)

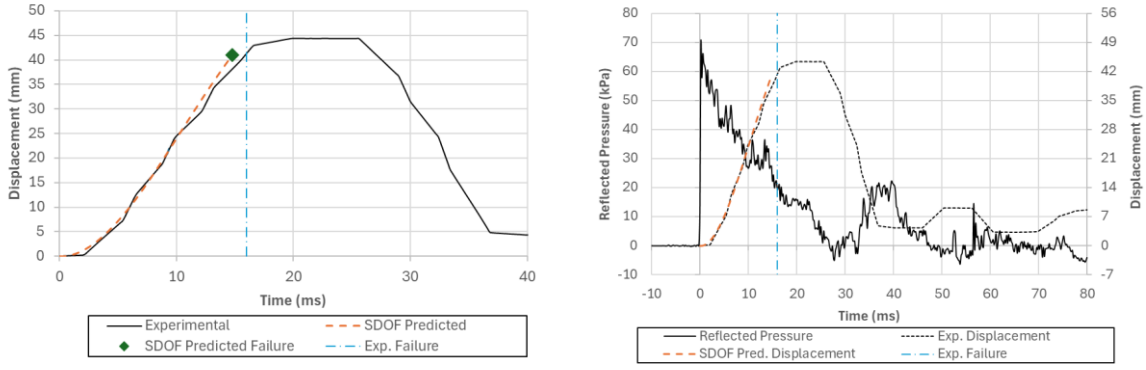

(c) (d)

Figure F-6 Uncharred panel SDOF Model results compared to experimental results, GLT10 [130]: (a) Dynamic resistance-time history; (b) Dynamic resistance curves; (c) Displacement- time histories; (d) Reflected pressure and displacement- time histories.

Specimen GLT11 [130]

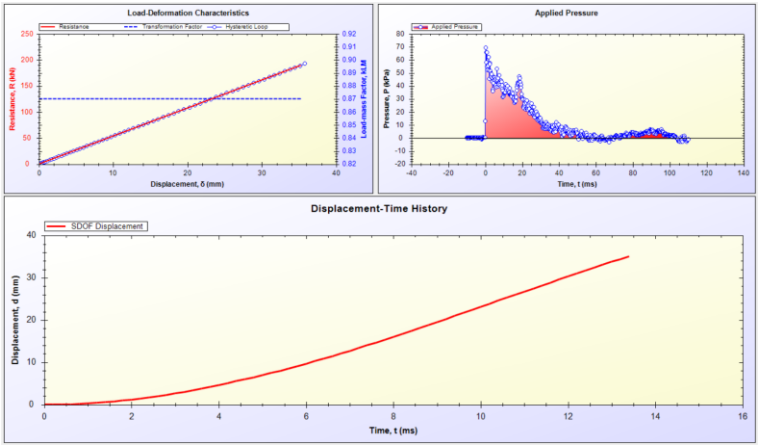

Figure F-7 SDOF Results – GLT11 [130]

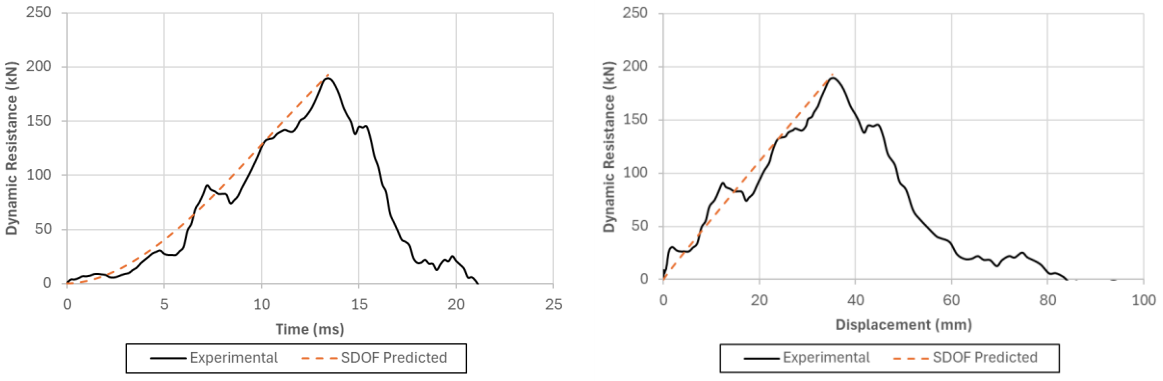

(a) (b)

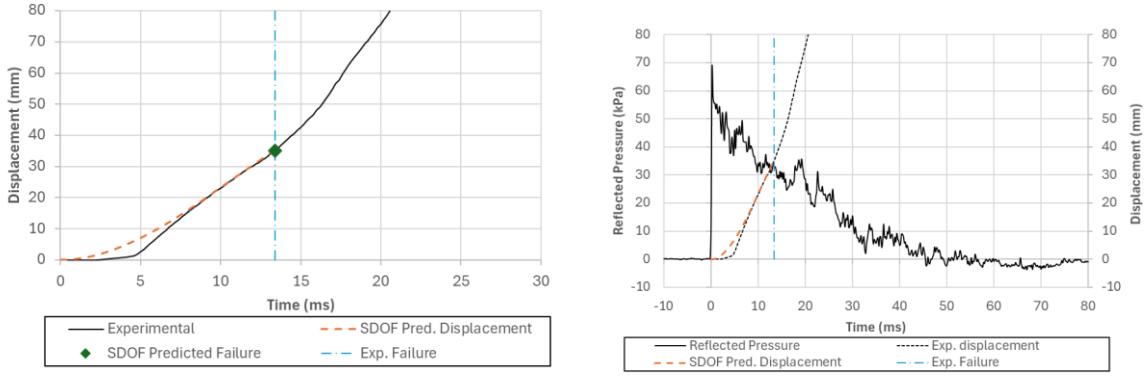

(c) (d)

Figure F-8 Uncharred panel SDOF Model results compared to experimental results, GLT11 [130]: (a) Dynamic resistance-time history; (b) Dynamic resistance curves; (c) Displacement- time histories; (d) Reflected pressure and displacement- time histories.

Specimen GLT12 [130]

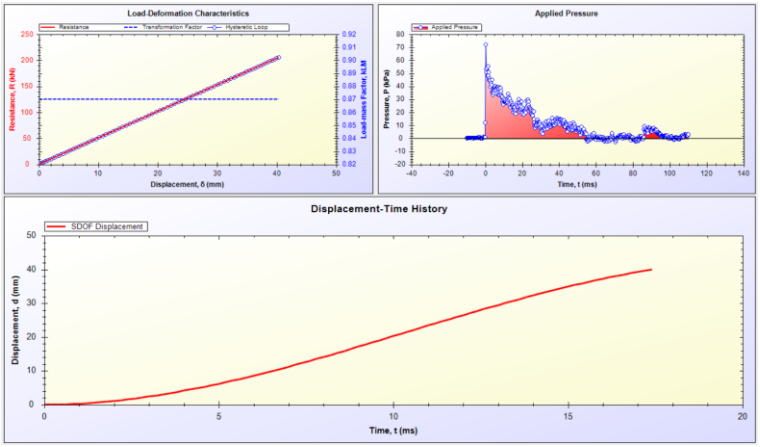

Figure F-9 SDOF Results – GLT12 [130]

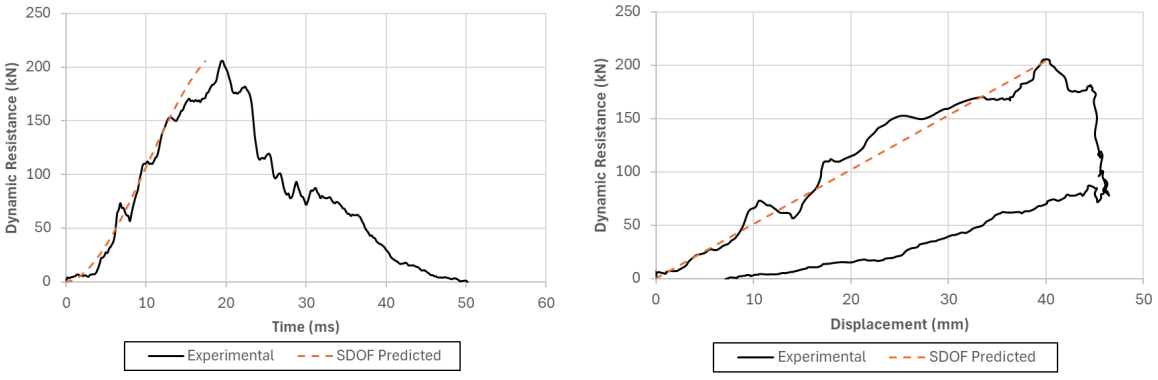

(a) (b)

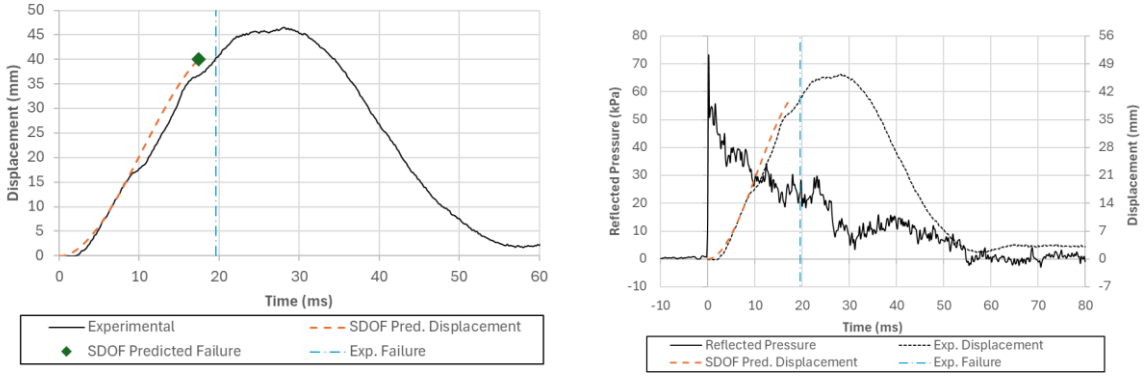

(c) (d)

Figure F-10 Uncharred panel SDOF Model results compared to experimental results, GLT12 [130]: (a) Dynamic resistance-time history; (b) Dynamic resistance curves; (c) Displacement- time histories; (d) Reflected pressure and displacement- time histories.

Specimen GLT13 [130]

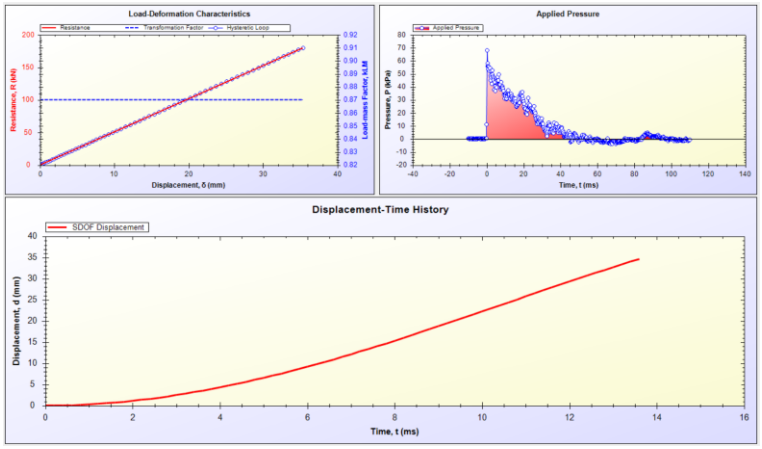

Figure F-11 SDOF Results – GLT13 [130]

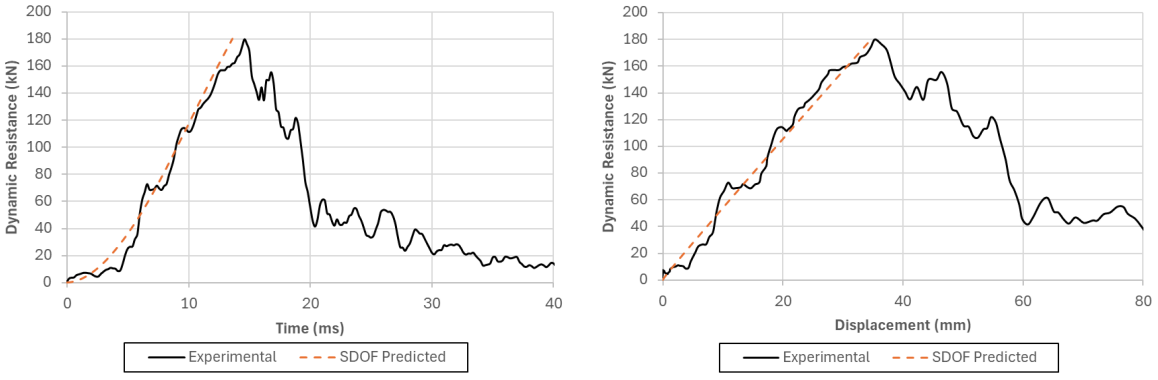

(a) (b)

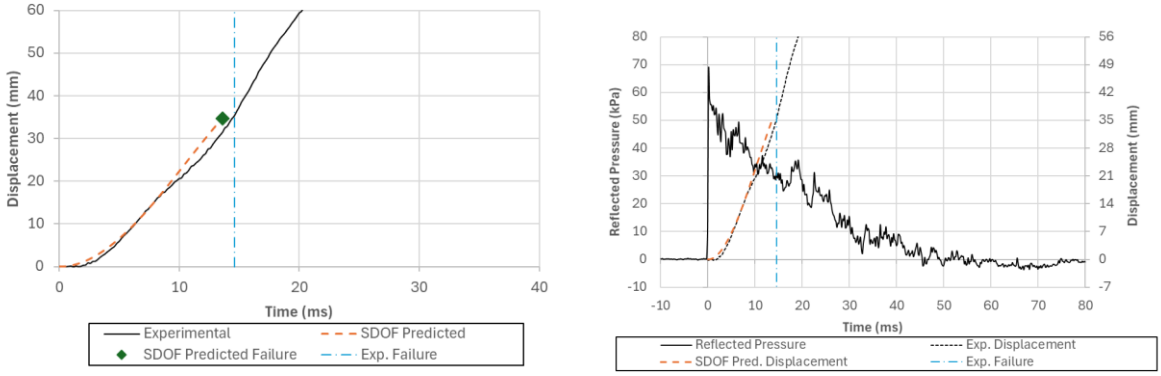

(c) (d)

Figure F-12 Uncharred panel SDOF Model results compared to experimental results, GLT13 [130]: (a) Dynamic resistance-time history; (b) Dynamic resistance curves; (c) Displacement- time histories; (d) Reflected pressure and displacement- time histories.

Specimen GLT14 [130]

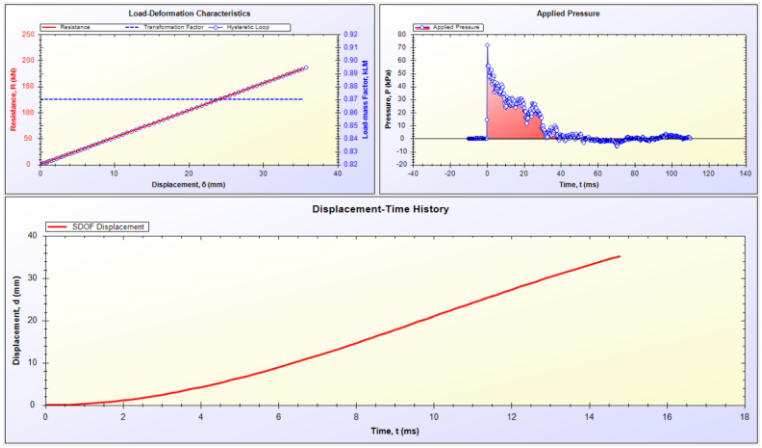

Figure F-13 SDOF Results – GLT14 [130]

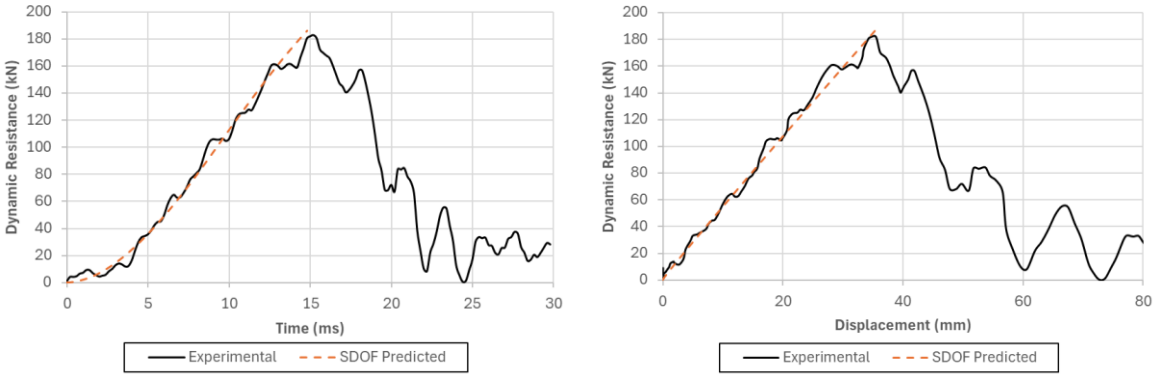

(a) (b)

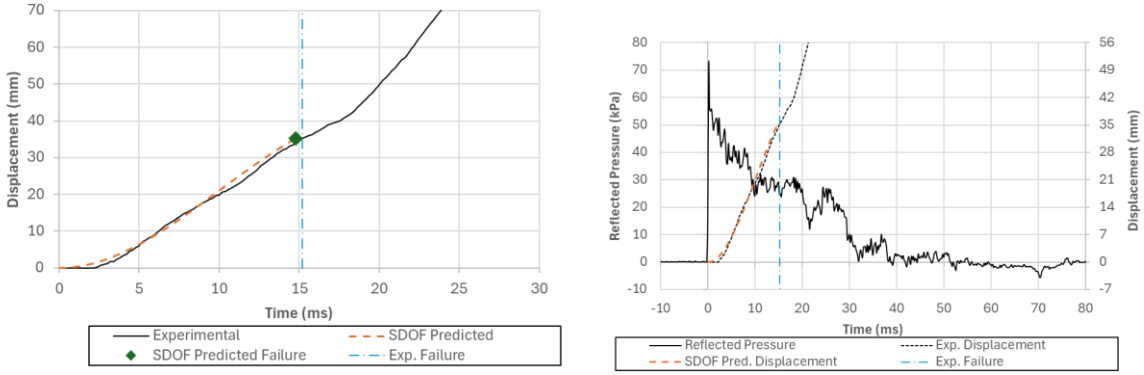

(c) (d)

Figure F-14 Uncharred panel SDOF Model results compared to experimental results, GLT14 [130]: (a) Dynamic resistance-time history; (b) Dynamic resistance curves; (c) Displacement- time histories; (d) Reflected pressure and displacement- time histories.

Specimen GLT15 [215]

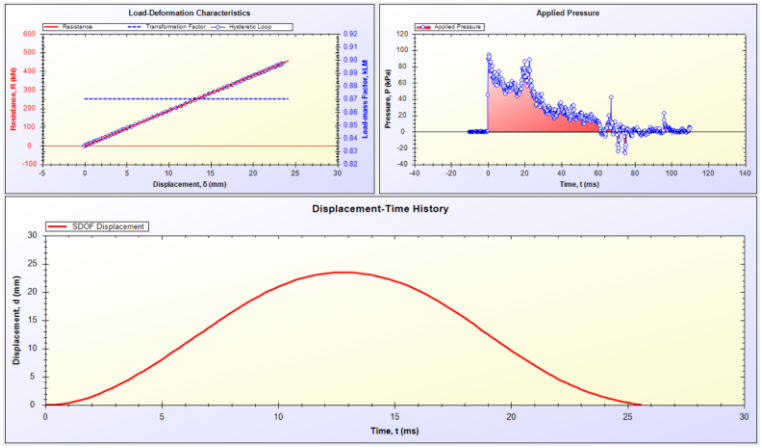

Figure F-15 SDOF Results – GLT15 [215]

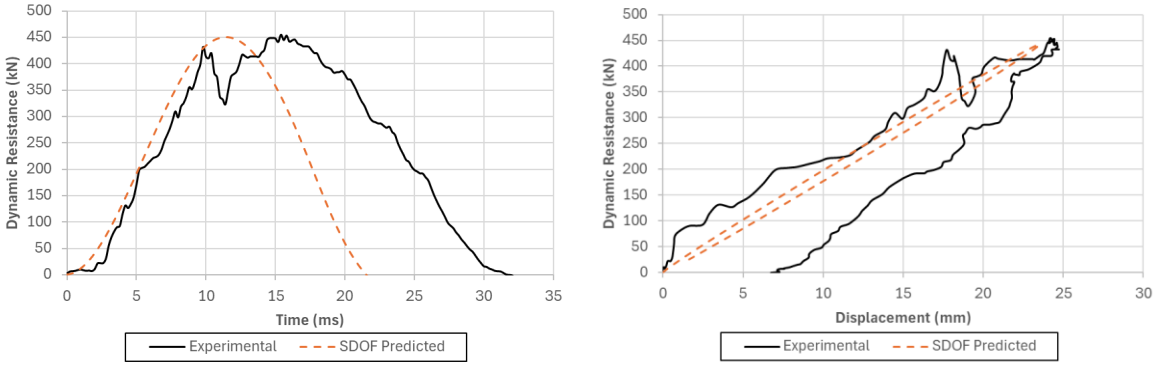

(a) (b)

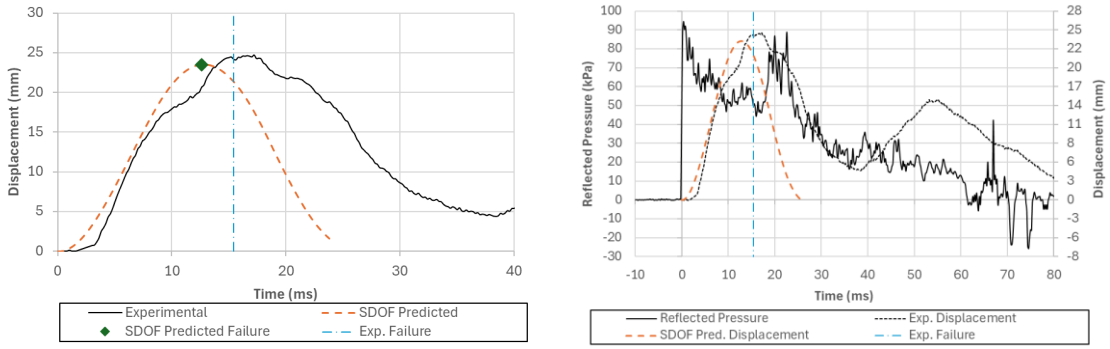

(c) (d)

Figure F-16 Uncharred panel SDOF Model results compared to experimental results, GLT15 [215]: (a) Dynamic resistance-time history; (b) Dynamic resistance curves; (c) Displacement- time histories; (d) Reflected pressure and displacement- time histories.

Specimen GLT16 [215]

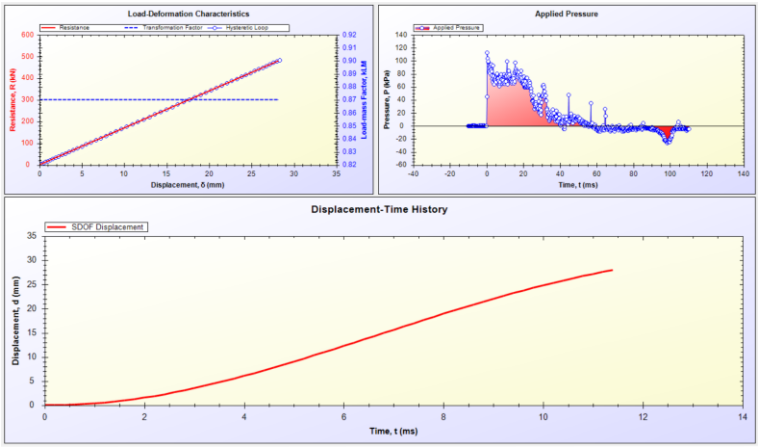

Figure F-17 SDOF Results – GLT16 [215]

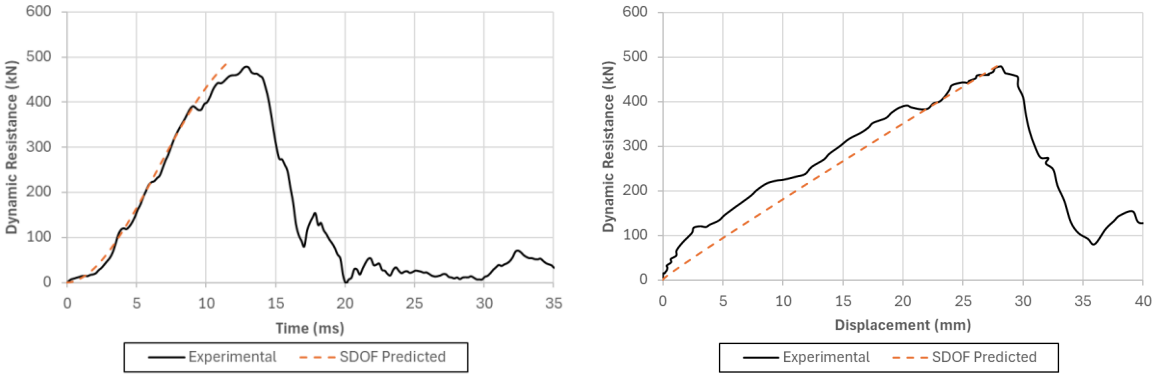

(a) (b)

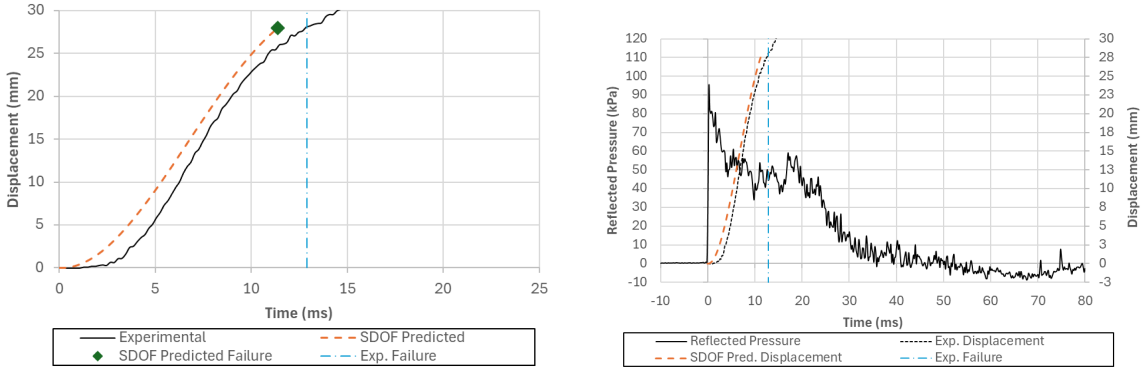

(c) (d)

Figure F-18 Uncharred panel SDOF Model results compared to experimental results, GLT16 [215]: (a) Dynamic resistance-time history; (b) Dynamic resistance curves; (c) Displacement- time histories; (d) Reflected pressure and displacement- time histories.

Specimen CGLT5 [215]

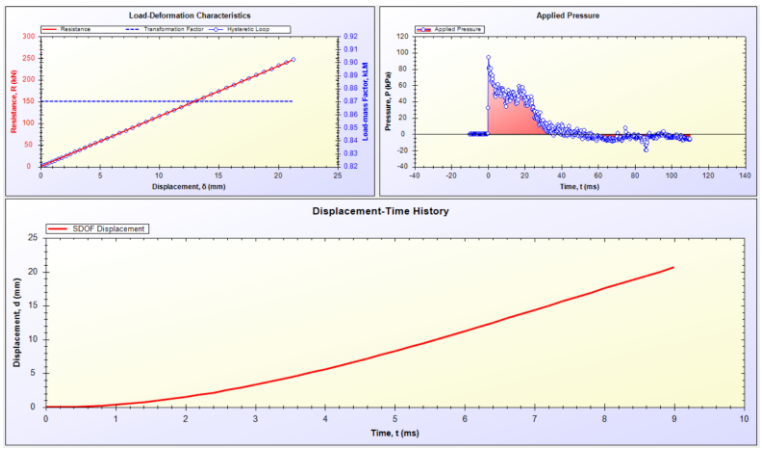

Figure F-19 SDOF Results – CGLT5 [215]

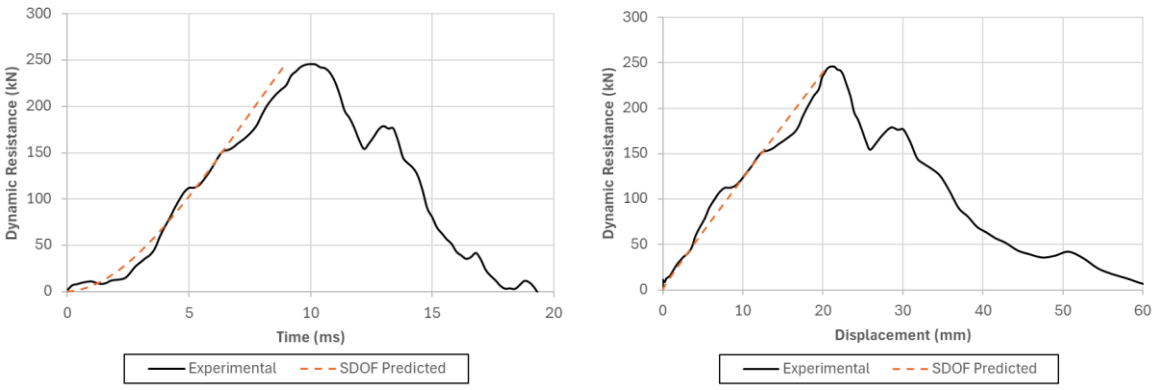

(a) (b)

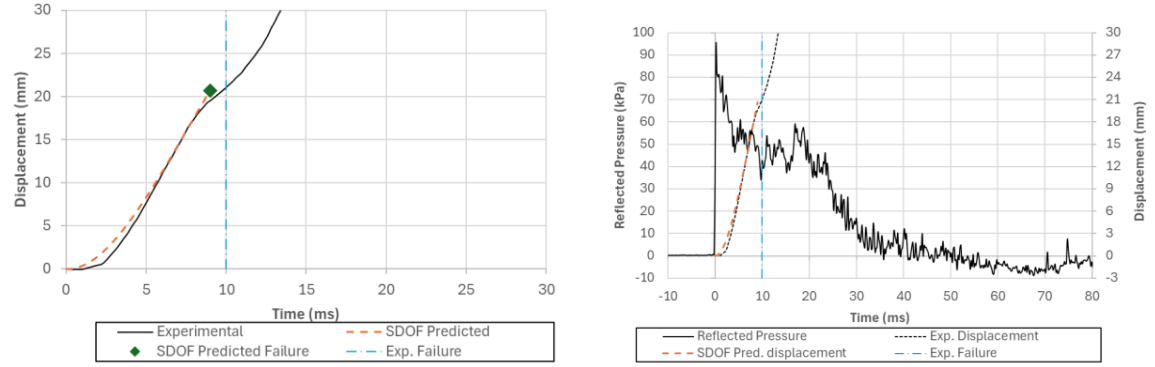

(c) (d)

Figure F-20 Charred panel SDOF Model results compared to experimental results, CGLT5 [215]: (a) Dynamic resistance-time history; (b) Dynamic resistance curves; (c) Displacement- time histories; (d) Reflected pressure and displacement- time histories.

Specimen CGLT6 [215]

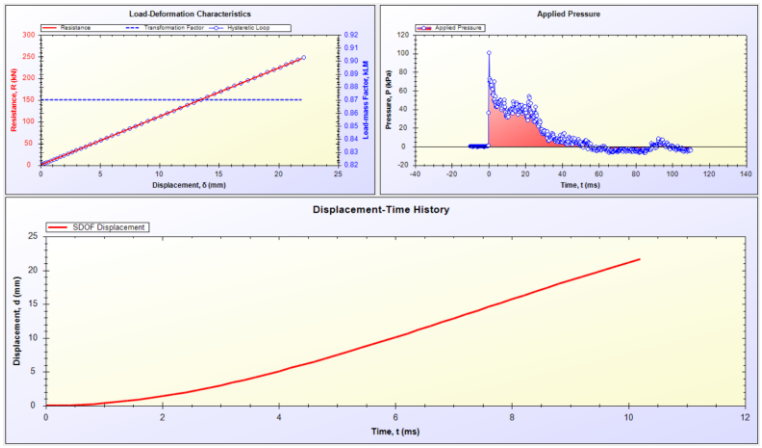

Figure F-21 SDOF Results – CGLT6 [215]

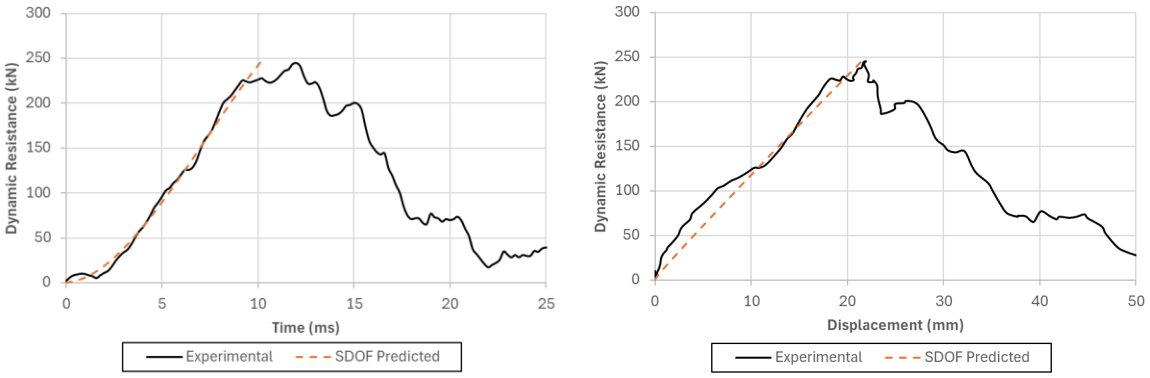

(a) (b)

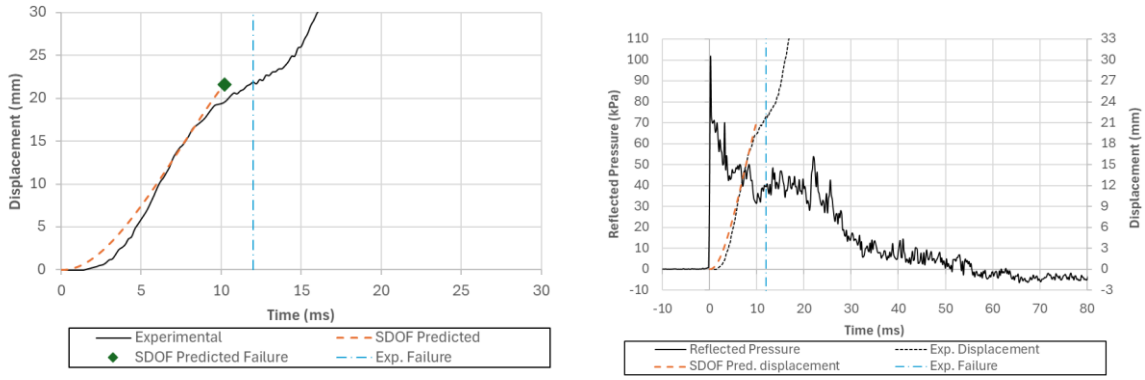

(c) (d)

Figure F-22 Charred panel SDOF Model results compared to experimental results, CGLT6 [215]: (a) Dynamic resistance-time history; (b) Dynamic resistance curves; (c) Displacement- time histories; (d) Reflected pressure and displacement- time histories.

Specimen CGLT7 [215]

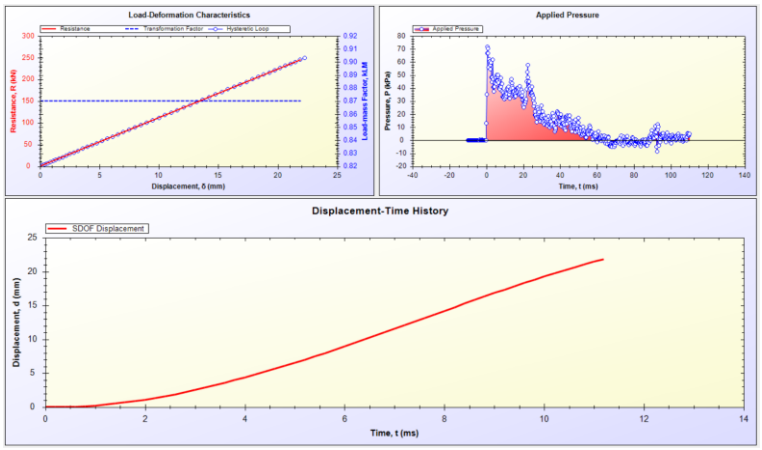

Figure F-23 SDOF Results – CGLT7 [215]

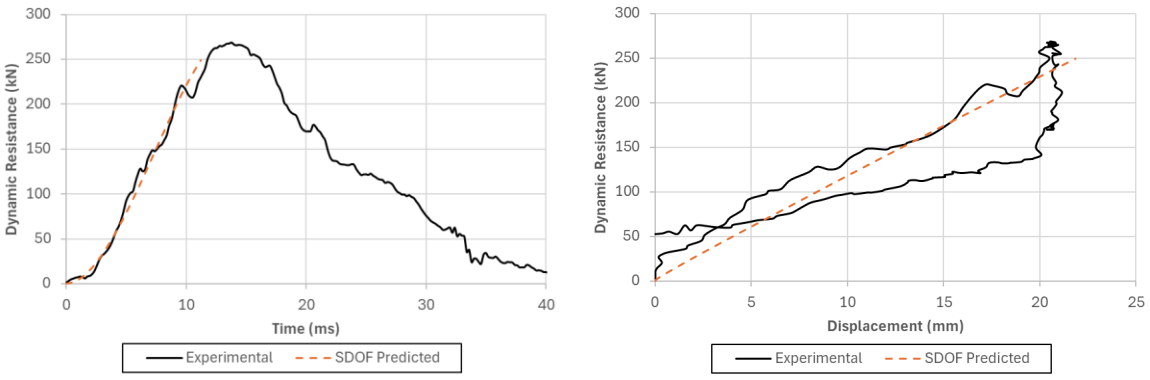

(a) (b)

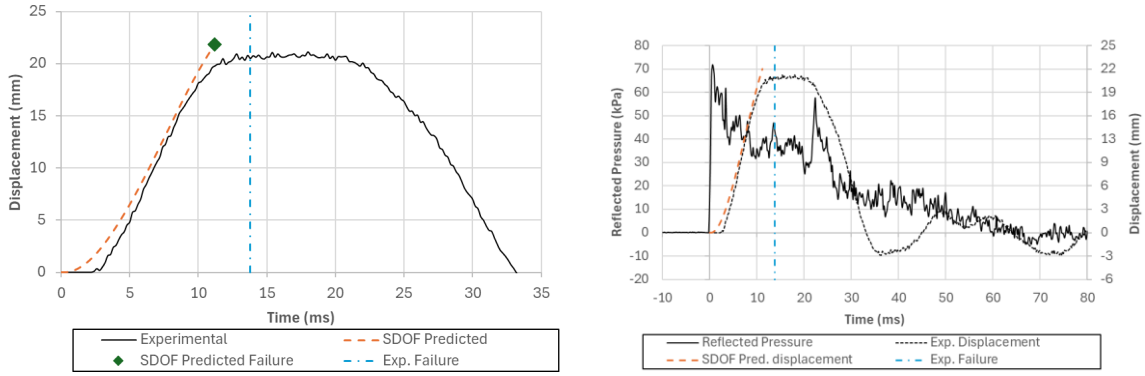

(c) (d)

Figure F-24 Charred panel SDOF Model results compared to experimental results, CGLT7 [215]: (a) Dynamic resistance-time history; (b) Dynamic resistance curves; (c) Displacement- time histories; (d) Reflected pressure and displacement- time histories.